Durham E-Theses

Probing the standard model and beyond at high-energy colliders

Heyssler, Matthias

How to cite:

Use policy

UNIVERSITY OF DURHAM
Centre for Particle Theory

Probing the Standard Model

and Beyond

at High–Energy Colliders

A thesis presented for the degree of
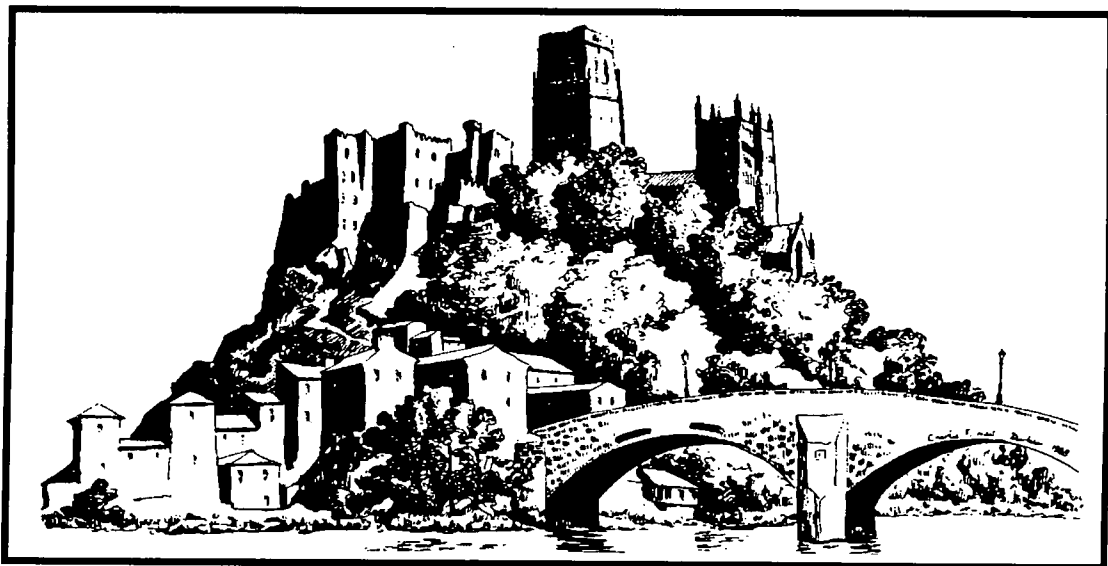
Doctor of Philosophy

by

Matthias Heyssler

Durham, March 1998.

Abstract

The thesis covers the following topics:

Assuming a partonic structure of the Pomeron we give predictions for diffractive heavy flavour production at the TEVATRON and the LHC and diffractive Higgs production at the LHC in leading–order approximation. For the latter the dominant background processes are also considered. We obtain results on single as well as double diffractive cross sections assuming a Donnachie–Landshoff–type Pomeron flux factor.

Measurements of the single inclusive jet cross section at the TEVATRON by the CDF Collaboration maybe suggest a modified picture of QCD in the large E_T range. A parameter fit of a neutral heavy vector boson Z' to the CDF data, in leading order perturbation theory, is performed, and the question of how the corresponding single inclusive jet cross sections and the dijet angular distributions at the LHC are affected by this additional Z' is discussed.

We test a model, motivated by the former R_b and R_c "crisis", which contains extra vector fermions. We suggest an alternative indirect test of the possible existence of new heavy quark flavours at the LEP2 collider, which turns out to give the clearest signal. We calculate $q\bar{q}$ cross sections within this framework, including one loop corrections.

Hadronic antenna patterns can provide a valuable diagnostic tool for probing the origin of the reported excess of high x, Q^2 events at HERA. We present quantitative predictions for the distributions of soft particles and jets in standard deep inelastic scattering $eq \rightarrow eq$ events and in events corresponding to the production of a narrow colour–triplet scalar resonance.

We also study the patterns corresponding to Higgs production and decay in high-energy hadron–hadron collisions. In particular, the signal $gg \rightarrow H \rightarrow b\bar{b}$ and background $gg \rightarrow b\bar{b}$ processes are shown to have very different radiation patterns, and this may provide a useful additional method for distinguishing Higgs signal events from the QCD background.

The process $eq \rightarrow eq + \gamma$ exhibits radiation zeros, i.e. configurations of the final–state particles for which the scattering amplitude vanishes. We study these zeros for both e^+u and e^+d scattering. The latter exhibits a new type of zero which to our knowledge has not previously been identified. The observability of radiation zeros at HERA is discussed. In the framework of this new type of zero we also study the process $e^+e^- \rightarrow q\bar{q}\gamma$. We calculate the positions of these zeros for u–quark and d–quark production and assess the feasibility of identifying the zeros in experiments at high energies. The radiation zeros are shown to occur also for massive quarks, and we discuss how the $b\bar{b}\gamma$ final state may offer a particularly clean environment in which to observe them.

Declaration

I declare that no material in this thesis has previously been submitted for a degree at this or any other university.

The work in this thesis has partially been carried out in collaboration with Prof. W.J. Stirling, Prof. Z. Kunszt, Prof. V.A. Khoze and Dr. V.C. Spanos. Any non-original material in this thesis is referenced and acknowledged. The thesis is mainly based on the following publications:

(1) Diffractive Heavy Flavour Production at the Tevatron and the LHC
M. Heyssler, *Z. Phys.* **C73** 299 (1997).

(2) A leptophobic massive Vector Boson at the Tevatron and the LHC
M. Heyssler, *Phys. Rev.* **D54** 5845 (1996).

(3) Testing a Model with additional Vector Fermions
M. Heyssler and V.C. Spanos, *Mod. Phys. Lett.* **A12** 393 (1997).

(4) Diffractive Higgs Production at the LHC
M. Heyssler, Z. Kunszt and W.J. Stirling, *Phys. Lett.* **B406** 95 (1997).

(5) Hadronic Antenna Patterns as a Probe of Leptoquark Production at HERA
M. Heyssler and W.J. Stirling, *Phys. Lett.* **B407** 259 (1997).

(6) Radiation Zeros at HERA – More about Nothing
M. Heyssler and W.J. Stirling, *European Physical Journal* **C** in press (1998).

(7) Radiation Zeros in High–Energy e^+e^- Annihilation into Hadrons
M. Heyssler and W.J. Stirling, *European Physical Journal* **C** in press (1998).

(8) Hadronic Radiation Patterns for Higgs Production at Hadron Colliders
M. Heyssler, V.A. Khoze and W.J. Stirling, *Durham preprint DTP/97/104*, submitted to *Phys. Rev.* **D** (1998).

and presentations at conferences and workshops.

Acknowledgement

It is a great pleasure for me to thank my supervisor Prof. W.J. Stirling. Within the last three years he certainly could not do wonders and make a *'phenomenology expert'* out of me, but he invoked the necessary enthusiasm inside of me for working on so many different topics. Thanks for letting me be part of the group. It was a great time.

Profs. A.D. Martin and J. Kwieciński are thanked for giving me the opportunity of a joint degree Durham–Kraków, as this meant *'hard work'* for both of them and finally leads to *'incredible fame'* for me. Prof. J. Kwieciński is especially thanked for finding me a physical home at the *H. Niewodniczański Institute of Nuclear Physics* in Kraków. I am very grateful to the TEMPUS scheme to enable me to undertake the Durham–Kraków degree.

Then there are the people from the third floor of the physics department in Durham. Too numerous to be thanked individually. Thanks to my (former) roommates John, Ricardo, Matt and Tom, my good old friends Nektaris and Alekos, and all the others who helped to make this place quite special. Special thanks to Pete and Sabine. We had a great laugh together.

Dr. K. Golec–Biernat, Dr. M. Melles and Dr. M. Wüsthoff are thanked for patiently reading parts of the manuscript and many discussions about various subjects. Michael (Mr. *Colour–Factor*) is thanked for sharing with me Borussia's fate on Saturdays.

Thanks also to Dr. Vassilis Spanos and Dr. Kostas Philippides for a wonderful collaboration in the past (Vassilis) or a great collaboration at present (Kostas). Anyway, we did not *always* discuss physics.

The DAAD is thanked for awarding me a grant which made my PhD in Durham possible.

This thesis is dedicated to Anna and Eryk.

Table of Contents

List of Tables

List of Figures

Preface

"God grant that no one else has done
The work I want to do,
Then give me the wit to write it up
In decent English, too."

The Standard Model (SM) of the elementary particles and their interactions can be regarded as well understood and well tested. However, many interesting issues need further investigations. These are essential

- to address open questions *within* the SM,

- to search for new physics *beyond* the SM.

In this thesis we present a phenomenological study of many subjects directly related to the SM (or going beyond the SM) which includes *both* points addressed above.

Chapter 1:

The first chapter studies one of the cornerstones of the SM, the strong interaction Quantum Chromodynamics (QCD), or more specifically: non–perturbative QCD in the framework of *Regge theory*. Regge theory is not yet understood at a '*first principles*' level. With the introduction of the *Pomeron*, a special kind of Reggeon, in order to explain *rapidity gaps* in high–energy collisions, many new open questions arose. The interplay of *soft* and *hard* interactions is certainly the most striking feature that the Pomeron has to deal with. We shall test the *soft Pomeron* at high–energy scales and discuss diffractive heavy flavour and Higgs production at present and future hadron–hadron colliders in this framework. These studies are essential to learn more about the '*nature*' of the Pomeron.

Chapter 2:

In this chapter we address topics that lead *beyond* the SM. Motivated by measured experimental anomalies from the TEVATRON and LEP colliders, we discuss the impact of a heavy equivalent to the SM Z boson at present and future hadron–hadron colliders. We introduce a new heavy vector quark triplet and test its impact at LEP1 and LEP2.

1

Chapter 3:

An important diagnostic tool for probing the SM and especially searching for new physics beyond the SM are soft photon and gluon *antenna patterns*, i.e. emission of additional gluons (photons) in high–energy processes. After some basic definitions and derivations we show how these antenna patterns can be used to help identify the Higgs boson at the future LHC proton–proton collider. Another topic of this chapter will be a study of the reported *high–Q^2* events from HERA. Again, using antenna patterns, we try to gain further insight into the underlying mechanism of this (possible) anomaly.

Chapter 4:

Finally, we discuss *radiation zeros* in processes emitting additional photons at the *tree–level*. These zeros are a consequence of complete destructive interference between initial– and final–state radiation and are a feature of any field theory. Thus radiation zeros are in principle present in *any* processes involving the emission of photons, gluons or other massless vector bosons. Very often, however, there are no physical solutions to be found. We study a *new type* of radiation zero, not discussed in the literature before. As these zeros are features of the SM, it is important to give predictions for their observability in high–energy processes. The appearance of radiation zeros is also very sensitive to gauge couplings and thus provides an excellent test of the SM and new physics beyond.

A very brief summary at the end highlights the most important results obtained during these studies.

Chapter 1

Diffraction and the Pomeron

"By trying to find a meaning to everything, you appear excessively suspicious."

(Laotse)

In this chapter we study the influence of the Pomeron in high–energy physics. Since the study of diffractive events at modern high–energy colliders (discussion in Section 1.1), the Pomeron gained a renewed interest to explain the observed *rapidity gaps*. The accepted explanation is the exchange of a colourless object, carrying the quantum numbers of the *vacuum*. In the following we shall give a brief introduction into the experimental situation as well as describe a model we adopted for our studies, the soft–Pomeron model by Donnachie and Landshoff in Section 1.2. To do this we shall also discuss the pinnacles of high–energy scattering that immensely contribute to our understanding of diffraction

- the optical theorem,

- the Froissart–Martin bound,

- the Pomeranchuk theorem.

This will be the scope of Section 1.2. Introducing parton distribution functions for the Pomeron in Section 1.3, we give predictions for diffractive Higgs (Section 1.4) and heavy flavour production (Section 1.5) at the TEVATRON and/or the LHC. A critical discussion of our results finishes this chapter, basically dealing with the breaking of factorisation in diffractive events and the possible problems with the Donnachie–Landshoff model in Section 1.7. Recent results on diffraction as measured at HERA and the TEVATRON are presented in Section 1.6. Throughout this study we shall present the results in *chronological* order, as they were published. This should clarify our approach to diffraction.

A short summary of the present status of the Pomeron and a presentation of a few alternative models conclude this chapter.
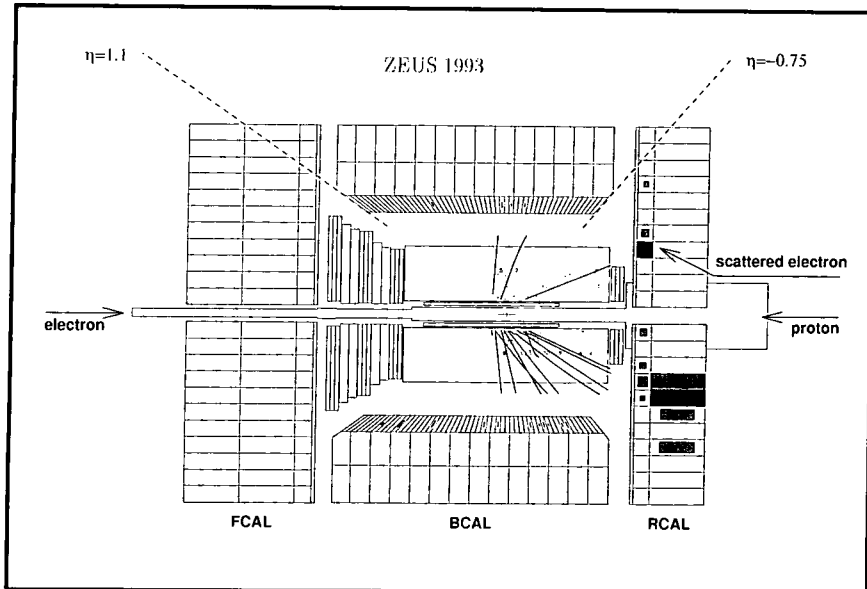
Figure 1.1: A typical rapidity gap event as seen by ZEUS in 1993. The picture sketches a schematic view of the ZEUS calorimeter and the central tracking unit. The directions of the incoming protons $E_p = 820$ GeV and electrons $E_e = 27$ GeV are indicated as well as some values of the pseudorapidity $\eta = -\ln\tan(\theta/2)$. The scattering angle θ is defined with respect to the incoming proton. The picture is taken from [ZEUS93].

1.1 Diffractive events seen at HERA

We shall briefly discuss the reason for a renewed interest in a concept that has already existed for more than 30 years, the Pomeron. In 1993 both the H1 [H1.94] and the ZEUS collaborations [ZEUS93, ZEUS94] at HERA reported a *new class of events* seen for the first time at the HERA *ep* collider. The characteristic feature of these events was large rapidity gaps in the forward direction of the incoming proton. An example is shown in Fig. 1.1. Standard deep inelastic scattering (DIS) events basically show energy deposition in the forward direction of the incoming proton, due to fragmentation of the latter, forming high–energy jets.

Introducing the *pseudorapidity* $\eta = -\ln\tan(\theta/2)$, where θ defines the scattering angle of a produced jet relative to the forward direction of the incoming proton one observes the following in a certain class of events: if one defines the quantity η_{max} as the most forward jet that can be observed, then some events show $\eta_{\mathrm{max}} < 1 - 2$ which means that there is no energy deposition in the forward direction. Even events with $\eta_{\mathrm{max}} < -2$ have been observed.

A second observation was the mass spectra distribution in the process $ep \to eX$. Large rapidity gaps have preferentially small M_X values (~ 10 GeV). The M_X^2 distribution falls off more rapidly, $dN/dM_X^2 \propto M_X^{-n}$ with $n = 2 - 4$. The diffractive events thus change the typical M_X^{-2} behaviour in the small M_X region.

One observes that approximately 10% of all events are diffractive and this ratio stays quite constant over the achievable Q^2 range. The first study of the 1993 data collected by ZEUS [ZEUS93, ZEUS94] and H1 [H1.94] yielded

- ZEUS (1993):
  integrated luminosity $\int dt\, \mathcal{L}(t) = 24.7$ nb^{-1}, 5.4% diffractive events ($\eta_{\max} < 1.5$), no Q^2 dependence found [ZEUS93]; additional factor 20 in statistics, 7.5% diffractive events ($\eta_{\max} < 1.5$), no Q^2 dependence found [ZEUS94];

- H1 (1993):
  integrated luminosity $\int dt\, \mathcal{L}(t) = 27.3$ nb^{-1}, 5% diffractive events ($\eta_{\max} < 1.8$), no Q^2 dependence found, evidence that 10% of these diffractive events are due to exclusive vector meson electroproduction [H1.94] with a scale dependence.

The observation of events with large rapidity gaps at high–energy colliders has some history. They were already observed at the $Sp\bar{p}S$ collider at CERN by the UA4 collaboration in 1984 [UA4.84] and later by the UA8 collaboration [UA8.88, UA8.92]. The observation by UA4 lead Ingelman and Schlein to an interesting model which we shall discuss in Section 1.2.

The explanation of these observed events has its roots in *Regge theory* and the introduction of the *Pomeron*. These will be the main topics in Section 1.2. The main idea is that the incoming proton *'emits'* an object that carries the quantum numbers of the vacuum (i.e. the Pomeron) while the proton remains intact (no fragmentation and thus no energy deposit in the forward direction) and travels down the beam line, while the Pomeron interacts with the virtual photon.

The experimental status of results on diffraction from HERA and the TEVATRON will be presented in Section 1.6.

1.2   Regge theory and the Pomeron

We shall start our theoretical investigations by deriving useful formulae for the understanding of the Donnachie–Landshoff model (DLM). Especially *unitarity* and the *optical theorem* play a pivotal role in this framework. We shall also briefly discuss *Reggeons* before introducing the DLM. An excellent introduction to this subject can be found in [ELOP66, Col77]. A collection of the most important papers on Regge theory has been published in [Can89].

1.2.1   Unitarity

An important feature of any scattering process is *unitarity*. We shall derive the unitarity condition for inelastic scattering and show how the DLM fits into this framework. For further discussion on the breaking of factorisation we refer to Section 1.7. To start with let us first study the unitarity condition for *elastic scattering*.

A scattering process is described by an overlap of two states of a system: the in–state $|i\rangle$ before interaction and the out–state $|f\rangle$ after interaction. For $t \to \pm\infty$ both states consist of free particles. The amplitude for finding the system in state $|f\rangle$ is given by the Lorentz invariant S matrix element

$$S_{if} = \langle f|S|i\rangle\,. \tag{1.1}$$

The fundamental postulate concerning the S matrix is *unitarity*, i.e. the probability for an $|i\rangle$ state to end up in a particular $|f\rangle$ state, summed over all possible $|f\rangle$ states, must

be *unity*

$$\sum_f |\langle f|\boldsymbol{S}|i\rangle|^2 \;=\; \sum_f \langle i|\boldsymbol{S}^\dagger|f\rangle\langle f|\boldsymbol{S}|i\rangle$$

$$=\; \langle i|\boldsymbol{S}^\dagger\boldsymbol{S}|i\rangle = 1\,. \tag{1.2}$$

The scattering amplitude $\mathcal{A}_{ab}(s,t)$ for scattering of an in–state $|a\rangle$ to an out–state $|b\rangle$ is related to the $\boldsymbol{S}$ matrix via

$$\mathcal{S}_{ab} = \langle b|\boldsymbol{S}|a\rangle = \delta_{ab} + i(2\pi)^4\delta^4\left(\sum_a p_a - \sum_b p_b\right)\mathcal{A}_{ab}\,. \tag{1.3}$$

Very often one introduces the $\boldsymbol{T}$ matrix

$$\mathcal{T}_{ab} = (2\pi)^4\delta^4\left(\sum_a p_a - \sum_b p_b\right)\mathcal{A}_{ab}\,, \tag{1.4}$$

such that

$$\mathcal{S}_{ab} = \delta_{ab} + i\mathcal{T}_{ab}\,. \tag{1.5}$$

From the unitarity constraint (1.2) we obtain

$$i\left(\mathcal{T}_{ab}^* - \mathcal{T}_{ab}\right) = (\mathcal{T}\mathcal{T}^*)_{ab} = \sum_c \mathcal{T}_{ac}\mathcal{T}_{cb}^*\,, \tag{1.6}$$

and thus

$$2\Im\mathrm{m}\,\mathcal{A}_{ab}(s,t) = (2\pi)^4\delta^4\left(\sum_a p_a - \sum_b p_b\right)\sum_c \mathcal{A}_{ac}(s,t)\mathcal{A}_{cb}^*(s,t)\,. \tag{1.7}$$
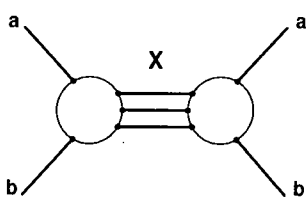
1.2.2   The optical theorem

The Cutkosky rule (1.7) [Cut60] provides a very interesting relation between the forward amplitude of an elastic process $a(p_1) + b(p_2) \to a(p_3) + b(p_4)$ and the total cross section. Forward scattering, $t = (p_1 - p_3)^2 = (p_2 - p_4)^2 = 0$, means $p_1 = p_3$ and $p_2 = p_4$. Thus
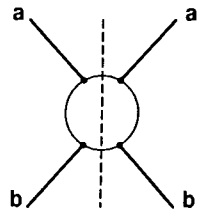
$$2\Im\mathrm{m}\,\mathcal{A}_{aa}(s,t=0) \;=\; 2\Im\mathrm{m}\,\langle p_1 p_2|\mathcal{A}|p_1 p_2\rangle$$

$$=\; (2\pi)^4\sum_n \delta^4\left(p_n - (p_1+p_2)\right)|\mathcal{A}(s,t)_{a\to n}|^2 = F\sigma_{\text{total}}\,. \tag{1.8}$$

Here, p_n indicates the total momenta of the final state and n indicates all possible final states. F stands for the flux factor $F = 4\sqrt{(p_1\cdot p_2)^2 - m_1^2 m_2^2}$. In the c.m.s. frame and negligible masses we find $F \simeq 2s$ and thus

$$\boxed{\sigma_{\text{total}} = \frac{1}{s}\,\Im\mathrm{m}\,\mathcal{A}(s,t=0)}\,. \tag{1.9}$$

1.2.3 The impact parameter space

The standard partial wave expansion for the scattering amplitude in the c.m.s. frame is given by (*cf.* Ref. [BC85])

$$\mathcal{A}(s,t) = 16\pi \sum_{\ell=0}^{\infty}(2\ell+1)P_\ell(\cos\theta)a_\ell(k)\,,\qquad(1.10)$$

with the ℓth partial amplitude of momentum k

$$a_\ell(k) = \frac{1}{2i}\left(e^{2i\chi_\ell}-1\right),\qquad(1.11)$$

and the ℓth Legendre polynomial $P_\ell(\cos\theta)$. The scattering angle is denoted by θ. If the scattering is purely *elastic* then $\Im\mathrm{m}\,\chi_\ell = 0$, if there is inelasticity then $\Im\mathrm{m}\,\chi_\ell > 0$. In the c.m.s. frame (massless particles) we find $\cos\theta = 1 + 2t/s$ and $s = 4k^2$.

Using the properties of Legendre polynomials one can show that the ℓth cross section (corresponding to the ℓth partial wave) is bound by

$$\sigma_\ell \le \frac{16\pi}{s}(2\ell+1)\,.\qquad(1.12)$$

Since the bound decreases with energy, an increasing number of partial waves must contribute in the high–energy limit. Thus an integral representation for the scattering amplitude should be preferred. Introducing the impact parameter b which measures the spatial separation of an incoming wave from the target ($bk = \ell + \frac{1}{2}$ [BC85]) we convert Eq. (1.10) into an integral via

$$\sum_\ell \;\to\; \int \mathrm{d}\ell \to \int k\mathrm{d}b\,,$$
$$a_\ell(k) \;\to\; a(s,b)\,,$$
$$P_\ell(\cos\theta) \;\to\; J_0((2\ell+1)\sin(\theta/2)) = J_0(qb)\,,$$

with $q^2 = -t = 4k^2\sin^2\frac{\theta}{2}$ and the Bessel function J_0. The last substitution is only true for large ℓ.

We may readily write down the integral representation for our scattering amplitude in impact–parameter space

$$\mathcal{A}(s,t) = 8\pi s \int_0^\infty b\,\mathrm{d}b\, J_0(qb)a(s,b)\,,\qquad(1.13)$$

or with

$$J_0(z) = \frac{1}{2\pi}\int_0^{2\pi}\mathrm{d}\phi\, e^{iz\cos\phi}\,,\qquad(1.14)$$

we finally arrive at

$$\mathcal{A}(s,t) = 4s \int_0^\infty \mathrm{d}^2b\, e^{i\vec{q}\cdot\vec{b}}a(s,b)\,,\qquad(1.15)$$

with $|\vec{\mathbf{b}}| = b$, $|\vec{\mathbf{q}}| = q$, $\vec{\mathbf{q}} \cdot \vec{\mathbf{b}} = qb \cos \phi$ and $\mathrm{d}^2 b = b \, \mathrm{d}b \, \mathrm{d}\phi$. The Fourier transform of Eq. (1.15) gives

$$a(s,b) = \frac{1}{16\pi^2} \frac{1}{s} \int_0^\infty \mathrm{d}^2 q \, e^{-i\vec{\mathbf{q}} \cdot \vec{\mathbf{b}}} \, \mathcal{A}(s,t) \,. \tag{1.16}$$

From the optical theorem (1.9) and (1.15) we derive

$$\Im m \, \mathcal{A}_{\mathrm{el}}(s, t=0) = 4s \int_0^\infty \mathrm{d}^2 b \, \Im m \, a_{\mathrm{el}}(s;b) = s\sigma_{\mathrm{total}} \,, \tag{1.17}$$

and thus

$$\sigma_{\mathrm{total}} = 4 \int_0^\infty \mathrm{d}^2 b \, \Im m \, a_{\mathrm{el}}(s,b) \,. \tag{1.18}$$

The elastic cross section reads

$$\sigma_{\mathrm{el}} = \frac{1}{16\pi} \frac{1}{s^2} \int_0^\infty \mathrm{d}t \, |\mathcal{A}_{\mathrm{el}}(s,t)|^2 = 4 \int_0^\infty \mathrm{d}^2 b \, |a_{\mathrm{el}}(s,b)|^2 \,. \tag{1.19}$$

We may finally write down our master equation for the scattering amplitude in impact–parameter space. From $\sigma_{\mathrm{total}} = \sigma_{\mathrm{el}} + \sigma_{\mathrm{in}}$, where σ_{in} denotes the *inelastic* cross section:

$$\boxed{\Im m \, \mathbf{a}_{\mathrm{el}}(\mathbf{s}, \mathbf{b}) = |\mathbf{a}_{\mathrm{el}}(\mathbf{s}, \mathbf{b})|^2 + \mathcal{G}_{\mathrm{in}}(\mathbf{s}, \mathbf{b})} \,. \tag{1.20}$$

$\mathcal{G}_{\mathrm{in}}$ represents all inelastic channels. It is straightforward to see that the general solutions of (1.20) can be written as

$$\mathcal{G}_{\mathrm{in}}(s,b) = \frac{1}{4} \left\{ 1 - e^{-\Omega(s,b)} \right\} \,, \tag{1.21}$$

$$a_{\mathrm{el}}(s,b) = \frac{1}{2i} \left\{ e^{-\frac{\Omega(s,b)}{2} + 2i\chi(s,b)} - 1 \right\} \,, \tag{1.22}$$

where $\chi(s,b)$ is a phase (elastic processes) and $\Omega(s,b)$ is the so–called *opacity* and $e^{-\Omega(s,b)}$ is the probability to have *no* inelastic interaction with the target ($\Omega(s,b) = 0$ for pure elastic scattering). For high–energy scattering we find the *real part* of the amplitude $\Re e \, a_{\mathrm{el}}(s,b) = \frac{1}{2} e^{-\Omega(s,b)/2} \sin(2\chi(s,b))$ very small and thus we might set $\chi(s,b) = 0$. Eq. (1.20) plays an important role in high–energy physics. Not only does it define unitarity in scattering processes, but it can also be used to derive important theorems. We shall briefly discuss two of them.

1.2.4   The Froissart–Martin bound

Froissart [Fro61] and Martin [Mar63, Mar66] showed that for the sake of unitarity (1.20) the total cross section σ_{total} can not rise indefinitely with the centre–of–mass energy s but should rather be bound. The asymptotic behaviour was shown to follow a $\ln^2 s$ behaviour and the cross section is restricted by an upper bound

$$\sigma_{\mathrm{total}} \le \mathcal{C}_{\mathrm{FM}} \ln^2 s \,. \tag{1.23}$$

To prove this theorem we consider the elastic process $a(1) + b(2) \to a(3) + b(4)$ with $s = (p_1 + p_2)^2 = (p_3 + p_4)^2$. In general $C_{FM} \propto 1/(k_\perp^{min})^2$, where $k_\perp^{min}$ is the minimal transverse momentum of the given process. We introduce a cut–off in b parameter space $\tilde{b}$ for which we postulate that the opacity $\Omega(s,b) \ll 1$ (elastic scattering) for $b > \tilde{b}$. From the optical theorem (1.9) we obtain

$$
\sigma_{total} = \frac{1}{s}\Im\,\mathcal{A}(s, t=0) \overset{(1.15)}{=} \lim_{t\to 0} 4 \int_0^\infty d^2b\,\Im\left[a_{el}(s,b)e^{i\vec{q}\cdot\vec{b}}\right]
$$

$$
\overset{(1.22)}{=} 2\int_0^\infty d^2b\left\{1 - e^{-\frac{\Omega(s,b)}{2}}\right\} = 4\pi \int_0^\infty db\,b\left\{1 - e^{-\frac{\Omega(s,b)}{2}}\right\}. \tag{1.24}
$$

We set the phase $\chi(s,b) = 0$ in Eq. (1.22) and used the fact that $\int d^2b = \int db\,d\phi\,b = 2\pi \int db\,b$.

The assumption we put into our proof is that at large values of b the elastic amplitude is bound by some power of s

$$
\Im\,a_{el}(s,b) \le \left(\frac{s}{s_0}\right)^N e^{-\kappa b}. \tag{1.25}
$$

One can introduce and interpret

$$
\mathcal{P}(s,b) = \mathcal{P}_0 \left(\frac{s}{s_0}\right)^N e^{-\kappa b}
$$

as the *interaction probability* with the target. This interpretation goes back to Feynman. The bigger b, the lower is the probability of inelastic scattering and thus at some $\tilde{b}$ we find $\mathcal{P}(s,\tilde{b}) \le \mathcal{P}_0$, which yields as an estimate for $\tilde{b}$

$$
\mathcal{P}(s,b) = \mathcal{P}_0 \left(\frac{s}{s_0}\right)^N e^{-\kappa \tilde{b}} \le \mathcal{P}_0 \quad \Longrightarrow \quad \tilde{b} \le \frac{N}{\kappa}\ln\left(\frac{s}{s_0}\right). \tag{1.26}
$$

Thus we may divide the integral in Eq. (1.24) into two parts

$$
\sigma_{total} = 4\pi \int_0^{\tilde{b}} db\,b\left\{1 - e^{-\frac{\Omega(s,b)}{2}}\right\} + \underbrace{4\pi \int_{\tilde{b}}^\infty db\,b\left\{1 - e^{-\frac{\Omega(s,b)}{2}}\right\}}_{\simeq 0 \text{ as } \Omega \ll 1 \text{ for } b > \tilde{b}}
$$

$$
\le 4\pi \int_0^{\tilde{b}} db\,b = \frac{2\pi}{\kappa^2} N^2 \ln^2\left(\frac{s}{s_0}\right) \simeq 30\text{mb } N^2 \ln^2\left(\frac{s}{s_0}\right). \tag{1.27}
$$

The minimum mass in the hadron spectrum is the mass of the pions and thus we find for pion–nucleon scattering $\kappa = 2m_\pi$. The power N can be calculated and one finds $C_{FM} \simeq 60$ mb. At the TEVATRON, e.g., we have a centre–of–mass energy of 1800 GeV and thus the Froissart–Martin bound tells us that the total cross section for pp should be bound via $\sigma_{total}(pp) \le \mathcal{O}(10^3 \text{ mb})$ at an energy scale of $\sqrt{s_0} = 100$ GeV. A comparison with Fig. 1.2 immediately shows that the data are far below the Froissart–Martin bound.

1.2.5   The Pomeranchuk theorem

Another prediction of the optical theorem on the basis of analytic properties is the *asymptotic equality* of particle and antiparticle cross sections from a given target. This theoretical observation is originally due to Pomeranchuk [Pom58].

The formulation of the theorem is as follows

> The ratios of the cross sections of any particle and its antiparticle approach unity at high energies (S. Weinberg, [Wei61]).

OR

> The total cross sections of two crossed processes should be equal to each other at high energies if the real part of the amplitude is smaller than the imaginary part (E.M. Levin, [Lev97]).

This is a manifestation of *crossing symmetry* ($s \leftrightarrow u$ channel) in the high–energy limit. To prove this theorem we compare the real part and the imaginary part of the amplitudes of the two elastic processes

$$a(1) + b(2) \quad \Rightarrow \quad a(3) + b(4)\,, \tag{1.28}$$

$$\bar{a}(1) + b(2) \quad \Rightarrow \quad \bar{a}(3) + b(4)\,, \tag{1.29}$$

with a and $\bar{a}$ being particle and antiparticle. We address the *dispersion relation* for the elastic amplitude at $t = 0$

$$\Re e\, \mathcal{A}(s, t=0) = \frac{1}{\pi} \int\limits_0^\infty \mathrm{d}\tilde{s}\, \frac{\Im m\, \mathcal{A}(\tilde{s}, t=0)}{\tilde{s} - s} + \frac{1}{\pi} \int\limits_0^\infty \mathrm{d}\tilde{u}\, \frac{\Im m\, \mathcal{A}(\tilde{u}, t=0)}{\tilde{u} - u}\,. \tag{1.30}$$

In practice a subtraction is necessary to make the integrals converge. Originally a dispersion relation was a formula giving the real part of the index of refraction in terms of an integral over its imaginary part. The modern approach to dispersion relations began with the work of Gell–Mann, Goldberger and Thirring [GGT54] deriving the analyticity of the scattering amplitude from microscopic causality. Goldberger very soon thereafter derived a very useful dispersion relation for the forward pion–nucleon scattering amplitude [Gol55].

From the optical theorem (1.9) we have

$$\Im m\, \mathcal{A}(\tilde{s}, t=0) \;=\; \tilde{s}\, \sigma_{\text{total}}^{ab}\,, \tag{1.31}$$

$$\Im m\, \mathcal{A}(\tilde{u}, t=0) \;=\; \tilde{u}\, \sigma_{\text{total}}^{\bar{a}b}\,, \tag{1.32}$$

where $\sigma_{\text{total}}^{ab}$ denotes the total cross section for process (1.28) and $\sigma_{\text{total}}^{\bar{a}b}$ for process (1.29). Furthermore we have $\tilde{u} \to -\tilde{s}$ for $\tilde{s} \gg 1$. Hence,

$$\Re e\, \mathcal{A}(s, t=0) = \frac{1}{\pi} \int\limits_0^\infty \mathrm{d}\tilde{s}\, \tilde{s} \left\{ \frac{\sigma_{\text{total}}^{ab}}{\tilde{s} - s} + \frac{\sigma_{\text{total}}^{\bar{a}b}}{\tilde{s} + s} \right\}\,. \tag{1.33}$$

As we have seen in the case of the Froissart–Martin bound, the assumption that the cross section follows a $\ln^N s$ behaviour is justified. We therefore assume

$$\sigma^{ab}_{\text{total}} \to \mathcal{C}^{ab} \ln^N \left(\frac{\widetilde{s}}{s_0} \right) \quad \text{and} \quad \sigma^{\bar{a}b}_{\text{total}} \to \mathcal{C}^{\bar{a}b} \ln^N \left(\frac{\widetilde{s}}{s_0} \right) , \tag{1.34}$$

for $\widetilde{s} \gg 1 \text{ GeV}^2 = s_0$.

Substituting (1.34) into Eq. (1.33) we finally arrive at

$$\Re e\, \mathcal{A}(s, t = 0) \to (\mathcal{C}^{ab} - \mathcal{C}^{\bar{a}b}) \frac{\ln^{N+1} \left(\frac{s}{s_0} \right)}{N + 1} \gg \Im m\, \mathcal{A}(s, t = 0) , \tag{1.35}$$

for $s \gg 1 \text{ GeV}^2 = s_0$.

This is in contradiction with the unitarity constraint (1.20) which has no solution if $\Re e\, \mathcal{A}(s, t = 0)$ increases with energy and is bigger than $\Im m\, \mathcal{A}(s, t = 0)$. The only way out of this contradiction is to postulate

$$\sigma^{ab}_{\text{total}} = \sigma^{\bar{a}b}_{\text{total}} \quad \text{as} \quad s/s_0 \to \infty . \tag{1.36}$$

This is a generalisation of the theorem due to Pomeranchuk, who only considered the case $N = 0$ [Pom58], while the observed behaviour of cross sections suggest that $N = 2$ is more likely. For a generalisation of Pomeranchuk's theorem see Ref. [Wei61].

In Fig. 1.2 we show some total cross sections as measured in high–energy experiments as a function of p_{lab}. Note the verification of Pomeranchuk's theorem at high energies.

1.2.6 Regge poles and the DLM

Today high–energy behaviour is usually inferred from *Regge pole theory* [Col77, Reg59, Reg60]. Experimentally one observes resonances in the t–channel with spin $\jmath > 1$. This leads to scattering amplitudes following a $s^\jmath$ behaviour. This would mean a fundamental violation of the Froissart–Martin bound (1.23) at high energies. A solution to this puzzle was the introduction of *Reggeons* formulated by Regge [Reg59, Reg60].

Let us consider a particle exchanged in the t–channel of the process $a(1) + b(2) \to c(3) + d(4)$ as shown in Fig. 1.3.

The Regge pole $\mathcal{R}$ couples with strength $g_{ij}(t)$ to the particles of the process. If one studies the scattering amplitude of the process in Fig. 1.3 using the angular momentum representation [Reg59, Reg60] one arrives at the following expression (see also [ELOP66, Col77]) for the scattering amplitude ($s \gg |t|$)

$$\mathcal{A}_\mathcal{R}(s, t) = g_{ac}(t) g_{bd}(t) \frac{e^{-i\pi\alpha_\mathcal{R}(t)} + \mathcal{S}_\mathcal{R}}{\sin(\pi\alpha_\mathcal{R}(t))} \frac{1}{\Gamma(\alpha_\mathcal{R}(t))} \left(\frac{s}{s_0} \right)^{\alpha_\mathcal{R}(t)} . \tag{1.37}$$

The Regge poles are the family of resonances that lie on a trajectory $\alpha_\mathcal{R}(t)$. If one plots the experimental results, i.e. the spin $\jmath$ of a given resonance versus its mass $m_\mathcal{R}^2 = t$, than these resonances group along a straight line

$$\alpha_\mathcal{R}(t) = \alpha_\mathcal{R}(0) + \alpha'_\mathcal{R} t , \tag{1.38}$$

according to their quantum numbers they can exchange in a given process, which is called a *Regge trajectory*. The different Regge trajectories with their values $\alpha_\mathcal{R}(0)$ (the
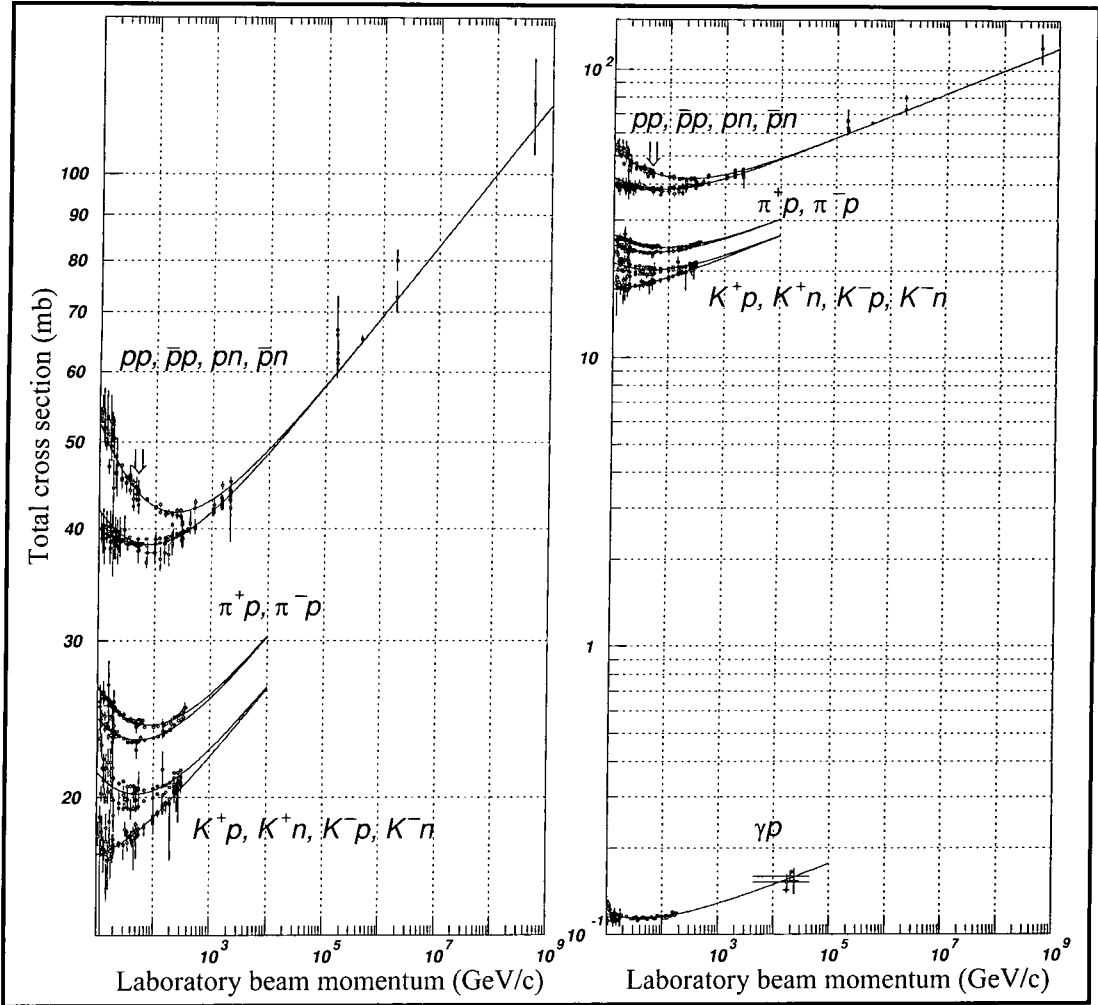
Figure 1.2: The cross sections for pp and $p\bar{p}$ as a function of the laboratory beam momentum $p_{\text{lab}} = \frac{\sqrt{s}}{2}\sqrt{\frac{s-4m^2}{4m^2}}$. Data for pion–nucleon and kaon–nucleon as well as γp scattering are also shown. Note the high–energy behaviour showing the crossing symmetry according to Pomeranchuk's theorem. The plots are taken from [PDG96].

intercept) and $\alpha'_{\mathcal{R}}$ (the *slope*) can be found, e.g., in [Col77]. Typically one finds for the leading meson trajectories an intercept $\alpha_{\mathcal{R}}(0) \simeq 0.5$ and the slope of the trajectory $\alpha'_{\mathcal{R}} \simeq 1$ GeV^{-2}. The studies of Regge [Reg59, Reg60] showed that in the asymptotic limit (large s and fixed t) the *elastic* cross sections for two–body processes should behave like

$$\frac{\text{d}}{\text{d}t}\sigma_{\text{el}} \propto F(t)\left(\frac{s}{s_0}\right)^{2\alpha_{\mathcal{R}}(t)-2}, \tag{1.39}$$

with s_0 again being the hadron mass scale $s_0 \simeq 1$ GeV^2. Substituting (1.38) into (1.39) yields

$$\frac{\text{d}}{\text{d}t}\sigma_{\text{el}} \propto F(t)\left(\frac{s}{s_0}\right)^{2\alpha_{\mathcal{R}}(0)-2} e^{2\alpha'_{\mathcal{R}}\ln\left(\frac{s}{s_0}\right)t}. \tag{1.40}$$

We observe two features for large s in Regge theory: first, the forward peak (*diffraction*
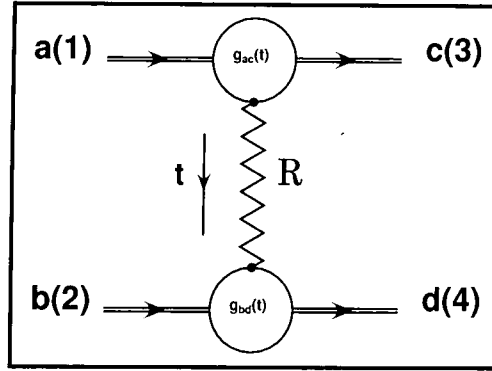
Figure 1.3: A Regge pole $\mathcal{R}$ is exchanged in the t–channel of the process $ab \to cd$. The vertex couplings of the Regge pole to the particles are denoted by $g_{ac}(t)$ and $g_{bd}(t)$, respectively.

peak) shrinks (becomes sharper) as $\ln s$ increases, and, second, with $\alpha_{\mathcal{R}}(0) \simeq 0.5$ (as seen experimentally) there is no violation of the Froissart–Martin bound if the exchange of Regge poles is the underlying mechanism at high energies. The cross section (for Regge pole exchange with the given intercept) is even *decreasing* at higher energies.

Now we have discussed the function $\alpha_{\mathcal{R}}(t)$ in Eq. (1.37) and showed how the total cross section σ_{total} depends on this trajectory (or its intercept). The function $1/\sin(\pi\alpha_{\mathcal{R}}(t))$ defines the Regge propagator and produces the required resonance poles in t whenever $\alpha_{\mathcal{R}}(t)$ passes through an integer (i.e. the spin of the resonance). Because of $s \leftrightarrow u$ crossing symmetry one has to introduce a signature $\mathcal{S}_{\mathcal{R}}$ for each Regge trajectory. This is easy to understand as the t–channel Reggeon is the sum of *two* terms [ELOP66, Col77], an s–channel and a 'crossed' u–channel contribution. Depending whether the exchanged Reggeon has even $(0,2,4,\cdots)$ or odd $(1,3,5,\cdots)$ spin, the s– and u– channel contributions either sum or subtract. We may write the total contribution (positive t) as

$$(-s)^{\alpha_{\mathcal{R}}(t)} + \mathcal{S}_{\mathcal{R}}(-u)^{\alpha_{\mathcal{R}}(t)} \overset{s\to\infty}{\Longrightarrow} (-s)^{\alpha_{\mathcal{R}}(t)} + \mathcal{S}_{\mathcal{R}} \, s^{\alpha_{\mathcal{R}}(t)}$$
$$= s^{\alpha_{\mathcal{R}}(t)} \left\{ e^{-i\pi\alpha_{\mathcal{R}}(t)} + \mathcal{S}_{\mathcal{R}} \right\}. \qquad (1.41)$$

The Regge trajectories have signature $\mathcal{S}_{\mathcal{R}} = \pm 1$ according to the $\mathcal{C}$–parity of the exchange.

There has to be taken care of the unphysical spin values, the *nonsense* poles as Collins called them [Col77], that appear for $\alpha_{\mathcal{R}}(t) = 0, -1, -2, \ldots$ To cancel these poles and to achieve that $\mathcal{A}_{\mathcal{R}}(s, t) = 0$ at these values one introduces the Γ function in (1.37). As $\Gamma(x) \sin(\pi x) = \pi/\Gamma(1 - x)$ we see from (1.37) that

$$\mathcal{A}_{\mathcal{R}}(s, t) \propto \left\{ e^{-i\pi\alpha_{\mathcal{R}}(t)} + \mathcal{S}_{\mathcal{R}} \right\} \Gamma(1 - \alpha_{\mathcal{R}}(t)). \qquad (1.42)$$

For example, the ρ meson has spin 1 and thus $\mathcal{S}_{\mathcal{R}} = -1$. So, if $\alpha_\rho(t) \to 0$, then $\mathcal{A}_\rho(s, t) = 0$ according to Eq. (1.42).

Employing the optical theorem one can show that the *total* cross section shows the behaviour

$$\sigma_{\text{total}} \propto s^{\alpha_{\mathcal{R}}(0)-1}, \qquad (1.43)$$

compared to the elastic cross section of Eq. (1.39).

We summarise the expressions for the total, the differential single diffractive and the double differential cross section using our notation we introduced so far. The graphical representation of the cross sections and their analytic form read
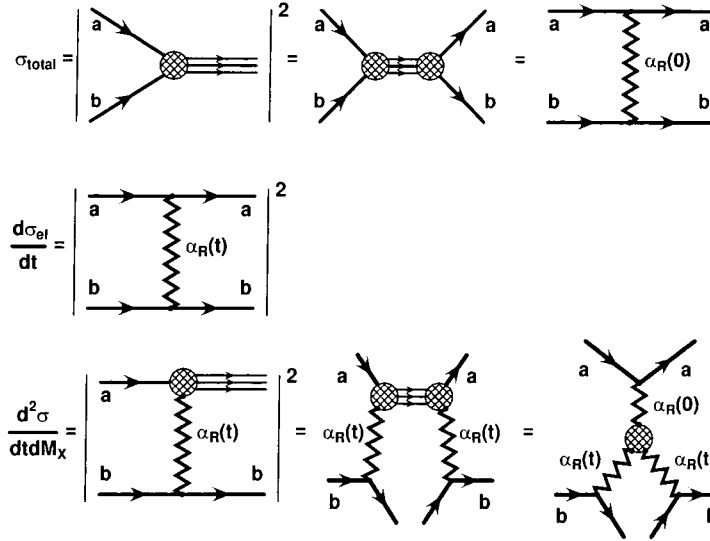
$$\sigma^{ab}_{\text{total}} = \sum_{\mathcal{R}} g_{\mathcal{R}a}(0)\, g_{\mathcal{R}b}(0)\, \frac{s^{\alpha_{\mathcal{R}}(0)-1}}{\Gamma(\alpha_{\mathcal{R}}(0))} , \tag{1.44}$$

$$\frac{d}{dt}\sigma^{ab}_{\text{el}} = \sum_{\mathcal{R}} \frac{g^2_{\mathcal{R}a}(t) g^2_{\mathcal{R}b}(t)}{16\pi} \left(\frac{(\cos(\pi\alpha_{\mathcal{R}}(t)) + \mathcal{S}_{\mathcal{R}})^2}{\sin^2(\pi\alpha_{\mathcal{R}}(t))} + 1 \right) \frac{s^{2\alpha_{\mathcal{R}}(t)-2}}{\Gamma^2(\alpha_{\mathcal{R}}(t))} , \tag{1.45}$$

$$\frac{d}{dt}\frac{d\sigma^{ab}}{dM^2_X} = \sum_{\mathbb{P},\mathcal{R}} \frac{g_{\mathbb{P}a}(0) g^2_{\mathcal{R}b}(t) g_{\mathbb{P}\mathcal{R}\mathcal{R}}}{16\pi s} \left(\frac{(\cos(\pi\alpha_{\mathcal{R}}(t)) + \mathcal{S}_{\mathcal{R}})^2}{\sin^2(\pi\alpha_{\mathcal{R}}(t))} + 1 \right)$$

$$\times \quad \frac{1}{\Gamma^2(\alpha_{\mathcal{R}}(t))} \left(\frac{s}{M^2_X} \right)^{2\alpha_{\mathcal{R}}(t)} (M^2_X)^{\alpha_{\mathbb{P}}(0)} , \tag{1.46}$$

where we introduce the triple Pomeron–Reggeon coupling $g_{\mathbb{P}\mathcal{R}\mathcal{R}}$. Note that these formulae are valid in the so-called *Regge regime*, i.e., t small and $s/M^2_X \to \infty$. For small $|t|$ one therefore finds

$$\frac{d}{dt}\sigma_{\text{el}} \simeq \frac{\sigma^2_{\text{total}}}{16\pi} e^{-b|t|} , \tag{1.47}$$

with a sharp diffraction peak.

A look at the experimental data (*cf.* Fig. 1.2), however, shows that at high energies the cross sections are *not* decreasing with energy, neither are they strictly constant, but slowly increase. Taking Eq. (1.43) into account, and holding strongly to Regge theory, then there should be a kind of trajectory with intercept $\alpha_{\mathcal{R}} \geq 1$. But as this postulate means a violation of the Froissart–Martin bound and unitarity, care has to be taken, even though the *violation zone* is far beyond today's collider energies. With the introduction of the Pomeron, with an intercept only an ϵ amount above unity, the increasing cross sections, that have been measured experimentally, could be explained. The Pomeron was introduced by V.N. Gribov into Regge theory and named after I.Ya. Pomeranchuk who contributed much to the understanding of the Pomeron.

The Pomeron trajectory (according to Eq. (1.38)) can be cast in the following form

$$\alpha_{\mathbb{P}}(t) = \alpha_{\mathbb{P}}(0) + \alpha'_{\mathbb{P}}t = 1 + \epsilon + \alpha' t. \tag{1.48}$$

The slope parameter α' can be deduced from measurements of the differential cross sections at high energies, i.e., the domain where the Pomeron exchange dominates. It is found to be $\alpha' = 0.25$ GeV^{-2}. With this value most models and measurements agree.

More subtle is the intercept ϵ: depending on its value one defines a *soft* Pomeron ($\epsilon \simeq 0.08$) or a *hard* Pomeron ($\epsilon \simeq 0.2 - 0.5$). In our calculations we shall adopt the model of the soft Pomeron fitted to experimental data by Donnachie and Landshoff [DL83, DL84, DL86]. They gave an elegant description of almost all existing experimental data in terms of an universal parametrisation for the total cross sections. They showed that any total cross section can be parametrised as[1]

$$\sigma_{\text{total}}(ab) = X_{ab}\left(\frac{s}{s_0}\right)^{-\eta} + Y_{ab}\left(\frac{s}{s_0}\right)^{\epsilon}, \tag{1.49}$$

with $\alpha_{\mathbb{P}}(0) = 1 + \epsilon$ being the Pomeron intercept ($\epsilon > 0$) and $\alpha_{\mathcal{R}}(0) = 1 - \eta$ being the intercept from leading–meson Regge trajectories $\rho, \omega, f, \ldots$ with $\eta \simeq 0.5$. Donnachie and Landshoff presented an update of their results in 1992 [DL92] and found

$$\begin{aligned} \alpha' &= 0.25 \text{ GeV}^{-2}, \\ \epsilon &= 0.0808, \\ \eta &= 0.4525. \end{aligned} \tag{1.50}$$

They extended the picture to virtual photons ($\gamma^*, Q^2 < 10$ GeV^2), to see what is the expected contribution of the non–perturbative mechanism to higher Q^2 [DL84, DL94].
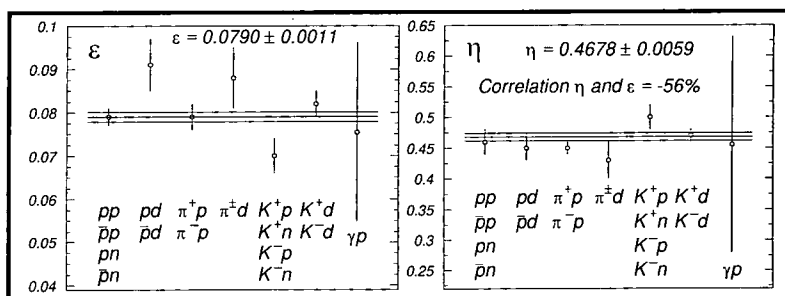
Figure 1.4: A fit of the parameters ϵ and η employing formula (1.49) [DL92] to different cross sections. This figure is taken from the Particle Data Group [PDG96] and shows an update of the data previously obtained by Donnachie and Landshoff (1.50) in [DL92].

The results of these fits are shown as solid lines in Fig. 1.2. An experimental update from different measurements on total cross sections is shown in Fig. 1.4. We note that the WA91 collaboration reported a measurement of a resonance at $\simeq 1.9$ GeV which could be interpreted as a $\mathcal{J}^{PC} = 2^{++}$ state glueball candidate [WA91.94]. The striking feature

---

[1]Note that $Y_{ab} = Y_{\bar{a}b}$ according to Pomeranchuk's theorem for large s.

of this glueball is that it would be located on a Regge trajectory defined by above (1.50) parameters.

The Pomeron intercept has been recently measured at HERA by the H1 [H1.97a] and the ZEUS [ZEUS97] collaborations using data from diffractive photoproduction. In this case a quasi–real photon interacts with a Pomeron emitted by the incoming proton and forms a system of mass M_X, so

$$\gamma p \stackrel{p \to \mathbb{P} p'}{\Longrightarrow} X p' . \qquad (1.51)$$

The double differential cross section of this process can be written as [Mul70, FF74]

$$\frac{\mathrm{d}^2\sigma}{\mathrm{d}t \mathrm{d}M_X^2}(\gamma p \to X p') = \left(\frac{1}{M_X^2}\right)^{\alpha_{\mathbb{P}}(0)} (s_{\gamma p})^{2\alpha_{\mathbb{P}}(0)-2} e^{-b|t|} , \qquad (1.52)$$

with $\sqrt{s_{\gamma p}}$ being the c.m.s. frame energy of the quasi–real photon and the incoming proton and $b = b_0 + 2\alpha'_{\mathbb{P}} \ln(s_{\gamma p}/M_X^2)$ (cf. Eq. (1.40)). Thus measuring the M_X^2 dependence of the differential cross section in (1.52) yields a value for the Pomeron intercept $\alpha_{\mathbb{P}}(0)$. The reported values for $\sqrt{s_{\gamma p}} \simeq 200$ GeV were ($Q^2 = 0$)

$$\text{ZEUS}: \quad \alpha_{\mathbb{P}}(0) \quad = \quad 1.12 \pm 0.04^{\text{stat.}} \pm 0.08^{\text{syst.}} \quad \text{for} \quad 8 < M_X < 24 \text{ GeV} ,$$

$$\text{H1}: \quad \alpha_{\mathbb{P}}(0) \quad = \quad 1.068 \pm 0.016^{\text{stat.}} \pm 0.022^{\text{syst.}} \quad \text{for} \quad 2 < M_X < 44 \text{ GeV} .$$

So both measurements seem to support the model of the soft Pomeron. However, care has to be taken, as will be discussed in Section 1.7 where we discuss data for higher energies.

The Pomeron intercept shows an energy dependence. This was shown by, e.g., the CDF collaboration [CDF94]. They studied events with single Pomeron exchange (*single diffractive events*) $p + \bar{p} \to \bar{p} + X$ and obtained from a data fit:

$$\alpha_{\mathbb{P}}(0) = 1 + \epsilon = 1.121 \pm 0.011 \quad \text{at} \quad \sqrt{s} = 546 \text{ GeV} ,$$

$$\alpha_{\mathbb{P}}(0) = 1 + \epsilon = 1.103 \pm 0.017 \quad \text{at} \quad \sqrt{s} = 1800 \text{ GeV} ,$$

for a fixed slope parameter $\alpha' = 0.25$ GeV^{-2}. They conclude that large screening effects have to be introduced to save the traditional Pomeron model. Also deduced experimentally by CDF was the sensitivity to α'. A change in α' by $\delta\alpha' = \pm 0.1$ GeV^{-2} results in a change in the single diffractive cross section σ_{SD} of only $\pm 0.1\%$ and ϵ changes at the same time by $\delta\epsilon = \pm 0.011$.

1.2.7 A partonic Pomeron

The Pomeron has been postulated to describe hard diffractive collider phenomenology. In the framework of Regge theory a colourless *object*, carrying the quantum numbers of the vacuum, is able to explain the new observations. A pure gluonic composite seemed to be the simplest explanation on the basis of partonic contents and proposed features [Low75, Nus75, Nus76]. The Pomeron was therefore assumed to behave essentially as a hadron and Ingelman and Schlein introduced the concept of a *Pomeron structure function* [IS85] motivated by data from the UA4 collaboration [UA4.84] measuring the diffractive component in the mass distribution $\mathrm{d}^2\sigma/\mathrm{d}t/\mathrm{d}M_X$ in the reaction $p\bar{p} \to X\bar{p}$ at the CERN $Sp\bar{p}S$ collider.

Further collider experiments, by for example the U A8 collaboration at CERN [UA8.88, UA8.92], gave evidence for a hard parton distribution inside the Pomeron but still could not distinguish between a gluon or quark dominated Pomeron. But they found that the partonic contents should be *hard*, i.e., their momentum distribution should be peaked at high Bjorken x and 57% of all events showed a $\propto 6x(1-x)$ distribution. Only 13% were found to be *soft*, i.e., $\propto 6(1-x)^5$. The remaining 30% even showed a superhard $\simeq \delta(1-x)$ contribution.

Exactly as one measures the structure function F_2 of the proton at HERA in DIS and is able to extract the parton distributions inside the proton, it is possible to measure the diffractive structure function F_2^D, i.e. the structure function of the Pomeron. The corresponding *handbag diagrams* are shown in Fig. 1.5.
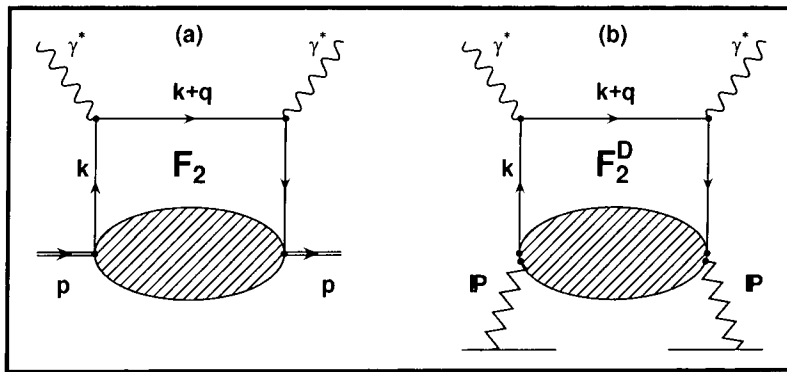
Figure 1.5: A sketch of the handbag diagrams used to measure the proton structure function F_2 (a) and the diffractive structure function F_2^D (b) at HERA.

The total deep inelastic structure function $F_2(x, Q^2)$, measured in the process $\gamma^* p \to X$ in Fig. 1.5(a), can be written as a sum over parton distributions times a short distance part

$$F_2(x, Q^2) = \sum_q \int dx' \, f_{q/p}(x', \mu^2) \times \widehat{F}_2^q(\frac{x}{x'}, Q^2, \mu^2), \qquad (1.53)$$

with $\widehat{F}_2^q(x/x', Q^2, \mu^2) = e_q^2 \delta(1 - x/x') + \mathcal{O}(\alpha_s)$. Now one can hypothesize that the diffractive structure function $F_2^{D(4)}(x_{\mathbb{P}}, t, x, Q^2)$, measured in the process $\gamma^* p \to p' X$ in Fig. 1.5(b), can be written in terms of *diffractive structure functions*

$$\frac{d^2 F_2^{D(4)}(x_{\mathbb{P}}, t, x, Q^2)}{dx_{\mathbb{P}} dt} = \sum_q \int dx' \frac{d^2 f_{q/p}^D(x_{\mathbb{P}}, t, x', \mu^2)}{dx_{\mathbb{P}} dt} \times \widehat{F}_2^q(\frac{x}{x'}, Q^2, \mu^2). \qquad (1.54)$$

In the following we shall make three fundamental assumptions:

1.) the Pomeron has a partonic structure,

2.) this partonic structure is universal, i.e., its determination at an *ep* collider should also hold at a *pp* collider, etc.

3.) factorisation of the diffractive structure function is valid.

It will turn out that the controversial assumption is the factorisation hypothesis **3.)**. With factorisation we mean *gap–* or *Regge–factorisation*,[2] i.e. the diffractive structure function can be written as a product of the structure function of the Pomeron F_2^{IP} and a *flux factor* f_{IP}, i.e. a measure of the probabilty that a Pomeron is being emitted from a hadron. If x_{IP} is the fraction of the proton momentum that is carried by the Pomeron, then we can write (*assuming gap–factorisation*)

$$\frac{\mathrm{d}^2}{\mathrm{d}x_{\text{IP}}\,\mathrm{d}t}F_2^{\text{D(4)}}(x_{\text{IP}},t,\xi,Q^2) = f_{\text{IP}}(x_{\text{IP}},t)\times F_2^{\text{IP}}(\xi,Q^2)\,, \tag{1.55}$$

with $\xi = x/x_{\text{IP}}$ (x is the standard DIS scaling variable) and $Q^2 \simeq M_X^2\xi/(1-\xi)$. Note that the flux factor in Eq. (1.55) only depends on x_{IP} and t. Any x dependence would certainly destroy factorisation. The crucial experimental observations are that $F_2^{\text{D(4)}}$ is a *leading twist* structure function, indicating deep inelastic scattering off point–like objects [ZEUS93, ZEUS94, H1.94].

The diffractive structure function can be determined in DIS by measuring the differential diffractive cross section σ^{D} in the reaction $ep \overset{p\to p'\,\text{IP}}{\Longrightarrow} ep'X$ [H1.95, ZEUS95a]

$$\frac{\mathrm{d}^4\sigma^{\text{D}}}{\mathrm{d}x_{\text{IP}}\mathrm{d}t\mathrm{d}\xi\mathrm{d}Q^2} = \frac{2\pi\alpha^2}{\xi Q^4}\left[\left(1+(1-y)^2\right)F_2^{\text{D(4)}} - y^2 F_{\text{L}}^{\text{D(4)}}\right](1+\Delta_{\text{rad}})(1+\Delta_Z)\,, \tag{1.56}$$

with $y = Q^2/(xs)$ and the corrections Δ_{rad} for the radiation and Δ_Z for the Z boson exchange which both can be neglected in the kinematic range of these measurements. Note that

$$x_{\text{IP}} = \frac{M_X^2 + Q^2 - t}{s_{\gamma^*p} + Q^2 - m_p^2} \simeq \frac{M_X^2 + Q^2}{Q^2}x\,,$$

with $\sqrt{s_{\gamma^*p}}$ being the centre–of–mass energy in the γ^*p frame and m_p being the proton mass. The outgoing proton p' just travels along the beam line and remains undetected, thus one integrates over t and finds

$$\begin{aligned}\frac{\mathrm{d}}{\mathrm{d}x_{\text{IP}}}F_2^{\text{D(3)}}(x_{\text{IP}},\xi,Q^2) &= \int\mathrm{d}t\,F_2^{\text{D(4)}}(x_{\text{IP}},t,\xi,Q^2)\\ &\propto (x_{\text{IP}})^{1-2\alpha_{\text{IP}}(0)}F_2^{\text{IP}}(\xi,Q^2) = (x_{\text{IP}})^{-1.16}F_2^{\text{IP}}(\xi,Q^2)\,,\end{aligned} \tag{1.57}$$

using the Donnachie–Landshoff intercept (1.50). The experimental results from ZEUS [ZEUS95a] and H1 [H1.95] are

$$\text{H1}:\quad n = 2\alpha_{\text{IP}}(0) - 1 = 1.19\pm0.06^{\text{stat.}}\pm0.07^{\text{syst.}}\,, \tag{1.58}$$

$$\text{ZEUS}:\quad n = 2\alpha_{\text{IP}}(0) - 1 = 1.30\pm0.08^{\text{stat.}}\pm^{0.08\,\text{syst.}}_{0.14}\,. \tag{1.59}$$

Thus ZEUS obtains a somewhat steeper x_{IP} dependence. These values are still valid even though new fits from both collaborations have been undertaken. Note that the Pomeron intercept has been probed at high–Q^2 values. The range was $8.5 < Q^2 < 50\ \text{GeV}^2$ for H1 and $10 < Q^2 < 63\ \text{GeV}^2$ for ZEUS. We shall discuss the high Q^2 results in Section 1.7. We only refer to the chronological appearance of experimental data here, as these data until 1995 were the motivation for our studies on diffraction. The experimental situation after 1995 will be summarised at the end of the chapter.

---

[2]A possible violation of gap–factorisation will be the topic of Section 1.7.

Assuming a pure Pomeron interchange, we can adopt the flux factor modelled by fitting this picture to data on total cross sections as was done by Donnachie and Landshoff. The flux factor then reads[3] [DL84, DL86] (see also Eq. (1.37))

$$f_{\mathbb{P}}(x_{\mathbb{P}}, t) = \frac{g_{\mathbb{P}q}^2(t)}{4\pi^2} (x_{\mathbb{P}})^{1-2\alpha_{\mathbb{P}}(t)}, \qquad (1.60)$$

where the normalisation $1/4\pi^2$ comes if one pretends that the Pomeron behaves kinematically like a photon. Of course the flux factor is a matter of convention and there is no compelling reason for any particular convention. Donnachie and Landshoff derived an expression for the Pomeron–quark coupling

$$g_{\mathbb{P}q}(t) = 3\beta F_1(t). \qquad (1.61)$$

Thus the Pomeron couples to each valence quark with the same strength $\beta = 1.8$ GeV^{-2} (fitted value). The function $F_1(t)$ is the electric form factor experimentally determined in eN scattering

$$F_1(t) = \frac{4m_p^2 - 2.8t}{4m_p^2 - t} \left(1 - \frac{t}{0.7 \text{ GeV}^2}\right)^{-2}. \qquad (1.62)$$

The magnetic form factor is small in the isoscalar channel.

We have collected now all bits and pieces to start calculations on single and double Pomeron exchange in the DLM. The missing piece in the mosaic is the structure function of the Pomeron.

1.3   Introducing parton distributions for the Pomeron

In the following we shall use a fit from HERA data to model partonic distributions for the Pomeron as performed by Kunszt and Stirling in [KS96]. As discussed in Ref. [KS96], the diffractive parton distributions are to be considered as referring to partons in an effective colour–neutral target which is presumably a sum over several Regge trajectories. We shall assume Pomeron exchange only.

Since the scattering evidently takes place off point–like objects, one may write the Pomeron structure function $F_2^{\mathbb{P}}$ as a sum over quark–parton distributions[4]

$$F_2^{\mathbb{P}}(\xi, Q^2) = \xi \sum_{f=q,\bar{q}} e_f^2 f_{f/\mathbb{P}}(\xi, Q^2). \qquad (1.63)$$

In this way we introduce diffractive parton distribution functions via (*cf.* Eq. (1.55))

$$\frac{\mathrm{d}^2 f_{i/p}^{\mathrm{D}}(x_{\mathbb{P}}, t, \xi, Q^2)}{\mathrm{d}x_{\mathbb{P}} \, \mathrm{d}t} = f_{\mathbb{P}}(x_{\mathbb{P}}, t) \times \frac{f_{i/\mathbb{P}}(\xi, Q^2)}{x_{\mathbb{P}}} \propto (x_{\mathbb{P}})^{-2\alpha_{\mathbb{P}}(t)} \times f_{i/\mathbb{P}}(\xi, Q^2), \qquad (1.64)$$

where $f_{\mathbb{P}}(x_{\mathbb{P}}, t)$ denotes the overall flux factor (1.60) and $x_{\mathbb{P}} \ll 1$ and $|t| \ll Q^2$. The $x_{\mathbb{P}}$ dependence of the diffractive structure function predicted by this type of *soft Pomeron*

---

[3]Note that we made an approximation in Eq. (1.57) by including the Pomeron intercept $\alpha_{\mathbf{P}}(0)$ rather than the full trajectory integrated over t: $\int \mathrm{d}t\, \alpha_{\mathbf{P}}(t)$. In formula (1.60) we include the full Pomeron trajectory as we shall later perform the integration over t implicitly.

[4]Note that at HERA only the quark content can be measured (gluons do not couple directly to DIS). Gluons enter indirectly into the formalism via $q\bar{q}$ pairs.

Model	$\xi f_{q/\text{I\!P}}(Q_0^2, \xi)$	$\xi f_{g/\text{I\!P}}(Q_0^2, \xi)$	N
1	$0.314\xi^{\frac{1}{3}}(1-\xi)^{\frac{1}{3}}$	0	1.62
2	$0.2\xi(1-\xi)$	$4.8\xi(1-\xi)$	2.85
3	$0.081\xi(1-\xi)^{\frac{1}{2}}$	$9.66\xi^8(1-\xi)^{0.2}$	1.57

Table 1.1: The parton distributions for quarks $f_{q/\text{I\!P}}(Q_0^2, \xi)$ and gluons $f_{g/\text{I\!P}}(Q_0^2, \xi)$ inside the Pomeron at the starting scale $Q_0^2 = 2$ GeV^2 taken from Ref. [KS96] with the different normalisation factors N. The parton distributions are fitted to the HERA measurements [H1.95, ZEUS95a] of the diffractive structure function $F_2^{\text{D}(3)}(x_{\text{I\!P}}, Q^2, \xi)$ with $\xi = x/x_{\text{I\!P}}$.

model is roughly consistent within errors with the H1 [H1.95] and ZEUS [ZEUS95a] data, although there is some indication from the latter that a somewhat steeper $x_{\text{I\!P}}$ dependence is preferred (*cf.* (1.59)).

Various models for the parton distributions $f_{i/\text{I\!P}}(\xi, Q^2)$ have been proposed, ranging from the two extremes of mainly gluons to mainly quarks. Recent studies in the framework of QCD DGLAP evolution can be found in [Cap95, Cap96, GBK95, GBP96, GS96, Phi95]. A more theoretical motivated picture for the Pomeron parton structure function is given in Ref. [BS96].

A key issue concerns the existence of a *momentum sum rule* for the Pomeron. There is no theoretical proof for the existence of such a sum rule, but as the *product* of $f_{i/\text{I\!P}}$ and $f_{\text{I\!P}}$ appears in the expression for the structure function, one can simply impose a momentum sum rule in the parton distributions and absorb an overall normalisation N, unchanged by Q^2 evolution, into $f_{\text{I\!P}}$. Assuming a light–quark distribution ($q = u, d, s$ + antiquarks) with SU(3) flavour symmetry, the momentum sum rule constraint at some starting scale Q_0^2 may be written as

$$\int\limits_0^1 \mathrm{d}\xi\, \xi \left(6 f_{q/\text{I\!P}}(\xi, Q_0^2) + f_{g/\text{I\!P}}(\xi, Q_0^2) \right) = 1. \qquad (1.65)$$

Table 1.1 summarises the ξ dependence of the three models of Ref. [KS96] at fixed starting scale $Q_0^2 = 2$ GeV^2.

Charm quarks are generated by massless DGLAP evolution ($g \to c\bar{c}$) at higher scales Q^2. Since in each case the quark content is constrained by structure function data, and since we choose to impose a momentum sum rule (1.65), the overall normalisation factors N are different in the three models and are specific for the Donnachie–Landshoff flux factor [DL84, DL86]. In each case the starting distributions of Table 1.1 give satisfactory agreement with the H1 [H1.95] and ZEUS [ZEUS95a] data. The main characteristics of all three models are:

• all three models are qualitatively very different concerning the partonic contents at the starting scale $Q_0^2 = 2$ GeV^2,

• all three models give satisfactory agreement with the H1 and ZEUS data,

- all models undergo leading–order DGLAP evolution as for the usual parton distributions.

In qualitative terms, the three models can be characterised as:

Model 1: At Q_0 the Pomeron is entirely composed of quarks. Gluons are dynamically generated via DGLAP evolution;

Model 2: A well balanced mix of quarks and gluons at starting scale Q_0, the ξ distribution in both cases is peaked at $\xi = 0.5$;

Model 3: A predominantly hard gluonic content at starting scale, the gluons inside the Pomeron carry large fractional momenta ($\xi \simeq 1$).

The DGLAP evolution for the gluon parton distributions for all three models is shown in Fig. 1.6. Note the qualitative differences in each model.

1.4 Diffractive Higgs production at the LHC

In the following we shall present numerical results for single diffractive[5] Higgs production at the future CERN LHC collider ($\sqrt{s} = 14$ TeV) with the underlying parton distributions of the Pomeron as presented in the previous section.

The process is depicted in Fig. 1.7. This model of diffractive Higgs production was first studied in Ref. [NSS90] (double diffractive inclusive process). Recently, it has been suggested [GV96] that triggering on single or double diffractive events may provide a cleaner environment for discovering Higgs bosons produced via $gg \to H$. The argument is that gluons should be more copious in the Pomeron, thus enhancing the Higgs signal relative to the background. However when assessing the usefulness of the single diffractive cross section in enhancing the Higgs signal, it is equally important to consider the corresponding single diffractive *background* processes. Naively, one might argue that since the important backgrounds originate in quark–antiquark annihilation ($q\bar{q} \to \gamma\gamma, ZZ$) the gluon–rich Pomeron may indeed enhance the signal to background ratio. However, care is needed with this argument. Higgs production probes parton distributions at a scale $Q^2 \sim M_H^2$, much larger than the typical Q^2 scales of diffractive deep inelastic scattering at HERA. Perturbative DGLAP evolution of the diffractive parton distributions to these high scales gives rise to a mixing of the quark and gluon distributions such that, for example, a large gluon/quark ratio at small scales is washed out at higher scales. It is *a priori* not clear, therefore, that the signal to background ratio is enhanced in diffractive events. It is precisely this question that we wish to study here.

The dominant mechanism for Higgs production at the LHC is gluon–gluon fusion via a top quark loop, see for example Ref. [KMS97].[6] The leading–order cross section is given by [Geo78]

$$\frac{d\sigma}{dy_H}(p_1 p_2 \to HX) = \frac{G_F \alpha_s^2(Q^2)}{32\sqrt{2}\pi} \frac{M_H^2}{s} \mathcal{I}\left(\frac{m_t^2}{M_H^2}\right) f_{g/p}(x_1, Q^2) f_{g/p}(x_2, Q^2), \qquad (1.66)$$

---

[5]The cross sections for double diffractive production, with two rapidity gaps, are readily estimated in this approach by combining two sets of diffractive parton distributions. Numerically, these are found to be much smaller (approximately 10% of the single diffractive cross sections).

[6]In our calculations we also include the direct $q\bar{q} \to H$ ($q = u, d, c, s, b$) quark–fusion processes, but these are numerically much less important.
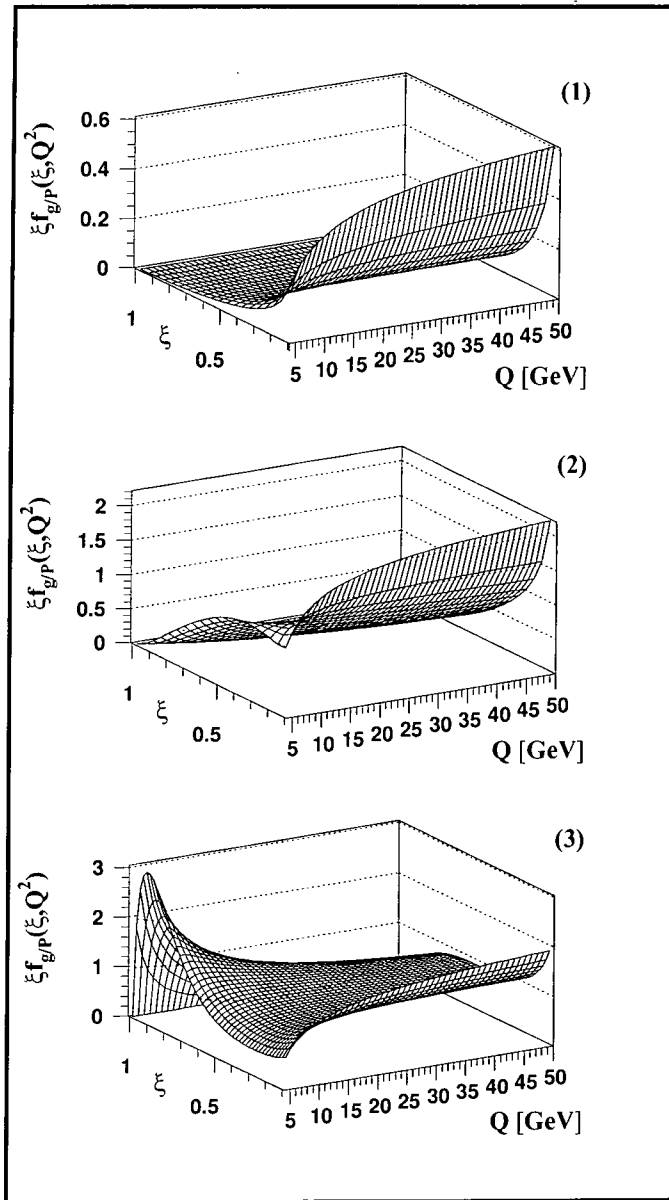
Figure 1.6: The Q^2 evolution of the gluon distributions $\xi f_{g/\mathbb{P}}(\xi, Q^2)$ in the three different Pomeron structure models of Ref. [KS96].

for a Higgs boson of mass M_H and rapidity y_H. The function $\mathcal{I}(x)$ in (1.66) can be approximated by

$$\mathcal{I}(x) \approx 1 + \frac{1}{4x}, \qquad \text{for } x > 1. \tag{1.67}$$

The longitudinal momentum fractions of the gluons inside the colliding protons are $x_{1,2} = (M_H/\sqrt{s})e^{\pm y_H}$. The single diffractive Higgs cross section is obtained from (1.66) by
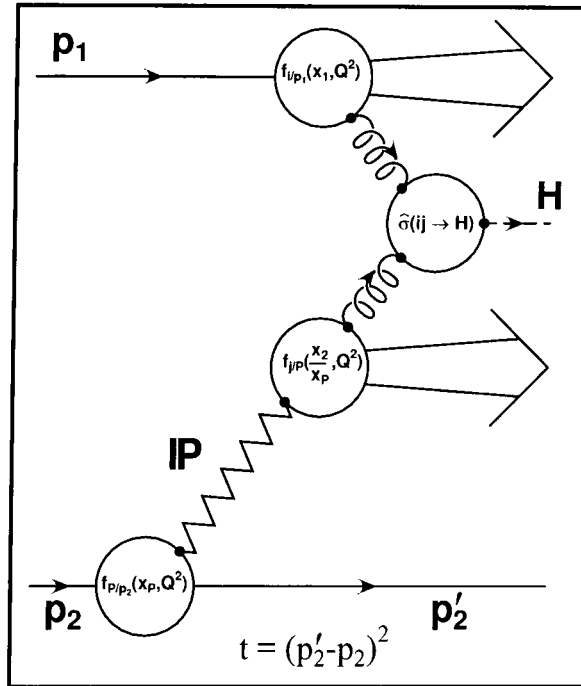
Figure 1.7: Kinematics of single diffractive Higgs production at the LHC via $p_1 p_2 \to p' H X$ and the subprocess $p_2 \to p'_2 \mathbb{P}$ with underlying gg fusion. All quantities of this figure are discussed and defined in the text.

replacing one of the $f_{g/p}(x, Q^2)$ by the corresponding diffractive parton distribution, i.e.

$$\frac{d\sigma_{SD}}{dy_H}(pp \to p' H X) = \frac{G_F \alpha_s^2(Q^2)}{32\sqrt{2}\pi} \frac{M_H^2}{s} \mathcal{I}\left(\frac{m_t^2}{M_H^2}\right)$$

$$\times \left[f_{g/p}^D(x_1, Q^2) f_{g/p}(x_2, Q^2) + f_{g/p}(x_1, Q^2) f_{g/p}^D(x_2, Q^2) \right], \quad (1.68)$$

where

$$f_{g/p}^D(x, Q^2) = \int dt \int \frac{dx_{\mathbb{P}}}{x_{\mathbb{P}}} f_{\mathbb{P}}(x_{\mathbb{P}}, t) \times f_{g/\mathbb{P}}(\xi, Q^2), \quad (1.69)$$

(cf. Eq. (1.64)). In the calculations which follow, the integration ranges are taken to be

$$x \le x_{\mathbb{P}} \le 0.1, \qquad 0 \le -t < \infty. \quad (1.70)$$

For the parton distributions $f_{i/p}(x, Q^2)$ in the proton we use the MRS(A$'$) set of partons [MRS95], with QCD scale parameter $\Lambda_{\overline{MS}}^{N_f=4} = 231$ MeV, which corresponds to $\alpha_s(M_Z^2) = 0.113$. At the level of accuracy to which we are working, all modern parton distribution sets give essentially the same results. The renormalisation/factorisation scale is chosen to be $Q^2 = M_H^2$. We use leading–order expressions for the signal and background cross sections, since our primary interest is in the ratio of diffractive to total cross sections, which should not be significantly affected by higher–order corrections to the basic subprocesses. In any case, the diffractive parton distribution fits to the deep inelastic data do not yet require NLO corrections.
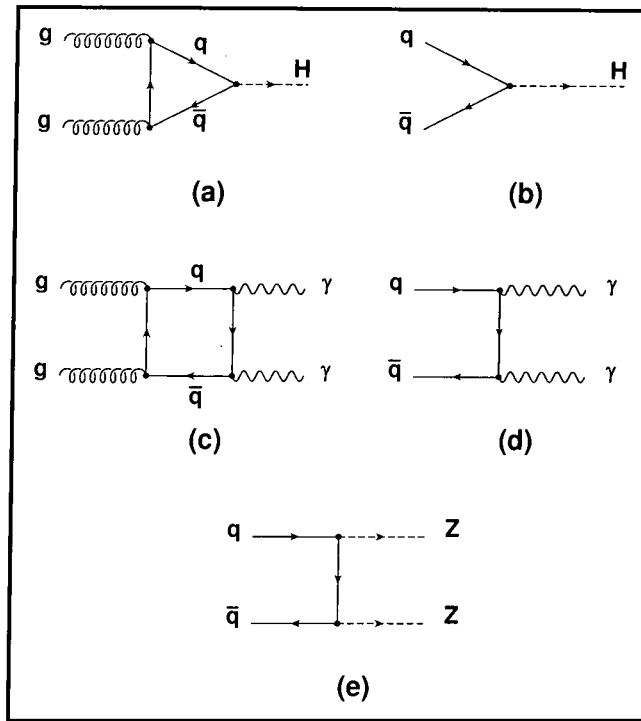
Figure 1.8: Feynman graphs for the production of Higgs bosons at the LHC via (a) gg fusion and (b) $q\bar{q}$ annihilation as well as the background contributions (c)–(e): $\gamma\gamma$ and ZZ.

The cleanest decay channel for searching for the intermediate mass Higgs boson at the LHC is $H \to \gamma\gamma$, with Br(H $\to \gamma\gamma$) $\sim 3 \times 10^{-4} - 3 \times 10^{-3}$ for 50 GeV$\leq M_H \leq$ 150 GeV [KMS97]. The irreducible background comes from the $\mathcal{O}(\alpha^2)$ $q\bar{q} \to \gamma\gamma$ [BBK71] and the $\mathcal{O}(\alpha^2\alpha_s^2)$ $gg \to \gamma\gamma$ [Com80] subprocesses. Note that these provide *lower* bounds to the background cross sections, since reducible backgrounds from e.g. $qg \to \gamma q(q \to \gamma, \pi^0, \ldots)$ can also be important in practice, see for example Ref. [KS89]. In what follows we will ignore these additional contributions, assuming that they can be suppressed by photon isolation cuts. For larger Higgs masses, i.e. for $M_H > 2M_Z$, the important decay channel is $H \to ZZ \to 4\ell^{\pm}$, with Br(H $\to$ ZZ) ≈ 0.3 [KMS97]. In this range, the dominant irreducible background is from $q\bar{q} \to ZZ$ [BM79]. We show the branching ratios of the Higgs in Fig. 1.9.

The Feynman graphs of signal and background processes are shown in Fig. 1.8.

In Fig. 1.10(a) we show the total (1.66) and single diffractive (1.68) Higgs cross sections, the latter calculated using the three sets of Pomeron parton distributions introduced above. As expected, Model 3 with the hard gluon gives the largest diffractive cross section. Model 1 has no gluons at all at the starting scale $Q_0 = 2$ GeV; gluons are dynamically created via DGLAP evolution at higher values of Q. However, the gluon distribution remains quite small compared to Models 2 and 3. Taking the models together, we see that between approximately 2% and 15% of Higgs events are expected to be singly diffractive.[7] Our results for the single diffractive and total Higgs cross sections

---

[7] Recall that we impose a cut $x_{\mathbb{P}} \leq 0.1$ when calculating the diffractive cross sections.
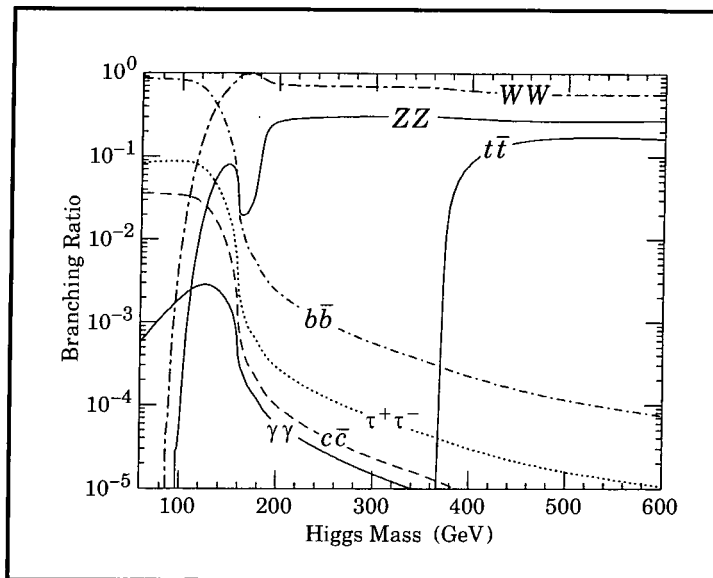
Figure 1.9: The branching ratios of the Higgs boson as a function of the Higgs mass. The $c\bar{c}$ rate depends sensitively on the poorly determined charm mass. The figure is taken from [PDG96].

are consistent with those obtained in Ref. [GV96] using similar models.

Fig. 1.10(b) shows the $\gamma\gamma$ background for the lower part of the mass range, with M_H now replaced by the $\gamma\gamma$ invariant mass $M_{\gamma\gamma}$. Note that in *both* Figs. 1.10(a) and 1.10(b) we impose a cut of $|y_\gamma| \leq 2$ to approximately account for the experimental acceptance. As the inset in Fig. 1.10(b) shows, the gluon–gluon fusion process dominates for very small $M_{\gamma\gamma}$ where small parton momentum fractions are probed. The $q\bar{q}$ subprocess dominates at large $M_{\gamma\gamma}$. The corresponding single diffractive cross sections are again largest for the gluon–richer Pomeron models, in particular Model 3. However, even the gluon–poor Model 1 becomes comparable to Model 2 due to the increasing $q\bar{q}$ contribution to the cross section at large $M_{\gamma\gamma}$.

The ZZ backgrounds, relevant for higher Higgs masses, are shown in Fig. 1.11(b). We see that in contrast to the $\gamma\gamma$ backgrounds of Fig. 1.10(b), all three Pomeron models give comparable diffractive cross sections over the entire M_{ZZ} range. This is because the diffractive quark distributions are constrained to be the same by the HERA F_2^D data.

Before discussing the single diffractive ratios of the signal and background processes, it is interesting to study in more detail the kinematics of diffractive Higgs production, in particular the typical values of the various momentum fractions in the calculation. Thus in Fig. 1.12 we show the average gluon momentum fraction $\langle x \rangle$ inside the Pomeron, the momentum fraction $x_{\mathbb{P}}$ of the Pomeron and the average value of the variable ξ with $\langle \xi \rangle = \langle x/x_{\mathbb{P}} \rangle$, as a function of M_H. The calculation of these quantities allows the Higgs cross sections in the different models to be related to the parton distributions of Fig. 1.6.

The gluon momentum fraction shows the typical $\langle x \rangle \propto M_H/\sqrt{s}$ behaviour which follows from the input $x_{1,2} = (M_H/\sqrt{s})e^{\pm y_H}$ for the momentum fractions of the gluons in $gg \rightarrow H$, Eq. (1.66). The fractional Pomeron momentum is of course constrained to
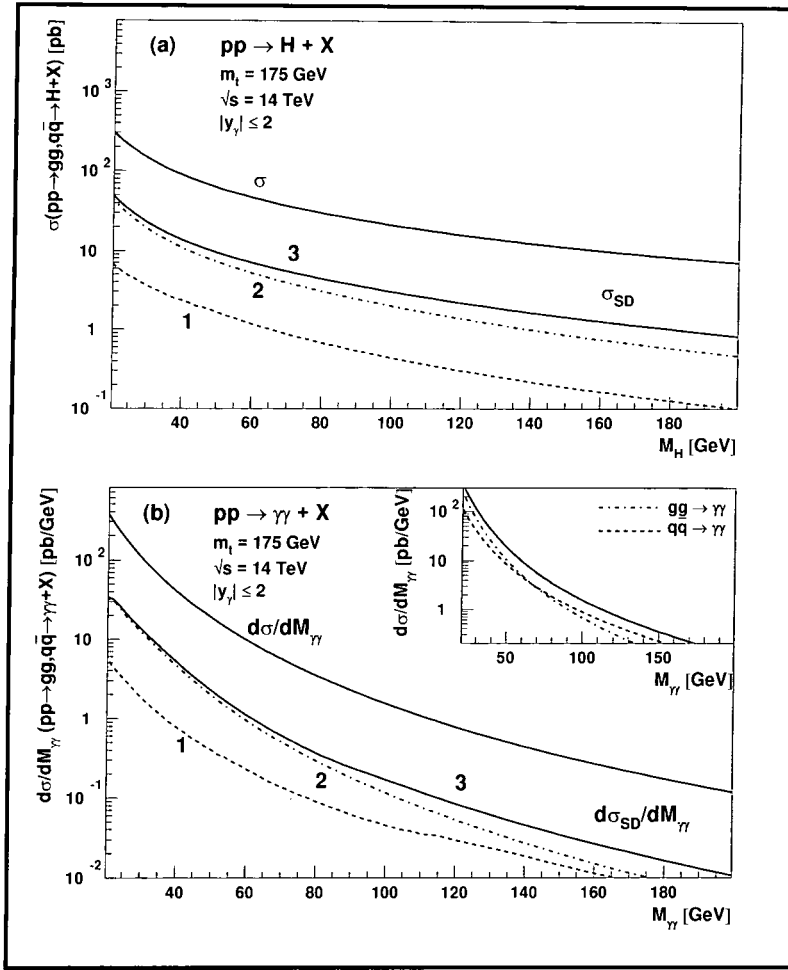
Figure 1.10: The total and the single diffractive cross sections for (a) Higgs production as a function of the Higgs mass M_H and (b) $\gamma\gamma$ production as a function of the invariant photon–photon mass $M_{\gamma\gamma}$ for the three different Pomeron models of Ref. [KS96]. For both signal (assuming the decay $H \to \gamma\gamma$) and background the photons are restricted to the central region by a cut in rapidity $|y_\gamma| \leq 2$. The inset in (b) shows the leading order cross section and the relative contributions from gluon–gluon fusion and quark–antiquark annihilation.

be $x_{\mathbb{P}} \leq 0.1$ and it stays very close to this upper limit throughout the complete range of M_H. It exhibits an almost linear but very weak M_H dependence for $M_H \geq 100$ GeV. The relevant variable for comparison with the parton distributions in Fig. 1.6 is $\xi = x/x_{\mathbb{P}}$. For light Higgs masses the values for $\langle\xi\rangle$ are small, ($\langle\xi\rangle < 0.1$ for $M_H < 100$ GeV). In this region of $Q = M_H$ Models 2 and 3 (cf. Figs. 1.6(b) and 1.6(c)) have approximately the same gluon content, which explains the similarity of the corresponding diffractive cross sections in Fig. 1.10(a). For higher values of M_H, the difference between Model 2 and Model 3 becomes more apparent: the gluon distribution in Model 3 remains roughly constant, while that of Model 2 decreases for higher values of M_H and ξ. This explains the differences between Models 2 and 3 in Figs. 1.10(a) and 1.10(b). We assume that the kinematics illustrated in Fig. 1.12 for the Higgs cross sections are also valid for the $\gamma\gamma$
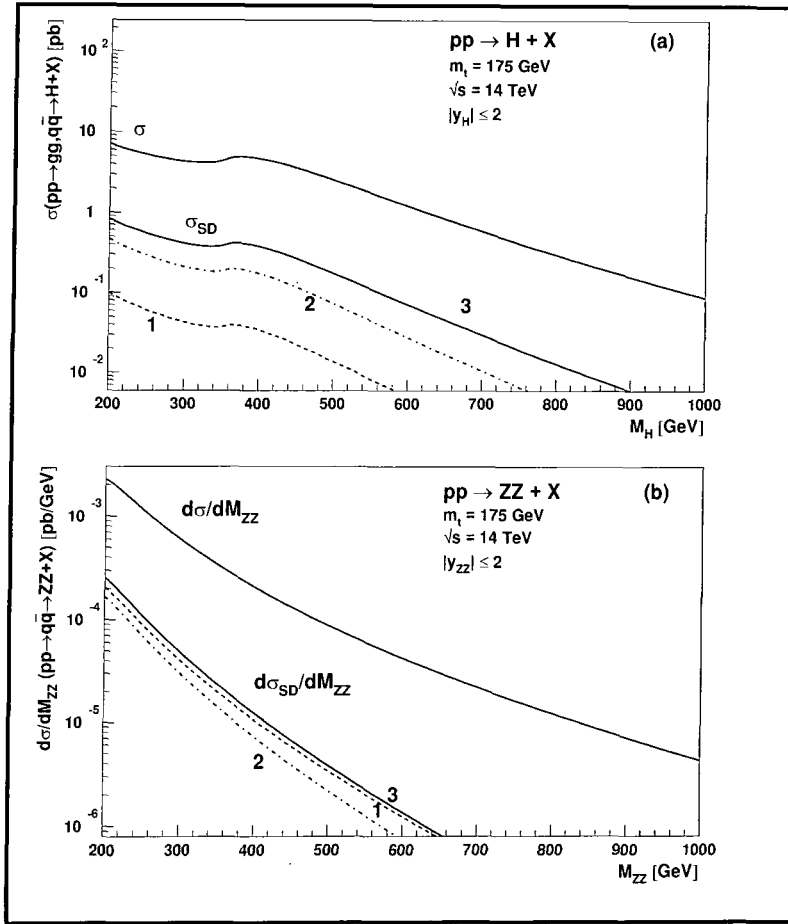
Figure 1.11: The total and the single diffractive cross sections for (a) Higgs production as a function of the Higgs mass M_H and (b) ZZ production as a function of the invariant ZZ mass M_{ZZ} for the three different Pomeron models. The Higgs and the ZZ pair are restricted to the central region by cuts $|y_{ZZ}|, |y_H| \leq 2$.

and ZZ backgrounds at the equivalent invariant mass.

Finally we present the single diffractive ratios $R_{\mathrm{SD}} = \sigma_{\mathrm{SD}}/\sigma$ for the signal $(pp \rightarrow H + X)$ and background contributions $(pp \rightarrow \gamma\gamma + X, pp \rightarrow ZZ + X)$ to see whether the signal to background ratio is indeed enhanced by the gluon–rich Pomeron. Fig. 1.13(a) shows the ratios for the Higgs mass range $M_H \leq 200$ GeV. For the gluon–rich Models 2 or 3, there is indeed a slight enhancement of R_{SD} for the signal compared to the background, for example in Model 3 for a Higgs mass of $M_H = 100$ GeV we find $R_{\mathrm{SD}}^H \sim 14\%$ compared to $R_{\mathrm{SD}}^{\gamma\gamma} \sim 11\%$. The enhancement persists over the whole Higgs mass range. For the gluon–poor Model 1, where the gluons are dynamically produced by DGLAP evolution, the background ratio is larger than the signal ratio for $M_H > 70$ GeV. This small enhancement has to be contrasted with the (at least) factor of 5 loss in the overall production rate.

The situation becomes even more dramatic if we go to higher Higgs masses (200 GeV $\leq M_H \leq 1000$ GeV) as shown in Fig. 1.13(b). In this case the important background
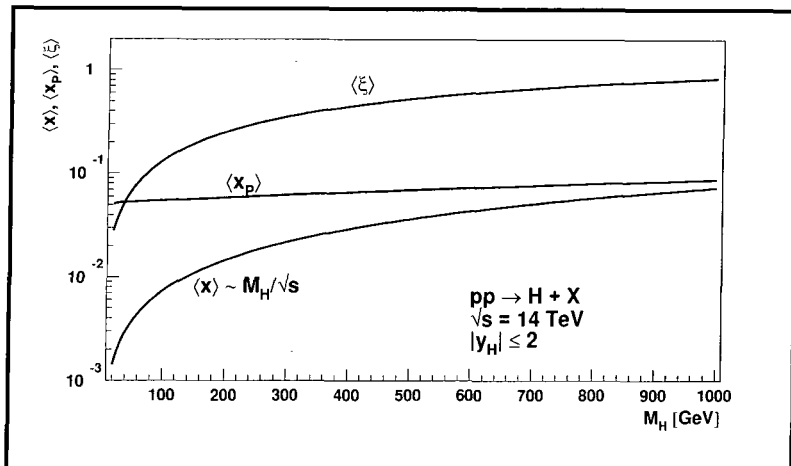
Figure 1.12: The average gluon fractional momentum $\langle x \rangle$, the average longitudinal momentum fraction of the Pomeron $\langle x_{\mathbb{P}} \rangle$ and the average value of the variable for the Pomeron parton distributions $\langle \xi \rangle = \langle x/x_{\mathbb{P}} \rangle$ for different values of M_H in the process $pp \to H + X$.

to Higgs production is direct ZZ pair production via quark–antiquark annihilation, as discussed above. As expected, in Model 1 the background ratio exceeds the signal ratio by a large factor (≈ 6 for $M_H = 200$ GeV). Even the gluon–richer Model 2 yields a higher background contribution for $M_H < 350$ GeV. Only at higher masses (i.e. evolution scales) are enough additional gluons produced to enhance the signal. Only the very gluon–rich Model 3, with enough gluons even at low scales, allows for a dominant signal ratio throughout the entire mass range.

In conclusion, we have calculated single diffractive Higgs cross sections for the LHC using diffractive parton distributions based on quark and gluon constituents of the Pomeron, fitted to HERA F_2^D data. In particular, we have considered three models which differ in the relative amounts of quarks and especially gluons. If the Pomeron is gluon–rich, then between 5% and 15% (depending on the Higgs mass) of Higgs events should have a single diffractive structure. Assuming the overall validity of this 'universal Pomeron structure' model, more precise measurements of F_2^D at HERA will allow more accurate predictions. However we have also shown that there is no significant enhancement of the signal to background ratio in such diffractive events. DGLAP evolution to high scales $Q \sim M_H$ automatically generates a mixture of diffractive quark and gluon distributions, and so the background processes $q\bar{q}, gg \to \gamma\gamma$ and $q\bar{q} \to ZZ$ also have a large diffractive component. It is not clear, therefore, that there is any advantage in searching for Higgs bosons at the LHC in events with rapidity gaps.

More on diffractive Higgs production

Nachtmann, Schäfer, Schöpf [NSS90]

The authors gave predictions for double diffractive inclusive Higgs production at future pp colliders using a partonic Pomeron picture as proposed by Ingelman and Schlein [IS85] with a soft–gluon distribution $\xi f_{g/\mathbb{P}}(\xi) = 6(1-\xi)^5$. This gluon distribution showed no evolution in Q^2. They conclude that approximately 1% of all events should be double
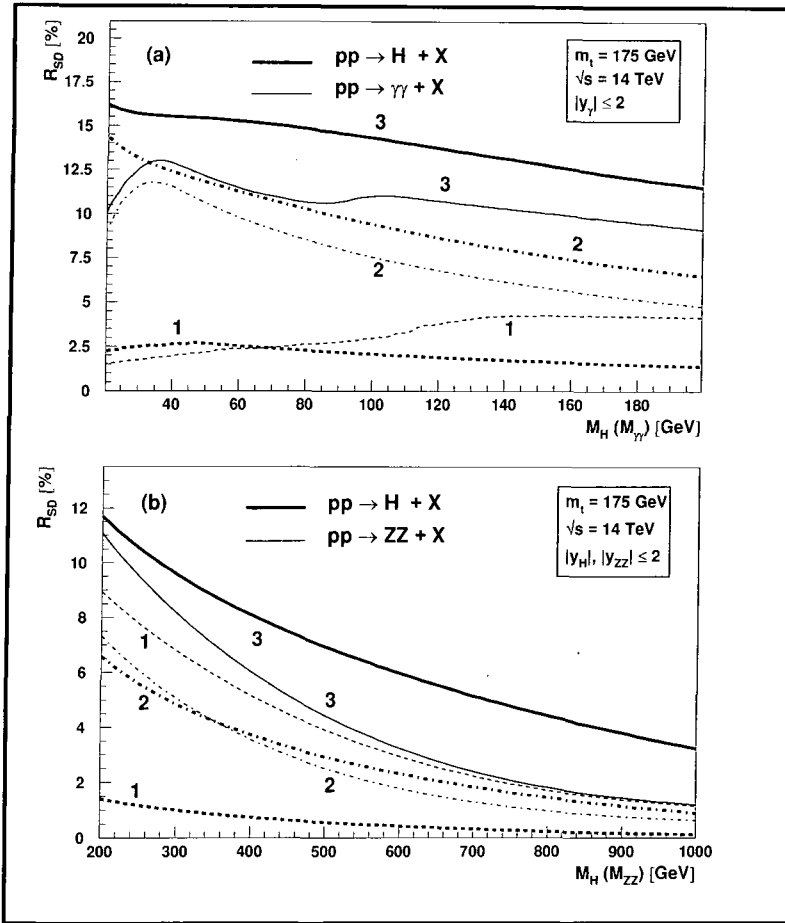
Figure 1.13: The single diffractive ratios $R_{\mathrm{SD}} = \sigma_{\mathrm{SD}}/\sigma$ for $pp \to H + X$ (thick lines) and the background contributions (a) $pp \to \gamma\gamma + X$ (thin lines) and (b) $pp \to ZZ + X$ (thin lines) for the three different Pomeron models. The absolute values of the cross sections σ and σ_{SD} are presented in Figs. 1.10 and 1.11.

diffractive.

Białas, Landshoff [BL91]

The authors worked with a pair of non–perturbative gluons exchanged between two quarks, addressing Regge theory. With the formulation of non–perturbative gluon propagators they also achieve a double diffractive ratio for inclusive Higgs production of $R_{\mathrm{DD}} \simeq 1\%$.

Bjorken [Bjo93]

Bjorken studied for the first time the survival probability of a rapidity gap in double diffractive dissociation. Assuming quark–quark scattering, he calculates (estimates) the ratio of the double diffractive total two–jet cross section in the process $pp \to pp + \mathrm{jet}_1 +$

jet$_2$, i.e. rapidity gaps between the two jets. His estimate yields

$$\frac{\sigma_{2j}^{\text{gap}}}{\sigma_{2j}} = \frac{1}{2}\left[\frac{4\pi}{33-2N_{\text{f}}}\right]^2 \langle |S|^2\rangle,\tag{1.71}$$

with $\langle |S|^2\rangle \simeq 5\%$ being the *survival probability* of a rapidity gap. Gotsman *et al.* [GLM93] calculated the quantity $\langle |S|^2\rangle$ to be approximately 30%.

Lu, Milana [LM95]

The authors study double diffractive *exclusive* Higgs production using a picture of *hard diffraction* which was supported by evidence from the UA8 collaboration [UA8.92] at CERN's $Sp\bar{p}S$ collider. They assume two–gluon exchange including triangle, box and pentagon top quark loops. They use as input a gluon distribution function of the type $xf_{g/p}(x, Q^2 = M_H^2) = 0.9x^{-\frac{3}{2}}(1-x)^5$.

Cudell, Hernandez [CH96]

The authors study single and double diffractive Higgs production at pp colliders assuming two–gluon exchange with the gluon form factor fitted to TEVATRON data. The double diffractive cross sections exceed the predictions by Białas and Landshoff by approximately 20%. Some values on R_{SD} are shown in Table 1.2.

Graudenz, Veneziano [GV96]

This work was the motivation for our studies. The authors studied single and double diffractive Higgs production at the LHC using different sets of parton distributions fitted by various groups to existing HERA data. A comparison of their results with our results is given in Table 1.2. Basically the only difference to our calculation are slightly different parton distributions for the Pomeron.

Khoze, Martin, Ryskin [KMR97]

The authors study exclusive and inclusive double diffractive Higgs production at LHC collider energies. The restriction on rapidity gap events is considered by the authors due to QCD radiative events: soft particles that may fill in the gaps. The inclusive cross sections are by an order of magnitude of four larger than the exclusive ones. They obtain, e.g., for a Higgs mass of $M_H = 100$ GeV an exclusive double diffractive cross section of $\sigma_{\text{DD}}^{\text{excl}} = 18 \times 10^{-5}$ pb and an inclusive double diffractive cross section of $\sigma_{\text{DD}}^{\text{incl}} = 0.3$ pb which gives $R_{\text{DD}} = 2\%$.

1.5 Diffractive heavy flavour production at the TEVATRON and the LHC

In this section we give predictions for single and double diffractive heavy flavour production at the TEVATRON $p\bar{p}$ collider ($\sqrt{s} = 1.8$ TeV) and the LHC pp collider, with a

M_H	[CH96]	[GV96]	our results
100 GeV	4.4%	$2\%^a$ - $27.5\%^b$	$2.5\%^c$ - $15.2\%^d$
500 GeV	11.2%	$0.6\%^a$ - $13.3\%^b$	$0.9\%^c$ - $7.1\%^d$

Table 1.2: Ratios $R_{\rm SD}$ for single diffractive Higgs production at the LHC ($\sqrt{s} = 14$ TeV) for two different Higgs masses M_H. We compare our results to results obtained by Cudell and Hernandez [CH96] and Graudenz and Veneziano [GV96].
[a]: H1 fit of the Pomeron partonic content with no gluons at starting scale and soft quark distribution;
[b]: H1 fit of the Pomeron partonic content with hard gluons at starting scale and soft quark distribution;
[c]: Model 1; [d]: Model 3.

centre–of–mass energy $\sqrt{s} = 10 - 14$ TeV. By heavy flavour we mean $Q\bar{Q}$ production with massive $Q = c, b$ or t quarks. In contrast to the diffractive Higgs production that we discussed in the previous section, we expect the cross sections of $Q\bar{Q}$ states to be typically larger and this makes their observation, especially in the diffractive context, easier in principle. Again we shall address the DLM presented in Section 1.2 and the three models of partonic structure functions for the Pomeron by Kunszt and Stirling [KS96], discussed in Section 1.3. For further studies on *diffractive heavy flavour production* using a two–gluon model, we refer to [BS92, Sze93].

We shall also consider double diffractive events. The procedure is analogous to the single diffractive scenario. Now *both* hadrons undergo Pomeron emission and therefore all hadronic parton distributions are replaced by the parton distributions of the Pomeron. However, the basic formulation of diffractive scattering was intended for reactions where one hadron scatters diffractively and one hadron is highly excited. In the double diffractive case now both colliding hadrons can in principle be detected in the final state. A typical reaction at the LHC would look like: $pp \rightarrow pp + Q\bar{Q} + X$. Double diffractive events thus are characterised by two quasi–elastic protons with rapidity gaps between them and the central heavy flavour products.

The subprocesses leading to heavy quark pairs are $q\bar{q}$ annihilation and gg fusion, the latter being the main mechanism at the LHC where antiquarks only show up as sea quarks in the colliding protons. The subprocesses are sketched in Fig. 1.14. The total cross section can be written as

$$\sigma(p_1 p_2 \rightarrow Q\bar{Q}\, X) = \sum_{i,j} \int {\rm d}x_1 \int {\rm d}x_2 \, f_{i/p_1}(x_1, Q^2) f_{j/p_2}(x_2, Q^2) \hat{\sigma}_{ij}(\hat{s}, m_Q^2, Q^2), \quad (1.72)$$

with $i, j = g, q, \bar{q}$. We only cite the expressions for the leading order subprocess cross
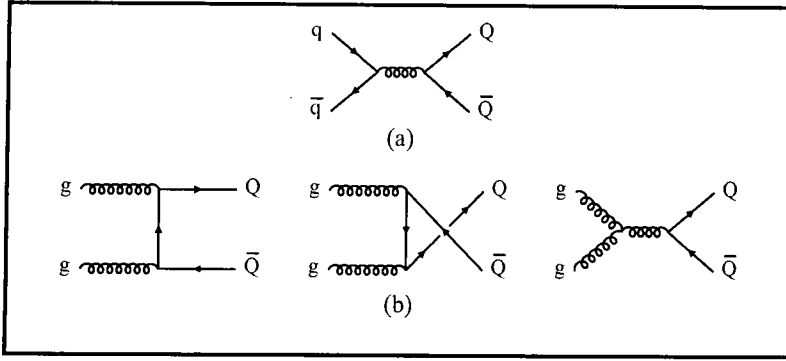
Figure 1.14: The leading–order Feynman diagrams for the subprocesses (a) $q\bar{q} \to Q\bar{Q}$ and (b) $gg \to Q\bar{Q}$.

sections [Com79, GOR78]

$$\hat{\sigma}_{q\bar{q}}(\hat{s}, m_Q^2, Q^2) = \frac{\alpha_s^2 \pi}{m_Q^2} \frac{\gamma\rho}{27} (2 + \rho), \tag{1.73}$$

$$\hat{\sigma}_{gg}(\hat{s}, m_Q^2, Q^2) = \frac{\alpha_s^2 \pi}{m_Q^2} \frac{\gamma\rho}{192} \left\{ \frac{1}{\gamma} \left(\rho^2 + 16\rho + 16 \right) \ln \left(\frac{1+\gamma}{1-\gamma} \right) - 28 - 31\rho \right\}, \tag{1.74}$$

$$\hat{\sigma}_{gq}(\hat{s}, m_Q^2, Q^2) = 0, \tag{1.75}$$

$$\hat{\sigma}_{g\bar{q}}(\hat{s}, m_Q^2, Q^2) = 0, \tag{1.76}$$

with $\hat{s} = x_1 x_2 s$, $\rho = 4m_Q^2/\hat{s}$ and $\gamma = \sqrt{1-\rho}$. Note that all $\hat{\sigma}_{ij}$ vanish at high energies ($\rho \to 0$) and at threshold ($\gamma \to 0$). Again we concentrate on studies at leading order as we are interested in single R_{SD} and double diffractive R_{DD} ratios and expect higher–twist corrections to cancel.

For the single diffractive cross section we proceed as we did in Section 1.4, replacing parton distribution functions by diffractive ones. In extension to Eq. (1.72) we write

$$\sigma_{\mathrm{SD}}(p_1 p_2 \to p' Q\bar{Q} X) = \sum_{i,j} \int \mathrm{d}x_1 \int \mathrm{d}x_2 \, \{ f_{i/p_1}^{\mathrm{D}}(x_1, Q^2) f_{j/p_2}(x_2, Q^2)$$
$$+ \; f_{i/p_1}(x_1, Q^2) f_{j/p_2}^{\mathrm{D}}(x_2, Q^2) \} \hat{\sigma}_{ij}(\hat{s}, m_Q^2, Q^2), \tag{1.77}$$

and for the double diffractive cross section

$$\sigma_{\mathrm{DD}}(p_1 p_2 \to p_1' p_2' Q\bar{Q} X) = \sum_{i,j} \int \mathrm{d}x_1 \int \mathrm{d}x_2 \, f_{i/p_1}^{\mathrm{D}}(x_1, Q^2)$$
$$\times \; f_{j/p_2}^{\mathrm{D}}(x_2, Q^2) \, \hat{\sigma}_{ij}(\hat{s}, m_Q^2, Q^2). \tag{1.78}$$

In analogy to Eq. (1.69) we substitute the diffractive parton distributions via

$$f_{\ell/p}^{\mathrm{D}}(x, Q^2) = \int \mathrm{d}t \int \frac{\mathrm{d}x_{\mathrm{IP}}}{x_{\mathrm{IP}}} \, f_{\mathrm{IP}}(x_{\mathrm{IP}}, t) \times f_{\ell/\mathrm{IP}}(\xi, Q^2), \tag{1.79}$$

using again the Donnachie–Landshoff flux factor $f_{\mathrm{IP}}(x_{\mathrm{IP}}, t)$ defined in Eq. (1.60) with the kinematical constraint (1.70).

The renormalisation scale is taken to be the subprocess collision energy, $Q^2 = \hat{s}$. One might however argue that for the $gg \to Q\bar{Q}$ subprocess the $\hat{t}$– and $\hat{u}$–channel contributions should dominate [GOR78], in which case a choice of $Q^2 = \frac{1}{2}\left((m_Q^2 - \hat{t}) + (m_Q^2 - \hat{u})\right) = \frac{1}{2}\hat{s}$ might be more reasonable. In fact the parton distributions *are* affected by the choice of Q^2 in the framework of DGLAP evolution. But as in [Com79] we could *not* find a significant sensitivity of our results to this choice compared to a general $Q^2 = \hat{s}$ for both subprocesses.

1.5.1 Diffraction at the TEVATRON

We calculate numerically the total inclusive, the single diffractive and the double diffractive cross sections for heavy flavour pair–production using the MRS(A$'$) [MRS95] set of partons and the three Pomeron models introduced in [KS96] and discussed in Section 1.3. Our results are shown in Fig. 1.15. In addition we show the pure gluon fusion contribution as dashed lines.

For the TEVATRON collider the $q\bar{q}$ process becomes dominant for $m_Q > 50$ GeV. This $q\bar{q}$ dominance is obviously visible in the total cross section but becomes even more striking for the single diffractive one. Due to this process, the single diffractive ratio R_{SD} defined as $R_{\text{SD}} = \sigma_{\text{SD}}/\sigma$ even *increases* for $m_Q > 70$ GeV before this process runs out of centre–of–mass energy due to the cut–off in the Pomeron spectrum ($x_{\mathbb{P}} \leq 0.1$) and steeply falls to zero. Note that this restriction on $\sqrt{\hat{s}}$ unfortunately takes place before the top quark production domain is reached. The single diffractive ratio R_{SD} for all three Pomeron models reaches its local maximum at slightly lower masses than the top quark mass. This gives little hope to observe diffractive top quark events at the TEVATRON but is promising for the LHC.

At TEVATRON energy the threshold for single diffractive events is reached when $m_Q = 270$ GeV. But single diffractive events might be *observed* only up to $m_Q \approx 150$ GeV with

$$\textbf{Model 3}: \quad \sigma_{\text{SD}}^{\text{max}} \;\;=\;\; 1.05 \text{ pb} \simeq 4.05\% \text{ of } \sigma\,,$$
$$\textbf{Model 1}: \quad \sigma_{\text{SD}}^{\text{min}} \;\;=\;\; 0.22 \text{ pb} \simeq 0.86\% \text{ of } \sigma\,,$$

for $m_Q = 150$ GeV. This is qualitatively what we expect. Model 3 with the hard gluon content gains more and more $q\bar{q}$ pairs via DGLAP evolution which dominantly contribute to the single diffractive cross section for higher masses. Model 2 with the quark–gluon mixture dominates for small masses, but at $m_Q \simeq 10$ GeV Model 3 takes over. The production rate of the important $q\bar{q}$ pairs for higher masses increases more rapidly in Model 3. Model 1, however, without any gluons at the initial Q_0 scale, marks the lower limit for single and double diffractive scattering over the whole mass range. The numerical values for the single and double diffractive production of charm, bottom and top are given in Table 1.3.

Let us now focus on Models 2 and 3: the ratios for single diffractive scattering range between $\sim 22\%$ for charm and $\sim 15\%$ for bottom quark production and reach their locally lowest values of $\sim 2\%$ for $m_Q = 70$ GeV, before the ratio even increases due to the $q\bar{q}$ contribution in the mass region 70 GeV $\leq m_Q \leq$ 150 GeV locally peaking at $m_Q = 150$ GeV with ratio $R_{\text{SD}} = 5.5\%(4.2\%)$ for Model 3 (2). *Qualitatively* Model 1 shows the same behaviour. But with only quarks in the starting distribution, the creation of gluons and $q\bar{q}$ pairs via DGLAP evolution proceeds only slowly. This can be seen in
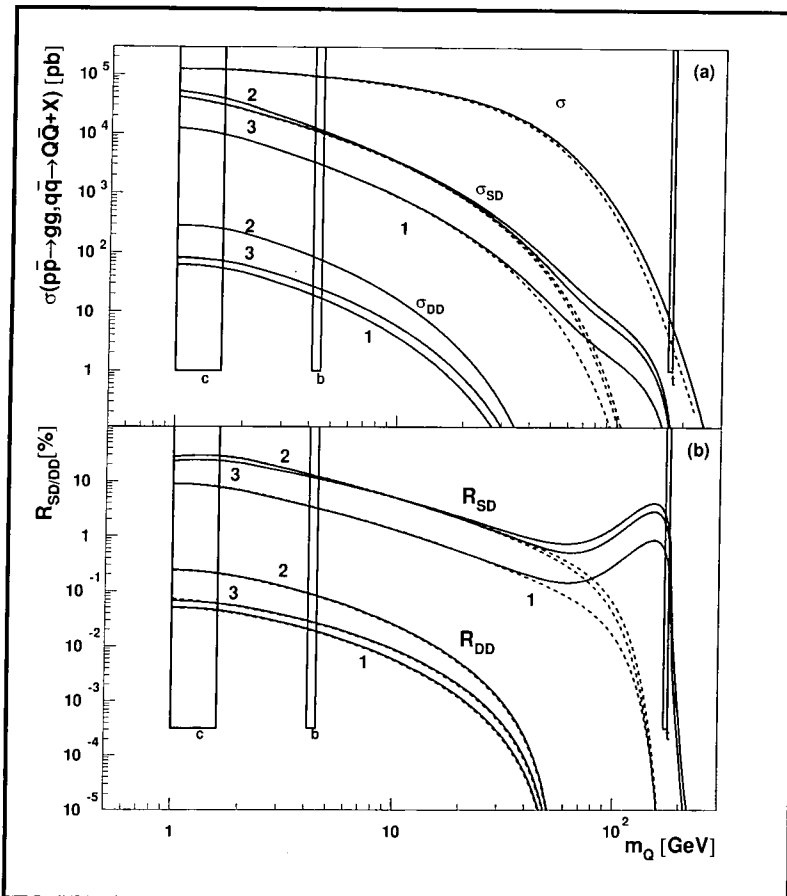
Figure 1.15: The numerical results of the total, single and double diffractive cross sections for the three Pomeron models are shown. The solid lines indicate the subprocess $gg + q\bar{q} \rightarrow Q\bar{Q}$, the dashed lines show solely the contribution from gluon fusion ($gg \rightarrow Q\bar{Q}$): (a) gives the absolute numbers for the cross sections (in pb), and (b) gives the ratios ($R_{\mathrm{SD}} = \sigma_{\mathrm{SD}}/\sigma$ and $R_{\mathrm{DD}} = \sigma_{\mathrm{DD}}/\sigma$). The mass regions of the charm (c), bottom (b) and top (t) quarks are indicated. The fixed centre–of–mass energy is 1.8 TeV.

Fig. 1.6. The difference is expressed in the large gap between Model 1 on the one hand and Models 2 and 3 on the other hand. So the conclusion is that at least for single diffraction a gluon rich Pomeron as input should be more easily detected. Model 1 and Model 3 for example differ by about one order of magnitude. This turns out to be a crucial difference with such absolutely small diffractive cross sections.

Double diffractive scattering seems to favour a balanced mixture of quarks and gluons in the starting distribution and during DGLAP evolution, as provided in Model 2. This can again be observed in Fig. 1.15.

Notice that the former dominant hard gluon Model 3 *quantitatively* shows about the same behaviour as Model 1. Why the behaviour of Model 3 in double diffraction is different from that in single diffraction can be understood by a further analysis of the kinematics among the partons inside the Pomeron and their distributions at different mass scales. Models 2 and 3 show a *crossing* in the case of single diffractive scattering

	TEVATRON ($\sqrt{s} = 1.8$ TeV)			LHC ($\sqrt{s} = 10.0$ TeV)		
	$\langle m_c \rangle$			$\langle m_c \rangle$		
model	1	2	3	1	2	3
$\sigma_{\rm SD}$[pb]	$7.81 \cdot 10^3$	$29.82 \cdot 10^3$	$24.32 \cdot 10^3$	$2.07 \cdot 10^6$	$3.59 \cdot 10^6$	$3.78 \cdot 10^6$
$R_{\rm SD}$[%]	6.83	26.15	21.27	21.43	37.21	39.21
$\sigma_{\rm DD}$[pb]	45.32	208.12	60.68	$4.05 \cdot 10^4$	$6.56 \cdot 10^4$	$4.44 \cdot 10^4$
$R_{\rm DD}$[%]	$3.96 \cdot 10^{-2}$	$18.21 \cdot 10^{-2}$	$5.31 \cdot 10^{-2}$	0.42	0.68	0.46
	$\langle m_b \rangle$			$\langle m_b \rangle$		
model	1	2	3	1	2	3
$\sigma_{\rm SD}$[pb]	$3.07 \cdot 10^3$	$11.59 \cdot 10^3$	$10.68 \cdot 10^3$	$4.50 \cdot 10^5$	$1.01 \cdot 10^6$	$1.11 \cdot 10^6$
$R_{\rm SD}$[%]	3.31	12.49	11.51	15.50	34.53	38.27
$\sigma_{\rm DD}$[pb]	17.82	78.85	25.26	$5.81 \cdot 10^3$	$1.51 \cdot 10^4$	$7.55 \cdot 10^3$
$R_{\rm DD}$[%]	$1.92 \cdot 10^{-2}$	$8.49 \cdot 10^{-2}$	$2.72 \cdot 10^{-2}$	0.20	0.52	0.26
	$\langle m_t \rangle$			$\langle m_t \rangle$		
model	1	2	3	1	2	3
$\sigma_{\rm SD}$[pb]	$1.86 \cdot 10^{-2}$	$6.06 \cdot 10^{-2}$	$8.72 \cdot 10^{-2}$	1.13	4.10	5.45
$R_{\rm SD}$[%]	0.31	1.01	1.45	0.34	1.25	1.66
$\sigma_{\rm DD}$[pb]	○	○	○	$1.04 \cdot 10^{-4}$	$1.86 \cdot 10^{-2}$	$3.71 \cdot 10^{-3}$
$R_{\rm DD}$[%]	○	○	○	$3.17 \cdot 10^{-4}$	$5.68 \cdot 10^{-3}$	$1.13 \cdot 10^{-3}$

Table 1.3: The values for single and double diffractive cross sections, as well as their ratios to the total cross sections, are shown for average quark masses $\langle m_c \rangle = 1.3$ GeV, $\langle m_b \rangle = 4.3$ GeV and $\langle m_t \rangle = 176$ GeV. We obtain numerical data for both the TEVATRON and the LHC. A ○ indicates that the threshold for this process was exceeded.

as can be observed in Fig. 1.15. Its existence can be immediately explained in terms of the gluon distributions which are shown in Fig. 1.6. As we have already pointed out, the gluon distributions govern the behaviour of the cross sections at the TEVATRON, especially for small quark masses. For small ξ and Q, the gluon distribution of Model 2 is slightly bigger than that of Model 3. For higher ξ and/or Q the situation is reversed.

In the case of double diffraction, an analysis of the average fractional gluon momentum inside the Pomeron $\langle \xi \rangle = \langle x/x_{\mathbb{P}} \rangle$ yields $\langle \xi \rangle \sim 0.11$ for $m_Q = 2$ GeV and $\langle \xi \rangle \sim 0.24$ for

$m_Q = 50$ GeV for all three models. In this regime the gluon distribution of Model 2 again exceeds that of Model 3. So, no crossing can be observed and Model 2 dominates throughout. In fact the crossing would take place at $m_Q \sim 80$ GeV, shortly before the threshold for double diffraction with $m_Q \sim 90$ GeV is reached.

The relatively broad gap between Model 2 and Model 3 appearing in Fig. 1.15 can again be explained by the same straightforward analysis of the average gluon momentum. Again a comparison with the corresponding gluon distributions of Model 2 and Model 3 in Fig. 1.6 shows the absolute difference of these distributions in the regime $0.1 \leq \langle \xi \rangle \leq 0.2$.

While diffractive charm and bottom quark production might be observable at the TEVATRON, there is no hope for diffractive $t\bar{t}$ pair production being visible at a total centre–of–mass energy of $\sqrt{s} = 1.8$ TeV. Either the top mass exceeds the kinematic threshold (double diffraction) or the effect of the threshold is already strongly influencing the process by a steep decrease in the diffractive cross section (single diffraction near top mass). However at the LHC such heavy flavour threshold suppression is less severe, as we shall see now.

1.5.2 Diffraction at the LHC

The LHC will provide a rich field of study for diffractive events, even in the top mass regime. With a centre–of–mass energy of at least $\sqrt{s} = 10$ TeV the double diffractive threshold is reached for $m_Q = 500$ GeV and the single diffractive one lies at $m_Q = 1500$ GeV. This upper bound is very promising in particular for diffractive top quark production at the LHC.

At a proton–proton collider, the dominant process for $Q\bar{Q}$ production is of course gluon–gluon fusion since antiquarks only appear as sea quarks inside the proton. For a top mass of 176 GeV the pure gg contribution is about 91% of the total cross section in our calculation. This also holds for the single and double diffractive case.

The numerical results are shown in Fig. 1.16 and the numerical values are again listed in Table 1.3. The single diffractive ratios R_{SD} for the three Pomeron models are between $20 - 40\%$ for charm and $10 - 40\%$ for bottom quarks. The maximal and minimal single diffractive top quark rates are

$$\mathbf{Model\ 3}: \quad \sigma_{\mathrm{SD}}^{\max} \; = \; 5.45 \ \mathrm{pb} \simeq 1.66\% \ \text{of} \ \sigma \,,$$
$$\mathbf{Model\ 1}: \quad \sigma_{\mathrm{SD}}^{\min} \; = \; 1.13 \ \mathrm{pb} \simeq 0.34\% \ \text{of} \ \sigma \,,$$

with $m_t = 176$ GeV. Even though the single diffractive ratios for top production are comparable to the TEVATRON rates, the *absolute* single diffractive cross sections are crucially enhanced. We find an enhancement of about a factor 100 at the LHC. For example Model 2 and Model 3 provide a single diffractive cross section of approximately 5 pb. This is about the total cross section for top production at the TEVATRON. So, single diffractive top quark events should be readily detected at the LHC.

The predictions for double diffractive scattering, however, are still not very promising. The maximal double diffractive cross section (for Model 2) is $1.86 \cdot 10^{-2}$ pb for top quarks. The qualitative behaviour of the three different Pomeron models is the same. Because the centre–of–mass energy at the LHC is larger by a factor of six, one can conclude from the qualitatively similiar behaviour of all three models at the LHC that the gluon distributions in all three models do indeed become similiar at higher Q, as already seen in Fig. 1.6.
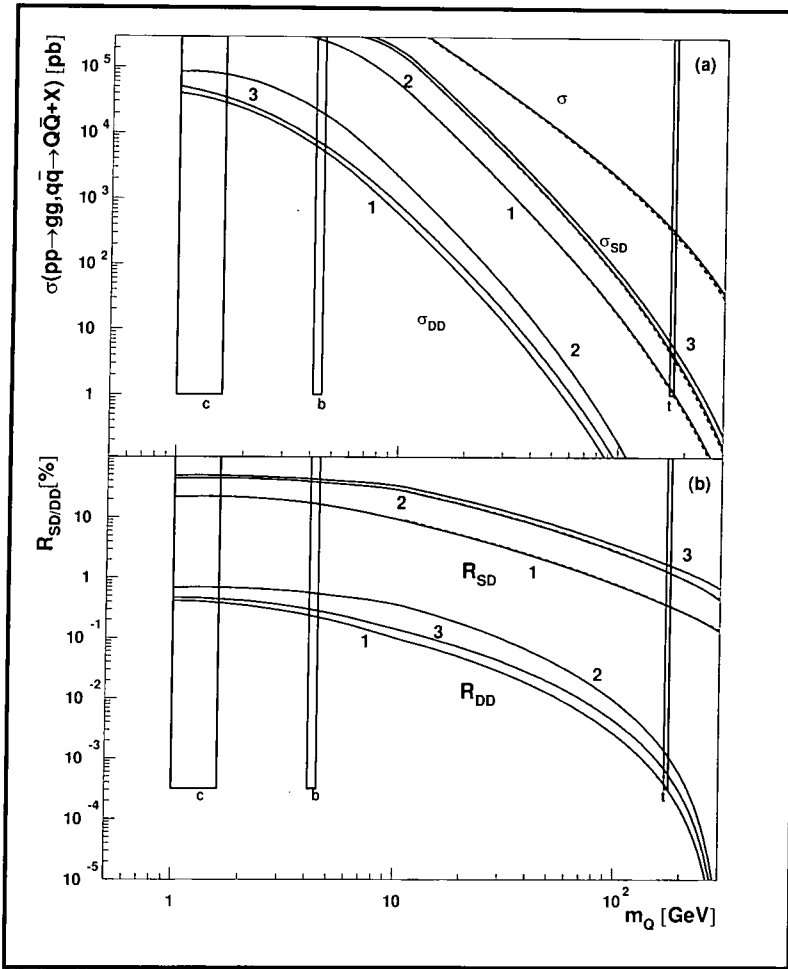
Figure 1.16: Same as Fig. 1.15 but now for a centre–of–mass energy of 10 TeV. The solid lines indicate the subprocess $gg + q\bar{q} \to Q\bar{Q}$, the dashed lines show solely the contribution from gluon fusion ($gg \to Q\bar{Q}$): (a) gives the absolute numbers for the cross sections (in pb), and (b) gives the ratios ($R_{SD} = \sigma_{SD}/\sigma$ and $R_{DD} = \sigma_{DD}/\sigma$).

All conclusions that were drawn for the TEVATRON still hold for the LHC, except that because of the higher centre–of–mass energy there are no kinematical artifacts in the considered flavour mass regime. Even for the top quark mass, the single as well as the double diffractive cross section behave rather smoothly. The influence of the threshold does not seriously affect the cross sections in this case.

Considering the ratios for single and double diffractive events in Fig. 1.16 again shows a qualitatively comparable picture to the TEVATRON. Again an analysis of the average fractional gluon momentum $\langle \xi \rangle$ will explain the differences in R_{SD} and R_{DD}. For R_{SD}, Models 2 and 3 are *quantitatively* equivalent, especially for the charm and bottom quarks. For a bottom quark mass of $m_b = 4.5$ GeV, we obtain as average fractional gluon momentum $\langle \xi \rangle = 0.42$ for $Q \sim 2m_b = 9$ GeV in the single diffractive case. A comparison with the gluon distributions in Fig. 1.6 shows that they are roughly equal for Model 2 and Model 3 in this region of ξ.

For the case of double diffraction the same analysis yields a lower average fractional momentum for the gluons, due to the energy–cut among both Pomeron emitting hadrons. Again for $m_b = 4.5$ GeV we obtain $\langle \xi \rangle = 0.22$. But in this region of ξ, the gluon distribution of Model 3 shows a local minimum, the hard gluons in this model give a rise of $\xi f_{g/\mathbb{P}}(\xi, Q^2)$ only for $\xi > 0.5$ in the low-Q regime. The gluon distributions inside Model 2 also show a local minimum around $\xi \sim 0.2$, but its absolute value is higher than that for Model 3 in this region. This fact is responsible for the gap between Model 2 and Model 3 as observed for R_{DD} in Fig. 1.16. For higher quark masses (higher values of Q^2) all three models become comparable concerning the gluon distributions, as already discussed.

Model 2 and Model 3 as descriptions of the parton distributions of the Pomeron yield very promising single diffractive ratios, at least for charm and bottom quarks. Model 3 predicts a single diffractive ratio of $\sim 40\%$ for $c\bar{c}$ and $b\bar{b}$ production. This is quantitatively comparable to the predictions of Model 2 as can be observed in Fig. 1.16 and numerically verified in Table 1.3. Thus about one third of the production of heavy flavours at the LHC including charm and bottom quarks should be single diffractive. But even Model 1, purely quark–like at starting scale $Q_0^2 = 2$ GeV^2, gives a single diffractive contribution of approximately 20% in this mass regime.

1.6   Results on diffraction from the TEVATRON and HERA

We shall briefly summarise the status of experimental results on diffraction obtained at the TEVATRON and HERA. We do not claim that this list is complete.
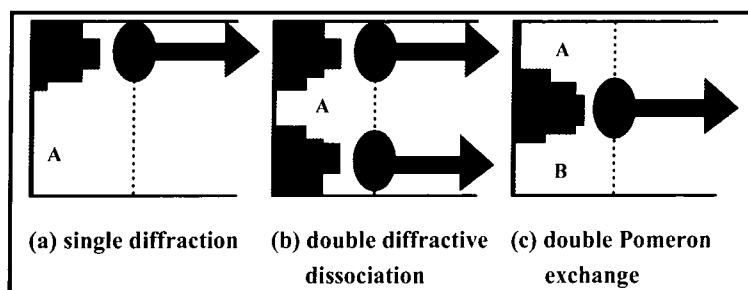
Figure 1.17: Schematic view of single and double diffractive events at hadron–hadron colliders. The energy deposition is indicated and so are the rapidity gaps A and B.

1.6.1   TEVATRON

We already reported on measurements of single diffractive cross sections (*cf.* Fig. 1.17(a)) at the TEVATRON [CDF94] in Section 1.2. The conclusion of this study was that the Pomeron intercept shows an energy dependence and shadowing corrections have to be introduced to save the traditional Pomeron picture.

The next investigation was the observation of rapidity gaps *between* two produced jets at the TEVATRON by the CDF [CDF95] and the D∅ [D∅.94] collaboration. The

observation is due to double diffractive dissociation (*cf.* Fig. 1.17(b)), mediated by, e.g. a colour–neutral two hard gluon exchange and no soft particles filling in the gap.

p ⟶ jet

gap

p̄ ⟶ jet
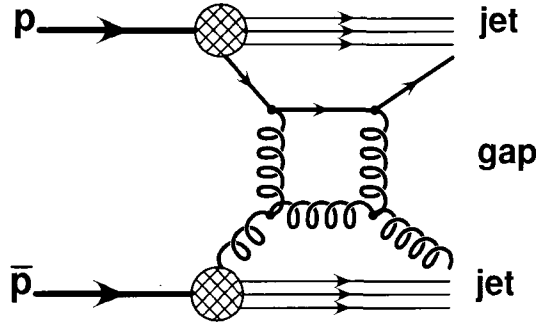
We discussed the estimate of such a model in terms of *rapidity gap survival probability* [Bjo93] in Section 1.4. At $\sqrt{s} = 1.8$ TeV the D∅ collaboration measured rapidity gaps in two–jet events. The constraint was no energy deposition in the rapidity interval between the two jets $\Delta\eta_{\mathrm{jj}}$. For $\Delta\eta_{\mathrm{jj}} > 3$ the integrated luminosity of all events fulfilling this constraint was $\int \mathrm{d}t\, \mathcal{L}(t) = 5.4$ pb^{-1}. They observed a ratio of events with rapidity gap (*jet–gap–jet events*) of

$$R^{\mathrm{gap}}_{\mathrm{jj}}(\Delta\eta_{\mathrm{jj}} > 3) = 0.53\% \pm 0.07\%^{\mathrm{stat.}} \pm 0.06\%^{\mathrm{syst.}}, \tag{1.80}$$

and thus could estimate the *rapidity gap survival probability* to be $\langle |S|^2 \rangle \simeq 0.1$ in accordance with [Bjo93].

The CDF collaboration obtained a slightly higher ratio

$$R^{\mathrm{gap}}_{\mathrm{jj}}(\Delta\eta_{\mathrm{jj}} > 0.8) = 0.85\% \pm 0.12\%^{\mathrm{stat.}} \,{}^{+0.24}_{-0.12}\%^{\mathrm{syst.}}, \tag{1.81}$$

with a lower separation in rapidity between the two jets allowed. Thus both results seem to be consistent with each other.

There are also data on single diffractive jet production available from CDF [CDF97a] and D∅ [D∅.96]. Both collaborations search for single diffractive events including a jet by looking at the measured multiplicity distributions. CDF looks, in the region opposite the dijet system, for correlations between the multiplicity measured in the forward part of the calorimeter ($2.4 < |\eta| < 4.2$) and the number of hits measured in a scintillator counter close to the beampipe (diffractively scattered proton). The ratio of single diffractive events to standard dijet events $R^{\mathrm{CDF}}_{\mathrm{SD}}(p\bar{p} \to p'X)$ is measured and reported to be

$$R^{\mathrm{CDF}}_{\mathrm{SD}}(p\bar{p} \to p'X) = 0.75\% \pm 0.05\%^{\mathrm{stat.}} \pm 0.09\%^{\mathrm{syst.}}. \tag{1.82}$$

D∅ looked for single diffractive events in the dijet sample ($E^{\mathrm{jet}}_{T} > 12$ GeV, $|\eta_{\mathrm{jet}}| > 1.6$) using a similar method to CDF. Their reported value is

$$R^{\mathrm{D0}}_{\mathrm{SD}}(p\bar{p} \to p'X) = 0.67\% \pm 0.05\%^{\mathrm{stat.+syst.}}. \tag{1.83}$$

We see that our results (taking single and double diffractive events together) for heavy quark production remarkably exceed the TEVATRON measurements. CDF conclude that the gluon fraction inside the Pomeron should be 0.7 ± 0.2 and thus yielding a gluon dominated Pomeron.

Also from CDF [CDF97b] there are data on diffractive W+jet production available

$$R_{\mathrm{SD}}^{\mathrm{CDF}}(p\bar{p} \to p'WX) = 1.15\% \pm 0.55\%\,. \tag{1.84}$$

The standard flux prediction for a three flavour hard–quark Pomeron structure is

$$R_{\mathrm{SD}}^{\mathrm{hard}\,q}(p\bar{p} \to p'WX) = 16\%$$

and for a full hard–gluon structure

$$R_{\mathrm{SD}}^{\mathrm{hard}\,g}(p\bar{p} \to p'WX) = 1.1\%\,.$$

The measured ratio thus favours a purely gluonic Pomeron.

Kunszt and Stirling used their three Pomeron Models to give theoretical predictions for the above ratio, proceeding in complete analogy to the diffractive Higgs and heavy flavour production discussed above. Their predictions for the three Pomeron models are [KS96]

$$R_{\mathrm{SD}}^{W} = \begin{cases} 5.3\% & : \quad \text{Model 1}\,, \\ 6.5\% & : \quad \text{Model 2}\,, \\ 7.4\% & : \quad \text{Model 3}\,. \end{cases} \tag{1.85}$$

Again, the theoretical predictions yield higher ratios than the experimental data. One can argue that the measurement of diffractive processes has not yet achieved the accuracy that is needed. Or the theoretical concept of the Pomeron model presented throughout this work needs some more thoughts. We shall discuss this question in Section 1.7.

1.6.2   HERA

We have already presented most of the results on diffraction obtained by the two HERA experiments H1 and ZEUS. From the first observation of rapidity gaps [H1.94, ZEUS93, ZEUS94] and the measurements of the Pomeron intercept [H1.97a, ZEUS97] up to the measurement of the diffractive structure function $F_2^{\mathrm{D}(4)}(x_{\mathrm{I\!P}}, t, \xi, Q^2)$ [H1.95, ZEUS95a].

The H1 collaboration studied the transverse energy flow E_T in the final state of ep processes, both for diffractive and non–diffractive events [H1.96]. Using the Monte Carlo RAPGAP they show that the measured energy distribution can be reproduced, assuming the exchange of a colourless object (i.e. Pomeron) with partonic structure.

The same observation has been made by the ZEUS collaboration [ZEUS95b] studying hard scattering in photoproduction events with large rapidity gaps. Again the comparison with Monte Carlo programmes having implemented the scattering of a quasi–real photon off a colourless object explains the data.

Another important feature is measuring the parton content of the Pomeron. As discussed above, measurements from UA8 and CDF at hadron–hadron colliders indicate a dominant gluon content of the Pomeron. There is, however, no direct method of measuring the gluon contents at HERA. Therefore any upper and lower limits on the gluon distribution have to be regarded with at least minor doubts. Mesurements of inclusive jet production as they were done by the ZEUS collaboration [ZEUS95c] indicate that between 30% and 80% of the momentum of the Pomeron carried by partons are due to hard gluons. This parton content was probed at a scale $(E_T^{\mathrm{jet}})^2$, with $E_T^{\mathrm{jet}} > 8$ GeV. At least the upper limit does not exclude the CDF or UA8 data and hence gives evidence

for an universal Pomeron structure. Note that the measured range for the hard gluon content in the Pomeron has been included in the Pomeron models we used throughout our studies. Model 1 yields approximately 10% hard gluons at the scale 100 GeV^2 and Model 3 yields 80% at the same scale.

H1 derived the gluon content from the Q^2 dependence of the diffractive structure function $F_2^{D(3)}$. By interpreting this dependence as arising from scaling violations, and fitting the data using DGLAP evolution, a QCD analysis led to the conclusion that gluons carry about 80% of the Pomeron momentum at scale $Q_0^2 = 2.5$ GeV^2. As Q^2 increases, H1 showed that the gluon content *decreases* while the quark content slightly *increases*. However, these variations are very slow and tuning Q^2 from 25 GeV^2 to 1000 GeV^2 the gluon fractions decrease to $\sim$70% while the quark fraction increases to $\sim$30%, with both distributions remaining fairly hard.

The ZEUS collaboration reports an update on the measurement of the $x_{I\!P}$ dependence of the diffractive structure function [ZEUS98]. The results of fitting the diffractive structure function to the form $F_2^{D(3)}(x_{I\!P}, \xi, Q^2) \propto (x_{I\!P})^{-n}$ (*cf.* Eq. (1.57)) yielded

$$n = 1.01 \pm 0.10^{\text{stat.}} \pm^{0.11}_{0.06}{}^{\text{syst.}} , \qquad (1.86)$$

which should be compared to the 1995 value given in (1.59) of $n = 1.30$ [ZEUS97]. The kinematical range of the latter corresponds to $0.1 < \xi < 0.8$ and $6.3 \times 10^{-4} < x_{I\!P} < 10^{-2}$ for $8 < Q^2 < 100$ GeV^2, and is compatible with a single $x_{I\!P}$ dependence in all ξ bins. The above analysis covers a different kinematic range, extending to lower ξ and higher $x_{I\!P}$ at $\langle Q^2 \rangle = 8$ GeV^2. This lower value of n may be ascribed to the presence of additional subleading trajectories contributing in the $x_{I\!P}$ range covered by this analysis [ZEUS98].

1.7 Breaking of gap–factorisation and the status of the Pomeron

One tendency during the HERA analysis became clear: at higher values of Q^2 there seems to be an increase in the value of the Pomeron intercept $\alpha_{I\!P}(0)$ as was presented above (especially from the ZEUS collaboration). With more statistics available and covering a higher Q^2 range ($4.5 < Q^2 < 75$ GeV^2), the H1 collaboration presented an update of their measurements on $F_2^{D(3)}(x_{I\!P}, \xi, Q^2)$, analysing the 1994 data obtained in diffractive DIS [H1.97b]. Measuring a forward rapidity gap in the process $ep \to eXY$ in–between the final state products X and Y, where Y corresponds to the observed fragmentation product closest to the beam line, they obtained values for the differential cross section of Eq. (1.56) (integrated over the mass M_Y of system Y) and thus on $F_2^{D(3)}$. Earlier indications showed that a purely Pomeron exchange in Regge parametrisation as in (1.55) cannot describe the data obtained sufficiently accurately, motivating the H1 collaboration to allow for additional Regge pole exchange, namely ρ, ω, a and f meson exchange.

They performed fits with and without subleading meson trajectories. These fits can be summarised as follows:

A: assuming Pomeron exchange only and factorisation (1.55);

B: additional exchange of mesons (ρ, ω, a and f), <u>no</u> interference between Pomeron and mesons;

Model	C_{IP}	$C_{\mathcal{R}}$	$C_{\mathcal{I}}$	χ^2/ndf
A	1	0	0	1.53
B	1	1	0	1.00
C	1	1	1	0.99

Table 1.4: Parameters and χ^2 values for the H1 1994 $F_2^{\text{D}(3)}$ fits.

C: additional exchange of mesons (ρ, ω, a and f), _maximal_ interference between Pomeron and mesons.

In this framework the diffractive structure function was defined in the following way

$$
\begin{aligned}
F_2^{\text{D}(3)}(x_{\text{IP}}, \xi, Q^2) \;=\; & \int dt \left\{ C_{\text{IP}} f_{\text{IP}}(x_{\text{IP}}, t) \times F_2^{\text{IP}}(\xi, Q^2) \right. \\
& + \; C_{\mathcal{R}} f_{\mathcal{R}}(x_{\text{IP}}, t) \times F_2^{\mathcal{R}}(\xi, Q^2) \\
& + \; \left. 2 C_{\mathcal{I}} f_{\mathcal{I}}(x_{\text{IP}}, t) \times \sqrt{F_2^{\text{IP}}(\xi, Q^2) F_2^{\mathcal{R}}(\xi, Q^2)} \right\}.
\end{aligned} \tag{1.87}
$$

The last term defines the interference between Pomeron and the additional Regge poles and the _coherence parameter_ $C_{\mathcal{I}}$ can be tuned between no interference ($C_{\mathcal{I}} = 0$) and maximal interference ($C_{\mathcal{I}} = 1$). Table 1.4 summarises the parameters of (1.87) for the three different fits.

The fluxes were of Regge type and parametrised as

$$
f_{\text{IP}}(x_{\text{IP}}, t) \;=\; \frac{e^{B_{\text{IP}} t}}{(x_{\text{IP}})^{2\alpha_{\text{IP}}(t)-1}}, \tag{1.88}
$$

$$
f_{\mathcal{R}}(x_{\text{IP}}, t) \;=\; \frac{e^{B_{\mathcal{R}} t}}{(x_{\text{IP}})^{2\alpha_{\mathcal{R}}(t)-1}}, \tag{1.89}
$$

$$
f_{\mathcal{I}}(x_{\text{IP}}, t) \;=\; \cos\left[\frac{\pi}{2}(\alpha_{\text{IP}}(t) - \alpha_{\mathcal{R}}(t))\right] \frac{e^{\frac{B_{\text{IP}}+B_{\mathcal{R}}}{2} t}}{(x_{\text{IP}})^{\alpha_{\text{IP}}(t)+\alpha_{\mathcal{R}}(t)-1}}. \tag{1.90}
$$

The Regge trajectories were assumed linear of the form

$$
\alpha_{\text{IP}}(t) \;=\; \alpha_{\text{IP}}(0) + 0.26 \text{ GeV}^{-2} t, \tag{1.91}
$$

$$
\alpha_{\mathcal{R}}(t) \;=\; \alpha_{\mathcal{R}}(0) + 0.90 \text{ GeV}^{-2} t, \tag{1.92}
$$

with the slopes being extracted from former measurements or results from hadron–hadron colliders. Both intercepts were kept unconstrained as fit–parameter throughout. The values B_{IP} and $B_{\mathcal{R}}$ were taken from available data, like $B_{\text{IP}} = 4.6$ GeV^{-2} (from former H1 data) and $B_{\mathcal{R}} = 2.0$ GeV^{-2} (from hadron–hadron colliders). The structure function $F_2^{\mathcal{R}}$ was taken from the Glück, Reya, Vogt pion parametrisation [GRV92] and the Pomeron structure function F_2^{IP} was kept as a free fit parameter as well.
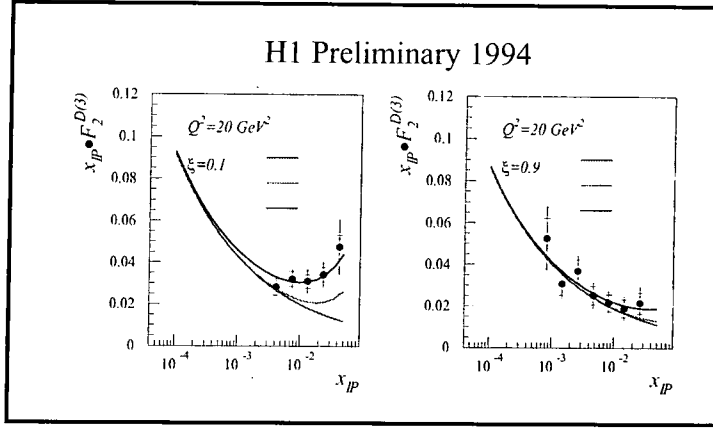
Figure 1.18: H1 data (dots) and fit of $x_{\mathbb{P}} F_2^{D(3)}(x_{\mathbb{P}}, \xi, Q^2)$ as a function of $x_{\mathbb{P}}$ with fixed $Q^2 = 20$ GeV^2 and two values of ξ. The upper solid line corresponds to fit C described in the text. Taking these fit parameters then the lower line shows the Pomeron contribution only. The middle line shows the Pomeron contribution plus interference with other Reggeons.

In Fig. 1.18 we show the H1 data for $x_{\mathbb{P}} F_2^{D(3)}(x_{\mathbb{P}}, \xi, Q^2)$ for fixed ξ and Q^2 as a function of $x_{\mathbb{P}}$ and their fit **C**.

Comparing the χ^2 values (over the number of degrees of freedom) in Table 1.4 shows that a pure Pomeron exchange (fit **A**) is unable to explain the data simultaneously for low and large values of $x_{\mathbb{P}}$, whereas the presence of additional Reggeons (fits **B** and **C**) describe the data very well. The results of fit **C** for the Pomeron and Reggeon intercept are

$$\alpha_{\mathbb{P}}(0) \quad = \quad 1.206 \pm 0.022^{\text{stat.}} \pm 0.013^{\text{syst.}}, \tag{1.93}$$

$$\alpha_{\mathcal{R}}(0) \quad = \quad 0.44 \pm 0.08^{\text{stat.}} \pm 0.07^{\text{syst.}}, \tag{1.94}$$

plus small additional corrections depending on the errors for the experimental values of $B_{\mathbb{P}}$ and $B_{\mathcal{R}}$. The Pomeron intercept does not change significantly if the interference between Pomeron and Reggeons is switched off (fit **B**). This higher value for the Pomeron intercept at larger Q^2 values is consistent with measurements from the ZEUS collaboration. In Fig. 1.19 we show the reported intercepts from both the H1 and ZEUS collaborations as a function of Q^2.

Furthermore the H1 collaboration reported no evidence for a change of $\alpha_{\mathbb{P}}(0)$ in the range $4.5 < Q^2 < 75$ GeV^2 and $0.04 < \xi < 0.9$.

The H1 collaboration also studied the Q^2 dependence of $F_2^{D(3)}(x_{\mathbb{P}}, \xi, Q^2)$ for fixed ξ. The behaviour of the diffractive structure function is very similar to the, e.g., proton structure function, i.e. nearly scale independence and a typical $\ln Q^2$ rise for small values of ξ. This indicates scattering off point–like particles and thus underlines the assumption of a partonic content inside the Pomeron. Typically one observes

$$\frac{\partial F_2^{D(3)}(x_{\mathbb{P}}, \xi, Q^2)}{\partial \ln Q^2} > 0, \qquad \text{for small } \xi,$$
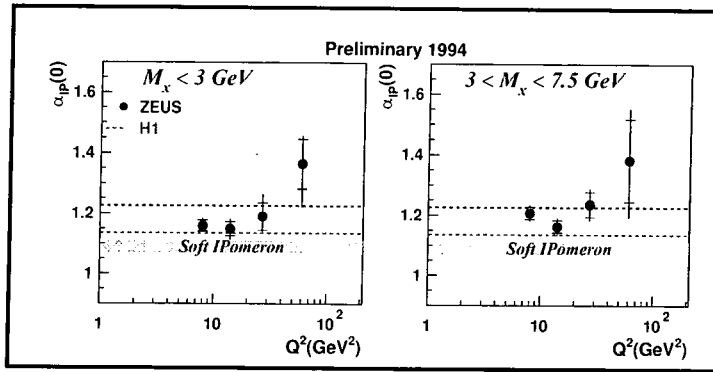
Figure 1.19: Experimental results on $\alpha_{\mathrm{IP}}(0)$ from H1 and ZEUS as a function of Q^2. The dots are the ZEUS data, the dashed lines represents upper and lower bounds from H1. The shaded band represents the domain of the soft Pomeron.

$$\frac{\partial F_2^{\mathrm{D}(3)}(x_{\mathrm{IP}}, \xi, Q^2)}{\partial \ln Q^2} < 0, \qquad \text{for large } \xi.$$

Thus H1 fitted the structure function of the Pomeron $F_2^{\mathrm{IP}}(\xi, Q^2)$ with different parton contents at a given starting scale Q_0^2 undergoing DGLAP evolution. They conclude that at $Q^2 = 4.5$ GeV^2 about 90% of the Pomeron's momentum should be carried by *gluons*. This fraction decreases very slowly and at $Q^2 = 75$ GeV^2 still 80% of the Pomeron's momentum must be due to gluons. A parametrisation with quarks only at the starting scale can be excluded according to the H1 studies. Thus the dominant mechanism of diffractive scattering at HERA seems boson–gluon fusion with the incoming gluons carrying a large fraction of the Pomeron's momentum.

Also the factorisation hypothesis seems to be shattered, as the x_{IP} dependence of $F_2^{\mathrm{D}(3)}$ varies with ξ and thus a *single* Pomeron flux f_{IP} independent of ξ does not seem plausible anymore. However, the inclusion of additional subleading Reggeon trajectories with (or without) interference with the Pomeron, seems to explain the data, but then the price one has to pay is the higher Pomeron intercept, obviously in disagreement with the *soft Pomeron* picture at high–energies. At low enough values of x_{IP} $(x_{\mathrm{IP}} < 10^{-3})$ there is no need for additional subleading Reggeons (*cf.* Fig. 1.18).

1.8 Summary

The experimental facts so far on diffraction may be summarised as follows

- the observation of rapidity gaps over a full energy range in *ep* and hadron–hadron scattering; i.e. they are present in the transition from *soft* to *hard* physics;

- the observation of an intact hadron remnant in the final state;

- interaction probes parton contents of a colour–neutral object.

Here we discussed the soft–Pomeron model in the Donnachie–Landshoff framework. It seems that this model is not applicable if probed at higher energies.

If one strongly holds on to the Pomeron as being the exchanged object in diffractive processes then the H1 data show that one has to introduce subleading meson trajectories and pay the price of a higher Pomeron intercept $\alpha_{I\!P}(0) \simeq 1.2$. The same observation (harder Pomeron at higher energies) has been made by the ZEUS collaboration. There is a strong indication of factorisation breaking. Here we mean the 'gap factorisation' introduced in Eqs. (1.55,1.64). For a discussion of possible factorisation breaking in QCD see Ref. [NZ92]. Our fits with the soft intercept then naturally overestimate the diffractive cross sections for diffractive Higgs and heavy quarks.

An indication is the discussed experimental value on single diffractive W production from the CDF collaboration, even though extracting data on diffractive processes is highly non–trivial.

Keeping the idea of a soft Pomeron alive, Goulianos argued [Gou95] that the flux factor should rather be normalised, i.e. allow for one Pomeron emitted per reaction. Even though this may give a better fit to the experimental data it still does not account for the observed breaking of factorisation.

A higher Pomeron intercept is, however, provided by the *perturbative* Pomeron or the Balitski, Fadin, Kuraev, Lipatov (BFKL) Pomeron [BL78, FKL76, FKL77]. The trajectory has the form

$$\alpha_{I\!P}^{\rm BFKL} = 1 + \frac{12\ln 2}{\pi}\alpha_{\rm s}(\text{scale?})\,. \tag{1.95}$$

The definition of *hard* Pomeron is quite vague. First, the value of the intercept which is usually taken as 1.5 is a very rough estimate using the expression of the expected power of the reggeised gluon. Using a leading order calculation in $\ln 1/x$, the momentum distribution of the gluon is expected to have the form $xg(x, Q^2) \simeq x^{-\lambda}$, where $\lambda = \alpha_{\rm s}/0.378$. As BFKL values are expected to be valid for *moderate* values of Q^2 the data require $\lambda = 0.5$ and thus $\alpha_{\rm s}(Q^2) = 0.18$ which obviously can only be achieved at *large* values of Q^2. The underlying scale for $\alpha_{\rm s}$ is less than clear. It is basically not the scale of the hard interaction, but the infrared momentum squared down the ladder evolution.

Another fact is that the slope of the BFKL Pomeron in (1.95) is taken to be zero. As we have seen in our former discussions, the slope of the Pomeron trajectory is proportional to $1/\langle p_\perp\rangle^2$ the average momentum squared of the hadrons. In hard interactions one naturally expects $\langle p_\perp\rangle$ being much larger than in soft interactions. However the transition from soft to hard physics or non–perturbative to perturbative physics is very unclear.

In the following we shall briefly discuss alternative models to describe diffractive processes. Many of these studies have their roots in the gluon model of Low [Low75] and Nussinov [Nus75, Nus76].

Nikolaev, Zakharov [NZ94]

Introducing light–cone variables for the photon virtuality $q_\pm = q_0 \pm q_3$, one can see that the light–cone *energy* of the virtual photon is of order $|q_-| \simeq Q^2/(xm_p)$ in the proton rest frame with m_p being the proton mass. The light–cone *momentum* is then (as $q^2 = -Q^2$ in every frame) $q_+ \simeq xm_p$. From the point of view of the proton the diffractive process seems to be very soft, although it is probed by a very hard virtual boson. With $\vec{q}_-$ pointing in the negative direction and being very large one can think of the vector boson as a system of quarks and gluons moving in the negative direction with very high momentum. In the easiest form, this *system* of quarks and gluons interacts with the proton by exchanging two *soft* gluons.
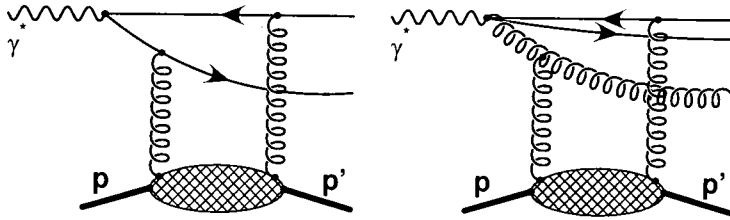
W. Buchmüller, A. Hebecker, M.F. McDermott [BHM97]

In this model the proton is chosen to be at rest. Partons in the virtual boson wave function pass through the soft colour field of the proton and undergo a colour rotation. If they emerge in an overall colour–singlet state, then the proton has a chance to stay intact. The difference to the Nikolaev–Zakharov picture sketched above is the fact that more than just two soft gluons can be exchanged. The model is sketched below, the big 'blob' indicates the soft colour field of the proton.
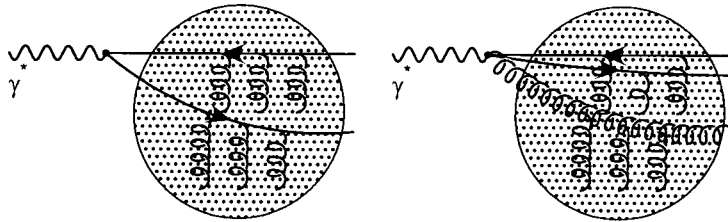
This model looks explicitly at leading twist contributions. In this case only aligned jet type configurations contribute. A similar approach can be found in Ref. [Wus97] by Wüsthoff.

A. Berera, D.E. Soper [BS96]

A travelling proton is hit by a virtual photon, knocking out one of its partons carrying the momentum fraction ξ of the proton. There is then a certain probability that the proton will reform from the debris. This probability is given by the diffractive parton distributions in (1.64) again assuming diffractive factorisation. This picture does not make use of Regge theory.

So far we have presented two different pictures of diffractive deep inelastic scattering, which physically have to be the same. Basically a *Lorentz transformation* from a model in which the proton is at rest (*cf.* Nikolaev *et al.*, Buchmüller *et al.* and Wüsthoff) to a frame where the proton has a large momentum (Berera *et al.*) which is also the picture we adopted throughout. These two *different* pictures are mediated by *Lorentz invariance* and are sketched below.
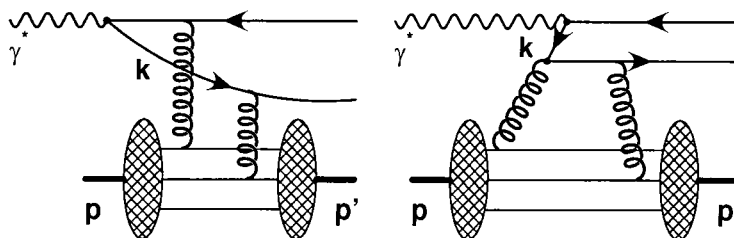
In the left picture the quark with momentum k travels *forward* in time from the boson vertex to the interaction with a gluon from the proton, thus the quark appears to be a constituent of the vector boson.

The right picture emerges from the left picture by applying a Lorentz transformation: now the *antiquark* travels forward in time from the interaction with the gluon to the boson vertex and thus the antiparticle appears to be a constituent of the proton.

Soft or hard?

The main task of adopting the soft–Pomeron model in processes with a hard scale is the question: **Up to which scale is the non–perturbative Pomeron picture valid and when enters perturbative QCD?** The most common explanation (J. Bartels at the Heidelberg conference 1997 on soft and hard interactions) is that the Pomeron is a non–trivial object consisting of a soft and a hard component. The important part is the understanding how the couplings of the soft and the hard part depend on the underlying scale, i.e. in which energy regime dominates the soft Pomeron, in which the hard Pomeron. So far, no concrete conclusions can be drawn.

The study of diffractive vector meson production is an ideal playground for this study, as, depending on the mass of the produced vector meson, one achieves a nearly complete scan over the Q^2 spectrum from *soft* to *hard* to judge the quality of a soft–Pomeron picture as a function of the scale.

There are many data available on diffractive vector meson production $\gamma + p \to p' + \mathcal{V}$ with $\mathcal{V} = \rho, \omega$ and J/Ψ. The production of light vector mesons as measured by HERA can be well described by *soft* Pomeron exchange in conjunction with the vector dominance model (VDM) [Sak60, Yen75], i.e. the photon first fluctuates into a virtual vector meson, which then scatters elastically from the target proton.

Following our former discussion, we have some expectations for the behaviour of the total γ^*p cross section $\sigma_{\text{total}}^{\gamma^*p}$ and the elastic one, which is in the HERA case $\sigma(\gamma^*p \to \mathcal{V}p')$.

observable	W dependence	soft Pomeron	hard Pomeron
$\sigma_{\text{total}}^{\gamma^*p}$	$(W^2)^{\alpha_{\mathbb{P}}(0)-1}$	$(W^2)^{0.08}$	$(W^2)^{0.5}$
slope b	$\simeq b_0 + 2\alpha'_{\mathbb{P}} \ln W^2$	shrinkage	no shrinkage
$\sigma(\gamma^*p \to \mathcal{V}p')$	$\left(\sigma_{\text{total}}^{\gamma^*p}\right)^2 / b$	$(W^2)^{0.16}/b$	$(W^2)^1$

Figure 1.20 shows the measurements of the total and 'elastic' vector meson photoproduction cross sections as a function of the γ^*p c.m.s. frame energy W. The light vector mesons are in excellent agreement with the Donnachie–Landshoff soft–Pomeron model. However, the cross section for J/ψ production rises much faster than the expected soft $W^{0.22}$ behaviour (shrinkage of the b slope included). This cross section is in quite well accordance with a $W^{0.8}$ rise, a harder Pomeron component. This can be understood if one considers the scale which is involved in the interaction. The energy scale is set by the mass of the vector meson and by the transverse momentum involved in the reaction. Thus, for lighter mesons, the scale is still low enough to follow a soft behaviour. The J/ψ, however, already seems to set a scale (charm quarks) that is beyond the soft region.
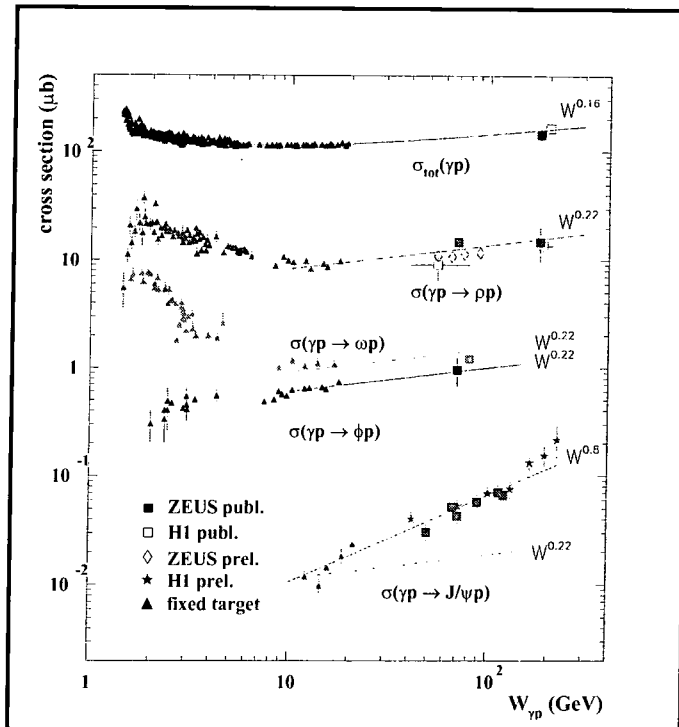
Figure 1.20: The total and 'elastic' vector meson photoproduction measurements as function of the $\gamma^* p$ c.m.s. frame energy W for the vector mesons ρ, ω, ϕ and J/ψ. The curve to the total photoproduction cross section is the Donnachie–Landshoff parametrisation ($W^{0.16}$). The other lines are curves of the form $W^{0.22}$ and $W^{0.8}$. Picture taken from [New97].

On the other side, the shrinkage of the forward elastic peak in ρ meson production, e.g., could be verified experimentally, which is a typical feature of the soft Pomeron. In elastic J/ψ production seems to be evidence of *no* shrinkage as was reported in [Levy97]. For a summary of recent results including references for the data of Fig. 1.20 see [New97].

These studies are essential for our understanding of what is still '*soft*' and what is already '*hard*'. It is essential to define a scale (experimentally) beyond which the soft–Pomeron picture is not sufficient anymore. From the theoretical point of view, it is necessary to explain the observed behaviour of cross sections in terms of couplings of the soft and the hard Pomeron. Our studies of diffractive Higgs and heavy flavour productions are certainly located inside the hard energy regime. But from our soft–Pomeron studies and future experiments it seems possible to gain more information, e.g. by how much a purely non–perturbative soft Pomeron overestimates the measured rates and how much 'perturbative QCD' gains influence at higher energy scales.

References for Chapter 1

— B —

[BBK71]   S.M. Berman, J.D. Bjorken and J.B. Kogut, *Phys. Rev.* **D4** (1971) 3388.

[BC85]   M.M. Block and R.N. Cahn, *Rev. Mod. Phys.* **57** (1985) 563.

[BHM97]   W. Buchmüller, A. Hebecker and M.F. McDermott, *Nucl. Phys.* **B487** (1997) 283.

[BL78]   Y.Y. Balitski and L.N. Lipatov, *Sov. J. Nucl. Phys.* **28** (1978) 822.

[BL91]   A. Białas and P.V. Landshoff, *Phys. Lett.* **B256** (1991) 540.

[BM79]   R.W. Brown and K.O. Mikaelian, *Phys. Rev.* **D19** (1979) 922.

[BS92]   A. Białas and W. Szeremeta, *Phys. Lett.* **B296** (1992) 191.

[BS96]   A. Berera and D.E. Soper, *Phys. Rev.* **D53** (1996) 6162;
          A. Berera, talk presented at the Workshop on Deep Inelastic Scattering and Related Phenomena (DIS96), Rome, 1996, published in the proceedings, eds. G. D'Agostini and A. Nigro (World Scientific), p. 246, 1997.

[Bjo93]   J.D. Bjorken, *Phys. Rev.* **D47** (1993) 101.

— C —

[CDF94]   CDF Collaboration: F. Abe *et al.*, *Phys. Rev.* **D50** (1994) 5535.

[CDF95]   CDF Collaboration: F. Abe *et al.*, *Phys. Rev. Lett.* **74** (1995) 855.

[CDF97a] CDF Collaboration: F. Abe *et al.*, *Phys. Rev. Lett.* **79** (1997) 2636.

[CDF97b] CDF Collaboration: F. Abe *et al.*, *Phys. Rev. Lett.* **78** (1997) 2698.

[CH96]   J.R. Cudell and O.F. Hernández, *Nucl. Phys.* **B471** (1996) 471.

[Can89]   L. Caneschi (editor), Regge Theory of low p_T Hadronic Interactions, (North-Holland), 1989.

[Cap95]   A. Capella, A. Kaidalov, C. Merino and J. Tran Thanh Van, *Phys. Lett.* **B343** (1995) 403.

[Cap96]   A. Capella, A. Kaidalov, C. Merino and J. Tran Thanh Van, *Phys. Rev.* **D53** (1996) 2309.

[Cho78]   J.B. Choi, H.W. Lee, P.Y. Pac and K. Soh, *Phys. Rev.* **D18** (1978) 751.

[Com79]   B.L. Combridge, *Nucl. Phys.* **B151** (1979) 429.

[Com80]   B.L. Combridge, *Nucl. Phys.* **B174** (1980) 243.

[Col77]   P.D.B. Collins, An Introduction to Regge Theory and High–Energy Physics, (Cambridge University Press), Cambridge 1977.

[Cut60]   R.E. Cutkosky, *J. Math. Phys.* **1** (1960) 429.

— D —

[D∅.94]   D∅ collaboration: S. Abachi *et al.*, *Phys. Rev. Lett.* **72** (1994) 2332.

[D∅.96]   D∅ collaboration: S. Abachi *et al.*, Hard Single Diffractive Jet Production at D∅, talk presented at the 28th International Conference on High Energy Physics, Warsaw, Poland, 1996.

[DL83]   A. Donnachie and P.V. Landshoff, *Nucl. Phys.* **B231** (1983) 189.

[DL84]   A. Donnachie and P.V. Landshoff, *Nucl. Phys.* **B244** (1984) 322.

[DL86]   A. Donnachie and P.V. Landshoff, *Nucl. Phys.* **B267** (1986) 690.

[DL92]   A. Donnachie and P.V. Landshoff, *Phys. Lett.* **B296** (1992) 227.

[DL94]   A. Donnachie and P.V. Landshoff, *Z. Phys.* **C61** (1994) 139.

— E —

[ELOP66]   R.J. Eden, P.V. Landshoff, D.I. Olive and J.C. Polkinghorne, The Analytic S–Matrix, (Cambridge University Press), Cambridge, 1966.

— F —

[FF74]   D. Field and G. Fox, *Nucl. Phys.* **B80** (1974) 367.

[FKL76]   V.S. Fadin, E.A. Kuraev and L.N. Lipatov, *Sov. Phys. JETP* **44** (1976) 443.

[FKL77]   V.S. Fadin, E.A. Kuraev and L.N. Lipatov, *Sov. Phys. JETP* **45** (1977) 199.

[Fro61]   M. Froissart, *Phys. Rev.* **123** (1961) 1053.

— G —

[GBK95]   K. Golec–Biernat and J. Kwieciński, *Phys. Lett.* **B353** (1995) 329.

[GBP96]   K. Golec–Biernat and J.P. Phillips, *J. Phys.* **G22** (1996) 921.

[GGT54]   M. Gell–Mann, M.L. Goldberger and W. Thirring, *Phys. Rev.* **95** (1954) 1612.

[GLM93]   E. Gotsman, E.M. Levin and U. Maor, *Phys. Lett.* **B309** (1993) 199.

[GOR78]   M. Glück, J.F. Owens and E. Reya, *Phys. Rev.* **D17** (1978) 2324.

[GRV92]   M. Glück, E. Reya and A. Vogt, *Z. Phys.* **C53** (1992) 651.

[GS96]   T. Gehrmann and W.J. Stirling, *Z. Phys.*, **C70** (1996) 89.

[GV96]   D. Graudenz and G. Veneziano, *Phys. Lett.* **B365** (1996) 302.

[Geo78]   H.M. Georgi, S.L. Glashow, M.E. Machacek and D.V. Nanopoulos, *Phys. Rev. Lett.* **40** (1978) 629.

[Gol55]   M.L. Goldberger, *Phys. Rev.* **99** (1955) 979.

[Gou95]   K. Goulianos, *Phys. Lett.* **B358** (1995) 379.

— H —

[H1.94]   H1 Collaboration: T. Ahmed *et al.*, *Nucl. Phys.* **B429** (1994) 477.

[H1.95]   H1 Collaboration: T. Ahmed *et al.*, *Phys. Lett.* **B348** (1995) 681.

[H1.96]   H1 Collaboration: S. Aid *et al.*, *Z. Phys.* **C70** (1996) 609.

[H1.97a] H1 Collaboration: C. Adloff *et al.*, *Z. Phys.* **C74** (1997) 221.

[H1.97b] H1 Collaboration: C. Adloff *et al.*, *Z. Phys.* **C76** (1997) 613.

— I —

[IS85]   G. Ingelman and P. Schlein, Phys. Lett. **B152** (1985) 256.

— K —

[KMR97]   V.A. Khoze, A.D. Martin and M.G. Ryskin, *Phys. Lett.* **B401** (1997) 330.

[KMS97]   Z. Kunszt, S. Moretti and W.J. Stirling, *Z. Phys.* **C74** (1997) 479.

[KS89]   Z. Kunszt and W.J. Stirling, in Proceedings of the ECFA Large Hadron Collider Workshop, Aachen, Germany, 1990, edited by G. Jarlskog and D. Rein (CERN Report No. 90–10, Geneva, Switzerland, 1989), Vol. II, p. 428.

[KS96]   Z. Kunszt and W.J. Stirling, Hard Diffractive Scattering: Partons and QCD, talk presented at the Workshop on HERA Physics, Durham, 1996 and Workshop on Deep Inelastic Scattering and Related Phenomena (DIS96), Rome, 1996, published in the proceedings, eds. G. D'Agostini and A. Nigro (World Scientific), p. 240, 1997.

— L —

[LM95]   H.J. Lu and J. Milana, *Phys. Rev.* **D51** (1995) 6107.

[Lev97]   E.M. Levin, Everything about Reggeons, lectures held at DESY, 16–18 September 1997.

[Levy97] A. Levy, Evidence for no shrinkage in elastic photoproduction of J/ψ, hep-ph/9712519.

[Low75]   F.E. Low, *Phys. Rev.* **D12** (1975) 163.

— M —

[MRS95]   A.D. Martin, R.G. Roberts and W.J. Stirling, *Phys. Lett.* **B354** (1995) 155.

[Mar63]   A. Martin, in Strong Interactions and High–Energy Physics, ed. R.G. Moorhouse (Edinburgh: Oliver and Boyd), 1963.

[Mar66]   A. Martin, *Nuovo Cimento* **42** (1966) 930;
          A. Martin, *Nuovo Cimento* **44** (1966) 1219.

[Mul70]   A.H. Mueller, *Phys. Rev.* **D2** (1970) 2963.

— N —

[NSS90]   O. Nachtmann, A. Schäfer and R. Schöpf, *Phys. Lett.* **B249** (1990) 331.

[NZ92]   N.N. Nikolaev and B.G. Zakharov, *Z. Phys.* **C53** (1992) 331.

[NZ94]   N.N. Nikolaev and B.G. Zakharov, *Z. Phys.* **C64** (1994) 631.

[New97]   P.R. Newman, talk presented at the Workshop on Deep Inelastic Scattering and Related and QCD (DIS97), Chicago, 1997, published in the proceedings, eds. J. Repond and D. Krakauer (American Institute of Physics), p. 157, 1997.

[Nus75]   S. Nussinov, *Phys. Rev. Lett.* **34** (1975) 1286.

[Nus76]   S. Nussinov, *Phys. Rev.* **D14** (1976) 246.

— P —

[PDG96]   R.M. Barnett *et al.*, *Phys. Rev.* **D54** (1996) 1;
            Particle Data Group www pages: http://pdg.lbl.gov.

[Phi95]   J.P. Phillips, talk presented at the Workshop on Deep Inelastic Scattering
            and Related Phenomena (DIS96), Rome, 1996, published in the proceedings,
            eds. G. D'Agostini and A. Nigro (World Scientific), p. 359, 1997.

[Pom58]   I.Ya. Pomeranchuck, *Sov. Phys.–JETP* **7** (1958) 499.

— R —

[Reg59]   T. Regge, *Nuovo Cimento* **14** (1959) 951.

[Reg60]   T. Regge, *Nuovo Cimento* **18** (1960) 947.

— S —

[Sak60]   J. Sakurai, *Ann. Phys.* **11** (1960) 1.

[Sze93]   W. Szeremeta, *Acta Phys. Pol.* **B24** (1993) 1159.

— U —

[UA4.84]   UA4 Collaboration: M. Bozzo *et al.*, *Phys. Lett.* **B136** (1984) 217.

[UA8.88]   UA8 Collaboration: R. Bonino *et al.*, *Phys. Lett.* **B211** (1988) 239.

[UA8.92]   UA8 Collaboration: A. Brandt *et al.*, *Phys. Lett.* **B297** (1992) 417.

— W —

[WA91.94]   WA91 Collaboration: S. Abatzis *et al.*, *Phys. Lett.* **B324** (1994) 509.

[Wei61]   S. Weinberg, *Phys. Rev.* **124** (1961) 2049.

[Wus97]   M. Wüsthoff, *Phys. Rev.* **D56** (1997) 4311.

— Y —

[Yen75]   D. Yennie, *Rev. Mod. Phys.* **47** (1975) 311.

— Z —

[ZEUS93]   ZEUS Collaboration: M. Derrick *et al.*, *Phys. Lett.* **B315** (1993) 481.

[ZEUS94]   ZEUS Collaboration: M. Derrick *et al.*, *Phys. Lett.* **B332** (1994) 228;
            ZEUS Collaboration: M. Derrick *et al.*, *Phys. Lett.* **B338** (1994) 483.

[ZEUS95a]   ZEUS Collaboration: M. Derrick *et al.*, *Z. Phys.* **C68** (1995) 569.

[ZEUS95b]   ZEUS Collaboration: M. Derrick *et al.*, *Phys. Lett.* **B346** (1995) 399.

[ZEUS95c]   ZEUS Collaboration: M. Derrick *et al.*, *Phys. Lett.* **B356** (1995) 129.

[ZEUS97]   ZEUS Collaboration: J. Breitweg *et al.*, *Z. Phys.* **C75** (1997) 421.

[ZEUS98]   ZEUS Collaboration: J. Breitweg *et al.*, *European Physical Journal* **C1**
            (1998) 81.

Chapter 2

Extensions to the Standard Model

"It's a jolly good rule to mistrust experimental results until they can be verified by theory."

(A. Eddington)

In this chapter we discuss two possible extensions to the Standard Model (SM), both motivated by experiments in 1994 and 1995.

In Section 2.1 we introduce a new heavy vector quark triplet mixing with the SM quarks. This study was motivated by reported anomalies on the R_b, R_c measurements from LEP. Even though after the publication of our work the former *anomaly* disappeared, i.e. these measurements are now in perfect agreement with the SM, we still want to present this model here, as it is both instructive and elegant.

In Section 2.2 we discuss the additional neutral vector boson Z', the heavy equivalent to the SM Z boson. Even though the Z' has been the topic of high–energy physics throughout the years, we use the Z' to explain the measured jet–excess rate, reported from the CDF collaboration. These high jet rates at large transverse energy E_T are still an unsolved topic and we give a possible explanation in the framework of Z' physics.

2.1 Additional heavy vector quark triplet at LEP

The motivation for introducing an additional vector quark triplet arose out of two important circumstances. First, there was a report in 1995 from the LEP working groups ALEPH, DELPHI, L3 and OPAL [LEP95] on deviations measured in the ratios $R_{b,c} = \Gamma(Z \to b\bar{b}, c\bar{c})/\Gamma(Z \to \text{hadrons})$ (*cf.* Table 2.1). Compared to the predictions of the SM they found a too *large* value for R_b at about the 3.5σ level and a too *small* value for R_c at about the 2.5σ level. As R_b and R_c are correlated one might, e.g., arbitrarily set R_c to the LEP1 experimental value, but the excess of R_b, now on a 3σ level, remains. Discussions continued on how to understand the LEP1/SLC data from a phenomenological point of view if the disagreement with the SM prediction was taken literally. To solve

the $R_{b,c}$ "crisis" several extensions to the SM emerged which we shall *not* cite here as, even though they were sometimes very subtle and innovative, they finally proved to be not necessary, as the $R_{b,c}$ crisis is no longer existent.

Two works, however, will be the focus of Section 2.2. By introducing a heavy analogue to the SM Z boson, the so-called Z' with mass of approximately $M_{Z'} = 1$ TeV, Altarelli *et al.* [Alt96] and Chiappetta *et al.* [Chi96] tried to simultaneously explain the $R_{b,c}$ anomalies and the measured jet excess rate. We shall discuss the latter in Section 2.2.

	LEP1 (1995) [LEP95]	LEP1 (1996) [Blo96]	Standard Model
R_b	0.2219 ± 0.0017	0.2178 ± 0.0011	0.2158 ± 0.0003
R_c	0.1543 ± 0.0074	0.1715 ± 0.0056	0.1723 ± 0.0002

Table 2.1: Experimental values of R_b and R_c from LEP1 as presented in 1995 [LEP95] and 1996 [Blo96] compared to the SM predictions.

Some studies considered extensions to the fermionic sector of the SM, by introducing new vector fermions, mixing with the SM fermions to *enhance* $\Gamma(Z \to b\bar{b})$ and thus R_b and simultaneously *reduce* $\Gamma(Z \to c\bar{c})$. One example is Ma [Ma96] who used a vectorial pair of singlet and a vectorial pair of triplet that mix with the quarks of the SM to solve simultaneously for R_b and R_c at tree level. The problem emerging is a reduction of the total hadronic width Γ_{had} and thus for the SM leptonic branching ratio $R_\ell = \Gamma_{\text{had}}/\Gamma_\ell$ which, however, undoubtly is in accordance with the data.

In another paper [BBH96, Yos96] the authors introduced a vectorial pair of singlet and hereby only accommodate for R_c, not solving the R_b deviation.

In this work we shall introduce a vectorial triplet and show how this might deal with a possible R_b and R_c anomaly and keep Γ_Z^{had} and thus Γ_{had} nearly unchanged, at least within the error bars of the experimental value.

One might, however, ask, where such an additional vector triplet might originate from. In GUT it can be found as (3,1,15) of $SU(2)_L \otimes SU(2)_R \otimes SU(4)$ which in turn is imbedded in $SO(10)$.

Possible tests of our model might be

(a) the calculation of, e.g., heavy flavour production, analogue to the Z' at hadron colliders, to judge whether a significant change in the cross section can be observed,

(b) the study of flavour–changing neutral current (FCNC) effects in, e.g., decay modes of some mesons like K_L^0 or B^0,

(c) low energy physics experiments, e.g., νN scattering,

(d) quark–antiquark production at $e^+ e^-$ colliders, especially at the CERN LEP2 collider.

An analogous treatment to the Z' model like in (a), however, is not possible because the new vector and axial–vector couplings induced by the mixing with the new vector

fermions are *still* of order α_w instead of order α_s, as they are for the Z' coupling. The introduction of new vector fermions produces new small FCNC effects (b) at the tree–level, which are, however, not in disagreement with the relevant experiments [LS93]. The limits, imposed by FCNC experiments, exclude the possibility of low energy measurements (c), like νN neutral current scattering, as discussed, e.g., in [McF96] for the case of the Z'. The test (d) thus looks most promising.

We employ the effect of the mixing between the new quark vector triplet and the SM quark flavours q on the production of $q\bar{q}$ pairs at the LEP2 collider. We do not claim that our $q\bar{q}$ studies are the unique testing ground: other studies could find a better *signal/background* ratio for this new vector fermions model.

2.1.1 The model

We introduce the following vector quark triplet

$$X_{L,R}^{(Q,T^3)} = \begin{pmatrix} x_1^{(\frac{5}{3},+1)} \\ x_2^{(\frac{2}{3},0)} \\ x_3^{(-\frac{1}{3},-1)} \end{pmatrix}_{L,R} , \tag{2.1}$$

with mass M_X and the stated quantum numbers for charge (Q) and third component of weak isospin (T^3), we allow a mixing of $(x_3)_L$ with the d–type quarks $(d,s,b)_L$ and $(x_2)_L$ with the u–type quarks $(u,c,t)_L$. Note that we allow for isospin violating effects. In the context of this model it is expected that M_X is much bigger than the top quark mass. However, we are exclusively interested in the mixing effects this new quark triplet shows with the quark flavours of the SM. The mixing of the left–handed components are proportional to $1/M_X$, while for the right–handed couplings a $1/M_X^2$ dependence can be found, assuming a large M_X approximation, and therefore the latter can be neglected (*cf.* Ref. [BL86]). The neutral–current Lagrangian, including γ and Z exchange, reads

$$\mathcal{L}_{\mathrm{NC}} = eJ_\mu^{\mathrm{em}}A^\mu + \sqrt{2}\left(\frac{G_\mathsf{F}}{\sqrt{2}}\right)^{1/2} M_Z \sum_q \overline{\Psi}_q\gamma_\mu(v_q - a_q\gamma_5)\Psi_q Z^\mu, \tag{2.2}$$

where the Ψ_q are meant to be *gauge–eigenstates*. One can immediately see that taking into account the unitary transformation matrix that shuffles *mass–* into *gauge–* eigenstates, $\Psi_{qL,R}^{\mathrm{gauge}} \to U_{L,R}\Psi_{qL,R}^{\mathrm{mass}}$, modifies the isospin matrices $T_q^{3L,R} \to \overline{U}_{L,R}T_q^{3L,R}U_{L,R}$. As a result, we finally conclude that the vector and axial–vector couplings defined by

$$v_q = g_q^L + g_q^R = T_q^{3L} + T_q^{3R} - 2Q_q\sin^2\Theta_W , \tag{2.3}$$

$$a_q = g_q^L - g_q^R = T_q^{3L} - T_q^{3R} , \tag{2.4}$$

are directly influenced by the presence of this new vector triplet. Consider, e.g., the new mass matrix M_D for d–type quarks[1]

$$\mathsf{M}_D = \begin{pmatrix} m_d & 0 & 0 & \mathcal{J}_1^D \\ 0 & m_s & 0 & \mathcal{J}_2^D \\ 0 & 0 & m_b & \mathcal{J}_3^D \\ 0 & 0 & 0 & M_X \end{pmatrix} = \begin{pmatrix} \widetilde{M}_D & \vec{\mathcal{J}}^D \\ 0 & M_X \end{pmatrix} , \tag{2.5}$$

---

[1] This matrix is diagonalised via a biunitary transformation.

where the matrix elements $\mathcal{J}_i^D$ measure the relative *strength* of the mixing between $(x_3)_L$ and the corresponding d–type quarks. U_L^D diagonalises the matrix product $M_D M_D^\dagger$. Assuming the most general form

$$
U_L^D = \begin{pmatrix} K^D & R^D \\ S^D & T^D \end{pmatrix}_L = \left(\begin{array}{ccc|c} U_{dd}^D & U_{ds}^D & U_{db}^D & U_{dx_3}^D \\ U_{sd}^D & U_{ss}^D & U_{sb}^D & U_{sx_3}^D \\ U_{bd}^D & U_{bs}^D & U_{bb}^D & U_{bx_3}^D \\ \hline U_{x_3d}^D & U_{x_3s}^D & U_{x_3b}^D & U_{x_3x_3}^D \end{array} \right)_L \;, \tag{2.6}
$$

we find in the large M_X approximation [BL86]

$$
R^D = \frac{1}{M_X} \mathcal{J}^D \,, \qquad S^D = -\frac{1}{M_X} \mathcal{J}^{D\dagger} K^D \,, \tag{2.7}
$$

with $K^D = \mathbb{1}_{3\times3}$ which diagonalises $\widetilde{M}_D \widetilde{M}_D^\dagger$.

In complete analogy we can study the u–type quark mixing mediated by the matrix

$$
U_L^U = \begin{pmatrix} K^U & R^U \\ S^U & T^U \end{pmatrix}_L = \left(\begin{array}{ccc|c} U_{uu}^U & U_{uc}^U & U_{ut}^U & U_{ux_2}^U \\ U_{cu}^U & U_{cc}^U & U_{ct}^U & U_{cx_2}^U \\ U_{tu}^U & U_{tc}^U & U_{tt}^U & U_{tx_2}^U \\ \hline U_{x_2u}^U & U_{x_2c}^U & U_{x_2t}^U & U_{x_2x_2}^U \end{array} \right)_L \;. \tag{2.8}
$$

The mass matrix for u–type quarks consequently reads

$$
M_U = \begin{pmatrix} \widetilde{M}_U & \vec{\mathcal{J}}^U \\ 0 & M_X \end{pmatrix} \,. \tag{2.9}
$$

However, $\widetilde{M}_U \widetilde{M}_U^\dagger$ is not diagonal anymore but is diagonalised by $V_{\rm CKM}$, the Cabibbo–Kobayashi–Maskawa matrix. In the large M_X approximation we find $K^U \approx V_{\rm CKM}^\dagger$ and

$$
S^U = -\frac{1}{M_X} \mathcal{J}^{U\dagger} V_{\rm CKM}^\dagger \,. \tag{2.10}
$$

Consequently we derive for the new vector and axial–vector couplings in the case of the u– and d–type quarks

$$
\widetilde{v}_u = v_u + (T_{x_2}^{3L} - T_u^{3L})|U_{x_2u}^U|_L^2 \,, \quad \widetilde{a}_u = a_u + (T_{x_2}^{3L} - T_u^{3L})|U_{x_2u}^U|_L^2 \,, \tag{2.11}
$$

$$
\widetilde{v}_d = v_d + (T_{x_3}^{3L} - T_d^{3L})|U_{x_3d}^D|_L^2 \,, \quad \widetilde{a}_d = a_d + (T_{x_3}^{3L} - T_d^{3L})|U_{x_3d}^D|_L^2 \,. \tag{2.12}
$$

This explains the former special choice for the isospin components of the vector triplet. As $\Gamma(e^+e^- \to q\bar{q}) \propto (\widetilde{v}_q^2 + \widetilde{a}_q^2)$, $T_{x_2}^{3L} = 0$ will *reduce* the hadronic width of the u–type quarks, whereas $T_{x_3}^{3L} = -1$ *enhances* the hadronic width of the d–type quarks and therefore lower the SM value of R_c and simultaneously raise R_b. In terms of the above formalism, the modified couplings of, e.g., the b and c quarks read now

$$
\widetilde{v}_c = v_c - \frac{1}{2}|S_2^U|^2 \,, \quad \widetilde{a}_c = a_c - \frac{1}{2}|S_2^U|^2 \,, \tag{2.13}
$$

$$
\widetilde{v}_b = v_b - \frac{1}{2}|S_3^D|^2 \,, \quad \widetilde{a}_b = a_b - \frac{1}{2}|S_3^D|^2 \,, \tag{2.14}
$$

where S^D and S^U are to be identified with the matrix elements used in the definition of U_L^D (2.6) and U_L^U (2.8). Thus the model depends on 6 parameters $(S_{1,2,3}^D, S_{1,2,3}^U)$. But because of the relation $S^U = S^D V_{CKM}^\dagger$, it is sufficient to constrain 3 parameters in order to calculate the full set. The input to constrain S_2^U and S_3^D will be R_c and R_b, respectively. After determining all modified vector and axial–vector couplings $\tilde{v}_q$ and $\tilde{a}_q$, we proceed to answer the question of how the total $q\bar{q}$ cross section at LEP2 is affected by the presence of the additional vector fermions.

2.1.2 Modified $e^+e^- \to q\bar{q}$ at LEP2

The total cross section for the subprocess $e^+e^- \overset{Z,\gamma}{\to} q\bar{q}$, where q stands for *one* quark flavour, via Z and γ exchange, reads in the finite–quark–mass Born approximation

$$\sigma(e^+e^- \overset{Z,\gamma}{\to} q\bar{q}) = \frac{\beta}{2}(3 - \beta^2)\sigma_V + \beta^3\sigma_A, \tag{2.15}$$

$$\sigma_V(e^+e^- \overset{Z,\gamma}{\to} q\bar{q}) = \frac{4\pi\alpha_s^2}{s}Q_e^2 Q_q^2 + \frac{4\alpha}{\sqrt{2}}G_F Q_e Q_q v_e \tilde{v}_q \frac{M_Z^2(s - M_Z^2)}{(s - M_Z^2)^2 + M_Z^2\Gamma_Z^2}$$

$$+ \frac{G_F^2}{2\pi}\tilde{v}_q^2(a_e^2 + v_e^2)\frac{sM_Z^4}{(s - M_Z^2)^2 + M_Z^2\Gamma_Z^2}, \tag{2.16}$$

$$\sigma_A(e^+e^- \overset{Z,\gamma}{\to} q\bar{q}) = \frac{G_F^2}{2\pi}\tilde{a}_q^2(a_e^2 + v_e^2)\frac{sM_Z^4}{(s - M_Z^2)^2 + M_Z^2\Gamma_Z^2}, \tag{2.17}$$

with the quark velocity $\beta = \sqrt{1 - 4\frac{m_q^2}{s}}$ and the electron couplings $v_e = -1/2 + 2\sin\Theta_W$ and $a_e = -1/2$. For further details we refer to, e.g., [JLZ81, JLZ82, CGN82]. We implemented in our calculations the following corrections:

- QCD $\mathcal{O}(\alpha_s)$ corrections due to real and virtual gluon emission [JLZ81],

- universal QED $\mathcal{O}(\alpha)$ corrections $3\alpha Q_q^2/(4\pi)$,

- initial state radiation up to $\mathcal{O}(\alpha^2)$ in QED and soft photon exponentiation [BBN88],

- universal electroweak corrections due to tt and tb loop corrections to the Z propagator and γ–Z mixing as well as vertex corrections for b quarks due to virtual t quark exchanges [ABR88, BH88, DKZ90]. We checked that the box–graph contributions turn out to be unimportant for our purposes.

propagator loop corrections

vertex corrections
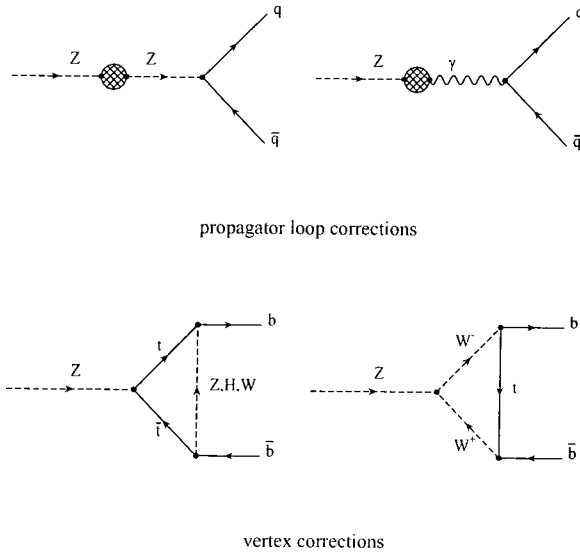
For our numerical analysis we used the *on–shell* scheme addressing the following electroweak data: $\alpha(M_Z) = 1/128.8, M_Z = 91.188$ GeV, $M_W = 80.33$ GeV with the strong coupling constant $\alpha_s(M_Z) = 0.123$. Furthermore we fixed the top quark mass to be $m_t = 175$ GeV. For the CKM–matrix elements we used the averaged values given in Ref. [PDG96].

We perform a three variable fit to the values of R_b and R_c as they were presented at the ICHEP conference in Warsaw in 1996 [Blo96]. At this time the average values of the four LEP collaborations were (see also Table 2.1)

$$R_b(\text{Warsaw}'96) \quad = \quad 0.2178 \pm 0.0011\,, \tag{2.18}$$

$$R_c(\text{Warsaw}'96) \quad = \quad 0.1715 \pm 0.0056\,. \tag{2.19}$$

Thus the R_c value was within the SM predictions and the reported R_b value was in excess by 1.9σ of the SM and expected to come further down. Our model, however, cures any deviations $\Delta R_{u,d}$ from the SM and a general fit is always possible. With only a small excess in R_b we nevertheless want to show whether in the framework of our model measurable effects in $e^+e^- \to q\bar{q}$ might or might not show up.

We first performed a general fit of the parameter space, including $|S_2^U|^2$ and $|S_3^D|^2$, as they directly govern the values for $\Gamma_{c\bar{c}}$ and $\Gamma_{b\bar{b}}$. Furthermore we set $|S_1^D|^2 \simeq 0$. This is invoked by taking into account the flavour–changing neutral current (FCNC) of the process $K_L^0 \to \mu^+\mu^-$, which does not support any sizeable d–s quark mixing. The missing values $|S_1^U|^2, |S_3^U|^2$ and $|S_2^D|^2$ are then calculated, according to the relation $S^U = S^D V_{\text{CKM}}^\dagger$. Although we found a weak dependence of the various widths $(\Gamma_Z, \Gamma_Z^{\text{had}})$ on the input parameters, the cross sections remain quite insensitive to the widths compared to the modified coupling–dependence, as can easily be deduced from the formal expression of the total cross section in Eqs. (2.15)–(2.17).

Fig. 2.1 shows our fitted values for $|S_2^U|^2$ and $|S_3^D|^2$, in particular the edges of the 1σ (68.3% confidence level of the normal distribution) and the 2σ (95.4% c.l.) regions of R_b and R_c. We find $|S_2^U|^2 = 0.01245$ and $|S_3^D|^2 = 0.00922$ for 1σ (corresponding to $R_b = 0.2189$ and $R_c = 0.1659$) and $|S_2^U|^2 = 0.02528$ and $|S_3^D|^2 = 0.01284$ for the 2σ case ($R_b = 0.2200$ and $R_c = 0.1603$).
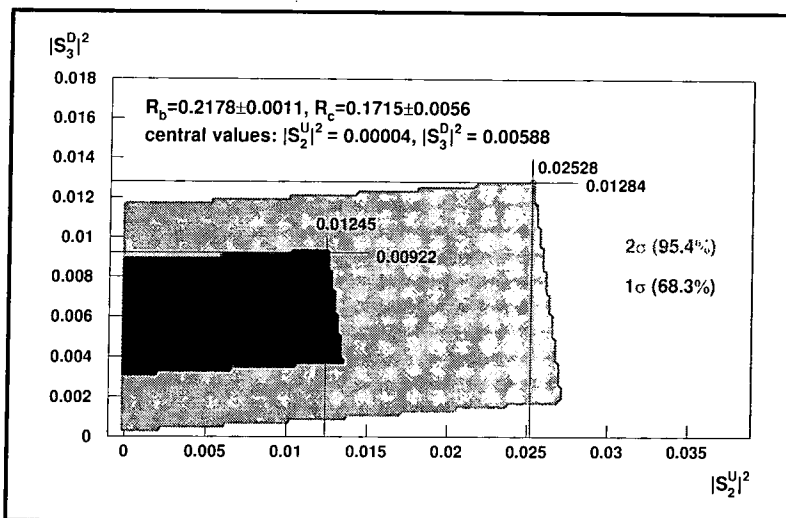
Figure 2.1: We show the allowed regions in the $|S_2^U|^2, |S_3^D|^2$ plane (as discussed in the text) obtained by fitting the experimental R_b, R_c values [Blo96] given in (2.18,2.19). We present the 1σ (68.3% c.l.) and 2σ (95.4% c.l.) regions, from which we read off our input parameters $|S_2^U|^2$ and $|S_3^D|^2$.

With these two sets of parameters deduced from R_b and R_c we first give predictions for the subprocess cross sections $\sigma(e^+ e^- \rightarrow s\bar{s}, c\bar{c}, b\bar{b})$, as they turn out to give the most significant signal. Specifically, Fig. 2.2(a) shows the $c\bar{c}$ production cross section as a function of the centre-of-mass energy. The contribution of the additional vector fermions to this cross section is negative, as it is for all u-type quarks, which can easily be checked from the structure of the new vector $\tilde{v}_u$ and axial-vector $\tilde{a}_u$ couplings for u-type quarks, as the former motivation is to *decrease* the SM value of R_c. The result is very sensitive to the values of R_b and R_c, as, e.g., the 1σ input and the 2σ input differ by a factor of roughly two. Moreover it can be observed that in the energy region of the LEP2 collider (160–190 GeV), the contribution is nearly insensitive to $\sqrt{s}$. The observed gaps in all figures which appear around the Z mass $M_Z = 91.188$ GeV, are due to the resonant behaviour of the total cross section.

All the argumentation drawn from Fig. 2.2(a) also holds for the discussion of the $s\bar{s}$ and $b\bar{b}$ cross sections, presented in Figs. 2.2(b,c). The main difference is that the total contribution of the additional vector fermions is *positive* for d-type quarks. Even though the absolute value of the $s\bar{s}$ contribution is comparable to Fig. 2.2(a), there is no hope to isolate this cross section in a LEP2 measurement. The $b\bar{b}$ cross section, however, will be measurable and according to Ref. [LR97] the experimental uncertainty in $\sigma_{b\bar{b}}$ is reported to be 2.5% for $\sqrt{s} = 190$ GeV and an assumed luminosity of 500 pb^{-1}, which allows for a clear signal. Although former studies at the LEP2 showed a general lower accuracy for the tagging of $c\bar{c}$ events, it still might be sufficient to detect our calculated 5% effect in $\sigma_{c\bar{c}}$ as shown in Fig. 2.2(a). All numerical results are summarised in Table 2.2 for two fixed LEP2 centre-of-mass energies of $\sqrt{s} = 175$ GeV and 190 GeV.

Finally we present in Fig. 2.3 the total cross sections for d- and u-type quarks. Again, we can see the overall tendency that the SM cross section is being lowered under the
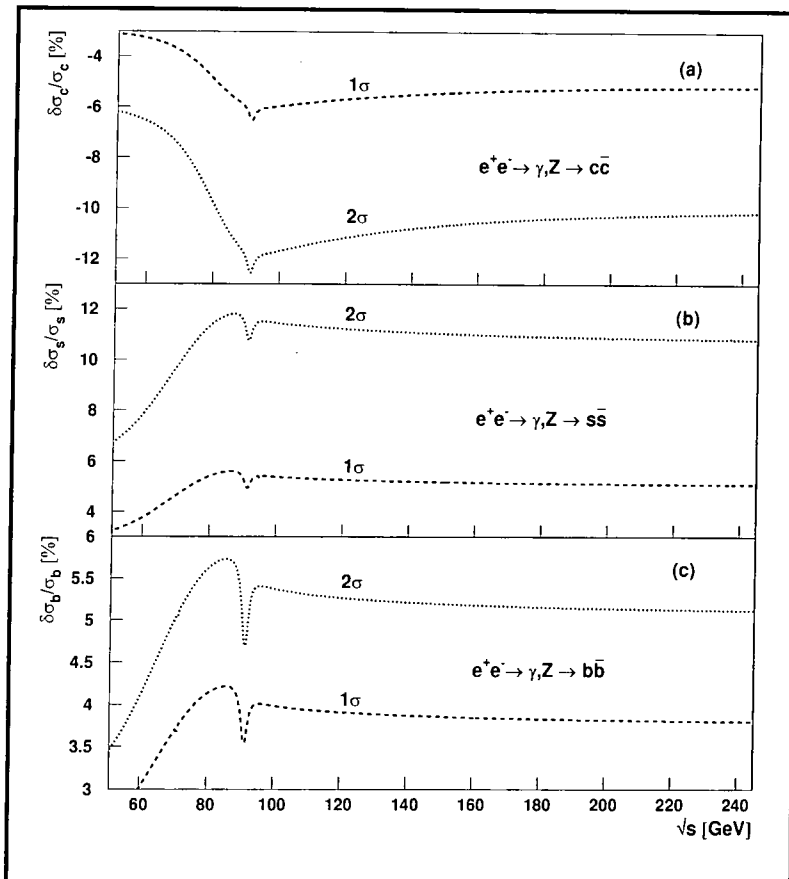
Figure 2.2: We present the relative differences between the predictions of the vector fermion (VF) model and the SM ($\delta\sigma_q/\sigma_q := (\sigma_{q\bar{q}}^{VF} - \sigma_{q\bar{q}}^{SM})/\sigma_{q\bar{q}}^{SM}$) in per cent as a function of $\sqrt{s}$, for three different flavours.

presence of the vector fermions for u–type quarks, whereas we find a proper enhancement for d–type quarks, which is the characteristic feature of this model. We can not expect a tagging of these individual cross sections at this level of accuracy at LEP2, but for reasons of completeness we want to mention it at this stage, especially to demonstrate that there will be no signal to be expected in the *total* cross section, as individual subprocess contributions will cancel each other to an almost zero level.

We studied the impact of a model with additional vector fermions at the LEP2 collider. We made predictions for various quark production cross sections and discussed their possible detectability based on a recent phenomenological analysis given in Ref. [LR97]. However, there is probably no evidence for new physics at this stage, especially after the experimental values of R_b and R_c are in agreement with the SM predictions, although, one can argue that exploiting the idea of additional vector fermions at energies beyond the Z pole is of considerable interest. A remarkable feature of the model we were dealing with throughout our studies is that it is anomaly free, in contrast to alternative ideas emerging from the reported "R_b, R_c crisis", and therefore seems to be more physically sound.

		1σ (68.3% c.l.)		2σ (95.4% c.l.)	
		$\sigma_{q\bar{q}}$ [pb]	$\delta\sigma_q/\sigma_q$ [%]	$\sigma_{q\bar{q}}$ [pb]	$\delta\sigma_q/\sigma_q$ [%]
$\sqrt{s} =$	$c\bar{c}$	36.69	-5.31	34.71	-10.44
175 GeV	$b\bar{b}$	12.75	$+3.83$	12.93	$+5.31$
$\sqrt{s} =$	$c\bar{c}$	29.75	-5.26	28.15	-10.35
190 GeV	$b\bar{b}$	10.16	$+3.82$	10.31	$+5.30$

Table 2.2: The numerical values for $\sigma_{q\bar{q}} = \sigma(e^+e^- \to q\bar{q})$ and $\delta\sigma_q/\sigma_q$ in the vector fermion model, for q being either a c or a b quark. The calculations were performed for two typical values of $\sqrt{s}$ at LEP2, and for the two confidence levels as discussed in the text.

We also checked a possible influence on the forward–backward asymmetries A_{FB}^q. At LEP1 energies the modified asymmetries are within the experimental errors. The accuracy at LEP2 for the corresponding measurements is expected to be even lower, such that it is difficult to draw any conclusions from forward–backward asymmetry measurements.

2.1.3 The situation in 1998

The LEP working group published their latest results on experimental SM data, including updated values for R_b and R_c. They report [LEP97]

$$R_b(1997) = 0.2170 \pm 0.0009\,, \qquad R_c(1997) = 0.1734 \pm 0.0048\,. \qquad (2.20)$$

The ratio R_b is only 1.3σ above the predictions of the SM (see Table 2.1) compared to the former 3.7σ in 1995.

The evolution in the experimental measurement of R_b and R_c from 1995 until 1997 is shown below. The dashed band indicates the predictions from the SM assuming $\alpha_{\mathsf{s}}(M_Z) = 0.123 \pm 0.004$ and $M_Z = 91.1884 \pm 0.0022$ GeV.
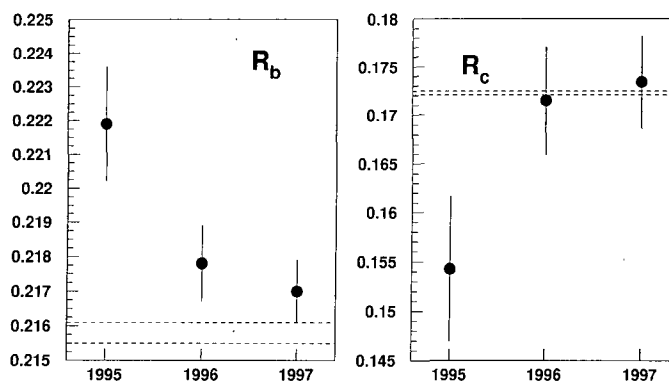
We surely may conclude that the R_b, R_c anomaly finally vanished and left a trail of
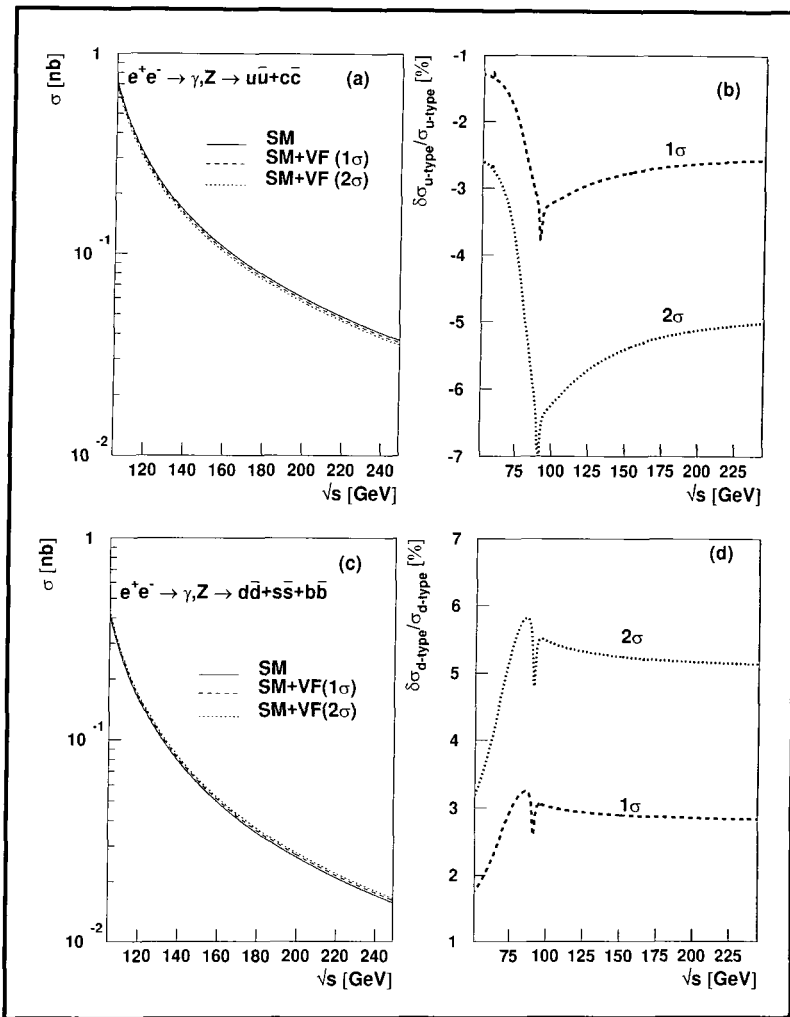
Figure 2.3: The total cross section for $u-$ (a) and d–type (c) quarks in the SM calculation and the two vector fermion fits as discussed in the text, including the relative changes (b) and (d) as already shown in Fig. 2.2.

approximately 25 papers dealing with an explanation of this effect. We presented one of them.

2.2 Additional neutral vector boson Z' at the Tevatron and the LHC

The analysis of the 1993 data from the CDF collaboration in 1996 on the single inclusive jet cross section at the Tevatron indicated a possible disagreement with QCD at high transverse jet energies. The reported excess rate exceeds next–to–leading order (NLO) QCD calculations by 10–50% for $200 < E_T < 400$ GeV [CDF96a]. One has to be cautious in drawing rash conclusions for the evidence of new physics, as the D0 collaboration has reported *agreement* with QCD in the same measured jet energy range [Bla96]. Still the

systematic errors in both experiments are too large to enable definite conclusions to be drawn.

Discussions continue on how to understand the CDF data from a phenomenological point of view if the reported anomaly (i.e. deviation from the SM) is taken literally. There are efforts to explain the observed jet–excess rate in terms of modified parton distributions, as it was suggested by Glover *et al.* [Glo96] and the CTEQ collaboration [CTEQ96]. The discussion about quark substructures was supported quite emphatically (*cf.* [AT97] and references therein). Other discussions included quark resonances inside the hadron (*cf.* [Ban96]) or new strong interactions (*cf.* [CCS96]).

Some authors believed that the simultaneous occurence of the R_b, R_c anomalies (as discussed in Section 2.1) and the CDF jet–excess rates are not only correlated in time, but also physics wise. As we already discussed in Section 2.1, Altarelli *et al.* [Alt96] and Chiappetta *et al.* [Chi96] re–invoked the concept of the Z' and tried to solve both anomalies in this framework. And quite successfully: both groups were able to find a set of vector and axial–vector couplings for the Z' to please both, the LEP and the CDF data. This Z' couples very strongly to u– and d–type quarks and contributes to the standard boson Z decay via a weak Z'–Z mixing angle δ. We shall exploit this idea and undertake a global analysis of the Z' model in the context of the CDF data only, to show the differences with the results of Refs. [Alt96, Chi96] if one only takes the CDF data into account. But the main intention of this study is to present predictions of the Z' model for further measurements at the TEVATRON, like dijet angular distributions, and of course at the LHC. As the Z' model seems a quantitatively plausible description of the observed deviations so far, it is important to give predictions for future experiments to either support or discard this explanation.

2.2.1   The Z' model

The Z' model introduced by Altarelli *et al.* in Ref. [Alt96] and independently by Chiappetta *et al.* in Ref. [Chi96], to explain recent experimental deviations from the SM, has the remarkable feature (as the experimental data demand) that the axial and vector couplings of the Z', especially to u–type quarks, are quite large. It will turn out that the effective $Z'u\bar{u}$ coupling is of the order of the strong (QCD) coupling constant α_s. Especially for large energies (transverse jet energies E_T) the contributions due to the additional Z' are becoming dominant and for a fitted set of coupling parameters will, for example, cure the measured jet excess. We shall be very cursory in the presentation of the Z' model as it is treated in almost complete analogy to the Z boson of the Standard Model. The Z' has been discussed in the literature before 1996. A few of the many references are [JS89, BR90].

To introduce the Z', the neutral sector of the Standard Model with the underlying $SU(3)_C \otimes SU(2)_L \otimes U(1)_Y$ gauge group is extended by an additional term in the neutral–current Lagrangian (*cf.* (2.2))

$$
\begin{aligned}
\mathcal{L}'_{\mathrm{NC}} &= \frac{g}{\cos\Theta_W} J'^{\,0}_\mu Z'^\mu \\
&= \frac{g}{2\cos\Theta_W} \sum_f \overline{\Psi}_f \gamma_\mu \left(v'_f + a'_f \gamma^5 \right) \Psi_f Z'^\mu .
\end{aligned}
\tag{2.21}
$$

The neutral current $J'^{\,0}_\mu$ includes the axial a'_f and vector v'_f coupling strengths of the

Z'. In the Standard Model there are three free coupling parameters for the Z boson: the left–handed coupling to the $(u, d)_\mathrm{L}$ doublets and the two right–handed couplings u_R and d_R. To preserve these degrees of freedom, we follow the quark family–independent parametrisation for u– and d–type quarks in [Alt96] for a'_f and v'_f

$$v'_u = x + y_u, \quad a'_u = -x + y_u,$$
$$v'_d = x + y_d, \quad a'_d = -x + y_d. \tag{2.22}$$

All couplings to leptons are set to zero (leptophobic Z'): $v'_l = v'_\nu = 0$ and $a'_l = a'_\nu = 0$. In [Alt96] this constraint was due to the fact that only deviations from R_b and R_c have been reported by the LEP1/SLC measurements. Apart from x, y_u and y_d there are two more parameters included in the Z' model: the mixing angle δ between Z and Z' as well as the mass $M_{Z'}$ of the Z'. With these parameters we can also fully determine the total decay width of the Z'

$$\Gamma_{Z'} = \frac{G_\mathsf{F} M_Z^2}{2\sqrt{2}\pi} N_\mathsf{c} M_{Z'} \left(v'^2_f + a'^2_f \right) = \frac{G_\mathsf{F} M_Z^2}{\sqrt{2}\pi} N_\mathsf{c} M_{Z'} \left(2x^2 + y_u^2 + y_d^2 \right), \tag{2.23}$$

where N_c is the number of quark colours. From fitting various electroweak observables to the LEP1/SLC data and taking the CDF results into account, the authors of Ref. [Alt96] find as a best set of parameters:

$$x = -1.0, \quad y_u = 2.2, \quad y_d = 0.0, \quad \delta = 3.8 \cdot 10^{-3}, \tag{2.24}$$

with the Z' mass fixed in this analysis to be $M_{Z'} = 1$ TeV. This parameter space gives the best numerical compromise to simultaneously obtain acceptable coincidence with the values for $R_{b,c}{}^2$ *and* the measured CDF jet rate. Such a heavy vector boson is in accordance with the lower mass limit of 412 GeV (at a 95% confidence level) reported from $p\bar{p}$ collider experiments in a search for a new neutral vector boson (with standard couplings) [PDG96]. The dependence on the y_d parameter was found to be weak, such that the somewhat arbitrarily choice of $y_d = 0.0$ was used as an input. We shall exploit these results and concentrate on finding the best set of parameters for x and y_u describing the CDF data within the Z' model, with δ, y_d and $M_{Z'}$ fixed to the values given in $(2.24)^3$.

2.2.2 Fit to the CDF single inclusive jet data

We shall perform a global χ^2 fit of the Z' model parameters x and y_u discussed in Section 2.2.1 to the 1992–93 measurements of the single inclusive jet cross section by the CDF Collaboration [CDF96a].

In leading order (LO) QCD the process $AB \to \text{jet} + X$ can be parametrised by [Ste95]

$$\frac{\mathrm{d}^2\sigma}{\mathrm{d}E_T\mathrm{d}\eta}(AB \to \text{jet} + X) = 4\pi\alpha_\mathsf{s}^2(Q^2)\frac{E_T}{s^2} \tag{2.25}$$

$$\times \sum_{abcd}\int_{x_a^{\min}}^{1} \frac{\mathrm{d}x_a}{2x_a - x_T e^\eta} \frac{f_{a/A}(x_a, Q^2)}{x_a} \frac{f_{b/B}(x_b, Q^2)}{x_b} |\overline{\mathcal{M}}_{ab \to cd}|^2,$$

---

[2]The 1995 LEP data on R_b and R_c as shown in Table 2.1.

[3]As we restrict ourselves to fitting the CDF data only, the mixing angle δ does not appear as a free parameter. However, because we later want to calculate $R_{b,c}$ for the sake of comparison with the Standard Model predictions and the LEP1 data, we shall fix δ to the value given by Altarelli *et al.* [Alt96] as cited in (2.24).

in terms of the transverse energy E_T of the observed jet and the directly measured pseudorapidity η. The expressions for the squared and averaged matrix elements of the subprocesses contributing to $|\overline{\mathcal{M}}_{ab \to cd}|^2$ in LO due to the partons a, b, c and d being quarks, antiquarks or gluons, can be found in, e.g., [CKR77] or any standard QCD textbook. We integrate over the kinematical variable x_a only, with $x_b = x_a x_T e^{-\eta}/(2x_a - x_T e^{\eta})$ and $x_a^{\min} = x_T e^{\eta}/(2 - x_T e^{-\eta})$. The variable x_T is the scaled counterpart of E_T being $x_T = 2E_T/\sqrt{s}$. Eq. (2.25) fully describes the single inclusive jet cross section. For the parton distributions $f_{(a,b)/(A,B)}(x_{(a,b)}, Q^2)$ we use again the MRS(A$'$) set of partons as we did in the previous chapter to calculate diffractive processes.

The inclusion of the Z' into the formalism is straightforward. One has to calculate those matrix elements in which the incoming and outgoing partons are quark and antiquark pairs. The only constraints at the $Z'q\bar{q}$ vertices are colour–charge and flavour neutrality. All possible Z' exchanges in the s– and t–channels have to be taken into account. We cite the results for identical and non–identical quark–flavour scattering in the t–channel (averaged and summed matrix element for the Z' contribution only)

$$
\frac{1}{16\pi^2} |\overline{\mathcal{M}}_{qq \to qq}^{Z'}|^2 = \frac{2}{9} \frac{g_w^2}{\pi \cos^2 \Theta_W} \alpha_s s^2
$$

$$
\times \quad \Re e \left\{ \frac{1}{t \left[(u - M_{Z'}^2) + iM_{Z'}\Gamma_{Z'} \right]} + \frac{1}{u \left[(t - M_{Z'}^2) + iM_{Z'}\Gamma_{Z'} \right]} \right\} (x^2 + y_q^2)
$$

$$
+ \quad \frac{g_w^4}{16\pi^2 \cos^4 \Theta_W} \left\{ s^2 (x^4 + y_q^4) \left[\frac{1}{(t - M_{Z'}^2)^2 + M_{Z'}^2 \Gamma_{Z'}^2} \right. \right.
$$

$$
+ \quad \frac{1}{(u - M_{Z'}^2)^2 + M_{Z'}^2 \Gamma_{Z'}^2} + \frac{2}{3} \Re e \left(\frac{1}{(t - M_{Z'}^2) + iM_{Z'}\Gamma_{Z'}} \frac{1}{(u - M_{Z'}^2) - iM_{Z'}\Gamma_{Z'}} \right) \right]
$$

$$
+ \quad 2x^2 y_q^2 \left(\frac{u^2}{(t - M_{Z'}^2)^2 + M_{Z'}^2 \Gamma_{Z'}^2} + \frac{t^2}{(u - M_{Z'}^2)^2 + M_{Z'}^2 \Gamma_{Z'}^2} \right) \right\} , \tag{2.26}
$$

$$
\frac{1}{16\pi^2} |\overline{\mathcal{M}}_{qq' \to qq'}^{Z'}|^2 = \frac{1}{16\pi^2} \frac{g_w^4}{\cos^4 \Theta_W}
$$

$$
\times \quad \frac{1}{(t - M_{Z'}^2)^2 + M_{Z'}^2 \Gamma_{Z'}^2} \left\{ s^2 (x^2 + y_q^2 y_{q'}^2) + u^2 (x^2 y_q^2 + x^2 y_{q'}^2) \right\} . \tag{2.27}
$$

The expressions for the s–channel may be obtained via *crossing*. Expressions (2.26) and (2.27) have to be added to the standard QCD matrix elements. In the limit $M_{Z'} \to \infty$ one obtains an effective four–point interaction (four–quark coupling) of strength $\propto q\bar{q}q\bar{q}g_w^2$.

Throughout this work we shall restrict ourselves to the LO calculation of the jet cross sections. For small values of $|\eta|$ it has been shown by, e.g., S.D. Ellis, Z. Kunszt and D.E. Soper [EKS90] and W.T. Giele, E.W.N. Glover and D.A. Kosower [GGK93] that for single inclusive jet production at high transverse energies the next–to–leading order (NLO) and the LO calculations only differ by a constant factor, independent of E_T, if one chooses $\mu = E_T/2$ as the underlying renormalisation scale. This renormalisation scale is imbedded into our calculations in the form of the four–momentum transfer $Q^2 = \mu^2$ as the defining scale for the running coupling constant $\alpha_s(Q^2)$ and the parton distributions. The difference between LO and NLO is then reported to be less than 10% and independent of E_T for $E_T > 100$–200 GeV [EKS90, GGK93]. The lower bound on E_T depends on the set of parton distributions used and the value of Λ_{QCD} implemented. For the MRS(A$'$) set the QCD scale parameter is found to be $\Lambda_{\overline{\text{MS}}}^{(N_f=4)} = 231$ MeV, which corresponds to $\alpha_s(M_Z^2) =$

0.113. The MRS(A$'$) NLO calculation was shown to be in good agreement [CDF96a] with the CDF single inclusive jet data up to $E_T \simeq 200$ GeV. We therefore normalise our LO calculations of the single inclusive jet cross section to the CDF measurements in the range $150 < E_T < 200$ GeV as shown in Fig. 2.4.
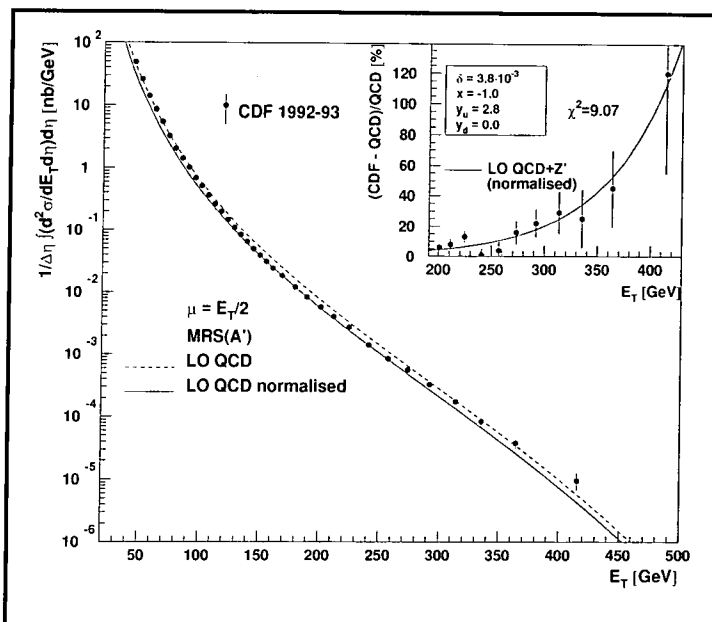
Figure 2.4: LO calculation of the single inclusive jet cross section (dashed line) and the normalised LO fit (solid line) to the CDF 1992–93 data [CDF96a] (as discussed in the text). The small inset shows the difference in per cent between our calculation and the measured cross sections by the CDF Collaboration. Also shown is our best-fit of the included Z' model with the parameters also presented.

The dashed curve represents the LO QCD calculation according to Eq. (2.25), the solid curve shows the corrected LO calculation normalised to the CDF data which are also presented. For $130 < E_T < 200$ GeV the difference between the central values of the CDF data and the normalised LO calculation is less than 5%. The normalisation factor is found to be $\mathcal{N} = 0.91 \pm 0.03$ according to the reported statistical errors of the CDF data. Comparing our results with those presented in [EKS90, GGK93] we conclude that for $E_T > 130$ GeV and $\mu = E_T/2$ our LO calculation is adequate to NLO assuming the constant factor $\mathcal{N}$. For our χ^2 analysis of the CDF data we shall therefore use the normalised LO calculation presented in Fig. 2.4.

The CDF collaboration reported a significant jet excess for $E_T > 200$ GeV [CDF96a]. In the inset of Fig. 2.4 we present the conspicuous deviations of the CDF data in the measured energy range to our LO calculation in per cent. The solid line shows the anticipated best-fit calculation in LO with the Z' incorporated and the smallest achievable χ^2 value. Let us therefore now briefly discuss our fit of the Z' model parameters x and y_u to the CDF data.

	our Z' fit	Altarelli *et al.* [Alt96]	LEP1 (1995)
R_b	0.2194	0.2203	0.2219 ± 0.0017
R_c	0.1642	0.1572	0.1543 ± 0.0074

Table 2.3: Comparison of the values $R_{b,c}$ from our calculation including the Z' model and the *best–fit* parameters of Eqs. (2.28) with the LEP1 measurements [LEP95] and the calculations of Altarelli *et al.* [Alt96].

2.2.3 χ^2 analysis of the Z' model

The *qualitative* difference of our Z' model fit to that of Altarelli *et al.* [Alt96] is that we only concentrate on the CDF data and disregard the values for the quark ratios R_b and R_c measured at the LEP1/SLC colliders for the moment. Furthermore we are using a different renormalisation scale ($\mu = E_T/2$ rather than $\mu = E_T$) and therefore approach NLO results in a natural way [EKS90, GGK93]. We also perform an implicit integration over the pseudorapidity η in the range $0.1 \leq |\eta| \leq 0.7$, more in line with the experimental cuts used by the CDF collaboration.

Nevertheless we expect our *best–fit* parameters to be very close to those found in [Alt96] such that we constrain three of the five parameters in exact analogy to this work, namely $\delta = 3.8 \cdot 10^{-3}$ (mixing angle), $M_{Z'} = 1$ TeV (Z' mass) and $y_d = 0.0$. We are left with two parameters x and y_u to define the χ^2 distribution of our problem. We show $\chi^2(x, y_u)$ in Fig. 2.5(a). Note that the pure QCD calculation yields $\chi^2(0,0) = 45.14$. Fig. 2.5(b) shows the 95.4% confidence ellipse (2σ for the normal distribution). The statistical analysis was performed using the programming package of Ref. [C++]. While x is bound according to this analysis to a very narrow band, the parameter y_u covers a much broader range. The narrowness of the x range is due to the fact that it influences both u– and d–type quarks simultaneously, and therefore its variation is much more constrained.

Finally in Fig. 2.5(c) we present the 68.3% confidence ellipse (1σ for the normal distribution) and deduce the best–fit parameters of our analysis to be

$$x = -1.0, \quad y_u = 2.8,$$
$$\text{with} \quad y_d = 0.0, \quad M_{Z'} = 1 \text{ TeV}, \quad \xi = 3.8 \cdot 10^{-3}. \tag{2.28}$$

Altarelli *et al.* [Alt96] report a slightly smaller value of $y_u = 2.2$. This is mainly due to the included $R_{b,c}$ fit as well as to the differences in the analysis procedure as discussed above. The improved result for the single inclusive jet cross section, due to incorporated Z' exchange with the parameters of Eqs. (2.28), was already shown in the inset of Fig. 2.4. Note that with this set of parameters the coincidence with the experimental LEP1 values of R_b and R_c from 1995 [LEP95] is still better than the predictions by the Standard Model (*cf.* Table 2.1), as shown in Table 2.3.

With (2.28) and $M_Z = 91.18$ GeV we find a total Z' decay width according to Eq. (2.23) of $\Gamma_{Z'} = 644.2$ GeV. This should be compared to the value for the standard Z boson of $\Gamma_Z = 2.493 \pm 0.004$ GeV [PDG96]. Our value for $\Gamma_{Z'}$ exceeds the one assumed
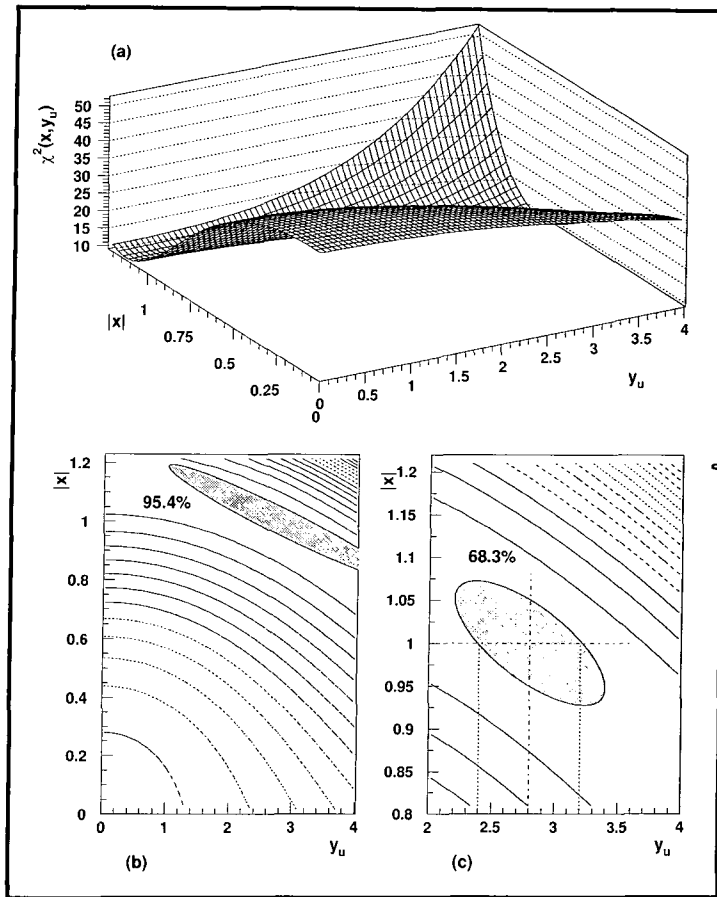
Figure 2.5: The statistical results of our Z' analysis: (a) the χ^2 distribution as a function of the two degrees of freedom x and y_u (the fitted parameters), (b) the 95.4% confidence ellipse and (c) the 68.3% confidence ellipse with the central values $x = -1.0$ and $y_u = 2.8$ being indicated (best–fit values).

by Chiappetta *et al.* [Chi96] by a factor of three. From Eq. (2.22) we find the vector and axial couplings of the Z' to u–type quarks being $v'_u = 1.8$ and $a'_u = 3.8$. These values should again be compared with the Standard Model predictions [PDG96] of $v_u = 0.19$ and $a_u = 0.50$ for the Z boson. As already mentioned, the effective $Z'u\bar{u}$ coupling is of order $(v'^2_u + a'^2_u)\alpha_W \sim \alpha_s$. So the main contribution of the Z' follows from its coupling to u–type quarks with an absolute strength that is comparable to QCD itself. The effects of this coupling can be observed in the inset of Fig. 2.4 where for $E_T \sim 400$ GeV, the Z' contribution already equals the pure QCD contribution.

Before we shall answer the question of how this Z' model with the new parameter fit will affect jet physics at the LHC we shall first discuss the comparison of our results to the already available and future data of the dijet angular distributions at the TEVATRON.

2.2.4 Comparison with the measurements of the dijet cross sections at the TEVATRON

The leading order differential dijet cross section in a hadron–hadron collision can be expressed in terms of the centre-of-mass scattering angle $\cos \Theta^*$ and the invariant mass of the two jets M_{jj} [Ste95]

$$\frac{\mathrm{d}^2\sigma}{\mathrm{d}\cos(\Theta^*)\mathrm{d}M_{jj}}(AB \rightarrow \mathrm{jet}_1 + \mathrm{jet}_2 + X) = 4\pi\alpha_s^2(Q^2)\frac{1}{8M_{jj}^2} \tag{2.29}$$

$$\times \sum_{abcd}\int_{x_a^{\min}}^{1}\mathrm{d}x_a f_{a/A}(x_a, Q^2)f_{b/B}(x_b, Q^2)|\overline{\mathcal{M}}_{ab\rightarrow cd}|^2 \, ,$$

with $x_a^{\min} = M_{jj}^2/s$ and $x_b = M_{jj}^2/x_a s$. Again a, b, c and d denote the different types of partons and A and B the scattering hadrons. The cross section is again factorised into one part that includes the information on the parton densities inside the hadrons and the averaged matrix element squared part that carries the $\cos \Theta^*$ information. So the jet angular distribution is sensitive to the form of the $2 \rightarrow 2$ matrix elements. For small angles, the partonic contributions to the total differential cross section show a typical Rutherford behaviour ($\sim \sin^{-4}(\Theta^*/2)$). To remove this singularity it is convenient to plot the angular distribution in terms of another variable χ defined as[4]

$$\chi = \frac{1 + |\cos \Theta^*|}{1 - |\cos \Theta^*|}. \tag{2.30}$$

It is clear that $\chi \in [1, \infty]$. In the small angle region (χ large) one expects therefore $\mathrm{d}\sigma/\mathrm{d}\chi \sim \mathrm{const.}$ as $\mathrm{d}\chi/\mathrm{d}\cos \Theta^* \sim \sin^{-4}(\Theta^*/2)$.

The vindication of restricting ourselves to a LO calculation has already been discussed in the case of the single inclusive jet analysis. We concluded that for $E_T > 130$ GeV LO is a very good approximation to NLO (cf. Fig. 2.4) if one chooses $\mu = E_T/2$ as the underlying renormalisation scale, and takes a normalisation factor $\mathcal{N}$ into account. The dijet mass, however, is connected to the transverse jet energy via the relation

$$M_{jj} = 2E_T \cosh |\eta^*| \, , \tag{2.31}$$

where we introduce the centre-of-mass pseudorapidity $\eta^* = (\eta_1 - \eta_2)/2$ (with η_1 and η_2 being the pseudorapidities in the laboratory frame).

With $\cos \Theta^* = \tanh \eta^*$ and Eq. (2.30) we find that $\chi = e^{2|\eta^*|}$. Therefore Eq. (2.31) yields $M_{jj} = E_T(\sqrt{\chi} + 1/\sqrt{\chi})$. So one could expect that for large M_{jj} ($M_{jj} > 260$ GeV) and small values of χ our argumentation concerning the validity of the LO approximation might still hold. However, if there is a large transverse boost $\eta_{\mathrm{boost}} = (\eta_1 + \eta_2)/2$ to the dijet system then χ can become as large as $|\eta^*| = |\eta_1 - \eta_{\mathrm{boost}}|$, but LO can still be adequate to NLO if $|\eta_1|$ is small. On the other hand, $|\eta_{\mathrm{boost}}|$ could be small and $|\eta_1|$ large: in this case the LO description fails. So one has to be cautious with the argumentation. However, S.D. Ellis et al. [EKS92] also determined the scale μ for which

---

[4]To minimise confusion we shall always denote the angular variable by χ whereas the statistical variable is denoted by χ^2.

the calculation approximately reproduces the less–scale–dependent NLO result in the case of dijet production. If we express their result in terms of the variable χ, one finds

$$\mu \approx k(\chi)\frac{E_T}{2}\,, \tag{2.32}$$

with $k(\chi) = (\chi + 1)/(\chi^{0.85} + \chi^{0.15})$. For $\chi = 1$ we find $\mu \approx E_T/2$, the value for the renormalisation scale we were using throughout. We conclude that also in the case of dijet production this scale yields a reliable approximation to NLO (at least in the small χ range). For $\chi = 5, 10, 20$ one finds $k(\chi) = 1.15, 1.29, 1.39$ such that nearly the complete range for small values of χ is in approximate accordance with NLO for $\mu = E_T/2$. However, to approach the NLO result in a pure LO calculation as good as possible, we shall use the *effective* renormalisation scale of Eq. (2.32) for the study of the dijet angular distributions throughout this section. With this choice of μ we do not have to worry about the normalisation factor $\mathcal{N}$ introduced for the case of the single inclusive cross section.

We show in Fig. 2.6 our calculations in lowest order QCD as well as in the extended model (QCD+Z') with the coupled Z'. The Z' model parameters are again fixed to the values given in Eqs. (2.28). We compare our results first with the data from the CDF Collaboration of 1992 [CDF92]. They measured the jet angular distribution with a jet data sample of 4.2 pb^{-1} in three different dijet mass regions (Figs. 2.6(a,b,c)). Only the statistical errors are shown. The systematic errors are reported to be 5–10% [CDF92]. The kinematical cut on the centre–of–mass pseudorapidity was chosen to be $|\eta^\star| < 1.6$ for $240 < M_{jj} < 475$ GeV and $M_{jj} > 550$ GeV; and $|\eta^\star| < 1.5$ for $475 < M_{jj} < 550$ GeV. Again with $\chi = e^{2|\eta^\star|}$ we get upper bounds for χ, such as $\chi < 24.5$ for $\eta^\star < 1.6$ and $\chi < 20.0$ for $\eta^\star < 1.5$. All cross sections in Fig. 2.6 are normalised to unity in the corresponding χ intervals, and integrated over the given M_{jj} range. As the cross section falls very steeply in a given χ bin ($\propto 1/M_{jj}^3$), we introduce a cut–off for the dijet mass in Fig. 2.6(c) of $M_{jj} = 700$ GeV. An analysis of the cut–off dependence showed that any higher upper bound on M_{jj} changes the result by less than 2%.

From a first look at Fig. 2.6 we notice that all angular cross sections are rising for higher values of χ. This is due to the fact that we incorporated our running coupling constant $\alpha_s(Q^2)$ with $Q^2 = k^2(\chi)E_T^2/4$. The Q^2 scale is a function of M_{jj} and χ. This can be deduced by examining Eq. (2.31). It follows directly that $Q^2 = M_{jj}^2\chi/4(\chi^{0.85} + \chi^{0.15})^2$ with $Q_{\max}^2 = M_{jj}^2/16$. For larger values of χ the values of Q^2 are therefore becoming smaller. The partons are probed at lower energies, but the effective coupling $\alpha_s(Q^2)$ is rising as Q^2 is shrinking.

A second feature becomes transparent from Fig. 2.6: the influence of the Z' is less striking for small and moderate dijet masses as shown in Fig. 2.6 but becomes more important for higher values of M_{jj}. We have to recall that a dijet mass of $M_{jj} = 500$ GeV for $\chi = 2.5$ corresponds to a transverse jet energy $E_T = 226$ GeV, whereas a dijet mass of $M_{jj} = 1000$ GeV corresponds to $E_T = 452$ GeV for the same value of χ. The Z' model, however, has been constructed in such way that its influence is only felt for $E_T > 200$ GeV. Therefore only calculations with a relatively high dijet mass at $\sqrt{s} = 1.8$ TeV are substantially affected by the Z' boson. But already for $\langle M_{jj}\rangle = 500$ GeV and $\langle M_{jj}\rangle = 600$ GeV the presence of the additional Z' becomes transparent (*cf.* Figs. 2.6(b,c)), especially for the large–angle–scattering (χ small). This is due to the fact that such a massive vector boson acts like an effective contact interaction [ELP89] between the
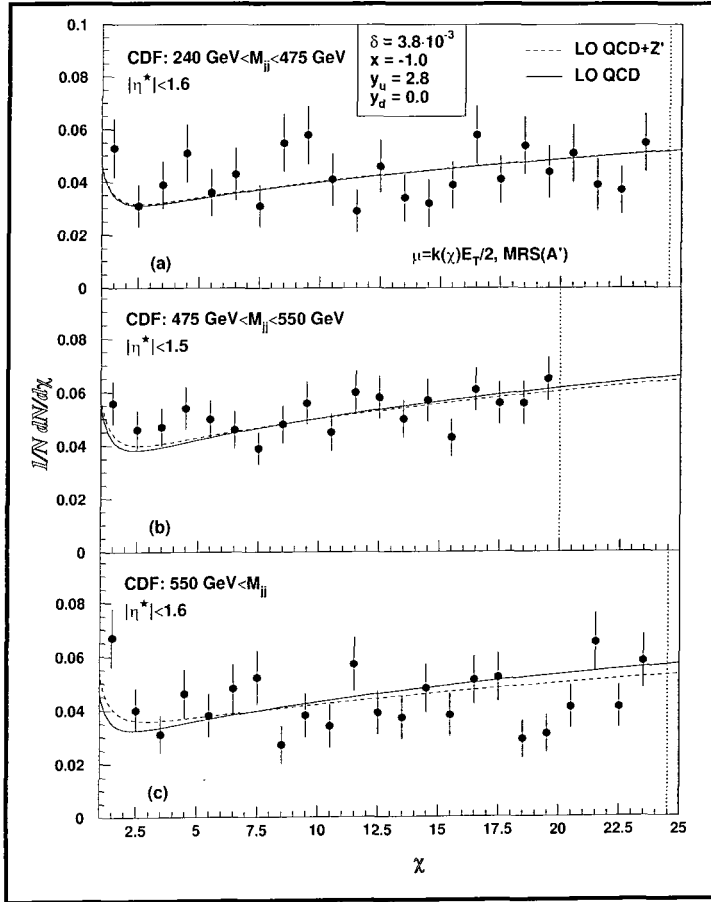
Figure 2.6: The normalised dijet cross sections at $\mathcal{O}(\alpha_s^2)$ for pure QCD (solid lines) and the additionally coupled vector boson Z' (dashed lines) in three different dijet mass bins: (a) $240 < M_{jj} < 475$ GeV, (b) $475 < M_{jj} < 550$ GeV and (c) $M_{jj} > 550$ GeV. The numerical results are compared to the CDF '92 analysis [CDF92]. The kinematical constraints on η^* and the normalisation intervals in χ are indicated and discussed in the text. All Z' calculations were performed for the central parameter fit: $x = -1.0$ and $y_u = 2.8$. As renormalisation scale we have chosen $\mu = k(\chi)E_T/2$ from Ref. [EKS92].

four quarks at small energy transfers in the s– and t–channels. As, for example, $|t| = M_{jj}^2/(\chi + 1)$ we obtain $|t| \ll M_{Z'}^2$, if $\chi \gg 1$ and $\mathcal{O}(M_{jj}^2) \simeq \mathcal{O}(M_{Z'}^2)$. Because of the general form of the Z' matrix elements squared, $|\mathcal{M}^{Z'}|^2 \propto 1/\{(t - M_{Z'}^2)^2 + M_{Z'}^2\Gamma_{Z'}^2\}$ (cf. Eqs. 2.26,2.27), we find the Z' contribution becoming flat for large χ. Therefore the observed enhancement of the dijet cross sections due to this additional vector boson only takes place for small values of χ.

The comparison with the CDF data should be regarded only as being illustrative, as for larger values of χ the NLO and LO calculations slightly differ. The main purpose of Fig. 2.6 is to show the influence of the Z' on the pure QCD calculations. As we expected from the a priori construction of the Z', its presence is emphatically felt for higher dijet masses (like in Fig. 2.6(c)) mainly for large scattering angles where, with

the choice of $\mu = k(\chi)E_T/2$, the authors of Ref. [EKS92] observe that LO and NLO are quite comparable. This underlines the assumption given by Altarelli *et al.* [Alt96] that the ratio Z'/QCD should merely remain unchanged (up to a few percent) in a transition to NLO.
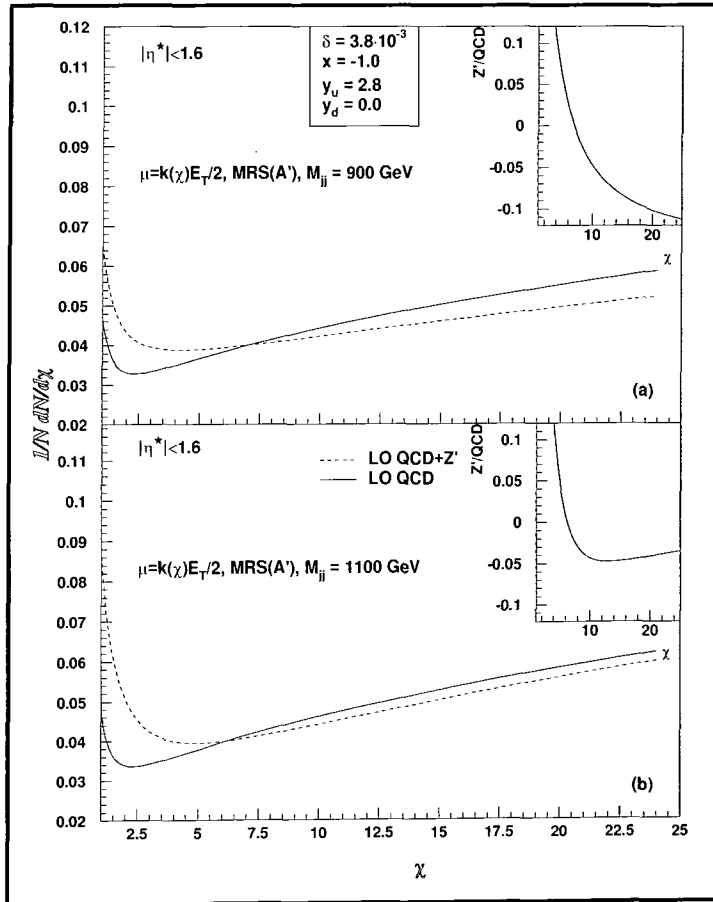
Figure 2.7: Same as Fig. 2.6, but now for the two fixed dijet mass bins: (a) $M_{jj} = 900$ GeV and (b) $M_{jj} = 1100$ GeV. The dijet cross sections are normalised to unity in the interval $1 \leq \chi \leq 24.5$. The relative contributions of the Z' to the LO QCD calculations (Z'/QCD) are also presented.

To emphasise the influence of the Z' even more, we increased in Fig. 2.7 the dijet masses up to the region of $M_{Z'}$ itself. For $M_{jj} = 1100$ GeV (Fig. 2.7(b)) we calculate for the dijet cross section in LO QCD: $dN/(Nd\chi)|_{\text{QCD}} = 0.0363$ for $\chi = 1.5$ ($\Theta^\star = 78°$). The LO QCD$+Z'$ calculation, however, yields a value of $dN/(Nd\chi)|_{\text{QCD}+Z'} = 0.0610$, which means an increase by a factor of 1.7 due to Z' exchange.

The ratios Z'/QCD of our calculations are also presented in Fig. 2.7. This gives even stronger evidence for the fact that for higher dijet masses the Z' contribution especially governs the larger scattering angles whereas for small angles the ratios behave smoothly. This can be observed in Fig. 2.7(b) where $|Z'/\text{QCD}|$ even shrinks for larger χ such that one might conclude that for high dijet masses but very small scattering angles the Z' contribution becomes irrelevant. Even though the LO calculations are not quite

compatible to NLO in the high χ range [EKS92], the corrections due to NLO are supposed to cancel, considering the ratios only, such that this observation should also hold in a NLO calculation.

We conclude this section with a comparison to recent very precise data from the D∅ collaboration [D∅96] and a remark on the latest CDF dijet results published in 1996/1997.
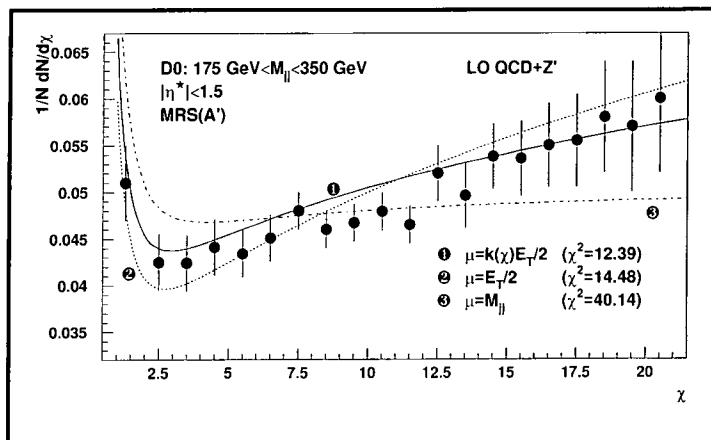
Figure 2.8: The dijet angular distributions in leading order with three different renormalisation scales including the scale defined in Eq. (2.32) and employed throughout this section. The cross sections are integrated over M_{jj} in the range $175 < M_{jj} < 350$ GeV. As before we present the *normalised* cross sections but now for the LO QCD+Z' calculation only. The results are compared to the data taken from the D∅ '96 analysis [D∅96].

In the measured dijet mass range $175 < M_{jj} < 350$ GeV the effect of the Z' is, of course, negligible as we have learned from the CDF data. However, as this data are the most precise available from D∅ at this stage, we might test our argumentation about the reliability of the LO calculations. It has been reported [D∅96] that the data are significantly consistent with NLO QCD calculations. In Fig. 2.8 we present the D∅ data and normalise our cross sections as before in the shown χ range. We restrict ourselves to a presentation of the QCD+Z' results only, as the differences to pure QCD are not striking in this mass regime (*cf.* Fig. 2.6(a)). The numerical values of the calculation with $\mu = k(\chi)E_T/2$ lie almost within the error bars. Recall that this choice of μ is in good agreement with NLO according to [EKS92]. A statistical analysis yields $\chi^2 = 12.39$, and so the LO calculation satisfactorily describes the experimental data, exactly as has been claimed throughout this section. A picture of consistency emerges out of the comparison to the experimental data. The dashed line shows the result for the calculation with $\mu = E_T/2$. The similarity in χ^2 is an indicator of how reliably this scale is again working in approximating NLO results for large scattering angles. For illustrative reasons we also present the result for a completely different renormalisation scale. This shows that a less dynamical scale like $\mu = M_{jj}$ cannot describe the experimental results (the χ^2 value is also presented). The curve is nearly flat over the whole χ range.

The analysis of the data obtained in the same run as the single inclusive jet data led the CDF collaboration to publications of results on dijet production. [CDF96b]. Within

the error bars the angular distributions agree with NLO predictions[5] of QCD in all dijet invariant mass M_{jj} regions. But again, the highest mass bin with statistical uncertainties of less than 5% showed a mass of only $M_{jj} \simeq 500$ GeV. And again, if the Z' is genuine, then the effect of this vector boson should be within the uncertainty of the error bars and thus no concluding remarks about whether to discard the Z' model can be made. We shall remark on this consequence further below after the discussion of the Z' model at the LHC.

2.2.5 The Z' at the LHC

The question we want to address in this section is how the Z' will influence the measured jet cross sections at the LHC. From our previous results we expect the influence to be generally enhanced due to a higher centre–of–mass energy of $\sqrt{s} = 10$–14 TeV. This allows the observation of higher transverse energies E_T and dijet masses M_{jj}. On the other hand, we expect background contributions like Drell–Yan processes [DY70], production of mini–jets [MN87, RT96], diffraction, etc. to become larger such that the signal–to–background ratio for the Z' will be even more reduced. We constructed the Z' such that it does not couple to leptons, and Drell–Yan processes via Z' exchange have to be completely excluded. Another feature somehow obstructs the detectability of the Z' at the LHC: at a pp collider and high centre–of–mass energies the main contributions to the two–parton jet events come from subprocesses involving gluons, like $gg \to gg(q\bar{q})$ and $gq \to gq$. But the Z' does not couple to gluons. And as antiquarks only appear as sea quarks in the proton we expect the main contribution from the Z' at the LHC to come from the t–channel exchange:
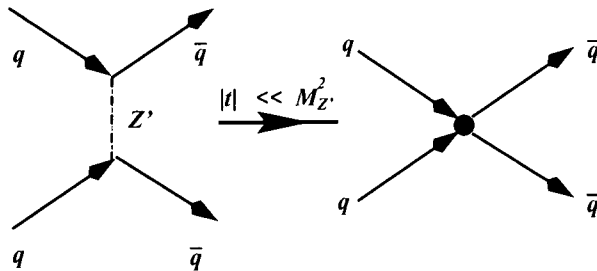
Again we want to perform all calculations in LO QCD. However, the new kinematical constraints at the LHC have to be taken into account and therefore we first perform a global NLO analysis of the single inclusive jet cross section to deduce the magnitude of the NLO corrections. Using the programming package of Ref. [EKS92], we find for a jet cone size $R = \sqrt{\Delta\eta^2 + \Delta\phi^2} = 0.7$, where ϕ is the azimuthal angle around the beam, the normalisation factors $\mathcal{N}$ shown in Table 2.4. The NLO corrections are quite comparable over the range $400 < E_T < 4000$ GeV for the achievable centre–of–mass energies $\sqrt{s}$ at the LHC. They differ only on the scale of a few per mille for $E_T > 2000$ GeV. In the following analysis for the LHC we shall use the global effective LO scale with an average normalisation factor $\mathcal{N} = 0.78$ and our standard renormalisation scale $\mu = E_T/2$ assuming a jet cone size of $R = 0.7$. This should be compared with the normalisation factor $\mathcal{N} = 0.91$ we found for the TEVATRON. NLO corrections, even for a small jet cone

---

[5]I am indebted to C. Wei from the CDF collaboration for providing me with preliminary results.

E_T [GeV]	$\sqrt{s} = 10$ TeV	$\sqrt{s} = 12$ TeV	$\sqrt{s} = 14$ TeV
400	0.75162	0.75162	0.75162
1200	0.77200	0.77200	0.77200
2000	0.78025	0.78023	0.78023
2400	0.78305	0.78301	0.78300
2800	0.78536	0.78529	0.78527
3200	0.78731	0.78722	0.78718
3600	0.78899	0.78890	0.78884
4000	0.79048	0.79036	0.79027

Table 2.4: The normalisation factor $\mathcal{N} := [\mathrm{d}^2\sigma/\mathrm{d}E_T\mathrm{d}\eta]_{\mathrm{NLO}}/[\mathrm{d}^2\sigma/\mathrm{d}E_T\mathrm{d}\eta]_{\mathrm{LO}}$ for different E_T bins and typical LHC centre–of–mass energies. The jet cone size chosen was $R = 0.7$ for $\eta = 0$ and the underlying renormalisation scale $\mu = E_T/2$.

size, become more striking at higher centre–of–mass energies. But at least for the ratios $(\mathrm{QCD} + Z')/\mathrm{QCD}$ we do not expect evident differences from a pure NLO calculation, as NLO corrections are expected to cancel.

In Fig. 2.9(a) we present the results for the single inclusive cross section at the LHC for fixed $\eta = 0$. The inset shows the ratios Z'/QCD for two different centre–of–mass energies as a function of E_T. We observe that for $E_T \sim 1000$ GeV the contribution from the Z' matches the QCD one for both curves. The curves are then rising very steeply but the typical $\propto E_T^4$ behaviour we observed in the inset of Fig. 2.4 for the TEVATRON is suppressed for $E_T \gtrsim 2500$ GeV. To understand the underlying mechanism for this observation we present in Figs. 2.9(b,c) the individual subprocesses $ab \to cd$ for the QCD and the Z' calculation. For higher centre–of–mass energies the gluons play the pivotal role and dominate the matrix elements of Eq. (2.25).

At typical LHC energies the $qg \to qg$ contribution dominates with about 40% of all other subprocess events. For still larger values of $\sqrt{s}$ also the gluon–gluon fusion rate is linearly growing whereas the number of subprocesses including quarks or antiquarks as initial partons is diminished as shown in Fig. 2.9(b). We also observe the ratio $(q\bar{q})/(qg) = 4/9$ as predicted by perturbative QCD [BG76] in Fig. 2.9(b).

The Z' does not couple to gluons and therefore the Z' contribution is rising more slowly for higher centre–of–mass energies as the gluons actually give the dominant contributions. The corresponding subprocesses governing the Z' contribution are shown in Fig. 2.9(c). This explains two features observable in Fig. 2.9(a): first, the ratio Z'/QCD is becoming flatter for higher values of $\sqrt{s}$ and second, the main high transverse jet energy is carried by the gluons. The latter is a well known fact and was theoretically dealt with in Ref. [Ant86]. The relative contributions of quarks and antiquarks to large E_T processes is small, which yields the observed smoothing in the ratios at larger E_T.
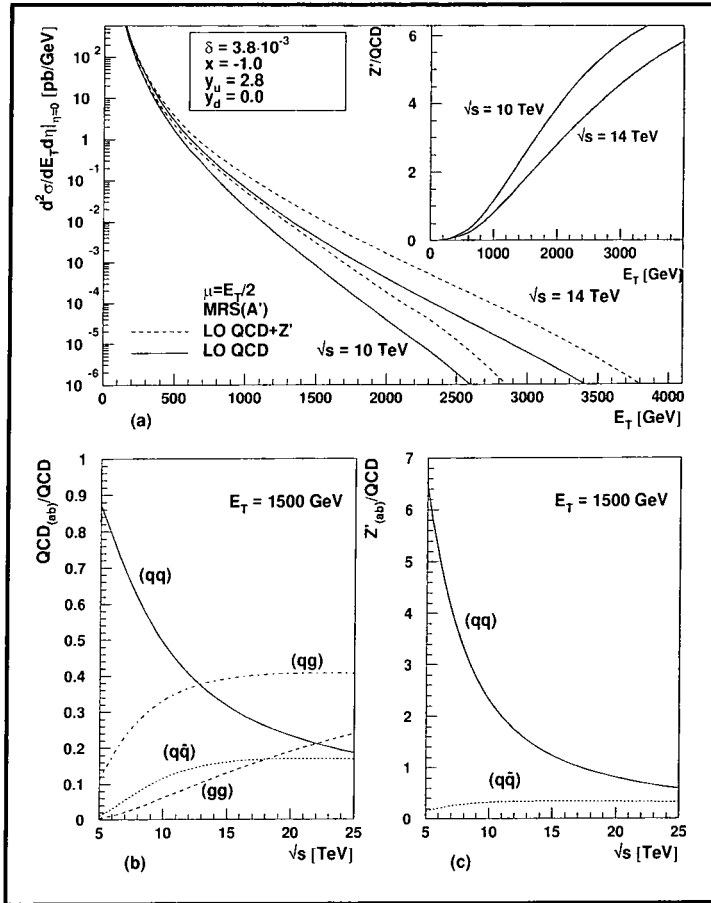
Figure 2.9: LO calculation of the single inclusive jet cross sections at the LHC for the two centre–of–mass energies 10 TeV and 14 TeV. The ratios Z'/QCD are shown in the inset of (a). The contributions of the different subprocesses $ab \to cd$ for (b) LO QCD and (c) Z', normalised to the full LO QCD calculation, as a function of the centre–of–mass energy are shown. The transverse jet energy was fixed to be $E_T = 1500$ GeV.

Note the absolute scales in Fig. 2.9(b,c). For $\sqrt{s} = 10$ TeV the $Z'_{(qq)}$ subprocess exceeds the corresponding $\mathrm{QCD}_{(qq)}$ rate by a factor of five. Fig. 2.9(c) also demonstrates the predominance of the Z' t–channel exchange compared to the s–channel exchange.

We also give predictions for the dijet angular distributions as we did for the TEVA-TRON. Fig. 2.10(a) shows the results for a calculation with $M_{jj} = 1000$ GeV and $M_{jj} = 2000$ GeV again for the two different centre–of–mass energies. Unlike the presentations for the TEVATRON we now show the *unnormalised* distributions for our best–fit parameters (2.28). Qualitatively we find the same results as for the TEVATRON: the Z' boson most strongly influences the small χ region (again we interpret the Z' acting as an *effective contact interaction* [ELP89] in this regime, contracting its propagator to an effective four–fermion point–like interaction) and this effect is again enhanced for higher dijet masses. The corresponding ratios shown in Fig. 2.10(b) underline the conclusions already drawn for the TEVATRON, but now on a much larger scale.
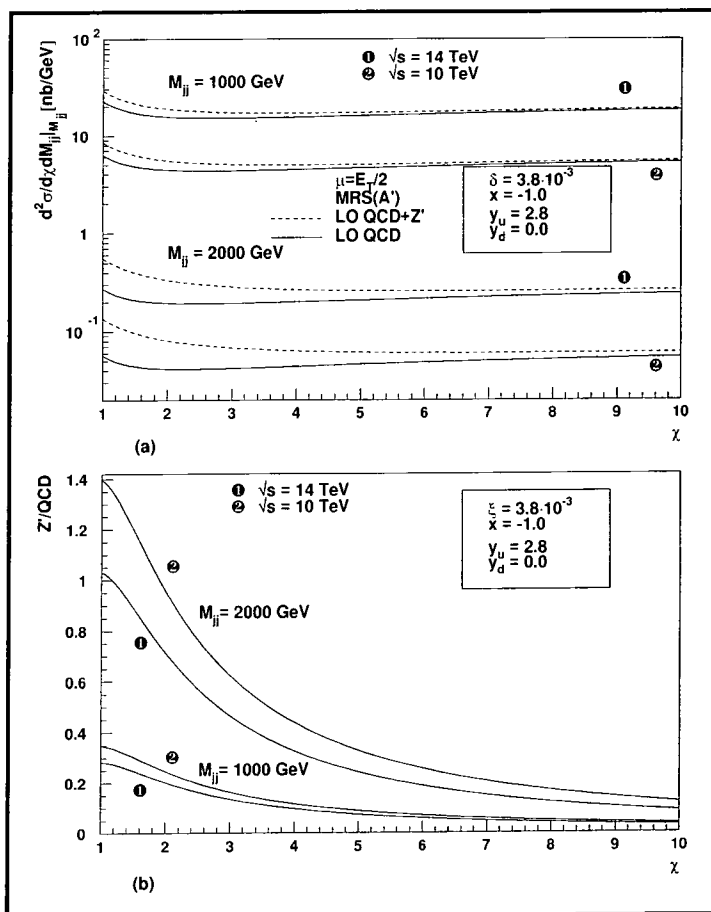
Figure 2.10: The dijet angular distributions at the LHC for two different invariant dijet masses. The unnormalised cross sections are shown in (a) for LO QCD and LO QCD+Z'. In (b) we show the corresponding ratios Z'/QCD again for the central fit parameters of the Z' model.

Because we have so far presented our numerical results for our best–fit values (2.28) only, we finally want to show the variations of the Z' impact due to upper and lower bounds in accord with our analysis. If we fix $x = -1.0$, as we found the central x value to be, then we get upper and lower bounds on y_u from our χ^2 analysis if we restrict our fit–acceptance to the 68.3% confidence ellipse shown in Fig. 2.5(c). For $x = -1.0$ we read off $y_u \in [2.4, 3.2]$. Fig. 2.11(a) shows the single inclusive jet ratios for the three different values of $y_u = 2.4, 2.8$ and 3.2 being the lower bound, central value and upper bound respectively. The discrepancy between the different choices of y_u becomes very striking for higher E_T values. The total decay width varies from $\Gamma_{Z'} = 508.0$ GeV ($y_u = 2.4$) up to $\Gamma_{Z'} = 801.4$ GeV ($y_u = 3.2$), which increases the phase space of the Z' especially at high transverse energies. So, large E_T measurements at the LHC might be an excellent probe to more precisely fix the value of y_u, as the cross sections are very strongly dependent on y_u in this energy range and so a clear y_u correspondence is achievable. The difference to the best–fit of Altarelli et al. [Alt96] ($y_u = 2.2$) is also shown. Note the difference of only 7% to our lower bound ($y_u = 2.4$) for $E_T = 3000$ GeV.

Fig. 2.11(b) finally shows the ratios Z'/QCD for the dijet angular distributions with the same values for y_u as in Fig. 2.11(a). The Z' impact on the small χ region is again significant. The extreme values of y_u differ by a factor of roughly two in the complete χ range shown. Again, future measurements of the dijet angular distributions at the LHC might further determine y_u more exactly according to the large dependence of the ratios to the choice of this coupling parameter.
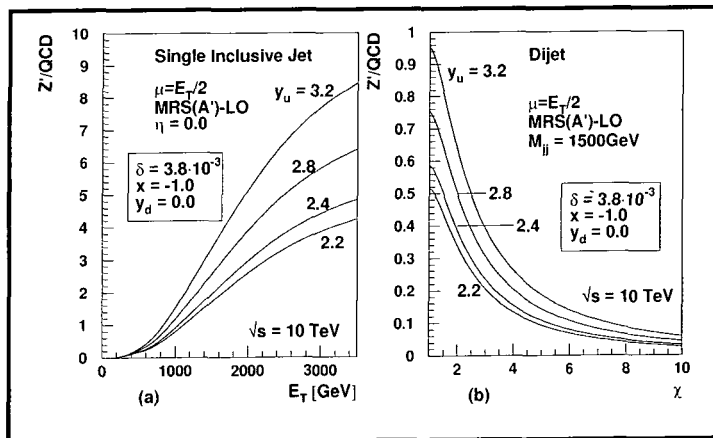
Figure 2.11: The ratios Z'/QCD for the (a) single inclusive jet cross sections ($\eta = 0$) and (b) dijet angular distributions ($M_{jj} = 1500$ GeV) at the LHC. We keep x, y_d, ξ and $M_{Z'}$ fixed to the values of our best–fit and vary y_u according to the 68.3% confidence ellipse shown in Fig. 2.5(c). We also present the calculations for the best–fit value $y_u = 2.2$ of Altarelli et al. [Alt96].

2.2.6 Status of the Z' and conclusions

We gave predictions for the Z' effect on future precision measurements at the LHC. We showed the corresponding physical parameter ranges for which the influence of the Z' is expected to be most striking and besides *qualitative* considerations we also provided *quantitative* predictions for single inclusive jet cross sections and angular dijet distributions at the LHC. We presented numerical results for different coupling parameters y_u that were allowed on the 68.3% (=1σ) confidence level from our previous CDF data fit. This will help to further determine the free parameters of the Z' model as soon as first LHC data are available.

As a final critical remark we want to point out that despite the very precise and reliable experiments there might still be <u>no</u> compelling reason to look for *new physics*. However, future data are necessary, and the LHC will play a pivotal role as a high–energy laboratory and new theoretical models and predictions, rising from such fundamental contradictions to the Standard Model, will become important.

We did not try to answer the question of where the Z', if it is indeed genuine, originates from. For an overview on several motivations for the existence of additional vector bosons and a list of the most studied models we refer to [HR89]. In addition we should mention a model for the neutral boson proposed in [FH90, FHR90, FHR91], where it originates

from the breaking of an extended colour group, such as $SU(4)_C$ or $SU(5)_C$. In this model the vector boson is very strongly coupled to $q\bar{q}$ pairs and weakly coupled to leptons. As reported by T.G. Rizzo [Riz93] its mass should be larger than 600 GeV. In view of the proposed features this model could be a promising Z' candidate.

The fate of the leptophobic Z'

The introduction of a <u>leptophobic</u> Z' into high–energy physics by [Alt96, Chi96] was motivated by

(1) a too small experimental value for R_c in the LEP (1995) measurement (-2.4σ from the SM),

(2) a too large experimental value for R_b in the LEP (1995) measurement ($+3.6\sigma$ from the SM),

(3) a large discrepancy between the measured and expected high–E_T jet rate by the CDF collaboration.

As there was no deviation from the leptonic branching ratio $R_\ell = \Gamma_{\text{hadr}}/\Gamma_\ell$ reported,[6] the assumption that the Z' has no (or very weak) couplings to the SM leptons was natural. The 1995 measurement also showed a remarkable numerical coincidence. Taking the two up–type quarks u and c and the three down–type quarks d, s and b one finds

$$2\delta R_c + 3\delta R_b = -0.0047 \pm 0.0134,$$

i.e. a number which is zero within the 1σ region. Therefore the authors of [Alt96, Chi96] naturally assumed a *family–independent coupling* of the Z' to up– and down–type quarks. Using the 1997 data still yields $2\delta R_c + 3\delta R_b = 0.0047 \pm 0.0057 \simeq 0$ at the 1σ level. But there seems no need to invoke new physics from the LEP measurements, the SM proved solid.

As this tendency seemed foreseeable when we applied the leptophobic Z' model, we only concentrated on fitting the CDF jet–excess data. Again a leptophobic Z' seemed sufficient concerning the underlying processes at the TEVATRON. The data available on dijet cross sections from the TEVATRON are in agreement with NLO QCD calculations. And we showed that a Z' cannot be outruled in the measured M_{jj} intervals. Data on higher dijet masses have to be available to "feel" the presence of the Z' within the still large statistical errors. We conclude:

> The CDF data on high–E_T jets are the only possible
> physical motivation for a leptophobic Z' at the moment,

even though attempts to reduce the large–E_T events by tuning the uncertainty in the gluon density [Lai97] proved successful.

Besides our studies more predictions for the TEVATRON in the leptophobic Z' framework have been done

---

[6] The 1995 LEP data yielded $R_\ell = 20.788 \pm 0.032$ [LEP95] and the updated 1997 show $R_\ell = 20.775 \pm 0.027$ [LEP97] compared to the SM value of $R_\ell = 20.754 \pm 0.020$.

- the enhancement of the $t\bar{t}$ cross section [GS96],

- the associated production of a light Z' and W, Z, γ in $b\bar{b}$ events [BCL96],

- the associated production of W and Z with neutral and charged Higgs [GG96],

- the decay of the Z' into exotic fermions $Z' \rightarrow f'\bar{f}'$ [Ros96].

The leptophobic Z' model is not *anomaly free*, as this would require the full set of fermions and the inclusion of a Higgs sector to provide anomaly cancellations. But this need should be fulfilled if there is more experimental evidence for a leptophobic Z'.

References for Chapter 2

— A —

[ABR88]   A. Akhundov, D. Bardin and T. Riemann, *Nucl. Phys.* **276** (1988) 1.

[AT97]   K. Akama and H. Terazawa, *Phys. Rev.* **D55** (1997) 2521.

[Alt96]   G. Altarelli, N. Di Bartolomeo, F. Feruglio, R. Gatto and M.L. Mangano, *Phys. Lett.* **B375** (1996) 292.

[Ant86]   N.G. Antoniou, E.N. Argyres, P.S. Dimitriadis, L.B. Papatsimpa and A. Valadakis, *Phys. Lett.* **B177** (1986) 437.

— B —

[BBH96]   G. Bhattacharyya, G.C. Branco and W.S. Hou, *Phys. Rev.* **D54** (1996) 2144.

[BBN88]   F.A. Berends, G. Burges and W.L. van Neerven, *Nucl. Phys.* **B297** (1988) 429; *Nucl. Phys.* **B304** (1988) 921.

[BCL96]   V. Barger, K. Cheung and P. Langacker, *Phys. Lett.* **B381** (1996) 226.

[BG76]   S.J. Brodsky and J.F. Gunion, *Phys. Rev. Lett.* **37** (1976) 402.

[BH88]   W. Beenakker and W. Hollik, *Z. Phys.* **C40** (1988) 141.

[BL86]   G. Branko and L. Lavoura, *Nucl. Phys.* **B278** (1986) 738.

[BR90]   V. Barger and T.G. Rizzo, *Phys. Rev.* **D41** (1990) 946.

[Ban96]   M. Bander, *Phys. Rev. Lett.* **77** (1996) 601.

[Bla96]   J. Blazey, talk presented at the XXXIst Recontres de Moriond, 1996.

[Blo96]   A. Blondel, talk presented at the 28th International Conference on High Energy Physics, Warsaw, Poland, 1996.

— C —

[C++]   B.P. Flannery, W.H. Press, S.A. Teukolsky and W.T. Vetterling, Numerical Recipes in C (Cambridge University Press), Cambridge, England 1991.

[CCS96]   R.S. Chivukula, A.G. Cohen and E.H. Simmons, *Phys. Lett.* **B380** (1996) 92.

[CDF92]   CDF Collaboration: F. Abe *et al.*, *Phys. Rev. Lett.* **69** (1992) 2896.

[CDF96a]   CDF Collaboration: F. Abe *et al.*, *Phys. Rev. Lett.* **77** (1996) 438.

[CDF96b]   CDF Collaboration: F. Abe *et al.*, *Phys. Rev. Lett.* **77** (1996) 5336; *ibid.* **78** (1997) 4307.

[CGN82]   T.H. Chang, K.J.F. Gaemers and W.L. van Neerven, *Nucl. Phys.* **B202** (1982) 407.

[CKR77]   B.L. Combridge, J. Kripfganz and J. Ranft, *Phys. Lett.* **B70** (1977) 234.

[CTEQ96]   CTEQ Collaboration: J. Huston *et al.*, *Phys. Rev. Lett.* **77** (1996) 444.

[Chi96]   P. Chiappetta, J. Layssac, F.M. Renard and C. Verzegnassi, *Phys. Rev.* **D54** (1996) 789.

— D —

[DØ96]   DØ Collaboration: S. Abachi *et al.*, talk presented at the 28th International Conference on High Energy Physics, Warsaw, Poland, 1996.

[DKZ90]   A. Djouadi, J.H. Kühn and P.M. Zerwas, *Z. Phys.* **C46** (1990) 411.

[DY70]   S.D. Drell and T.M. Yan, *Phys. Rev. Lett.* **24** (1970) 181.

— E —

[EKS90]   S.D. Ellis, Z. Kunszt and D.E. Soper, *Phys. Rev. Lett.* **64** (1990) 2121.

[EKS92]   S.D. Ellis, Z. Kunszt and D.E. Soper, *Phys. Rev. Lett.* **69** (1992) 1496.

[ELP89]   E.J. Eichten, K.D. Lane and M.E. Peskin, *Phys. Rev. Lett.* **50** (1989) 811.

— F —

[FH90]   R. Foot and O. Hernández, *Phys. Rev.* **D41** (1990) 2283.

[FHR90]   R. Foot, O. Hernández and T.G. Rizzo, *Phys. Lett.* **B246** (1990) 183.

[FHR91]   R. Foot and O. Hernández and T.G. Rizzo, *Phys. Lett.* **B261** (1991) 153.

— G —

[GG96]   H. Georgi and S.L. Glashow, *Phys. Lett.* **B387** (1996) 341.

[GGK93]   W.T. Giele, E.W.N. Glover and D.A. Kosower, *Nucl. Phys.* **B403** (1993) 633.

[GS96]   T. Gehrmann and W.J. Stirling, *Phys. Lett.* **B381** (1996) 221.

[Glo96]   E.W.N. Glover, A.D. Martin, R.G. Roberts and W.J. Stirling, *Phys. Lett.* **B381** (1996) 353.

— H —

[HR89]   J.L. Hewett and T.G. Rizzo, *Phys. Rep.* **C183** (1989) 193.

— J —

[JLZ81]   J. Jersák, E. Lärmann and P.M. Zerwas, *Phys. Lett.* **B98** (1981) 363.

[JLZ82]   J. Jersák, E. Lärmann and P.M. Zerwas, *Phys. Rev.* **D25** (1982) 1218.

[JS89]   E. Jenkins and E.H. Simmons, *Phys. Rev. Lett.* **62** (1989) 2789.

— L —

[LEP95]   The LEP collaborations ALEPH, DELPHI, L3 and OPAL and the LEP Electroweak Working Group, CERN preprint LEPEWWG/95–172, 1995.

[LEP97]   The LEP collaborations ALEPH, DELPHI, L3 and OPAL and the LEP Electroweak Working Group, CERN preprint LEPEWWG/97–02, 1997.

[LR97]   A. Leike and S. Riemann, *Z. Phys.* **C75** (1997) 341.

[LS93]   L. Lavoura and J.P. Silva, *Phys. Rev.* **D47** (1993) 1117.

[Lai97]   H.L. Lai, J. Huston, S. Kuhlmann, F. Olness, J. Owens, D. Soper, W.K. Tung and H. Weerts, *Phys. Rev.* **D55** (1997) 1280.

— M —

[MN87]   A.H. Mueller and H. Navelet, *Nucl. Phys.* **B282** (1987) 727.

[Ma96]   E. Ma, *Phys. Rev.* **D53** (1996) 2276.

[McF96]   K.S. McFarland, talk presented at the XXXIst Recontres de Moriond, 1996.

— P —

[PDG96]   R.M. Barnett *et al.*, *Phys. Rev.* **D54** (1996) 1;
          Particle Data Group www pages: http://pdg.lbl.gov.

85

— R —

[RT96]   R. Ragazzon and D. Treleani, *Phys. Rev.* **D53** (1996) 55.

[Riz93]   T.G. Rizzo, *Phys. Rev.* **D48** (1993) 4470.

[Ros96]   J.L. Rosner, *Phys. Lett.* **B387** (1996) 113.

— S —

[Ste95]   G. Sterman *et al.*, *Rev. Mod. Phys.* **67** (1995) 157.

— Y —

[Yos96]   T. Yoshikawa, *Prog. Theor. Phys.* **96** (1996) 269.

Chapter 3

Soft γ and gluon emission – antenna patterns

> *"Science is always doomed: she never solves a problem without creating another ten."*
>
> (G.B. Shaw)

In the following chapter we investigate (tree–level) amplitudes with additional soft photons or soft gluons in the final state. We show that the matrix element with additional soft radiation can be written as $\mathcal{M}^1 \propto \epsilon \cdot J \, \mathcal{M}^0$, where $\mathcal{M}^0$ defines the lowest order matrix element without additional radiation and J denotes the soft current. We thus present general Feynman rules for soft emission off spin–1/2 particles. This will be the scope of Section 3.1.

These studies finally lead to a discussion of colour coherence phenomena in Section 3.2, which plays a pivotal role for processes with soft gluon radiation. We focus on interjet coherence and review the well–known *"drag"* or *"string"* effect. A presentation of some experimental results on colour coherence rounds this section up.

In Section 3.3 we use the theoretical framework of the previous sections to present hadronic radiation patterns for Higgs production at the LHC. We give predictions for both Higgs signal and QCD processes and discuss how radiation patterns might be useful to pin down the Higgs in a given process.

Section 3.4 investigates soft photon and gluon radiation at HERA. In this study we show how further insight can be gained in the reported high–Q^2 measurements from the H1 and ZEUS collaboration. We discuss in particular the case of an s–channel resonance ("leptoquark") and discuss the difference to standard t–channel γ^*, Z exchange.

A short summary of our results and colour coherence is provided in Section 3.5.

3.1   Soft photon and gluon amplitudes

In this section we provide the universal formulae we shall use throughout this chapter. We present general expressions for emission of an additional very–low–energy photon and

gluon in a process

$$
\begin{aligned}
1, 2, \ldots, l &\;\to\; (l+1, l+2, \ldots, n) + \gamma\,, \\
1, 2, \ldots, l &\;\to\; (l+1, l+2, \ldots, n) + g\,.
\end{aligned}
$$

We allow single photon and gluon emission from all internal and external legs (one photon or gluon in final state). For soft multi–gluon and multi–photon emission we refer to Appendix B at the end of this chapter.

By <u>soft</u> we mean that the energy $\omega_{\gamma/g}$ and momentum $|\vec{\mathbf{k}}_{\gamma/g}|$ of the emitted particles is much less than the energies E_i characteristic of the processes in question, in particular we shall call

$$
\frac{\omega_{\gamma/g}}{E_i} = \frac{|\vec{\mathbf{k}}_{\gamma/g}|}{\sqrt{m_i^2 + |\vec{\mathbf{p}}_i|^2}} \to 0\,, \tag{3.1}
$$

the *soft limit*. Soft photons (gluons) play a pivotal role in the study of radiative corrections. Often these corrections are so large that they must be summed to all orders in perturbation theory. But they are so simple that their summation is no hard challenge for the ambitious theorist and in the end all *infrared divergencies* will cancel as was first shown by F. Bloch and A. Nordsieck [BN37] (see also [FSY61] for a *Feynman approach*).

3.1.1   Soft photons

If we attach the soft photon line with outgoing momentum k and polarisation index μ to an outgoing charged–particle line[1] p_i that leaves some connected Feynman diagram for the process, then we include besides an additional $\gamma f f$–vertex a charged propagator with four momentum $p_i + k$. For a spin–$\frac{1}{2}$ fermion we have to add the additional contribution $(\mathcal{M}_{i,\mathrm{ex}}^\gamma)^\mu$ (vertex $V_{\gamma ff} = -iee_f\gamma^\mu$ and propagator $i\frac{\not{p}_i + \not{k} + m_i}{(p_i+k)^2 - m_i^2}$ in the Feynman–'t Hooft gauge). The amplitude for single soft–photon emission $(\mathcal{M}_i^\gamma)^\mu = (\mathcal{M}_{i,\mathrm{ex}}^\gamma)^\mu \times \mathcal{M}_{\mathrm{in}}^c$ then reads
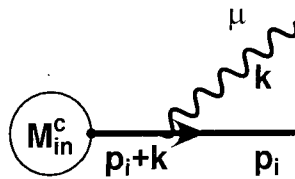
$$
\overline{u}(p_i)\,[-iee_f\gamma^\mu]\left[i\frac{\not{p}_i + \not{k} + m_i}{(p_i+k)^2 - m_i^2}\right] \times \mathcal{M}_{\mathrm{in}}^c \;\xrightarrow{k\to 0}\; ee_f\boxed{\frac{p_i^\mu}{p_i\cdot k}}\,\overline{u}(p_i) \times \mathcal{M}_{\mathrm{in}}^c\,. \tag{3.2}
$$

For the transition to the soft limit we used the facts that

$$
\begin{aligned}
\overline{u}(p_i)\gamma^\mu(\not{p}_i + m_i) &= 2\overline{u}(p_i)p_i^\mu - \overline{u}(p_i)(\not{p}_i - m_i)\gamma^\mu \\
&= 2p_i^\mu\overline{u}(p_i), \qquad \text{with} \\
\overline{u}(p_i)(\not{p}_i - m_i) &= 0 \qquad\qquad \text{Dirac equation} \\
\text{and} \qquad \gamma^\mu\gamma^\nu &= 2g^{\mu\nu} - \gamma^\nu\gamma^\mu\,.
\end{aligned}
$$

---

[1]Here and in the following we shall address spin–$\frac{1}{2}$ particles only, but what we derive also holds for emission off spin–1 and higher spin particles.

The prefactor $p_i^\mu/(p_i \cdot k)$ is called the *eikonal factor*. In Appendix A.1 we present the general rules for the emission of an additional soft photon from external and internal legs. Note that $\mathcal{M}_{\text{in}}^{\text{c}}$ denotes the part of the matrix amplitude that has no additional photon attached to. The matrix element $\left(\mathcal{M}_{i,\text{ex}}^\gamma\right)^\mu$ has to be multiplied with the polarisation vector $\epsilon^\mu(\lambda)$, where μ denotes the polarisation index and λ defines the helicity. So finally we can write

$$\mathcal{M}_i^\gamma = ee_f \frac{p_i^\mu}{p_i \cdot k} \epsilon_\mu^*(\lambda) \times \mathcal{M}_i^0 . \tag{3.3}$$

for the emission of a soft photon off an external leg of a final state particle. It is easy to show that there is a relative change in sign for the eikonal factor if the emission takes place off an incoming leg, and a relative sign for emission off antiparticles.

More subtle are internal legs. Imagine again the soft emission off a fermion as shown below.[2]
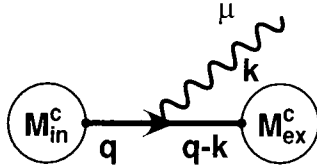
$$\begin{aligned}
\mathcal{M}_q^\gamma &= \mathcal{M}_{\text{ex}}^{\text{c}} i \frac{\slashed{q} + m}{q^2 - m^2} (-iee_f\gamma^\mu) i \frac{\slashed{q} - \slashed{k} + m}{(q-k)^2 - m^2} \mathcal{M}_{\text{in}}^{\text{c}} \epsilon_\mu^*(\lambda) \\
&= iee_f \mathcal{M}_{\text{ex}}^{\text{c}} (\slashed{q} + m) \gamma^\mu (\slashed{q} - \slashed{k} + m) \mathcal{M}_{\text{in}}^{\text{c}} \epsilon_\mu^*(\lambda) \mathcal{D}(q) \mathcal{D}(q-k)
\end{aligned}$$

with

$$\mathcal{D}(q) = \frac{1}{q^2 - m^2 + i\epsilon} . \tag{3.4}$$

In the soft limit this expression reads

$$\mathcal{M}_q^\gamma = iee_f \mathcal{M}_{\text{ex}}^{\text{c}} \frac{q^\mu}{q \cdot k} \mathcal{M}_{\text{in}}^{\text{c}} \epsilon_\mu^*(\lambda) \left\{ \mathcal{D}(q-k) - \mathcal{D}(q) \right\} , \tag{3.5}$$

where we made use of the fact that

$$\mathcal{D}(q)\mathcal{D}(q-k) = \frac{1}{2q \cdot k} \left\{ \mathcal{D}(q-k) - \mathcal{D}(q) \right\} . \tag{3.6}$$

In general one can show that the complete matrix element can be written as

$$\begin{aligned}
\mathcal{M}^\gamma(1,2,\ldots,l \to (l+1, l+2, \ldots, n) + \gamma) &= \sum_{i=1}^n \mathcal{M}_i^\gamma + \sum_q \mathcal{M}_q^\gamma \\
&= e \left\{ \sum_i e_i J_i^\mu \epsilon_\mu^*(\lambda_i) \right\} \mathcal{M}^0 , \quad (3.7)
\end{aligned}$$

where $\mathcal{M}^0$ denotes the matrix element of the process without additional photon emission. All extra propagators and eikonal factors are included in the definition of the currents J_i^μ. The coefficients e_i denote the couplings of the soft photon to each internal or external line i in units of the elementary charge e.

---

[2]Note that only on–shell particles contribute to (enhance) the soft radiation pattern.

As an example we study the process $e^-(1)e^+(2) \to e^-(3)e^+(4)+\gamma(k)$. As this process is mediated by an internal γ^* or Z there is only emission from the external legs. With the rules given in Appendix A.1 we can immediately write down the weighted current

$$\sum_{i=1}^{4} e_i J_i^\mu = \frac{p_1^\mu}{p_1 \cdot k} - \frac{p_2^\mu}{p_2 \cdot k} - \frac{p_3^\mu}{p_3 \cdot k} + \frac{p_4^\mu}{p_4 \cdot k} . \tag{3.8}$$

We define the <u>antenna pattern</u> as

$$\boxed{\mathcal{F}^\gamma = -\sum_{i,j} e_i e_j J_i^\mu J_{\mu,j}} . \tag{3.9}$$

The *minus sign* follows from the fact that for the four–vector product of the photon polarisation vectors we have $\epsilon^2 = -1$. Assuming massless fermions we finally arrive at

$$\frac{1}{2}\mathcal{F}^\gamma_{e^-e^+\gamma} = [12] + [34] + [13] + [24] - [14] - [23] , \tag{3.10}$$

with

$$[ij] = \frac{p_i \cdot p_j}{(p_i \cdot k)(p_j \cdot k)} . \tag{3.11}$$

For the production of two massless quarks $e^-(1)e^+(2) \to q(3)\bar{q}(4) + \gamma(k)$ we have as underlying current

$$\sum_{i=1}^{4} e_i J_i^\mu = \frac{p_1^\mu}{p_1 \cdot k} - \frac{p_2^\mu}{p_2 \cdot k} + e_q\frac{p_3^\mu}{p_3 \cdot k} - e_q\frac{p_4^\mu}{p_4 \cdot k} , \tag{3.12}$$

and thus

$$\frac{1}{2}\mathcal{F}^\gamma_{q\bar{q}\gamma} = [12] + e_q^2[34] - e_q \{[13] + [24] - [14] - [23]\} . \tag{3.13}$$

We want to mention another interesting feature concerning the emission of an additional soft photon. From Eq. (3.7) we see

$$(\mathcal{M}^\gamma)^\mu \propto \sum_i e_i J_i^\mu \mathcal{M}^0 \tag{3.14}$$

and we found that

$$\sum_i e_i J_i^\mu = \sum_{i=1}^{n} \eta_i e_i \frac{p_i^\mu}{p_i \cdot k} , \tag{3.15}$$

with $\eta_i = -1$ for emission from an *incoming* and $\eta_i = +1$ for emission off an *outgoing* particle and e_i being the charge of the ith particle. Care has to be taken for *internal lines* as will be explained in Appendix A.1. We shall not discuss emission from internal lines for the moment. To calculate the amplitude for the emission of a photon of *definite helicity* λ, we must contract above expression with the corresponding photon polarisation vector $\epsilon_\mu(\vec{k}, \pm)$. Under Lorentz transformation $\epsilon_\mu(\vec{k}, \pm)$ is transformed into $\Lambda_\nu^\mu \epsilon^\nu(\vec{k}, \pm)$ plus a term proportional to k^μ. In order for this last term not to spoil Lorentz invariance of $(\mathcal{M}^\gamma)^\mu$ it is important that $k_\mu (\mathcal{M}^\gamma)^\mu = 0$, and thus from Eq. (3.15)

$$k_\mu (\mathcal{M}^\gamma)^\mu = \left(\sum_{i=1}^{n} \eta_i e_i \right) \mathcal{M}^0 \tag{3.16}$$

follows *charge conservation*. For massless particles with spin 1 (photons, gluons), Lorentz invariance requires the conservation of whatever coupling constant like electric charge governs the interaction of these particles at low energies.

In case there would be the emission of a spin–2 particle, like a *graviton*, then we deal with a tensor of rank 2 instead of a simple four vector for the current

$$\sum_j c_{\text{grav},j} \mathcal{T}^{\mu\nu} = \sum_{i=1}^{n} \eta_i g_i \frac{p_i^\mu p_i^\nu}{p_i \cdot k} \qquad (3.17)$$

and thus

$$\sum_{i=1}^{n} \eta_i g_i p_i^\nu = 0 \qquad (3.18)$$

with g_i being the coupling of the graviton to particle i. So $\sum\limits_{i=1}^{n} g_i p_i^\nu$ plays the role of the "charge" and must be conserved. Only the *total* four-momentum can be conserved which means that all g_i have to be the same. These couplings may be identified with $\sqrt{8\pi G_N}$, with G_N being Newton's gravitation constant. This goes a long way towards showing that Einstein's *principle of equivalence* is a necessary consequence of Lorentz invariance as applied to massless particles of spin 2.
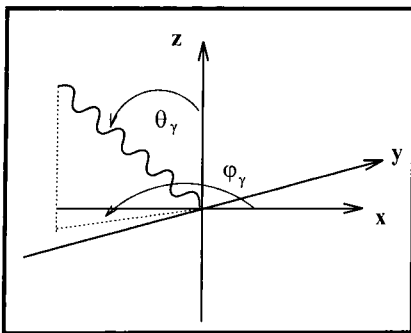
In the soft photon approximation we may parametrise the photon by its energy ω_γ, the polar angle θ_γ and the azimuthal angle ϕ_γ. As $\omega_\gamma/E_i \ll 1$ we may simply multiply the phase space $\omega_\gamma \, d\omega_\gamma \, d\Omega_{\vec{n}}(\theta_\gamma, \phi_\gamma)$ to the exact phase space of the residual contribution (without additional photon).

The differential cross section with an additional photon in the final state thus reads [Dok91, Dok93]

$$\frac{1}{\sigma_0} \frac{d^2\sigma}{d\omega_\gamma d\Omega_{\vec{n}}} = \frac{\alpha}{4\pi^2} \omega_\gamma \mathcal{F}^\gamma, \qquad (3.19)$$

with the antenna pattern $\mathcal{F}^\gamma$ defined in Eq. (3.9) and normalised to the tree level cross section σ_0 without additional photon.

3.1.2 Soft gluons

Emission of soft gluons off fermions can be formulated in complete analogy to soft–photon emission by introducing the strong coupling constant g_s and the SU(3) colour matrix T^a. Thus we derive for emission of a gluon off an incoming quark line
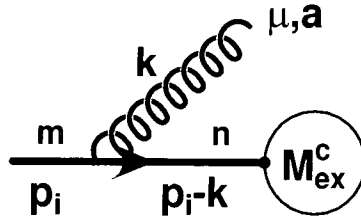
with the gluon vertex $V_{gff} = -ig_{\rm s}T^a_{mn}\gamma^\mu$

$$\left[i\frac{\not{p}_i - \not{k} + m_i}{(p_i - k)^2 - m_i^2}\right][-ig_{\rm s}T^a_{mn}\gamma^\mu]\,u(p_i) \times \mathcal{M}^c_{\rm ex} \xrightarrow{k \to 0} g_{\rm s}T^a_{mn}\left[-\frac{p_i^\mu}{p_i \cdot k}\right]u(p_i) \times \mathcal{M}^c_{\rm ex}. \quad (3.20)$$

A summary of rules is given in Appendix A.2. In analogy to Eq. (3.7) we find

$$\mathcal{M}^g(1, 2, \ldots, l \to (l+1, l+2, \ldots, n) + g) = g_{\rm s}\sum_{i=1}^n T^a_{kl}J^\mu_i \epsilon^{*a}_\mu(\lambda_i)\mathcal{M}^0, \quad (3.21)$$

with the current

$$J^\mu_i = \eta_i \frac{p^\mu_i}{p_i \cdot k} \quad (3.22)$$

(again $\eta_i = -1$ for incoming and $\eta_i = +1$ for outgoing external lines). The antenna pattern for emission off external fermions reads

$$\mathcal{F}^g = -\sum_{i,j}\mathcal{C}_{ij}J^\mu_i J_{\mu,j}, \quad (3.23)$$

where again we note $\epsilon^2 = -1$. The colour factors are denoted by $\mathcal{C}_{ij}$.

As an example we calculate the gluon antenna pattern for the production of massive quarks $e^-e^+ \to Q\bar{Q} + g(k)$. It is straightforward to write down the current (cf. Appendix A.2)

$$\sum_i J^\mu_i = \frac{p^\mu_Q}{p_Q \cdot k} - \frac{p^\mu_{\bar{Q}}}{p_{\bar{Q}} \cdot k}, \quad (3.24)$$

and thus

$$\sum_{i,j} J^\mu_i J_{\mu,j} = \frac{m^2_Q}{p_Q \cdot k} + \frac{m^2_Q}{p_{\bar{Q}} \cdot k} - 2[Q\bar{Q}]. \quad (3.25)$$

The colour factor reads

$$\boxed{\mathcal{C}_{Q\bar{Q}} = \sum_a T^a_{k_1 l}T^a_{lk_2} = C_{\rm F}\delta_{k_1 k_2}}.$$
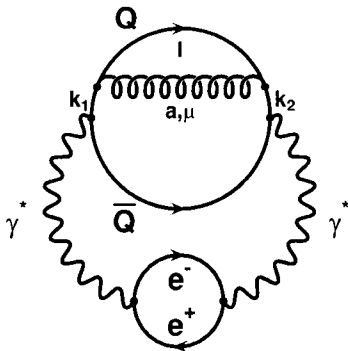
and thus

$$\mathcal{F}^g_{Q\bar{Q}} = C_\mathsf{F}\left\{2[Q\bar{Q}] - m_Q^2\left(\frac{1}{(p_Q\cdot k)^2} + \frac{1}{(p_{\bar{Q}}\cdot k)^2}\right)\right\}.$$ (3.26)

The differential cross section for above process reads [Jik91, KOS92]

$$\frac{1}{\sigma_0}\frac{\mathrm{d}^2\sigma}{\mathrm{d}\omega_g\mathrm{d}\Omega_{\vec{n}}} = \frac{\alpha_\mathsf{s}}{4\pi^2}\omega_g\,2C_\mathsf{F}\left\{[Q\bar{Q}] - \frac{m_Q^2}{2}\left(\frac{1}{(p_Q\cdot k)^2} + \frac{1}{(p_{\bar{Q}}\cdot k)^2}\right)\right\},$$ (3.27)

Important are now also soft–gluon emissions off gluons. We show an explicit example below, soft–gluon radiation off an incoming boson line.
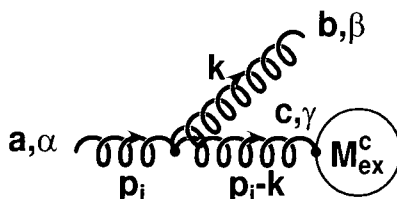
With the directions for the momenta as indicated above, we may readily write down the triple gluon vertex for this graph

$$V_{ggg} = ig_\mathsf{s}f^{abc}\left\{(k - 2p_i)^\beta g_{\alpha\gamma} + (p_i - 2k)^\alpha g_{\beta\gamma} + (k + p_i)^\gamma g_{\alpha\beta}\right\},$$ (3.28)

which reads in the soft limit

$$V_{ggg}^{\text{soft}} = ig_\mathsf{s}f^{abc}\left\{p_i^\gamma g_{\alpha\beta} + p_i^\alpha g_{\beta\gamma} - 2p_i^\beta g_{\alpha\gamma}\right\}.$$ (3.29)

Additionally we introduce a propagator for gluon c in the Feynman–'t Hooft gauge

$$\Pi_c = i\frac{g_{\gamma\mu}}{(p_i - k)^2} \xrightarrow{k\to 0} ig_{\gamma\mu}\frac{1}{-2p_i\cdot k}.$$ (3.30)

Collecting all results for additional emission of a soft gluon yields

$$\epsilon^\alpha\epsilon^{*\beta}V_{ggg}^{\text{soft}}\Pi_c^{\text{soft}} = -g_\mathsf{s}f^{abc}\left\{p_i^\mu\epsilon^\alpha\epsilon^{*\alpha} + p_i^\alpha\epsilon^\alpha\epsilon^{*\mu} - 2p_i^\beta\epsilon^{*\beta}\epsilon^\mu\right\}\frac{1}{-2p_i\cdot k}.$$

Two comments on above equation:

- we note that $p_i^\alpha\epsilon^\alpha = 0$ as p_i^α is the four momentum of the incoming gluon,

- the term including p_i^μ vanishes as well if contracted with the vertex of the process.

Therefore we find in complete analogy to Eq. (3.3)

$$\mathcal{M}_i^g = g_\mathsf{s}f^{abc}\boxed{-\frac{p_i^\beta}{p_i\cdot k}}\epsilon^{*\beta}(\lambda_1)\epsilon^\mu(\lambda_2) \times \left(\mathcal{M}_i^0\right)_\mu,$$ (3.31)

for above soft–gluon correction, i.e. we find the same eikonal factor by studying soft–gluon emission off bosons as we found for emission off quark lines. The antenna pattern, however, obtains a different colour factor of type
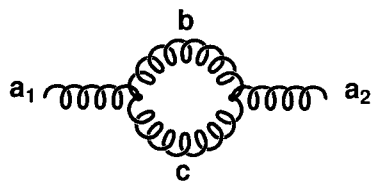
$$\sum_{b,c} f^{a_1 bc} f_{a_2 bc} = N_c \delta^{a_1}_{a_2}$$.

Again we refer to Appendix (A.2) for a summary of the rules for soft–gluon emission off gluon lines. Now we are in the position to write down the antenna pattern for the important Higgs signal process at the LHC with additional soft gluons in the final state, assuming massless particles.
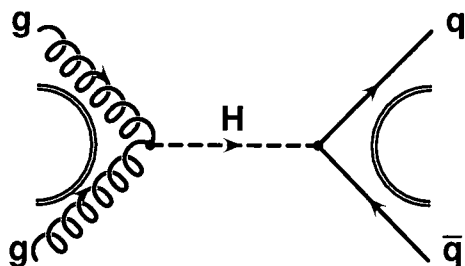
$$g(1)g(2) \to H \to q(3)\bar{q}(4) + g(k) .$$

There is only colour flow *in–between* the incoming particles (gg antenna) and *in–between* the outgoing particles ($q\bar{q}$ antenna). The colour neutral Higgs boson in the s–channel of above process *obstructs* colour flow between initial and final state. Thus the only contributing antennae are $[gg] = [12]$ and $[q\bar{q}] = [34]$. With the appropriate colour factors we readily obtain for massless quarks

$$\frac{1}{2}\mathcal{F}^g(gg \to H \to q\bar{q} + g) = N_c[12] + C_F[34] . \tag{3.32}$$

We shall study this process in detail in Section 3.3.

Again we can show that the formalism also holds for soft–gluon emission off *internal lines*, with an appropriate redefinition of the colour–charged currents.

3.2   Colour coherence and partonometry

During recent years many discussions have been provoked by the theoretical prediction of *coherent colour emission* and its exerimental study. Coherence effects are basic to any gauge theory. Two types of coherence phenomena occur in QCD jet dynamics

- intrajet coherence ,

- interjet coherence .

For a recent review of these topics see Ref. [KO97].

3.2.1 Intrajet coherence

This effect describes the character of a jet (hardness, opening angle) and finally closes the gap between the parton level interaction and the observed hadrons. Monte Carlo methods basically include intrajet coherence in an appropriate jet algorithm. A manifestation of intrajet phenomena is the *angular ordering*, i.e. the shrinkage of the emission angle in a parton cascade. Marchesini and Webber were the first to include this fact into a Monte Carlo program [MW84, Web84].

A simple example [Dok91] shall clarify the phenomenon. Imagine a relativistic e^+e^- pair produced in some reaction and the emission of an additional photon off either e^+ or e^-.
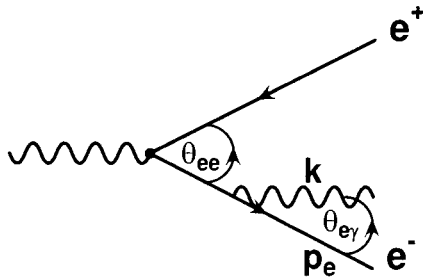
From the *uncertainty relation* we can estimate the *"lifetime"* of the e^- until it radiates off the photon

$$\Delta t_{\text{emission}} \simeq \frac{E^*}{(p_e + k)^2} \simeq \frac{E^*}{2E_e\omega_\gamma} \frac{1}{1 - \cos\theta_{e\gamma}} \simeq \frac{1}{\omega_\gamma\theta_{e\gamma}^2}. \tag{3.33}$$

During this time interval the e^+e^- system gained a transverse separation of

$$\rho_\perp^{e^+e^-} \simeq \theta_{ee}\Delta t_{\text{emission}} \xrightarrow{(3.33)} \frac{1}{\omega_\gamma\theta_{e\gamma}} \frac{\theta_{ee}}{\theta_{e\gamma}}. \tag{3.34}$$

But there is also an interpretation for $\omega_\gamma\theta_{e\gamma}$. As

$$\omega_\gamma\theta_{e\gamma} = |\vec{k}|\theta_{e\gamma} \simeq |\vec{k}_\perp|, \tag{3.35}$$

we may define $|\vec{k}_\perp| = (\lambda_\perp^\gamma)^{-1}$ as the inverse of the transversal wavelength of the emitted photon. If the separation $\rho_\perp^{e^+e^-}$ of the two emitters is <u>smaller</u> than $\lambda_\perp^\gamma$, then the photon is unable to resolve both emitters *individually* and thus probes the total electric charge of the e^+e^- system, which is zero. Thus for $\rho_\perp^{e^+e^-} < \lambda_\perp^\gamma$ there is a suppression of additional photon emission. This effect was first studied by A.E. Chudakov [Chu55]. Thus in order to have additional photon emission one needs

$$\rho_\perp^{e^+e^-} > \lambda_\perp^\gamma \xrightarrow{(3.34)} \theta_{e^+e^-} > \theta_{e\gamma}. \tag{3.36}$$

This simple exercise should give a basic idea how to prove angular ordering from first principles. For a further discussion of intrajet phenomena we refer to [Dok91]. A recent theoretical study of angular ordering in multiple hadroproduction can be found in [KKT96].

3.2.2 Interjet coherence

Throughout this thesis, however, we shall focus on *interjet coherence*, i.e. colour coherence *between* particle jets. We developed the theoretical framework using the technique of Feynman diagrams in the soft photon (gluon) approximation in Section 3.1. Here we shall discuss the physical interpretation and background. To follow the classical line [Azi85b] we shall study the processes

(a) $e^+e^- \to q\bar{q}\gamma$

(b) $e^+e^- \to q\bar{q}g$

with <u>additional</u> soft gluon radiation.

In the Feynman–'t Hooft gauge, we used throughout, the gluon propagator reads

$$\Pi_g = i\delta_{ab}\frac{d_{\mu\nu}}{k^2 + i\epsilon}, \tag{3.37}$$

$$d_{\mu\nu} = \sum_\lambda \epsilon_\mu(\lambda)\epsilon_\nu(\lambda) = -g_{\mu\nu}. \tag{3.38}$$

According to Eqs. (3.11,3.22,3.23) we can write the antenna pattern for additional soft gluon emission as

$$\begin{aligned}
\mathcal{F}^g &= \sum_{i,j} \mathcal{C}_{ij}\eta_i\eta_j \frac{p_i^\mu}{p_i \cdot k}\epsilon_\mu^*\epsilon_\nu \frac{p_j^\nu}{p_j \cdot k} \\
&= -\sum_{i,j} \mathcal{C}_{ij}\eta_i\eta_j \frac{p_i \cdot p_j}{(p_i \cdot k)(p_j \cdot k)} = -\sum_{i,j} \mathcal{C}_{ij}\eta_i\eta_j[ij].
\end{aligned} \tag{3.39}$$

where $\mathcal{C}_{ij}$ denote the colour factors.

As next step we want to discuss rules for the construction of the antenna pattern $\mathcal{F}^g$ in order to gain further insight into the whole mechanism of soft gluon emission. If the soft gluon connects two harder partons i and j then we might define an *interference term*

$$\mathcal{I}_{ij}^g = -\eta_i\eta_j \frac{p_i \cdot p_j}{(p_i \cdot k)(p_j \cdot k)}, \tag{3.40}$$

and if the soft gluon connects two identical particles we readily obtain a *self–energy term*

$$\mathcal{S}_i^g = \mathcal{I}_{ii}^g = -\frac{m_i^2}{(p_i \cdot k)^2}. \tag{3.41}$$

We note that $\eta_i^2 = 1$. Thus we may write the antenna pattern as

$$\mathcal{F}^g = \sum_{i,j} \mathcal{C}_{ij}\mathcal{I}_{ij}^g + \sum_i \mathcal{C}_i\mathcal{S}_i^g, \tag{3.42}$$

a sum of *interference* and *self–energy* terms.

Schematically the antenna pattern for the process $e^+e^- \to Q\bar{Q} + g(k)$ where Q represents massive quarks can be written as the sum of the four contributions
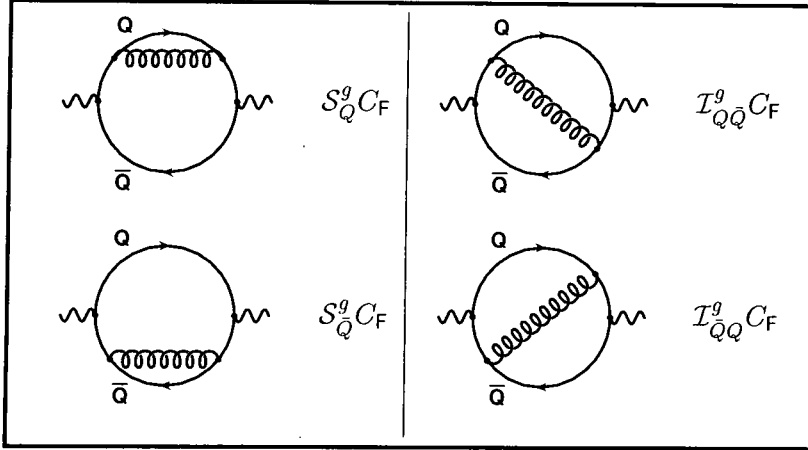
To calculate the colour factors we used the relation

$$T^a T^b = \frac{1}{2N_c} \delta^{ab} \mathbf{1} + \frac{1}{2} d_{abc} T^c + \frac{i}{2} f_{abc} T^c.$$

(3.43)

Collecting our results immediately yields the result

$$\mathcal{F}^g_{Q\bar{Q}} = C_F \left\{ 2[Q\bar{Q}] - m_Q^2 \left(\frac{1}{(p_Q \cdot k)^2} + \frac{1}{(p_{\bar{Q}} \cdot k)^2} \right) \right\}$$

(3.44)

we derived before (cf. (3.26)). For our process (a) it is straightforward to write down the corresponding antenna pattern. The additional γ in the final state does not influence the colour flow and thus we obtain for massless quarks

$$\mathcal{F}^g_{q\bar{q}\gamma} = 2 C_F [q\bar{q}].$$

(3.45)

In the Feynman–'t Hooft gauge the self–energy term becomes $\mathcal{S}^g = 0$ for massless quarks according to Eq. (3.41). The formalism for soft gluons should be *gauge independent*. To see this we shall formulate our antenna pattern in the most general *planar gauge*, i.e.

$$\tilde{d}_{\mu\nu} = -g_{\mu\nu} + \frac{k_\mu c_\nu + c_\mu k_\nu}{k \cdot c},$$

(3.46)

with an arbitrary gauge vector c^μ. In the planar gauge the interference term now reads

$$\tilde{\mathcal{I}}^g_{ij} = \eta_i \eta_j \frac{p_i \cdot k + p_j \cdot k - p_i \cdot p_j}{(p_i \cdot k)(p_j \cdot k)},$$

(3.47)

and for the self–energy term we find

$$\tilde{\mathcal{S}}^g_i = \tilde{\mathcal{I}}^g_{ii} = \frac{2}{p_i \cdot k} - \frac{m_i^2}{(p_i \cdot k)^2}.$$

(3.48)

Thus in the planar gauge the self–energy term receives a non–vanishing contribution even for massless particles. One can easily show that we obtain for the antenna pattern in the planar gauge

$$\tilde{\mathcal{F}}^g_{q\bar{q}\gamma} = C_F \left\{ \tilde{\mathcal{S}}^g_q + \tilde{\mathcal{S}}^g_{\bar{q}} + \tilde{\mathcal{I}}^g_{q\bar{q}} + \tilde{\mathcal{I}}^g_{\bar{q}q} \right\} = \mathcal{F}^g_{q\bar{q}\gamma},$$

(3.49)

i.e. exactly the same result as before due to cancellation of gauge dependent terms.

We shall now present the antenna pattern for process **(b)**, i.e. $e^+e^- \to q\bar{q}G + g$ with g being soft and G denoting a hard final state gluon. For the sake of simplicity we consider massless partons only. In this case we immediately see from Eq. (3.41) that

$$\mathcal{S}_q^g = \mathcal{S}_{\bar{q}}^g = \mathcal{S}_G^g = 0$$

in the Feynman–'t Hooft gauge. Therefore the antenna pattern for above process reduces to

$$\mathcal{F}_{q\bar{q}G}^g = \sum_{i,j \in \{q,\bar{q},G\}} \mathcal{C}_{ij} \, \mathcal{I}_{ij}^g \,. \tag{3.50}$$

We can schematically present the topological different graphs contributing to $\mathcal{I}_{Gq}, \mathcal{I}_{G\bar{q}}$ and $\mathcal{I}_{q\bar{q}}$.
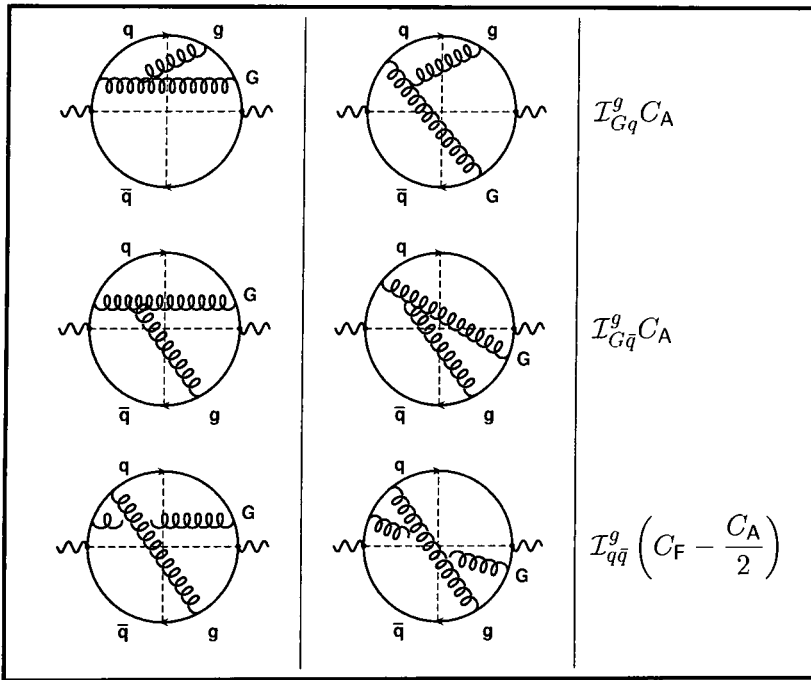
The colour factors indicate the soft gluon contribution *only*. Every graph has to be multiplied with C_F to obtain the full colour factors for both gluons. These are of course not all graphs that contribute, but they are the (colour) topological different ones. Using symmetry relations like $\mathcal{I}_{ij}^g = \mathcal{I}_{ji}^g$ and noting that $C_A = N_c$ we finally arrive at

$$
\begin{aligned}
\mathcal{F}_{q\bar{q}G}^g &= N_c[G\bar{q}] + N_c[Gq] + 2\left(C_F - \frac{C_A}{2}\right)[q\bar{q}] \\
&= N_c\left\{[Gq] + [G\bar{q}] - \frac{1}{N_c^2}[q\bar{q}]\right\} \,.
\end{aligned} \tag{3.51}
$$

Again we used the definition of $\mathcal{I}_{ij}^g$ as given in Eq. (3.40). Let us now study the difference of the two antenna patterns $\mathcal{F}_{q\bar{q}G}^g$ (3.51) and $\mathcal{F}_{q\bar{q}\gamma}^g$ (3.45), i.e. where the hard gluon G is replaced by a hard γ.

To do so, let us assume a completely symmetric configuration for the hard particles such that

$$\theta_{q\bar{q}} = \theta_{q\kappa} = \theta_{\bar{q}\kappa} = 120^\circ \,, \tag{3.52}$$

with $\kappa = G, \gamma$. This "*Mercedes*" type configuration [Dok91] is sketched below.
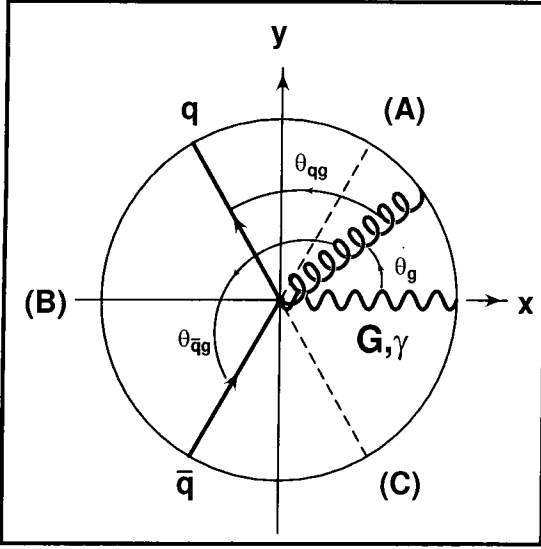
Assuming equal energies for all three hard particles, i.e. $E_Q = E_{\bar{q}} = E_\kappa = \frac{\sqrt{s}}{3}$, all antenna patterns of Eqs. (3.45, 3.51) can be written as

$$[ij] = \frac{1}{\omega_g^2} \frac{1 - \cos\theta_{ij}}{(1 - \cos\theta_{ig})(1 - \cos\theta_{jg})}$$

$$= \frac{1}{\omega_g^2} \frac{1 - \cos\theta_{ij}}{(1 - z_i)(1 - z_j)}, \quad (3.53)$$

with the angles as indicated in the figure and $z_i = \cos\theta_{ig}$. Thus the two antenna patterns can be written as

$$\omega_g^2 \mathcal{F}_{q\bar{q}\gamma}^g = 3C_F \frac{1}{(1 - z_q)(1 - z_{\bar{q}})}, \quad (3.54)$$

$$\omega_g^2 \mathcal{F}_{q\bar{q}G}^g = \frac{3}{2} N_c \left\{ \frac{1}{(1 - z_G)(1 - z_q)} + \frac{1}{(1 - z_G)(1 - z_{\bar{q}})} \right.$$

$$\left. - \frac{1}{N_c^2} \frac{1}{(1 - z_q)(1 - z_{\bar{q}})} \right\}. \quad (3.55)$$

The additional factor 3/2 results from assumption (3.52) and $1 - \cos\left(\frac{2}{3}\pi\right) = 3/2$.

In Fig. 3.1 we show the flow (antenna) pattern of the soft gluon g inside the plane of our symmetric configuration.

It is straightforward to present analytic values for the dimensionless ratio

$$\mathcal{R}_\gamma^G(\theta_g) = \frac{\mathcal{F}_{q\bar{q}G}^g(\theta_g)}{\mathcal{F}_{q\bar{q}\gamma}^g(\theta_g)} \quad (3.56)$$

inside the scattering plane. We shall focus on the three directions of the soft gluon indicated as (A), (B) and (C), i.e. centered between the outgoing particle directions

(A): centre of $[Gq]$ antenna, $\theta_g = 60°$,
(B): centre of $[q\bar{q}]$ antenna, $\theta_g = 180°$,
(C): centre of $[G\bar{q}]$ antenna, $\theta_g = 300°$.

After some algebra one finds

$$(A): \quad \mathcal{R}_\gamma^G(\theta_g = 60°) = \frac{5N_c^2 - 1}{N_c^2 - 1} = 5.5, \quad (3.57)$$

$$(B): \quad \mathcal{R}_\gamma^G(\theta_g = 180°) = \frac{N_c^2 - 2}{2(N_c^2 - 1)} \simeq 0.44, \quad (3.58)$$

$$(C): \quad \mathcal{R}_\gamma^G(\theta_g = 300°) = \frac{5N_c^2 - 1}{N_c^2 - 1} = 5.5. \quad (3.59)$$
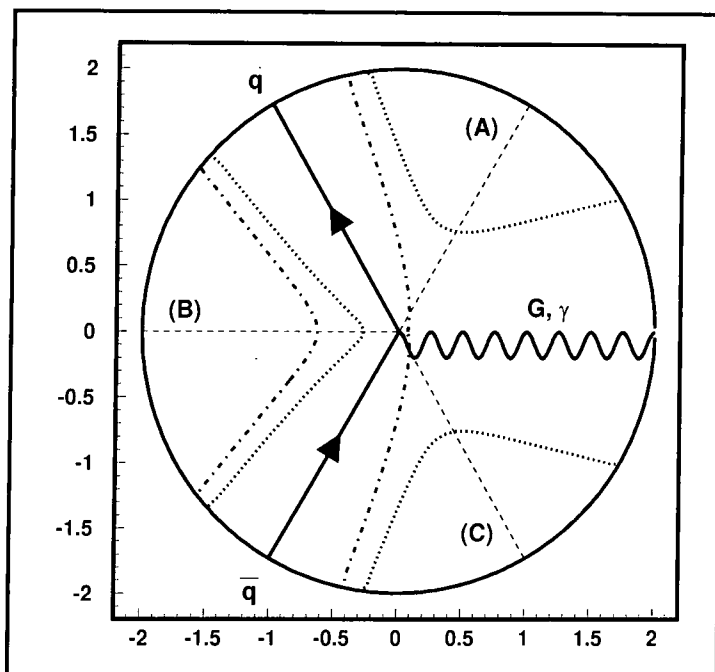
Figure 3.1: Polar plot of the flow patterns $\mathcal{F}^g_{q\bar{q}\gamma}$ (3.45) (dash–dotted line) and $\mathcal{F}^g_{q\bar{q}G}$ (3.51) (dotted line) inside the scattering plane for a soft gluon energy of $\omega_g = 5$ GeV.

It is easy to understand that the flow patterns of the soft gluon are symmetric to the axis defined by the hard G, γ in this symmetric configuration. The $q \leftrightarrow \bar{q}$ symmetry is due to the '*blindness*' of the soft gluon to discern between quark and antiquark.

We observe that replacing γ by a hard gluon G changes the flow pattern of the soft gluon quite essentially because the antenna element G now participates in the emission as well. However, contrary to naive intuition, this change does not only lead to the appearance of an additional particle flow in the G direction (due to the collinear singularity) but also changes the flow pattern opposite to the G direction, i.e. region (B). Fig. 3.1 illustrates that the particle flow in this direction appears to be *considerably lower* than in the photon case. The additional G reduces the flow to about 44% of the $q\bar{q}\gamma$ flow in this direction (3.58).

We note that Eqs. (3.45, 3.51) provide not only the planar picture, but the global three–dimensional pattern of particle flows. It is worth noting that the destructive interference proves to be strong enough to dump the particle flow in the direction opposite to G to even smaller values than that in the most kinematically *unfavourable* direction, which is transverse to the event plane ($\phi_g = 90°$). In the transverse direction we find

$$\frac{\mathcal{F}^g_{q\bar{q}G}(\phi_g = 90°)}{\mathcal{F}^g_{q\bar{q}G}(\theta_g = 180°, \phi_g = 0°)} = \frac{N_c + 2C_F}{2(4C_F - N_c)} \simeq 1.2 \,. \tag{3.60}$$

This is an impressive example of '*particle drag*' [Azi85a, Azi85b] by the hard gluon jet G in the $q\bar{q}$ sector inside the scattering plane. For the photon case one finds

$$\frac{\mathcal{F}^g_{q\bar{q}\gamma}(\phi_g = 90°)}{\mathcal{F}^g_{q\bar{q}\gamma}(\theta_g = 180°, \phi_g = 0°)} = \frac{1}{4} \,. \tag{3.61}$$

How to interpret the drag effect?

In the structure of $\mathcal{F}^{g}_{q\bar{q}G}$ of Eq. (3.51) we see that the $[q\bar{q}]$ antenna is strongly colour suppressed (factor $1/N_{c}^{2}$) and contributes with a relative minus sign. The remaining two antennae $[qG]$ and $[\bar{q}G]$ are independent and can be interpreted as boosted from their respective rest frames into the overall $q\bar{q}G$ c.m.s. frame [Azi85a, Azi85b]. The hard gluon can thus be treated as a quark–antiquark pair in the large–N_{c} approximation.
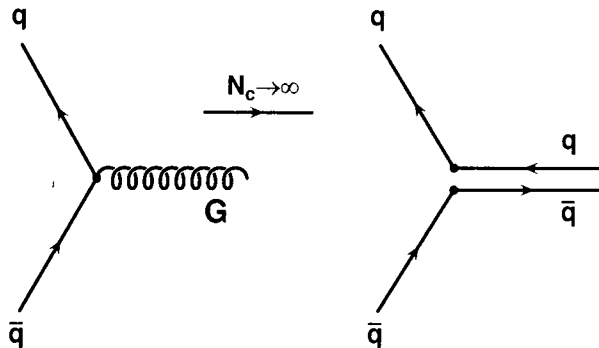
In this approximation each external quark line is uniquely connected to an antiquark line of the same colour, forming what is called a colourless $[q\bar{q}]$ antenna. In the general case, when calculating the resulting soft radiation pattern, one can only deal with a set of such colour–connected $q\bar{q}$ pairs because the interference between gluons emitted from non–colour–connected lines proves to by suppressed by powers of $1/N_{c}^{2}$ [Dok91].

The depletion of radiation in the $q\bar{q}$ sector due to the hard gluon G in the opposite direction is a direct consequence of *Lorentz boosts*. This explanation was originally employed to explain the *Lund string* model [AGS80, AGIS83], formulated by B. Anderson, G. Gustafson and T. Sjöstrand. In the string model particles are created from the breakup of a colour flux–tube, stretching from the quark to the gluon and from the gluon to the antiquark. There is no string piece spanned directly between the quark and antiquark. Therefore no particles are produced between q and $\bar{q}$, except by some minor 'leakage' from the qG and $\bar{q}G$ sectors.

Therefore:

The depletion is due to the colour-suppressed $[q\bar{q}]$ antenna in Eq. (3.51) as was pointed out by Yu.L. Dokshitzer, V.A. Khoze and S.I. Troyan . And this interpretation bases on a Lorentz boosted hard gluon which behaves like a $q\bar{q}$ pair in the large–N_{c} approximation. So, q and $\bar{q}$ are no longer colour connected, thus soft gluon emission is suppressed in this sector. The hard gluon '*drags*' the colour flow out of the $q\bar{q}$ valley. This drag effect explains the Lund string.

or in other words: the Lund string scenario reproduces QCD particle flows in the large–N_{c} limit.

The *string effect* is a non–perturbative, the *drag effect* (interjet coherence) a purely perturbative phenomenon, but both models respect the right colour flow topology.

Local Parton Hadron Duality (LPHD)

Describing the colour flow correctly in a given process directly leads to the description of hadronisation. Important is the link between the angular distribution of the produced

hadrons with respect to the angular distribution of the (soft) partonic flow pattern. The Lund string has been, e.g., implemented into the Monte Carlo programs JETSET, PYTHIA and LEPTO.

The LPHD [Azi85a] states that the angular distribution of soft gluon radiation equals the angular distribution of soft hadrons.

Experimental test of colour coherence

The first experimental studies of the interjet colour coherence in three jet events were successfully performed about ten years ago at PEP/PETRA energies [TPC86, JADE88]. More recently colour coherence has been successfully studied at LEP1 [DEL96, L3.95, OPAL95]. They compared the colour flow in the $q\bar{q}$ valley in three jet events $q\bar{q}\gamma$ and $q\bar{q}G$ which we studied as an ideal test case.
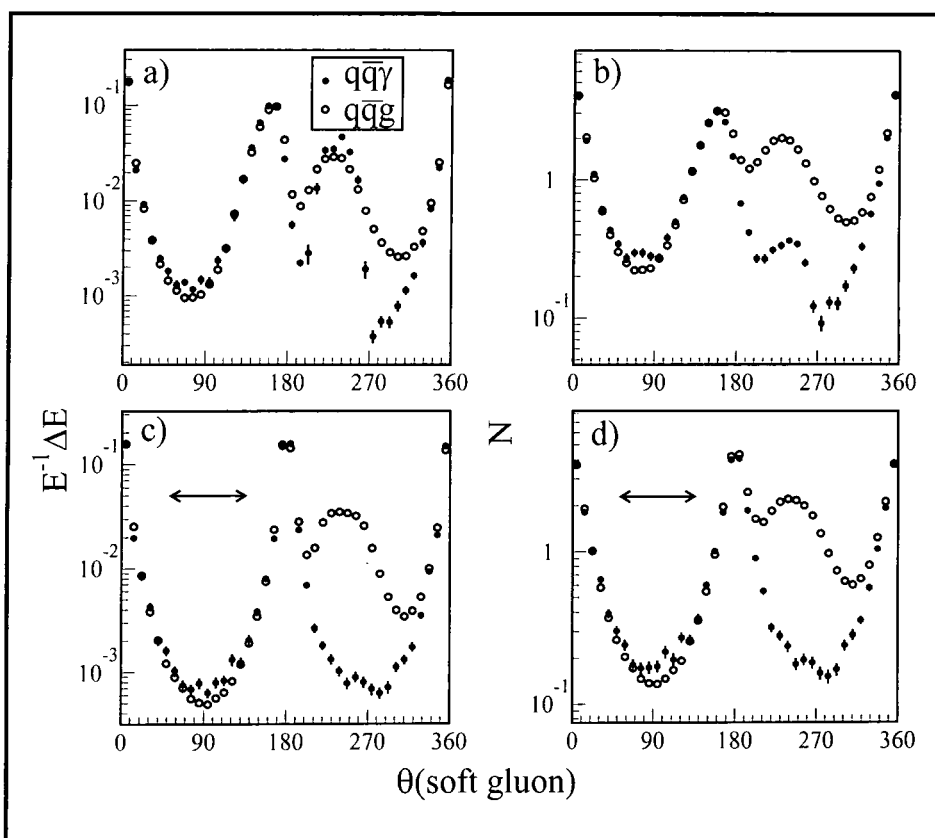
Figure 3.2: Distribution of the normalised energy flow (a) and particle flow (b) in the laboratory frame. (c) and (d) are the corresponding distributions in the $q\bar{q}$ c.m.s. frame, after the photon has been removed. The arrows show the angular region of the $q\bar{q}$ valley where Eq. (3.58) can be verified. Taken from Ref. (3.5).

In Fig 3.2 we present the results of one of the studies [L3.95]. The quark is located at angle $0°$ in this figure, the antiquark at $\approx 170°$. From Figs. 3.2(a,b) the depletion of radiation in the $q\bar{q}$ sector, i.e. $0°$–$170°$ is quite obvious. All LEP collaborations verify an approximate 40% depletion of radiation in $q\bar{q}G$ events compared to $q\bar{q}\gamma$ events in this

region.

Same results are reported from the DELPHI [DEL96] and OPAL [OPAL95] collaborations.

But also at hadron–hadron colliders colour coherence has been studied in high-$p_\perp$ processes. First results from the CDF [CDF94] and the D∅ collaboration [D∅.95] look rather promising. The studies in the $p\bar{p} \to$ 3jet $+ X$ events of the spatial correlations between soft and leading jets in multi–jet events have clearly demonstrated the presence of initial-to-final state interference effects in $p\bar{p}$ interactions. The D∅ data indicate [D∅.95], that the observed coherence phenomena are in agreement with the tree–level parton level calculations adopted throughout this chapter.

Recently the first data on W+jet production from D∅ have been presented [D∅.97]. The hadronic antenna patterns for this process are entirely analogous to that in $e^+e^- \to q\bar{q}G$. The colour coherence effects are clearly seen in this process. Theoretical calculations were performed in Refs. [KS97b, APS98] using the formalism of this chapter.

At HERA a comparative study of jet properties produced in different reactions could be a powerful proof for colour coherence. At the time when this thesis was written, there was no such direct search for colour coherence from HERA available.

3.3   Hadronic radiation patterns for Higgs production at hadron colliders

As we discussed in Section 3.2 the distribution of soft hadrons or jets accompanying energetic final–state particles in hard scattering processes is governed by the underlying colour dynamics at short distances. The soft hadrons paint the colour portrait of these dynamics, and can therefore act as a 'partonometer' (cf. [DKT87, Dok91, DKS92, MW90]). Since signal and background processes at hadron colliders can have very different colour structures (compare for example the s–channel colour singlet process $q\bar{q} \to Z' \to q'\bar{q}'$ with the colour octet process $q\bar{q} \to g^* \to q'\bar{q}'$), the distribution of accompanying soft hadronic radiation in the events can provide a useful additional diagnostic tool for identifying new physics processes. As we discussed in Section 3.2 because of the property of Local Parton Hadron Duality the distribution of soft hadrons can be well described by the amplitudes for producing a single additional soft gluon. These take the form of a soft antenna pattern distribution multiplying the leading-order hard scattering matrix element.

One of the most important physics goals of the CERN LHC pp collider is the discovery of the Higgs boson [LHC90]. Many scenarios, corresponding to different production and decay channels, have been investigated, see for example the studies reported by the ATLAS [Atlas94] and CMS [CMS94] groups. While final states containing leptons and photons are relatively background free, they generally have very small branching ratios. In contrast, the more probable decay channels involving (heavy) quarks have large QCD backgrounds. The question naturally arises whether hadronic radiation patterns could help distinguish such signals from backgrounds. We have in mind the following type of scenario. Suppose an invariant mass peak is observed in a sample of (tagged) $b\bar{b}$ events. If these correspond to Higgs production, then the distribution of accompanying

soft radiation in the event[3] will look very different from that expected in background QCD production of $b\bar{b}$ pairs. One could imagine, for example, comparing the radiation patterns 'on and off resonance'.

In this study we will consider the hadronic radiation patterns for two of the standard Higgs processes at LHC: direct production $gg \to H \to b\bar{b}$ and associated production $q\bar{q}' \to WH \to \ell\nu_\ell b\bar{b}$. Although the non–zero b–quark mass is largely irrelevant when computing the radiation patterns, we will also consider the case when the final–state quark mass is large, so that our analysis can also be applied for example to $H \to t\bar{t}$. This Higgs analysis is a natural extension of the theoretical studies of Ref. [EKS97], where the radiation patterns for Z' in $p\bar{p}$ collisions were calculated and shown to be different from those of the QCD backgrounds.

The analysis presented here should be regarded as a 'first look' at the possibilities offered by hadronic radiation patterns in searching for the Higgs. Of course ultimately there is no substitute for a detailed Monte Carlo study including detector effects. However the results presented here indicate that the effects can be potentially large, and therefore that more detailed studies are definitely worthwhile.

The study is organised as follows. In the following section we consider direct production and $q\bar{q}$ decay of the Higgs boson, first for massless and then for massive quarks. Then we extend the analysis to associated production and finally present our conclusions.

3.3.1 Hadronic radiation patterns for signal and background processes

We begin by considering the hadronic radiation patterns for the signal $g(1)g(2) \to H \to q(3)\bar{q}(4) + g(k)$ and background $g(1)g(2) \to q(3)\bar{q}(4) + g(k)$ production of a massless $q\bar{q}$ pair. The impact of non–zero quark masses will be considered later. The radiation pattern is defined as the ratio of the $2 \to 3$ and $2 \to 2$ matrix elements using the soft–gluon approximation for the former. The dependence on the soft gluon momentum k then enters via the eikonal factors ('antennae') defined in Eq. (3.11).

For the QCD background process we have

$$
\frac{1}{g_s^6}|\overline{\mathcal{M}}_3|^2(gg \to q\bar{q} + g) = \frac{1}{2}(t^2 + u^2)\left[\left(1 - \frac{1}{N_c^2}\right)\frac{1}{tu} - \frac{2}{s^2}\right]\left\{\frac{N_c}{C_F}[12] + [34]\right\}
$$
$$
- \frac{1}{8}(t^2 + u^2)\left[\left(1 - \frac{2}{N_c^2}\right)\frac{1}{tu} - \frac{2}{s^2}\right]\left\{\frac{N_c}{C_F}[12;34]\right\}
$$
$$
+ \frac{1}{8}(t^2 - u^2)\left[\frac{1}{tu} - \frac{2}{s^2}\right]\left\{\frac{N_c}{C_F}([14] + [23] - [13] - [24])\right\}, \tag{3.62}
$$

with

$$
[ij; kl] = 2[ij] + 2[kl] - [ik] - [il] - [jk] - [jl]. \tag{3.63}
$$

This is to be normalised by the matrix element for the leading–order scattering process $gg \to q\bar{q}$:

$$
\frac{1}{g_s^4}|\overline{\mathcal{M}}_2|^2(gg \to q\bar{q}) = \frac{1}{2}(t^2 + u^2)\left[\frac{1}{N_c}\frac{1}{tu} - \frac{1}{C_F}\frac{2}{s^2}\right]. \tag{3.64}
$$

The antenna pattern is then

$$
\mathcal{F}^g_{\text{QCD}} = g_s^{-2}\frac{|\overline{\mathcal{M}}_3|^2(gg \to q\bar{q} + g)}{|\overline{\mathcal{M}}_2|^2(gg \to q\bar{q})}. \tag{3.65}
$$

---

[3]We take this to mean the angular distribution of hadrons or 'minijets' with energies of at most a few GeV, well separated from the beam and final–state energetic jet directions.

Note that because of the non–trivial colour structure of the leading–order Feynman diagrams, see Figs. 3.3(a,b), there is no simple factorisation of the eikonal factors. This is in contrast to the signal (Higgs) process, for which

$$\mathcal{F}_H^g = g_s^{-2} \frac{|\overline{\mathcal{M}}_3|^2 (gg \xrightarrow{H} q\bar{q} + g)}{|\overline{\mathcal{M}}_2|^2 (gg \xrightarrow{H} q\bar{q})} = 2N_c[12] + 2C_F[34], \qquad (3.66)$$

the result we already derived in Eq. (3.32).
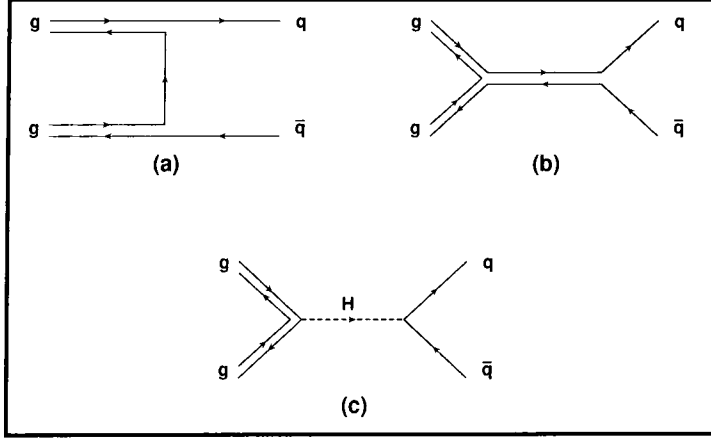
Figure 3.3: The colour flow diagrams for the processes $gg \to q\bar{q} + g$ and $gg \to H \to q\bar{q} + g$.

The two terms correspond to gluon radiation off the initial state gluons (colour factor N_c) and the final–state quarks (colour factor C_F). With colour–singlet exchange in the s–channel (Fig. 3.3(c)), there is no interference between the initial– and final–state emission, in contrast to the QCD background antenna pattern (cf. Section 3.1.2). It is this feature which will give rise to significant quantitative differences between the radiation patterns.

The next step is to define the kinematics. The four momenta are labelled by

$$g(p_1) + g(p_2) \to q(p_3) + \bar{q}(p_4) + g(k), \qquad (3.67)$$

where the gluon is assumed soft relative to the two large–E_T partons q and $\bar{q}$, i.e. $k_T \ll E_T$. Ignoring the gluon momentum in the energy–momentum constraints, working in the subprocess centre–of–mass frame, and using the notation $p^\mu = (E, p_x, p_y, p_z)$, we have

$$\begin{aligned}
p_1^\mu &= (E_T \cosh\eta, 0, 0, E_T \cosh\eta), \\
p_2^\mu &= (E_T \cosh\eta, 0, 0, -E_T \cosh\eta), \\
p_3^\mu &= (E_T \cosh\eta, 0, E_T, E_T \sinh\eta), \\
p_4^\mu &= (E_T \cosh\eta, 0, -E_T, -E_T \sinh\eta), \\
k^\mu &= (k_T \cosh(\eta + \Delta\eta), k_T \sin\Delta\phi, k_T \cos\Delta\phi, k_T \sinh(\eta + \Delta\eta)). \quad (3.68)
\end{aligned}$$

This is the appropriate form for studying the angular distribution of the soft gluon jet relative to the large–E_T jet 3, the separation between these being parametrised by $\Delta\eta$ and $\Delta\phi$. In terms of these variables, the soft gluon phase space is

$$\frac{1}{(2\pi)^3} \frac{d^3 k}{2\omega_g} = \frac{1}{16\pi^3} k_T dk_T \, d\Delta\eta \, d\Delta\phi. \qquad (3.69)$$

We will be particularly interested in the shape of the radiation pattern as a function of the variables $\Delta\eta$ and $\Delta\phi$. Note that the direction of the soft gluon is measured with respect to the p_3 jet. Thus for massless $2 \to 2$ scattering, collinear singularities are located at $\Delta\eta = 0$, $\Delta\phi = 0$ and $\Delta\eta = -2\eta$, $\Delta\phi = \pi$.
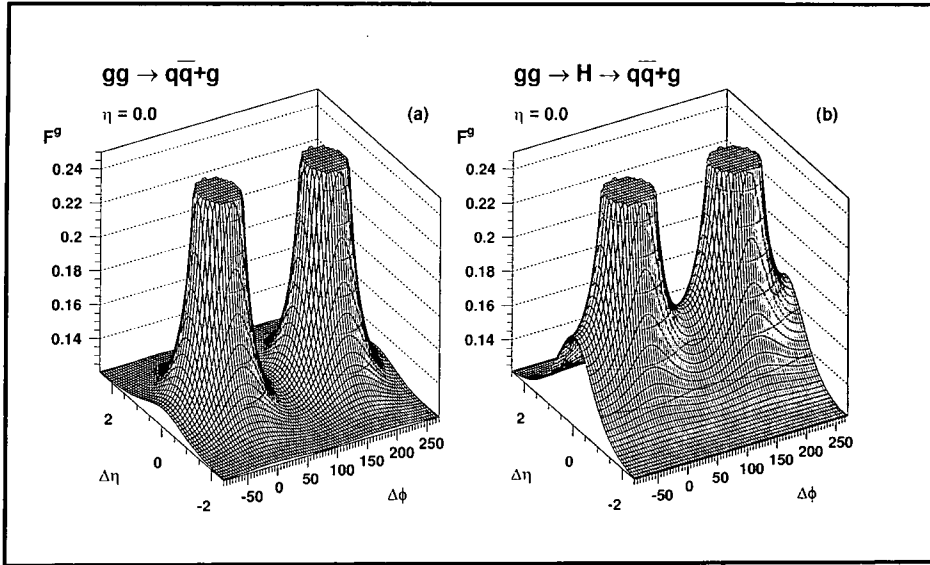
Figure 3.4: The antenna patterns $\mathcal{F}^g_{\mathrm{QCD}}$ of Eq. (3.65) and $\mathcal{F}^g_H = 2N_c[12] + 2C_F[34]$ of Eq. (3.66) for the processes $gg \to q\bar{q}+g$ and $gg \to H \to q\bar{q}+g$, with $\eta = 0$ and $k_T = 10$ GeV.

We first study the QCD and Higgs radiation patterns for central $q\bar{q}$ jets, i.e. $\eta = 0$. Using the kinematics of Eq. (3.68) with $\eta = 0$, Eq. (3.66) gives

$$\mathcal{F}^g_H\big|_{\eta=0} = \frac{4}{k_T^2} \frac{N_c \left(\cosh^2(\Delta\eta) - \cos^2(\Delta\phi)\right) + C_F}{\cosh^2(\Delta\eta) - \cos^2(\Delta\phi)} , \tag{3.70}$$

and

$$\mathcal{F}^g_{\mathrm{QCD}}\big|_{\eta=0} = \frac{2}{k_T^2} \frac{N_c^3 \left(2\cosh^2(\Delta\eta) - \cos^2(\Delta\phi) - 1\right)}{N_c \left\{ (4C_F - N_c) \left(\cosh^2(\Delta\eta) - \cos^2(\Delta\phi)\right) \right\}}$$
$$+ \frac{4}{k_T^2} \frac{2N_c \left(1 - \cosh^2(\Delta\eta)\right) + C_F \left(N_c^2 - 2\right)}{N_c \left\{ (4C_F - N_c) \left(\cosh^2(\Delta\eta) - \cos^2(\Delta\phi)\right) \right\}} . \tag{3.71}$$

Note that the radiation patterns are independent of E_T. Fig. 3.4 shows the dependence $\mathcal{F}^g_H$ and $\mathcal{F}^g_{\mathrm{QCD}}$ on $\Delta\eta$ and $\Delta\phi$. It is straightforward to show that the patterns are identical close to the beam direction,

$$\lim_{|\Delta\eta|\to\infty} \mathcal{F}^g_{H,\mathrm{QCD}} = \frac{4}{k_T^2} N_c , \tag{3.72}$$

independent of $\Delta\phi$, and close to the directions of the final state quarks,

$$\lim_{\Delta\eta,\Delta\phi\to 0} \mathcal{F}^g_{H,\mathrm{QCD}} \to \frac{4C_F}{k_T^2} \frac{1}{\cosh^2(\Delta\eta) - \cos^2(\Delta\phi)} . \tag{3.73}$$

The main difference arises from the amount of radiation *between* the final-state quark jets (*cf.* Section 3.2).
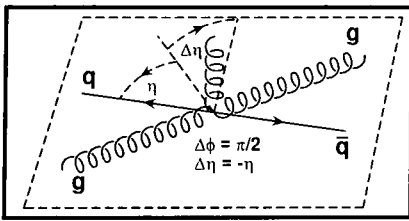
To study this further we consider the distributions at the symmetric point $\mathcal{P}_c$ located at ($\Delta\eta = 0, \Delta\phi = \pi/2$). This corresponds to soft gluon radiation perpendicular to the plane of the $gg \to q\bar{q}$ scattering and in the transverse direction, see figure on the left hand side.

Again using the kinematics of Eq. (3.68), we find for the QCD background process

$$\mathcal{F}^g_{\text{QCD}}|_{\eta=0}(\mathcal{P}_c) = \frac{2}{k_T^2} \frac{2C_{\mathsf{F}}(N_c^2 - 2) + N_c^3}{N_c(4C_{\mathsf{F}} - N_c)} \sim 0.1304 \,, \tag{3.74}$$

where the numerical value corresponds to $N_c = 3$ and $k_T = 10$ GeV.

In contrast, for the Higgs signal process we find

$$\mathcal{F}^g_H|_{\eta=0}(\mathcal{P}_c) = \frac{4}{k_T^2} \left(C_{\mathsf{F}} + N_c\right) \sim 0.1733 \,. \tag{3.75}$$

There is therefore approximately $4/3$ more radiation between the jets for the Higgs production process. This is due to the absence of a colour string connecting the final state quarks in the QCD background process, see Fig. 3.3 and Section 3.2.

The QCD background process does, however, have colour strings connecting the initial- and final-state quarks, and this leads to an enhancement of soft radiation between the jets *in the plane of the scattering*. We can illustrate this by considering the radiation patterns around the direction of the final state quark. In particular we introduce (as in [EKS97]) the variables $(\Delta R, \beta)$, where

$$\Delta\eta = \Delta R \cos\beta \,, \quad \Delta\phi = \Delta R \sin\beta \,. \tag{3.76}$$

For fixed $\Delta R > 0$, varying β between 0 and 2π describes a circle in the $(\Delta\eta, \Delta\phi)$ plane around the quark direction. In addition, if we fix $\Delta R = \pi/2$ then the symmetric point $\mathcal{P}_c$ corresponds to $\beta = \pi/2$ (or equivalently $3\pi/2$), and the soft gluon is in the $2 \to 2$ scattering plane for $\beta = 0, \pi$. Figure 3.5 shows the dependence of the radiation patterns $\mathcal{F}^g_{H,\text{QCD}}$ on β for $\Delta R = \pi/2$, as before for $\eta = 0$ final-state quarks. At $\beta = \pi/2$ we have $\mathcal{F}^g_H > \mathcal{F}^g_{\text{QCD}}$, as discussed above, whereas at $\beta = 0, \pi$ we have $\mathcal{F}^g_{\text{QCD}} = \mathcal{F}^g_H$.[4] The *shape* of the β distribution therefore provides a powerful discriminator between signal and background.

How does the inter–jet radiation enhancement depend on the jet rapidity η? Again we consider the symmetric point located at $\mathcal{P}_c = (\Delta\eta = -\eta, \Delta\phi = \pi/2)$. At this point $\mathcal{F}^g_H$ is completely independent of η,

$$\mathcal{F}^g_H(\mathcal{P}_c) = \frac{4}{k_T^2} \left(N_{\mathsf{c}} + C_{\mathsf{F}}\right). \tag{3.77}$$

which follows immediately from Eq. (3.66) since $[12] = [34] = 2/k_T^2$ at $\mathcal{P}_c$. The result is slightly more complicated for $\mathcal{F}^g_{\text{QCD}}$. Here we find

$$\mathcal{F}^g_{\text{QCD}}(\mathcal{P}_c) = \frac{2}{k_T^2} \frac{1}{N_c} \frac{4C_{\mathsf{F}} \cosh^2(\eta) \left(N_c^2 - 1\right) + N_c^2 \left(N_{\mathsf{c}} - 2C_{\mathsf{F}}\right)}{4C_{\mathsf{F}} \cosh^2(\eta) - N_c} \,. \tag{3.78}$$

---

[4]In fact, the equality of the distributions at $\beta = 0, \pi$ is true for all ΔR.
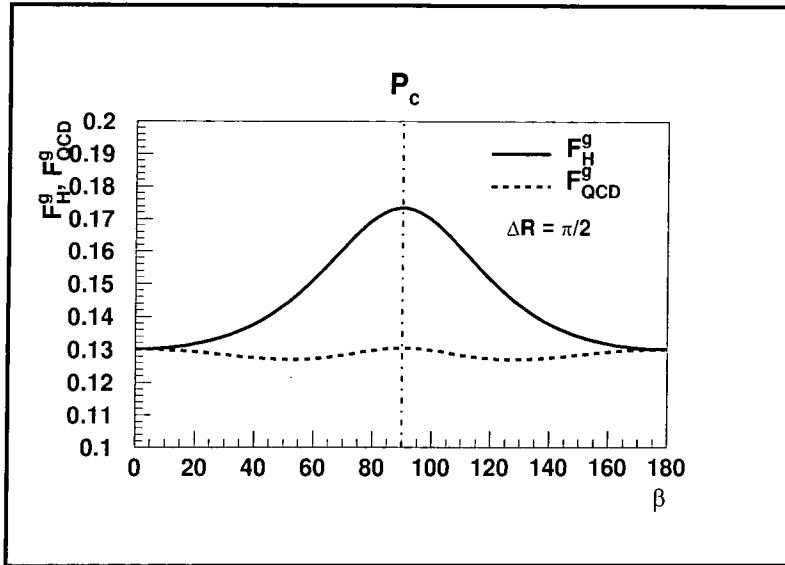
Figure 3.5: The dependence of the radiation patterns $\mathcal{F}_H^g$ and $\mathcal{F}_{\rm QCD}^g$ on the angular variable β defined in Eq. (3.76).

At $\mathcal{P}_c$, $\mathcal{F}_{\rm QCD}^g$ is maximal for $\eta = 0$ with the value given in Eq. (3.74). As $|\eta| \to \infty$ $\mathcal{F}_{\rm QCD}^g$ approaches its minimum value,

$$\lim_{|\eta| \to \infty} \mathcal{F}_{\rm QCD}^g(\mathcal{P}_c) = \frac{4}{k_T^2} C_{\rm F}. \tag{3.79}$$

Note that in the large–η limit the ratio $\overline{\mathcal{R}} \equiv \mathcal{F}_H^g / \mathcal{F}_{\rm QCD}^g$ at $\mathcal{P}_c$ is significantly larger than its value at $\eta = 0$:

$$\overline{\mathcal{R}}(\eta = 0, \mathcal{P}_c) = \frac{3N_c^4 - 7N_c^2 + 2}{2N_c^4 - 3N_c^2 + 2} = 1.3285,$$

$$\overline{\mathcal{R}}(|\eta| \to \infty, \mathcal{P}_c) = \frac{3N_c^2 - 1}{N_c^2 - 1} = 3.25. \tag{3.80}$$

In other words, the difference in the signal and background radiation patterns at the symmetric inter–jet point increases with increasing jet rapidities. Note that the large–N_c limits of the ratios in Eq. (3.80) are simply $3/2$ and 3, and also that $\overline{\mathcal{R}}(\eta = 0, \mathcal{P}_c) = 1$ for $N_c = 2$. This is illustrated in Fig. 3.6 which shows the dependence of $\overline{\mathcal{R}}$ evaluated at $\mathcal{P}_c$ on η and N_c.

Massive quarks

So far we have only considered massless quarks. In fact for $H \to b\bar{b}$, with $m_b \ll M_H$, this should be an excellent approximation, since the soft gluon only 'feels' the finite b–quark mass very close to the jet axis, where our analysis does not in any case apply. Far from the jet direction, and in particular at the symmetric point $\mathcal{P}_c$, the effect of the non–zero b mass will be negligible. The situation is however very different for the case of $H \to t\bar{t}$,
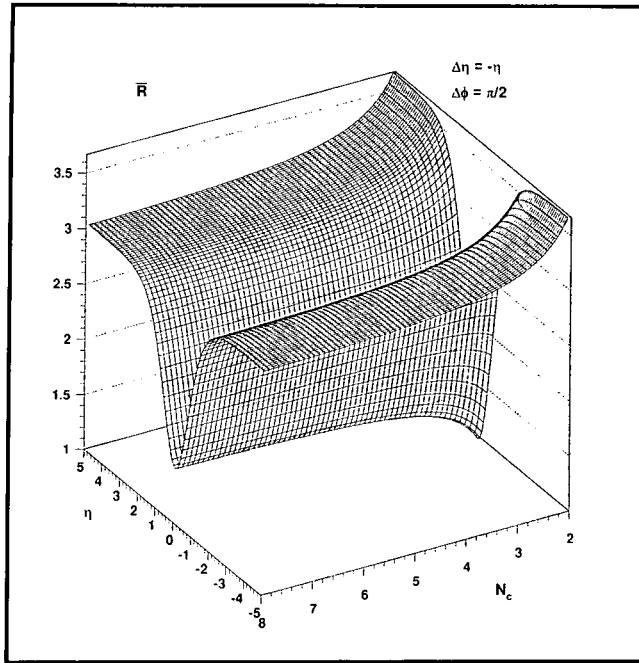
Figure 3.6: The ratio $\overline{\mathcal{R}} = \mathcal{F}_H^g / \mathcal{F}_{\mathrm{QCD}}^g$ as a function of N_c and η at the symmetric inter–jet point $\Delta\eta = -\eta$ and $\Delta\phi = \pi/2$.

where $M_H \gtrsim 2m_t$. Now mass effects *are* important in the radiation pattern, as we shall demonstrate below.

If we allow a finite mass for the produced quarks then the kinematics have to be changed accordingly. Thus we replace the kinematics of Eq. (3.68) by

$$
\begin{aligned}
p_1^\mu &= (E_Q, 0, 0, E_Q), \\
p_2^\mu &= (E_Q, 0, 0, -E_Q), \\
p_3^\mu &= (E_Q, 0, p_T, E_Q \tanh\eta), \\
p_4^\mu &= (E_Q, 0, -p_T, -E_Q \tanh\eta), \\
k^\mu &= k_T(\cosh(\eta + \Delta\eta), \sin\Delta\phi, \cos\Delta\phi, \sinh(\eta + \Delta\eta)),
\end{aligned} \tag{3.81}
$$

i.e. we denote the energy of the quark jets by E_Q and their transverse momentum by p_T. Thus

$$
E_Q = \cosh(\eta)\sqrt{m_Q^2 + p_T^2}. \tag{3.82}
$$

We again work in the subprocess centre–of–mass frame. It is convenient to introduce the dimensionless variable Θ as the ratio of the final–state quark mass m_Q to its energy

$$
\Theta = \frac{m_Q}{E_Q}. \tag{3.83}
$$

For non–zero m_Q the antenna patterns receive additional contributions. For example, the antenna pattern of $\mathcal{F}_H^g$ of Eq. (3.66) becomes

$$
\mathcal{F}_{H,\Theta}^g = \mathcal{F}_H^g - C_F[33] - C_F[44], \tag{3.84}
$$

where the massive equivalents of $\mathcal{F}_H^g$ and $\mathcal{F}_{\mathrm{QCD}}^g$ are labelled with the suffix Θ. One effect of the additional terms is to cancel the final–state collinear singularities, leading instead to the well–known *dead cone* [DKT91] phenomenon. Using the results of Ref. [KOS94], we obtain a somewhat more complicated expression for the massive equivalent to $\mathcal{F}_{\mathrm{QCD}}^g$:

$$
\begin{aligned}
\mathcal{F}_{\mathrm{QCD},\Theta}^g &= (2N_c - 2C_F + 2\mathcal{Y})\,[12] + (C_F - \mathcal{X} - \mathcal{Y})\,\{[13] + [24]\} \\
&+ (C_F + \mathcal{X} - \mathcal{Y})\,\{[14] + [23]\} + 2\mathcal{Y}[34] - C_F[33] - C_F[44],
\end{aligned} \tag{3.85}
$$

with

$$
\begin{aligned}
\mathcal{X} &= \frac{N_c^2}{4C_F}\left[(1+2\mu)\left(\frac{1}{U} - \frac{1}{T}\right) - \mu^2\left(\frac{1}{U^2} - \frac{1}{T^2}\right) + 2(U - T)\right] \\
&\times \left[\frac{1}{UT} - \frac{N_c}{C_F}\right]^{-1}\left[T^2 + U^2 + 2\mu - \frac{\mu^2}{UT}\right]^{-1},
\end{aligned} \tag{3.86}
$$

and

$$
\mathcal{Y} = \frac{1}{4C_F}\left[\frac{1}{N_c^2 UT} + 2\right]\left[\frac{1}{UT} - \frac{N_c}{C_F}\right]^{-1}. \tag{3.87}
$$

The variables T, U and μ are defined as

$$
T = \frac{p_1 \cdot p_3}{p_1 \cdot p_2}, \qquad U = \frac{p_1 \cdot p_4}{p_1 \cdot p_2}, \qquad \mu = \frac{m_Q^2}{p_1 \cdot p_2}. \tag{3.88}
$$

It is straightforward to show that the massless results are recovered in the limit $m_Q(\Theta) \to 0$.

Threshold behaviour ($\Theta = 1$)

We first study the behaviour of the radiation patterns $\mathcal{F}_{\mathrm{QCD},\Theta}^g$ and $\mathcal{F}_{H,\Theta}^g$ in the threshold limit in which $m_Q = E_Q = M_H/2$, i.e. $\Theta = 1$. In fact setting $\eta = 0$ we can readily derive the general expressions for the antennae for any value of Θ. Figures 3.7 and 3.8 show the radiation patterns for various values of Θ near and at threshold.

Notice how the strong peaking structure seen in the massless case (Fig. 3.4) disappears as the threshold is approached. In fact for $\Theta = 1$, the patterns do not depend on $\Delta\phi$ at all. This can be seen from the analytic results. First, for $\Theta = 1$ we have $[34] = [33] = [44]$ and so, from Eq. (3.66),

$$
\mathcal{F}_{H,\Theta=1}^g = 2N_c[12] = \frac{4}{k_T^2}N_c, \tag{3.89}
$$

independent of $\Delta\eta$ and $\Delta\phi$, see Fig. 3.8(d).

For $\mathcal{F}_{\mathrm{QCD},\Theta}^g$ at threshold, we first note from (3.88) that $T = U = \mu = \frac{1}{2}$ and thus

$$
\mathcal{X}_1 = 0, \qquad \mathcal{Y}_1 = \frac{2 + N_c^2}{2N_c^2(4C_F - N_c)}. \tag{3.90}
$$

From Eq. (3.85) we then have

$$
\begin{aligned}
\mathcal{F}_{\mathrm{QCD},\Theta=1}^g &= 2\,(N_c - C_F + \mathcal{Y}_1)\,[12] \\
&+ (C_F - \mathcal{Y}_1)\,\{[13] + [24] + [14] + [23]\} + 2(\mathcal{Y}_1 - C_F)[34] \\
&= \frac{2}{k_T^2}\left(2N_c - \frac{C_F - \mathcal{Y}_1}{\cosh^2(\Delta\eta)}\right), \tag{3.91}
\end{aligned}
$$
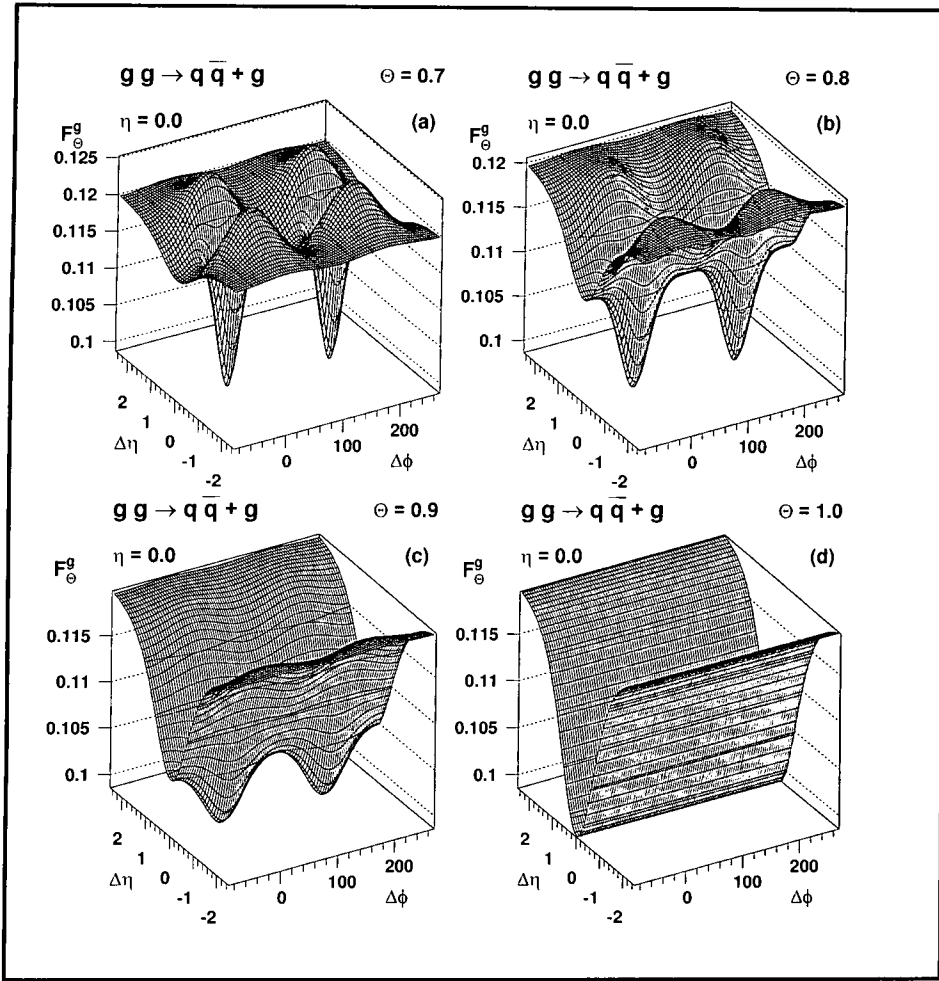
Figure 3.7: The antenna patterns $\mathcal{F}^g_{\mathrm{QCD},\Theta}$ of Eq. (3.85) for the process $gg \to q\bar{q} + g$ with different values of the mass parameter Θ of Eq. (3.83). The pseudorapidity of both quark jets is fixed at $\eta = 0$, and the transverse momentum of the soft gluon is $k_T = 10$ GeV. In (d) we show the threshold result $\Theta = 1$ ($E_Q = m_Q$).

which depends on $\Delta\eta$ but not on $\Delta\phi$. For $|\Delta\eta| \to \infty$ $\mathcal{F}^g_{\mathrm{QCD},\Theta=1}$ approaches the constant value

$$\lim_{|\Delta\eta|\to\infty} \mathcal{F}^g_{\mathrm{QCD},\Theta=1} = 2N_{\mathrm{c}}[12] = \frac{4}{k_T^2}N_{\mathrm{c}}, \qquad (3.92)$$

and becomes equal to $\mathcal{F}^g_{H,\Theta=1}$, as in the massless case. We also see from Fig. 3.7(d) that $\mathcal{F}^g_{\mathrm{QCD},\Theta=1}$ has an absolute minimum at $\Delta\eta = 0$,

$$\mathcal{F}^g_{\mathrm{QCD},\Theta=1}(\Delta\eta = 0) = \frac{2}{k_T^2}\left(2N_{\mathrm{c}} - C_{\mathrm{F}} + \mathcal{Y}_1\right) = \frac{N_{\mathrm{c}}}{k_T^2}\frac{3N_{\mathrm{c}}^2 - 4}{N_{\mathrm{c}}^2 - 2}, \qquad (3.93)$$

which is numerically 18% lower than the large $\Delta\eta$ value. Note the singularity in Eq. (3.93) for $N_{\mathrm{c}} = \sqrt{2}$.

We next consider the patterns for arbitrary η and Θ. With the exception of [12] all antennae exhibit an η dependence. We are again especially interested in the value of $\mathcal{F}^g_{H,\Theta}$
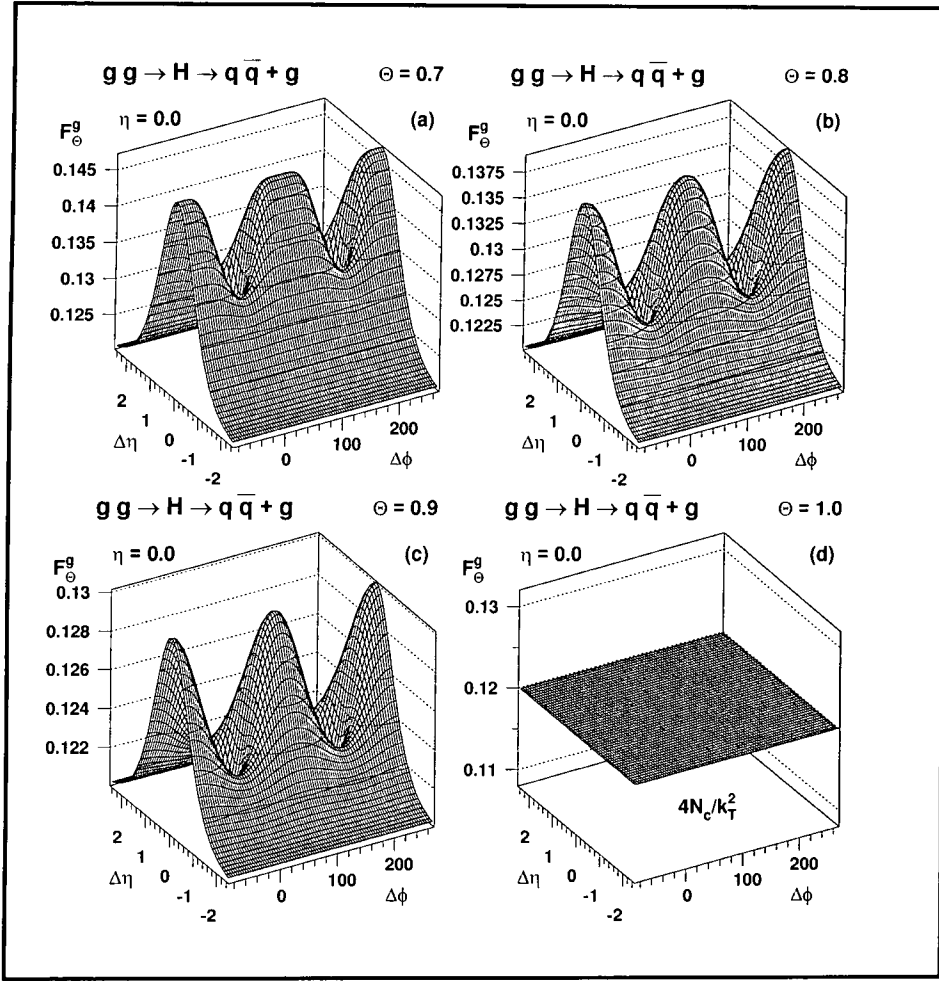
Figure 3.8: The antenna patterns $\mathcal{F}^g_{H,\Theta}$ of Eq. (3.85) for the process $gg \to H(\to q\bar{q}) + g$ with different values of the mass parameter Θ of Eq. (3.83). The pseudorapidity of both quark jets is fixed at $\eta = 0$, and the transverse momentum of the soft gluon is $k_T = 10$ GeV. In (d) we show the threshold result $\Theta = 1$ $(E_Q = m_Q)$.

and $\mathcal{F}^g_{\text{QCD},\Theta}$ at the symmetric point between the two jets at $\mathcal{P}_c = (\Delta\eta = -\eta, \Delta\phi = \pi/2)$, as the massless study suggests that at this point the differences between the signal and background radiation patterns should be maximal. When evaluated at $\mathcal{P}_c$, only [13], [14], [23] and [24] have an explicit η dependence ($\sim \tanh(\eta)$), whereas

$$[12] = \frac{2}{k_T^2}, \tag{3.94}$$

$$[34] = \frac{2 - \Theta^2}{k_T^2},$$

$$[33] = [44] = \frac{\Theta^2}{k_T^2}.$$

All antennae that are η dependent exhibit an absolute maximum at $\mathcal{P}_c$ of $2/k_T^2$ for $\eta \to -\infty$ ([13], [24]) or for $\eta \to \infty$ ([14], [23]) and vanish for $\eta \to \pm\infty$ accordingly. The

fact that there is no η dependence at $\mathcal{P}_c$ for [12], [34], [33] and [44] immediately yields (see Eq. (3.84))

$$\mathcal{F}^g_{H,\Theta}(\mathcal{P}_c) = \frac{4}{k_T^2}\left(N_c + C_F(1 - \Theta^2)\right) \tag{3.95}$$

for all η, i.e. the radiation between the two jets is completely independent of their separation in rapidity. This is illustrated in Fig. 3.9(a).
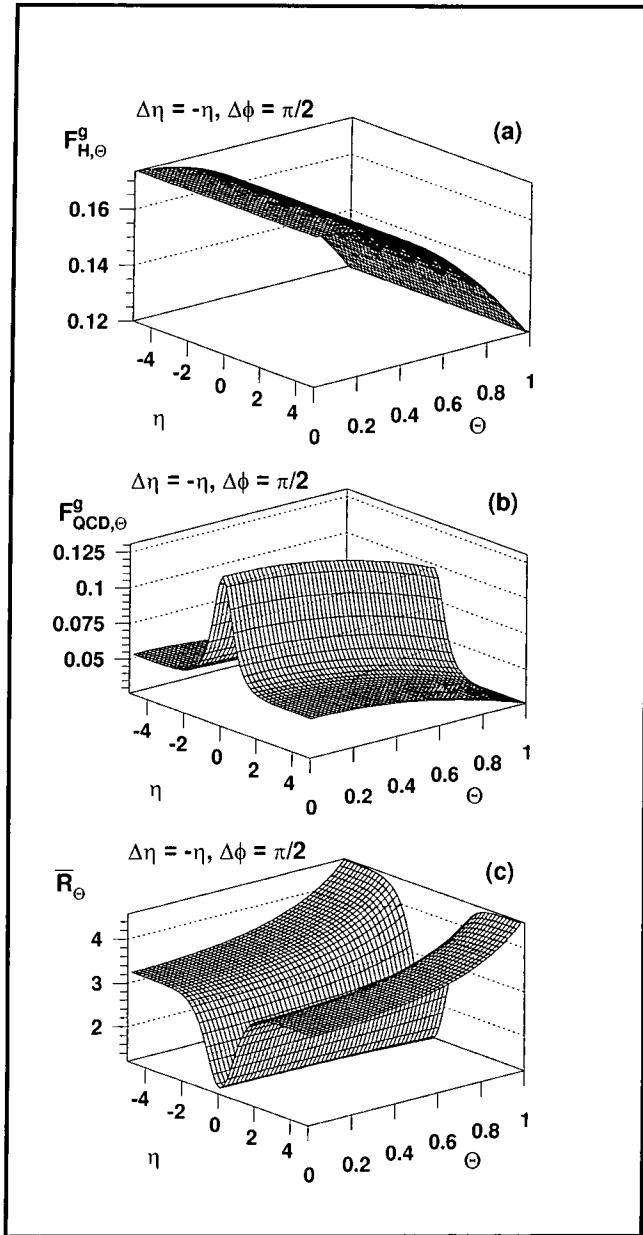
Figure 3.9: The radiation patterns for $\mathcal{F}^g_{H,\Theta}$, $\mathcal{F}^g_{QCD,\Theta}$ and $\overline{\mathcal{R}}_\Theta$ at the symmetric inter–jet point $\mathcal{P}_c$, for different values of the quark jet rapidity η and the mass parameter Θ. The soft gluon transverse momentum is taken to be $k_T = 10$ GeV.

Note that the massless result of Eq. (3.77) is reproduced for $\Theta = 0$. The corresponding

expression for $\mathcal{F}^g_{\mathrm{QCD},\Theta}$ *is* η dependent and reads

$$\mathcal{F}^g_{\mathrm{QCD},\Theta}(\mathcal{P}_c) = \tag{3.96}$$

$$\frac{1}{k_T^2} \frac{\{4(1 - \Theta^2) + 2N_c^2(N_c^2 - 2)(2 - \Theta^2)\}\cosh^2(\eta) + N_c^2\{2 - \Theta^2(2 - N_c^2)\}}{N_c^2(4C_F\cosh^2(\eta) - N_c)}.$$

For fixed Θ, $\mathcal{F}^g_{\mathrm{QCD},\Theta}(\mathcal{P}_c)$ always shows an absolute maximum for $\eta = 0$ (see Fig. 3.9(b)) with a Θ dependence which again is maximal for the massless case $\Theta = 0$, with the value given in Eq. (3.74). Once again defining the ratio of signal to background radiation patterns as $\overline{\mathcal{R}}_\Theta = \mathcal{F}^g_{H,\Theta}/\mathcal{F}^g_{\mathrm{QCD},\Theta}$, we see that $\overline{\mathcal{R}}_\Theta$ has a local maximum at $\mathcal{P}_c$, the value of which depends on η and Θ, see Fig. 3.9(c). The value at $\eta = 0$ is

$$\overline{\mathcal{R}}_\Theta(\mathcal{P}_c, \eta = 0) = \frac{4N_c^2(4C_F - N_c)(C_F(\Theta^2 - 1) - N_c)}{(N_c^4 + 4)(\Theta^2 - 1) + 2N_c^2(3 - \Theta^2)}, \tag{3.97}$$

which actually shows a very weak Θ dependence. It is maximal for massless quarks ($\Theta = 0$) with the value ($= 1.3285$) already given in Eq. (3.80), and is minimal for $\Theta = 1$ with the value

$$\overline{\mathcal{R}}_{\Theta=1}(\mathcal{P}_c, \eta = 0) = 4\frac{N_c^2 - 2}{3N_c^2 - 4} = 1.2174. \tag{3.98}$$

For the massless case, $\overline{\mathcal{R}}(\mathcal{P}_c)$ increased with increasing jet separation (i.e. increasing η). This is again true for the massive case, as shown in Fig. 3.9(c). In the limit $|\eta| \to \infty$ we find

$$\lim_{|\eta|\to\infty} \overline{\mathcal{R}}_\Theta(\mathcal{P}_c, \eta) = \frac{4\left(N_c + C_F(1 - \Theta^2)\right)N_c(N_c^2 - 1)}{2(1 - \Theta^2) + N_c^2(N_c^2 - 2)(2 - \Theta^2)}, \tag{3.99}$$

which is a monotonically increasing function of Θ. The values at $\Theta = 0, 1$ are $3.25, 4.57$ respectively, for $N_c = 3$.

In summary, the relative difference between the radiation patterns for the Higgs signal and QCD background processes is maximal at the symmetric inter–jet point. The ratio (signal/background) of the radiation patterns at this point depends on the rapidity of the jets and the quark mass. It is smallest ($\overline{\mathcal{R}} = 1.33$) for massless, central jets, and largest for massive, large–rapidity jets ($\overline{\mathcal{R}} = 4.57$).

Radiation inside the 'dead cone'

A final point concerns the radiation *inside* the dead cone of the final-state (massive) quark jets. In this section for simplicity we will only consider centrally produced jets with $\eta = 0$ – the generalisation to forward jet production is entirely straightforward.

First we recall the result for the Higgs signal process $gg \to H \to q\bar{q}$ for massless quarks:

$$\mathcal{F}^g_H|_{\eta=0} = \frac{4}{k_T^2}\left(N_c + \frac{C_F}{\cosh^2(\Delta\eta) - \cos^2(\Delta\phi)}\right). \tag{3.100}$$

The second term is singular at the jet centre, $\Delta\eta, \Delta\phi \to 0$, whereas the first term represents a constant 'pedestal' of radiation from emission off the incoming gluons. In the massive case ($\Theta > 0$), however, the singularity is removed and in fact the net contribution

to the radiation pattern from the combination $C_F(2[34] - [33] - [44])$ vanishes at the jet centre $\mathcal{P}_{dc} = (\Delta\eta = \Delta\phi = 0)$, hence

$$\mathcal{F}^g_{H,\Theta}(\mathcal{P}_{dc}, \eta = 0) = \frac{4}{k_T^2} N_c\,. \tag{3.101}$$

The corresponding result for the QCD background radiation pattern inside the dead cone is straightforward to calculate from the results already presented. We find, again for $\eta = 0$,

$$\mathcal{F}^g_{QCD,\Theta}(\mathcal{P}_{dc}, \eta = 0) = \frac{N_c}{k_T^2}\frac{3N_c^2 - 4}{N_c^2 - 2}\,. \tag{3.102}$$

Interestingly, the results (3.101,3.102) are independent of the quark mass, provided of course that $m_Q > 0$. The effect can be seen in Figs. 3.7 and 3.8, where the value of the radiation patterns at their minima (i.e. inside the dead cones of the quark jets) is the same for all Θ. The signal to background ratio in the dead cone is therefore equal to the value obtained at threshold and given already in Eq. (3.98).

3.3.2   Associated Higgs production

Higgs production in association with a W boson $q\bar{q}' \to W^* \to WH$ is a potentially important discovery channel at both the TEVATRON and LHC colliders, especially for the 'intermediate mass' Higgs. The non–hadronic final state $WH \to \ell\nu_\ell\gamma\gamma$ should be relatively easy to distinguish, but unfortunately has a very small branching ratio, see for example the recent study in Ref. [KMS97]. This raises the question as to whether a search in the decay channel

$$q\bar{q}' \longrightarrow W^* \longrightarrow W(\to \ell\nu_\ell)H(\to b\bar{b})\,, \tag{3.103}$$

might be feasible, especially with flavour tagging of both final–state b quarks [SMW94].

Now there is a potentially large irreducible background from the QCD process

$$q\bar{q}' \longrightarrow W(\to \ell\nu_\ell) + b\bar{b}\,, \tag{3.104}$$

when $M_{b\bar{b}} \sim M_H$.

The signal and background processes are illustrated in Fig. 3.10.

We wish to study the radiation patterns for the processes (3.103) and (3.104), in analogy with the $gg \to (H \to)b\bar{b}$ study of the previous section. We first notice that the colour flows are exactly the same as those for the $2 \to 2$ scattering processes $q\bar{q} \to H \to b\bar{b}$ and $q\bar{q} \to g^* \to b\bar{b}$ [KOS94]. We can therefore immediately write down the antenna patterns of the soft gluon radiation:

$$\mathcal{F}^{WH}_\Theta = 2C_F\left\{[12] + [34]\right\} - C_F[33] - C_F[44]\,. \tag{3.105}$$

$$\mathcal{F}^{Wg}_\Theta = \frac{1}{N_c}[14;23] + 2C_F\left\{[13] + [24]\right\} - C_F[33] - C_F[44]\,, \tag{3.106}$$

with $[14;23]$ defined in Eq. (3.63). Note that the Higgs pattern is the same as for $gg \to H \to b\bar{b}$ apart from colour factor replacement $N_c \to C_F$ for the initial–state $[12]$ antenna.

In order to illustrate the quantitative differences between these radiation patterns it is necessary to define appropriate kinematics. Since the leading order processes are now
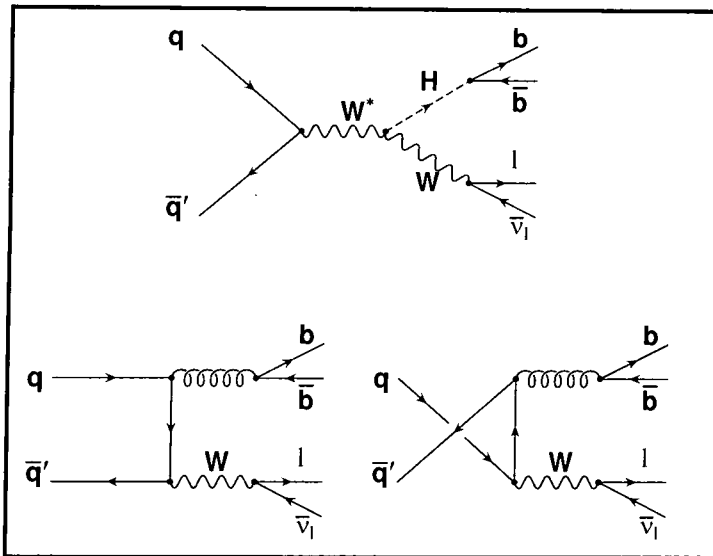
Figure 3.10: Feynman graphs for the process $q\bar{q}' \to W^* \to W(\to \ell\bar{\nu}_\ell)H(\to q\bar{q})$ (associated Higgs production) and the background process $q\bar{q}' \to W(\to \ell\bar{\nu}_\ell)g^*(\to q\bar{q})$.
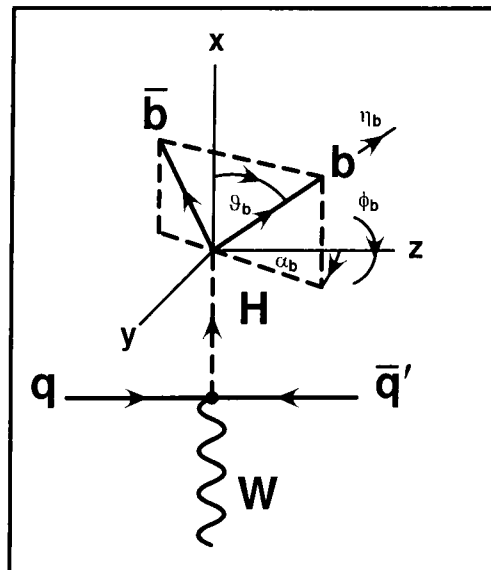
Figure 3.11: The kinematics for back–to–back Higgs($\to b\bar{b}$)–W production. The variables are defined in Eq. (3.107).

effectively three–body final states, it is convenient to make some simplifying assumptions. Thus we assume that the H and the W are produced with zero rapidity, and that the b and $\bar{b}$ quarks have equal energy and have polar and azimuthal angles ϑ_b and α_b with respect to the H direction. This configuration is illustrated in Fig. 3.11 and corresponds

to the four momenta (we only present the massive particles)

$$
\begin{aligned}
p_H^\mu &= (E_H, p_{TH}, 0, 0)\,, \\
p_W^\mu &= (E_W, -p_{TH}, 0, 0)\,, \\
p_b^\mu &= (E_b, p_b \cos(\vartheta_b), p_b \sin(\vartheta_b) \sin(\alpha_b), p_b \sin(\vartheta_b) \cos(\alpha_b))\,, \\
p_{\bar b}^\mu &= (E_b, p_{TH} - p_b \cos(\vartheta_b), -p_b \sin(\vartheta_b) \sin(\alpha_b), -p_b \sin(\vartheta_b) \cos(\alpha_b))\,. \quad (3.107)
\end{aligned}
$$

Conservation of energy and momentum gives

$$
E_H = 2E_b = \frac{\hat{s} + M_H^2 - M_W^2}{2\sqrt{\hat{s}}}, \quad p_{TH} = \sqrt{E_H^2 - M_H^2},
$$

$$
p_b = \sqrt{E_b^2 - m_b^2}, \quad \cos(\vartheta_b) = \frac{p_{TH}}{2p_b}. \quad (3.108)
$$

The pseudorapidities and azimuthal angles of the b and $\bar b$ quarks are readily found to be

$$
\tan(\phi_{b,\bar b}) = \frac{p_{(b,\bar b)y}}{p_{(b,\bar b)x}} = \tan(\vartheta_{b,\bar b}) \sin(\alpha_{b,\bar b})\,, \quad (3.109)
$$

such that $\alpha_{b,\bar b} = \frac{\pi}{2}$ corresponds to $\phi_{b,\bar b} = \vartheta_{b,\bar b}$, and

$$
\eta_{b,\bar b} = \frac{1}{2} \ln\left(\frac{E_b + p_{(b,\bar b)z}}{E_b - p_{(b,\bar b)z}}\right)\,. \quad (3.110)
$$

The soft gluon momentum is defined relative to the b-quark jet:

$$
k^\mu = k_T(\cosh(\eta_b + \Delta\eta), \cos(\phi_b + \Delta\phi), \sin(\phi_b + \Delta\phi), \sinh(\eta_b + \Delta\eta))\,. \quad (3.111)
$$

Note that the opening angle $2\vartheta_b$ between the two b quarks is a function of the partonic subprocess energy $\sqrt{\hat{s}}$. The dependence is illustrated in Fig. 3.12. Note that at threshold $(\sqrt{\hat{s}} = M_W + M_H)$ $2\vartheta_b = 180°$.

Let us now study the radiation patterns in more detail. We assume parameter values of $M_H = 130$ GeV, $m_b = 4.3$ GeV and $M_W = 80.33$ GeV, and we again fix the transverse momentum of the soft gluon to be $k_T = 10$ GeV. The first thing to note is that for the symmetric configuration defined above, the radiation pattern for the signal process is independent of the azimuthal angle α_b. This follows from the absence of antenna involving both initial- and final-state quarks in (3.105). In contrast, there is no such symmetry for the background process (3.106).

A more striking difference is seen if we vary $\sqrt{\hat{s}}$. According to Fig. 3.12 the angle between the final-state quarks decreases with increasing $\sqrt{\hat{s}}$ with the effect that the two quark jets eventually merge for large centre–of–mass energies. Figs. 3.13 and 3.14 show the signal (3.105) and background (3.106) radiation patterns for the average value $(\sqrt{\hat{s}} = 310$ GeV) and for an extreme value $(\sqrt{\hat{s}} = 14$ TeV) respectively.[5] The azimuthal angle α_b is fixed at 90° in both cases.

For $\sqrt{\hat{s}} = 310$ GeV the opening angle between the b and the $\bar b$ quarks is approximately 100°. As $\alpha_b = 90°$ the $b - \bar b$ plane is orthogonal to the $q\bar q' - WH$ scattering plane (see

---

[5]Notice that at threshold, $\sqrt{\hat{s}_0} = M_H + M_W$, the b and $\bar b$ are produced back–to–back, and the discussion is almost identical to the direct production case studied earlier, apart from colour factor differences arising from having incoming quarks instead of gluons.
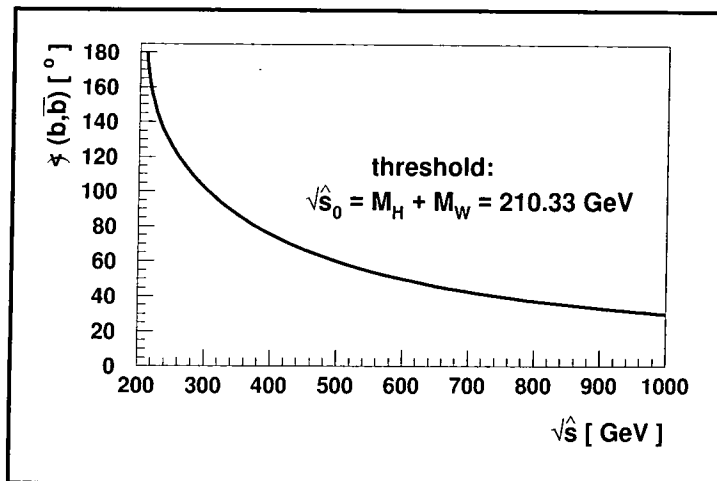
Figure 3.12: The opening angle of the $b\bar{b}$ quark pair as a function of the partonic subprocess energy $\sqrt{\hat{s}}$.

Fig. 3.11) and thus $\eta_b = \eta_{\bar{b}} = 0$. We see immediately that the main feature of our direct production study described earlier still holds. The most striking difference between the signal $\mathcal{F}_{\Theta}^{WH}$ and the background $\mathcal{F}_{\Theta}^{Wg}$ is the relative suppression of radiation *between* the b–quark jets for the latter. There is a factor of approximately 2 difference between signal and background radiation in the inter–jet region, in qualitative agreement with the results obtained for direct Higgs production.

If we now increase the subprocess centre–of–mass energy the two b–quark jets merge, forming a narrow colour singlet and octet state for the signal and background respectively. The situation for the extreme case $\sqrt{\hat{s}} = 14$ TeV is shown in Fig. 3.14. Notice that for the signal process the soft gluon radiation becomes trapped in a very small tube. Outside the merged jets the radiation pattern completely flattens out. In contrast, for the background process there is still significant radiation between the initial– and final–state quark directions. In fact the distribution here is essentially identical to that for the $q\bar{q}' \to Wg$ process studied in Ref. [KS97b]. In other words, the radiation pattern acts as a 'partonometer' [EKS97] in measuring the colour charge of the outgoing large p_T partonic system.

3.3.3 Concluding remarks

We studied in this section the Higgs signal at the LHC and the corresponding QCD background process for

- direct Higgs production $gg \to H \to q\bar{q}g$,

- associated Higgs production $q\bar{q}' \to WH(\to b\bar{b})g$,

a two (four) particles final state plus additional (soft) gluon. The aim of this study was to use gluon 'partonometry' to obtain a maximal ratio between Higgs signal and QCD background. Studying the radiation pattern of the soft gluon for both processes (and both background processes) we conclude
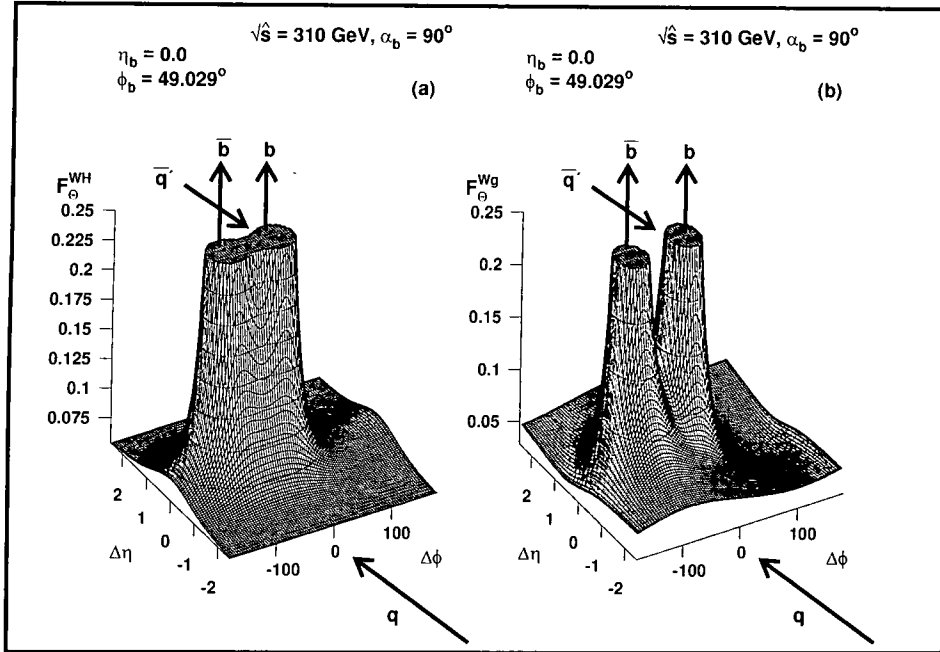
Figure 3.13: The radiation patterns for the signal $\mathcal{F}_\Theta^{WH}$ (Eq. (3.105)) and the background $\mathcal{F}_\Theta^{Wg}$ (Eq. (3.106)) for associated Higgs production at subprocess centre–of–mass energy $\sqrt{\hat{s}} = 310$ GeV. The directions of the incoming quarks q and $\bar{q}'$ and of the b and $\bar{b}$ quarks are indicated.

- for the direct Higgs production the clearest signal can be expected by measuring hadronisation between the two outgoing quark jets. From the different antenna patterns (signal and background) a clear depletion of radiation in the interjet region for the background process should be observable. The signal/background ratio at this point is dependent on the pseudorapidity (i.e. kinematics) of the outgoing jets. For back–to–back scattering we found the Higgs signal yielding approximately 30% more radiation than the QCD background at the inter-jet point. The higher $|\eta|$ the higher becomes the signal/background ratio, but it stays always below $4C_F/k_T^2$, where k_T denotes the transverse momentum of the soft gluon.

- this observation is also qualitatively true for the associated Higgs production but the signal/background ratio is quantitatively even slightly higher than in direct Higgs production.

We accept that there is no substitute for a detailed Monte Carlo study, but our work should be regarded as a guide into this direction. We also studied the phenomenon of the "*dead cone*" and included massive quarks. Both phenomena play a minor role at typical LHC energies.
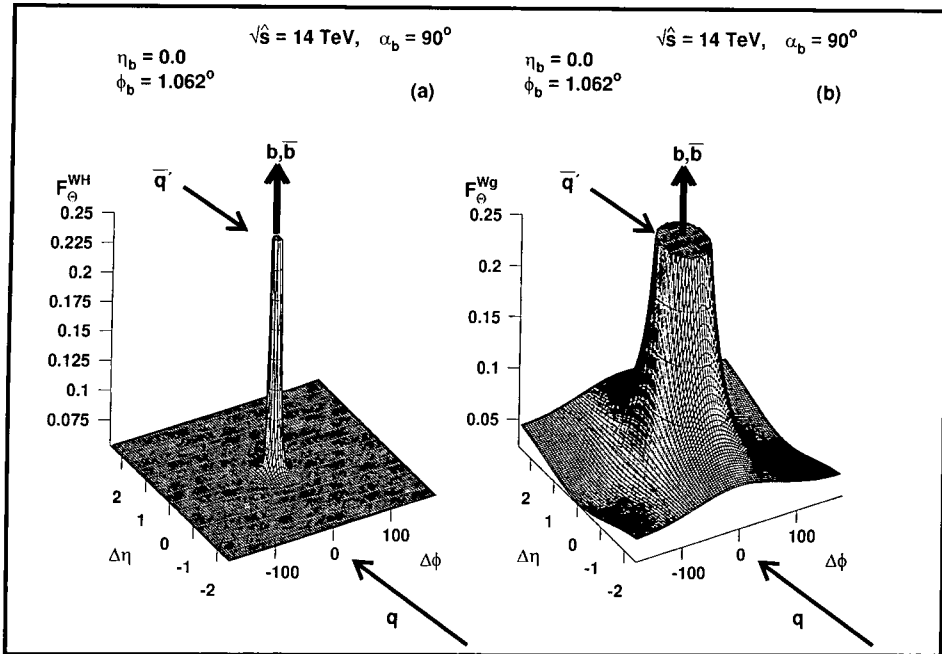
Figure 3.14: Same as Fig. 3.13 but now for a subprocess centre–of–mass energy of $\sqrt{\hat{s}} = 14$ TeV.

3.4 HERA s–channel resonances: antenna patterns of "leptoquarks"

The observation of an apparent excess of deep inelastic scattering events in positron–proton collisions at high Q^2 by both the H1 [H1.97] and ZEUS [ZEUS97] collaborations at HERA has prompted much speculation about possible new physics explanations. Obvious candidates are a new four–fermion contact interaction $\Lambda^{-2}\bar{e}e\bar{q}q$ with $\Lambda \sim \mathcal{O}(1-2\ \text{TeV})$, or the production of a new heavy "leptoquark" resonance $e^+q \to LQ \to e^+q$ with $M_{LQ} \sim 200$ GeV. For a general discussion of the various new physics possibilities see for example [Alt97, HR97]. The electric charge of such an object is not yet known, but if $e_{LQ} = +2/3$, corresponding to $e^+d \to LQ$ for example, then the new particle could be a heavy squark in an R–parity violating supersymmetric extension of the Standard Model. A discussion of R–parity violating squarks is presented in Section 3.4.3.

It is important to investigate all possible ways in which one could distinguish between a conventional explanation (i.e. a fluctuation of the SM DIS process) and new physics scenarios. We shall address again the study of the energy flow in the event as diagnostic tool to search for new physics. The events at high x and Q^2 at HERA seem ideally suited to such a study, being characterised by an energetic, well–separated lepton and jet in the final state. Furthermore the various candidate underlying $eq \to eq$ processes (t–channel γ^*, Z exchange, contact interaction, s–channel colour–triplet resonance production, ...) have distinctive antenna patterns, as we shall see. In practice one could, with sufficiently high statistics, use an additional soft (gluon) jet as a probe of the antenna pattern. With fewer events the distribution of soft hadrons can be used instead. Both of these

quantities are related to the inclusive soft gluon distribution in the next–to–leading order $eq \to eqg$ processes, the former directly and the latter through the hypothesis of Local Parton Hadron Duality (LPHD) [Azi85a, Azi86a] in which the angular distribution of soft particles emitted at wide angles to the energetic jets follows that of the underlying soft partons, with the rate being determined by overall multiplicative energy–dependent cascading factors [DKT87, Azi85b, Azi86b].

The idea, then, is to use the angular distributions of soft particles or jets as a probe of new physics contributions to high–Q^2 e^+q scattering. We imagine a situation where a larger sample of (presumably SM DIS) events at slightly lower Q^2 is used as a control, to check the approximate validity of our quantitative predictions for the antenna pattern. This can then be compared with the observed antenna pattern for the sample of excess events. As we shall see, in some cases the 'signal' and 'background' distributions can differ by factors of two or more. The variation of the patterns with the DIS variable y will also be a useful discriminant.

In the following we derive the basic antenna pattern results for standard DIS and leptoquark production. The case of a new contact interaction is obtained as a limiting case of the latter.

The distribution of soft radiation is controlled by the basic antenna pattern (*cf.* Eq. (3.11))

$$[ij] \equiv \frac{p_i \cdot p_j}{p_i \cdot k \, p_j \cdot k} = \frac{1 - \vec{n}_i \cdot \vec{n}_j}{\omega_{\gamma,g}^2 (1 - \vec{n} \cdot \vec{n}_i)\,(1 - \vec{n} \cdot \vec{n}_j)} , \tag{3.112}$$

where the $p_i^\mu = E_i(1, \vec{n}_i)$ are the four–momenta of the energetic quarks and leptons participating in the hard scattering process, and $k^\mu = \omega_{\gamma,g}(1, \vec{n})$ is the four–momentum of the soft photon (gluon). The radiation patterns presented below correspond to the (soft) $\omega_{\gamma/g}/E_i \to 0$ limits of the exact $eq \to eq\gamma$ ($eq \to eqg$) matrix elements.

3.4.1 Additional soft gluons

We start by considering the Standard Model process $e^+(p_1) + q(p_2) \to e^+(p_3) + q(p_4)$ with an additional *soft gluon* by t–channel γ^*, Z exchange. If the invariant mass of the e^+q system is M, and if the angle between the incoming and outgoing quarks (in the e^+q c.m.s. frame) is Θ_q, i.e. $\cos\Theta_q = \vec{n}_2 \cdot \vec{n}_4$, then the usual DIS variables are

$$x = \frac{M^2}{s} , \quad y = \frac{1}{2}(1 - \cos\Theta_q) , \quad Q^2 = yM^2 . \tag{3.113}$$

The scattering process with the various momenta labelled is shown in Fig. 3.15.

Since our aim is to distinguish the patterns for resonance production and the normal DIS, we consider fixed M and variable Θ_q, i.e. variable y. For the Standard Model process the gluon energy and angular distribution is given by Eq. (3.27) where[6]

$$\mathcal{F}_{\text{SM}}^g = 2[24] = \frac{2p_2 \cdot p_4}{p_2 \cdot k \, p_4 \cdot k} = \frac{2(1 - \cos\Theta_q)}{\omega_g^2 (1 - \cos\theta_2)\,(1 - \cos\theta_4)} , \tag{3.114}$$

where $\cos\theta_i = \vec{n} \cdot \vec{n}_i$ denotes the angle between the soft gluon and the corresponding quark. The gluon emission is coherent, and depends on the relative orientation of the

---

[6]Note that in the following we shall suppress the universal colour factor C_F in the presentation of $\mathcal{F}^g$, i.e. $\mathcal{F}^g = -\sum\limits_{i,j} J_i^\mu J_{\mu,j}$ rather than the definition given in Eq. (3.23).
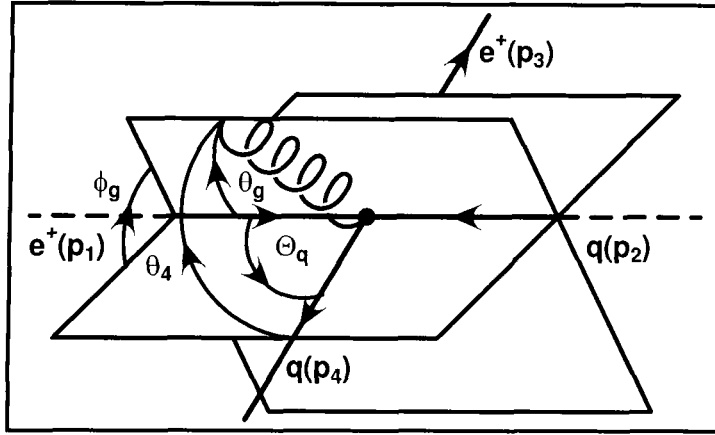
Figure 3.15: Parametrisation of the kinematics for $e^+(p_1)q(p_2) \rightarrow e^+(p_3)q(p_4) + g(k)$ scattering in the e^+q c.m.s. frame. The orientation of the soft gluon relative to the scattering plane is denoted by θ_g and ϕ_g or, alternatively, by the angles with respect to the directions of the participating quarks: θ_4 and $\theta_2 = \theta_g$.

incoming and outgoing quark directions. Eq. (3.114) can be interpreted as a *colour string* connecting the incoming and outgoing quarks [AGS80, Azi85b, Azi86b], and is closely related to the familiar result $\mathcal{F}^g = 2[q\bar{q}]$ for the crossed process $e^+e^- \rightarrow q\bar{q}$ (*cf.* Eq. (3.26) and [Dok91]).

We now turn to the radiation pattern corresponding to the production of an unstable colour–triplet, s–channel scalar resonance LQ of mass M and decay width Γ_{LQ}, i.e. $e^+q \rightarrow \mathrm{LQ} \rightarrow e^+q + g$. We first note that the emission of a soft gluon off an on–shell colour–triplet *scalar boson* is described by the same factor as emission off a colour–triplet *fermion*, i.e. (*cf.* Eq. (3.21))

$$\mathcal{M}^g \simeq T_{ij}^a g_s \frac{P^\mu \cdot \epsilon_\mu^{*a}(k)}{P \cdot k} \mathcal{M}^0 \,, \tag{3.115}$$

where T^a is a SU(3) colour matrix, P^μ is the momentum of the emitting particle, and ϵ_μ^a is the gluon polarisation vector. We can therefore use results already obtained for heavy quark production and decay to write down the result for leptoquark production and decay:[7]

$$\mathcal{F}_{\mathrm{LQ}}^g = 2\left([2P] + [4P] - [PP]\right) + 2\chi_{\mathrm{LQ}}\left([PP] + [24] - [2P] - [4P]\right) \tag{3.116}$$

where $P = p_1 + p_2$ is the leptoquark momentum. Eq. (3.116) is derived in Appendix A.2. The factor χ_{LQ} in (3.116) is given by

$$\chi_{\mathrm{LQ}}^2 = \frac{M^2 \Gamma_{\mathrm{LQ}}^2}{(P \cdot k)^2 + M^2 \Gamma_{\mathrm{LQ}}^2} = \frac{\Gamma_{\mathrm{LQ}}^2}{\omega_g^2 + \Gamma_{\mathrm{LQ}}^2} \tag{3.117}$$

where the second expression corresponds to the LQ c.m.s. frame. Eqs. (3.116,3.117) are derived in Appendix A.2. As discussed at length in Ref. [KOS92], the radiation

---

[7]In fact the soft gluon distribution for $eq \rightarrow \mathrm{LQ} \rightarrow eq$ is identical to that for $Wb \rightarrow t \rightarrow Wb$ with $m_t = M_{\mathrm{LQ}} = M$, $\Gamma_t = \Gamma_{\mathrm{LQ}}$ and $m_b = 0$ [Dok93].

pattern depends, through the factor χ_{LQ}, on the relative size of the gluon energy and the leptoquark decay width. In this respect it is instructive to consider the two (formal) limits $\Gamma_{\mathrm{LQ}} \to \infty$ ($\chi_{\mathrm{LQ}} \to 1$) and $\Gamma_{\mathrm{LQ}} \to 0$ ($\chi_{\mathrm{LQ}} \to 0$), for fixed ω_g. In the former, the leptoquark decays immediately after it is produced and has no time to radiate gluons of wavelength $\sim 1/\omega_g$. In this limit

$$\mathcal{F}_{\mathrm{LQ}}^g \overset{\Gamma_{\mathrm{LQ}} \to \infty}{\longrightarrow} 2[24] , \tag{3.118}$$

which is identical to the standard DIS pattern (3.114) corresponding to *coherent* emission. In contrast, for $\Gamma_{\mathrm{LQ}}/\omega_g \to 0$ the emission takes place on two very different timescales, corresponding to the *production* stage and the *decay* stage [KOS92]:

$$\mathcal{F}_{\mathrm{LQ}}^g \overset{\Gamma_{\mathrm{LQ}} \to 0}{\longrightarrow} \{2[2P] - [PP]\} + \{2[4P] - [PP]\} . \tag{3.119}$$

At threshold, where there is essentially no radiation from the heavy leptoquark, the two terms in $\{\}$ correspond to independent radiation off the initial and final state (massless) quarks, see (3.121) below. Note that it is straightforward to verify that the first term on the right–hand side of (3.119) does indeed correspond to the $k^\mu \to 0$ limit of the real gluon emission matrix element squared for $e + q \to \mathrm{LQ} + g$ calculated in Refs. [KS97a, PSZ97].

With no *a priori* knowledge of the decay width of the new heavy particle, the antenna pattern (3.116) could in principle be used to obtain a measurement. This was the approach advocated in Ref. [KOS92] for the top quark. As we shall see in the following section, in certain regions of phase space the antenna pattern is very sensitive to χ_{LQ}, and therefore to Γ_{LQ}. In practice, it seems that for the class of leptoquark models proposed [Alt97, HR97] to explain the excess of high–Q^2 events at HERA, the decay width is rather small. In particular, a scalar leptoquark coupling with strength λ to eq has a corresponding decay width $\Gamma_{\mathrm{LQ}} = M\lambda^2/(16\pi)$. For 'first generation' leptoquarks values of $\lambda^2 < \mathcal{O}(10^{-2})$ are allowed by low–energy data (see for example Ref. [KS97a] and references therein). This implies that such resonances should be very narrow, i.e. $\Gamma_{\mathrm{LQ}} < \mathcal{O}(40 \text{ MeV})$ for $M \sim 200$ GeV. If we are interested in the distributions of soft hadrons or jets with energies of order a few GeV, then $\chi_{\mathrm{LQ}} \ll 1$ and (3.119) is the appropriate distribution for the leptoquark signal.

Finally, we note that the antenna pattern for a $\bar{e}e\bar{q}q$ contact interaction corresponds to the limit $\chi_{\mathrm{LQ}} \to 1$, and is therefore identical to the standard DIS result, Eq. (3.114).

In the following we present numerical results for the SM DIS and leptoquark soft gluon distributions. We work in the eq c.m.s. frame with angles defined as in Fig. 3.15, and focus on the dependence of the dimensionless quantity $\mathcal{N} = \omega_g^2 \mathcal{F}^g$, where $\mathcal{F}_{\mathrm{SM}}^g$ and $\mathcal{F}_{\mathrm{LQ}}^g$ are defined in (3.114) and (3.119) respectively, on the gluon direction $\vec{n}$. Simple algebra gives

$$\mathcal{N}_{\mathrm{SM}} = \frac{2(1 - \cos\Theta_q)}{(1 - \cos\theta_2)(1 - \cos\theta_4)} , \tag{3.120}$$

$$\mathcal{N}_{\mathrm{LQ}} = \frac{1 + \cos\theta_2}{1 - \cos\theta_2} + \frac{1 + \cos\theta_4}{1 - \cos\theta_4} , \tag{3.121}$$

$$\frac{\mathcal{N}_{\mathrm{LQ}}}{\mathcal{N}_{\mathrm{SM}}} = \frac{1 - \cos\theta_2 \cos\theta_4}{1 - \cos\Theta_q} . \tag{3.122}$$

The patterns and their ratio are displayed in Figs. 3.16 and 3.17, as functions of θ_g and ϕ_g, the polar and azimuthal gluon angles with respect to the incoming quark
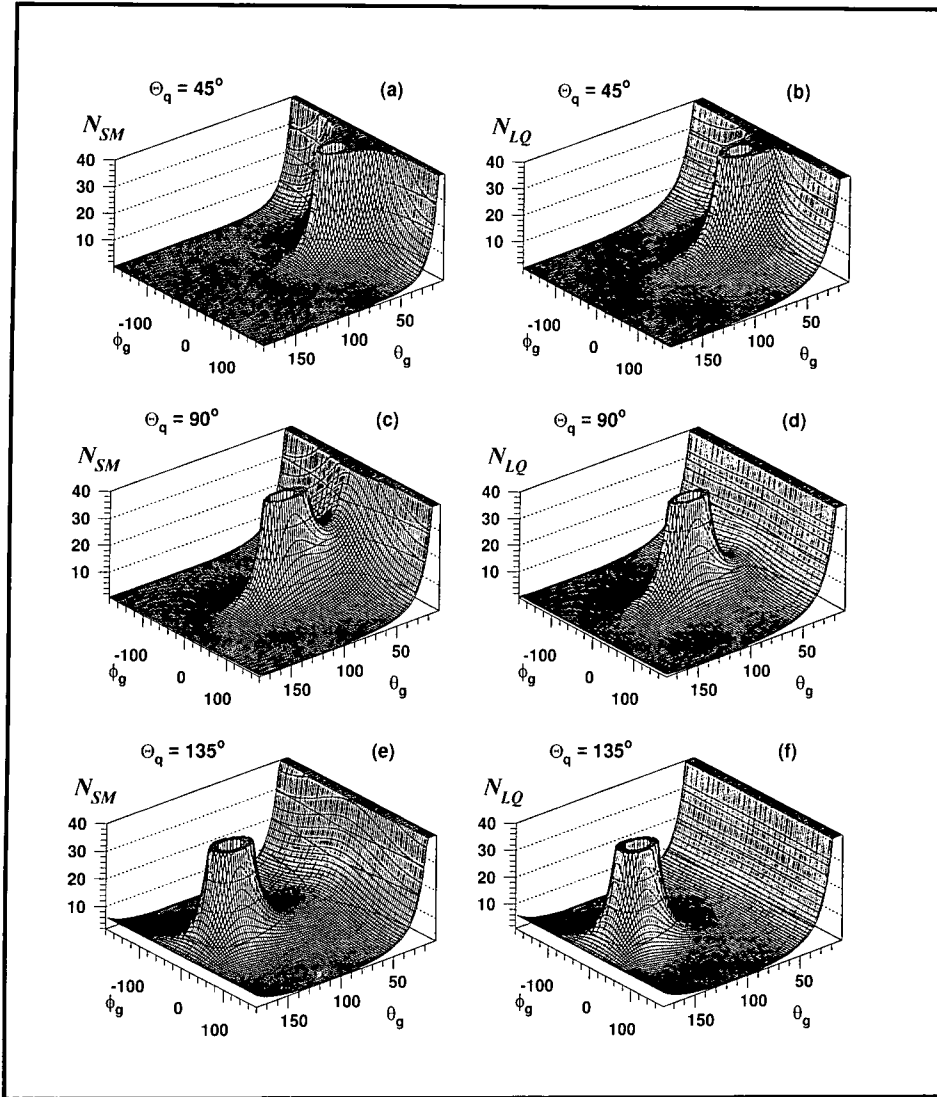
Figure 3.16: The dimensionless antenna patterns $\mathcal{N}_{\mathrm{SM}} = \omega_g^2 \mathcal{F}_{\mathrm{SM}}^g$ [(a),(c),(e)] and $\mathcal{N}_{\mathrm{LQ}} = \omega_g^2 \mathcal{F}_{\mathrm{LQ}}^g$ [(b),(d),(f)] of Eqs. (3.120,3.121) for different c.m.s. scattering angles Θ_q (cf. Fig. 3.15). Note the cut of $10°$ imposed around the incoming and outgoing quark directions.

direction,[8] and for fixed values of $\Theta_q = 45°, 90°, 135°$, i.e. $y = 0.146, 0.5, 0.854$. To avoid the collinear–singular regions of phase space, cuts $\theta_2, \theta_4 > 10°$ are imposed.[9]

We note the following points:

(i) For the SM distribution, there is a significant enhancement of radiation in the region between the quark directions (i.e. $\phi_g \sim 0°$, $0° \lesssim \theta_g \lesssim \Theta_q$), as expected. This enhancement is largely absent in the LQ case, where the radiation pattern is simply a superposition of independent radiation off the initial and final state

---

[8]i.e. $\theta_2 = \theta_g$, $\cos\theta_4 = \cos\phi_g \sin\theta_g \sin\Theta_q + \cos\theta_g \cos\Theta_q$.

[9]The cuts on θ_2, θ_4 are omitted in Fig. 3.17, since the ratios are finite ($= 1$) in the two collinear limits.
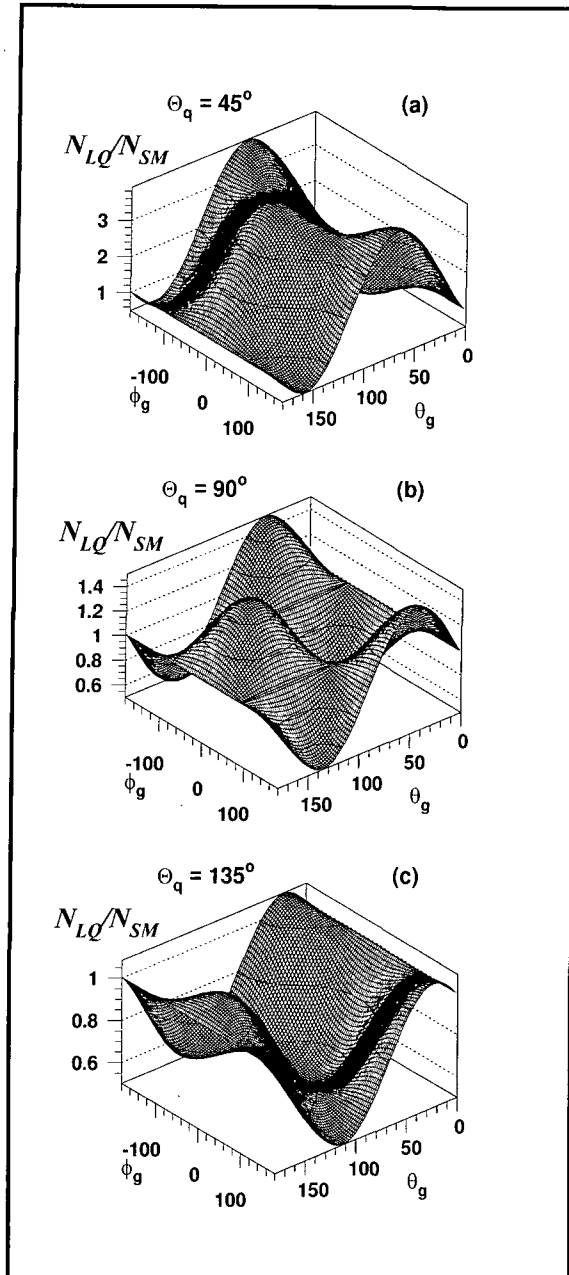
Figure 3.17: The ratios $\mathcal{N}_{\mathrm{LQ}}/\mathcal{N}_{\mathrm{SM}}$ of the distributions in Fig. 3.16 for the three different c.m.s. scattering angles. In this case no angular cuts have been imposed.

quarks.

(ii) In the limit $\Theta_q \to 0°$, $\mathcal{N}_{\mathrm{SM}}$ vanishes everywhere since the final state comoving colour triplet and antitriplet behave as a colour singlet, whereas $\mathcal{N}_{\mathrm{LQ}}$ is simply twice the radiation off a single quark. In Ref. [Dok93], similar effects where discussed for $e^+e^- \to t\bar{t} \to W^+W^-b\bar{b}$ production at threshold.

(iii) For $\Theta_q = 90°$ scattering, the ratio of the SM and LQ distributions achieves its

minimum and maximum values in the plane of the scattering, thus $\mathcal{N}_{\text{LQ}} = \frac{1}{2}\mathcal{N}_{\text{SM}}$ for $(\phi_g, \theta_g) = (0°, 45°)$ and $(180°, 135°)$ and $\mathcal{N}_{\text{LQ}} = \frac{3}{2}\mathcal{N}_{\text{SM}}$ for $(\phi_g, \theta_g) = (0°, 135°)$ and $(180°, 45°)$. The distributions are the same for gluon directions in the planes perpendicular to $\vec{n}_2$ and $\vec{n}_4$, i.e. $\theta_2, \theta_4 = 90°$.

Finally, from the above discussion we would expect that the azimuthal distribution of soft gluons (hadrons) around the final state quark (jet) direction would be more uniform for quarks from leptoquark decay than from standard DIS. To see this, we show in Fig. 3.18 the azimuthal $\widetilde{\phi}_g$ distribution of the gluon around the final state quark direction $\vec{n}_4$, for $\Theta_q = 90°$ and various fixed θ_4. A significant azimuthal asymmetry for $\mathcal{N}_{\text{SM}}$ is observed with a maximum in the plane of the scattering between the quark directions ($\widetilde{\phi}_g = 0°$), as expected. In contrast, the dependence of $\mathcal{N}_{\text{LQ}}$ on $\widetilde{\phi}_g$ is very weak, particularly for small θ_4.
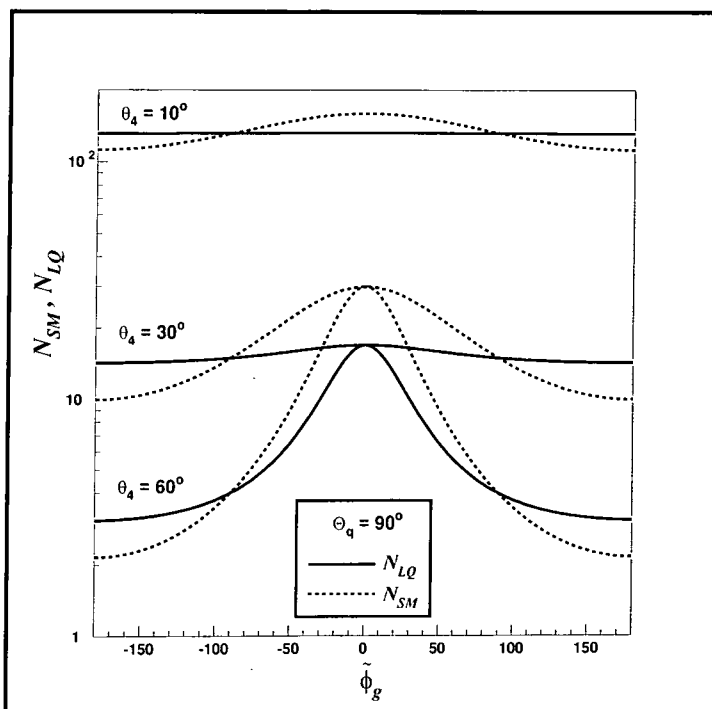
Figure 3.18: The dependence of the antenna patterns $\mathcal{N}_{\text{SM}}$ and $\mathcal{N}_{\text{LQ}}$ on the azimuthal angle $\widetilde{\phi}_g$ of the soft gluon around the outgoing quark $q(p_4)$. The gluon direction describes a cone around the quark of half–angle θ_4. The direction of the incoming quark $q(p_2)$ is defined by $\widetilde{\phi}_g = 0°$, and the incoming positron $e^+(p_1)$ is at $\widetilde{\phi}_g = \pm180°$. The overall c.m.s. scattering angle is fixed at $\Theta_q = 90°$.

3.4.2 Additional soft photons

As discussed in the introduction, it would be of considerable interest in distinguishing new physics models of the HERA high-Q^2 events to know the electric charge of the quarks in the $eq \rightarrow eq$ process. In principle, this information is contained in the distribution of soft *photon* radiation, which can be obtained in an analogous way to the soft

gluon distributions. The main difference is the presence of additional contributions from emission off the incoming and outgoing positrons.[10] The result for the antenna patterns is

$$\frac{1}{2}\mathcal{F}_{\text{SM}}^{\gamma} = e_q^2[24] - e_q\{[12] + [34] - [14] - [23]\} + [13], \qquad (3.123)$$

$$\begin{aligned}
\frac{1}{2}\mathcal{F}_{\text{LQ}}^{\gamma} = {} & e_q(1 + e_q)\{[2P] + [4P]\} + (1 + e_q)\{[1P] + [3P]\} \\
& - e_q\{[12] + [34]\} - (1 + e_q)^2[PP] \\
& + \chi_{\text{LQ}}\Big((1 + e_q)^2[PP] - e_q(1 + e_q)\{[2P] + [4P]\} \\
& - (1 + e_q)\{[1P] + [3P]\} + e_q^2[24] + e_q\{[14] + [23]\} + [13]\Big), \quad (3.124)
\end{aligned}$$

and, as before, $\mathcal{F}_{\text{SM}}^{\gamma} = \mathcal{F}_{\text{LQ}}^{\gamma}$ for $\chi_{\text{LQ}} = 1$. As argued in the previous section, it is the $\chi_{\text{LQ}} \to 0$ limit of $\mathcal{F}_{\text{LQ}}^{\gamma}$ which is relevant in practice, i.e. for photons with energy $\omega_\gamma \gg \Gamma_{\text{LQ}}$. In this limit we have

$$\begin{aligned}
\frac{1}{2}\mathcal{F}_{\text{LQ}}^{\gamma} = {} & e_q(1 + e_q)\{[2P] + [4P]\} + (1 + e_q)\{[1P] + [3P]\} \\
& - e_q\{[12] + [34]\} - (1 + e_q)^2[PP] \\
= {} & H(\cos\theta_2) + H(\cos\theta_4) \qquad (3.125)
\end{aligned}$$

where

$$H(z) = \frac{1}{1+z} + \frac{e_q^2}{1-z} - \frac{1}{2}(1 + e_q)^2. \qquad (3.126)$$

An interesting feature of the above distributions is the presence of _radiation zeros_, i.e. directions of the photon three–momentum $\vec{n}$ for which the cross section vanishes. A detailed study of radiation zeros is presented in Chapter 4. To see this for the distribution (3.125) we note that

$$H = 0 \qquad \text{for} \qquad z = z_0 \equiv \frac{1 - e_q}{1 + e_q}. \qquad (3.127)$$

For the two cases of interest $e_q = \frac{2}{3}, -\frac{1}{3}$ for which $z_0 = \frac{1}{5}, 2$. Therefore only for e^+u scattering is the radiation zero in the physical region.[11] For the full distribution (3.125) to vanish we obviously require

$$\cos\theta_2 = \cos\theta_4 = z_0. \qquad (3.128)$$

Thus for e^+u scattering the radiation zero is in the direction given by the intersection of the two cones of half–angle $\theta_0 = \arccos(1/5) = 78.46°$ centred on the quark directions $\vec{n}_2$ and $\vec{n}_4$. Three cases can be distinguished:

(i) For $0° < \Theta_q < 2\theta_0$ there are two solutions, corresponding to

$$\theta_\gamma = \theta_0, \qquad \phi_\gamma = \pm\arccos\left(\frac{\tan(\Theta_q/2)}{\tan\theta_0}\right). \qquad (3.129)$$

---

[10]The results in this section are for $e^+q \to e^+q$ scattering. Those for $e^-q \to e^-q$ can be obtained by an appropriate change of sign.

[11]We shall, however, discover a special kind of radiation zeros for $e^+d + \gamma$ processes in Chapter 4.
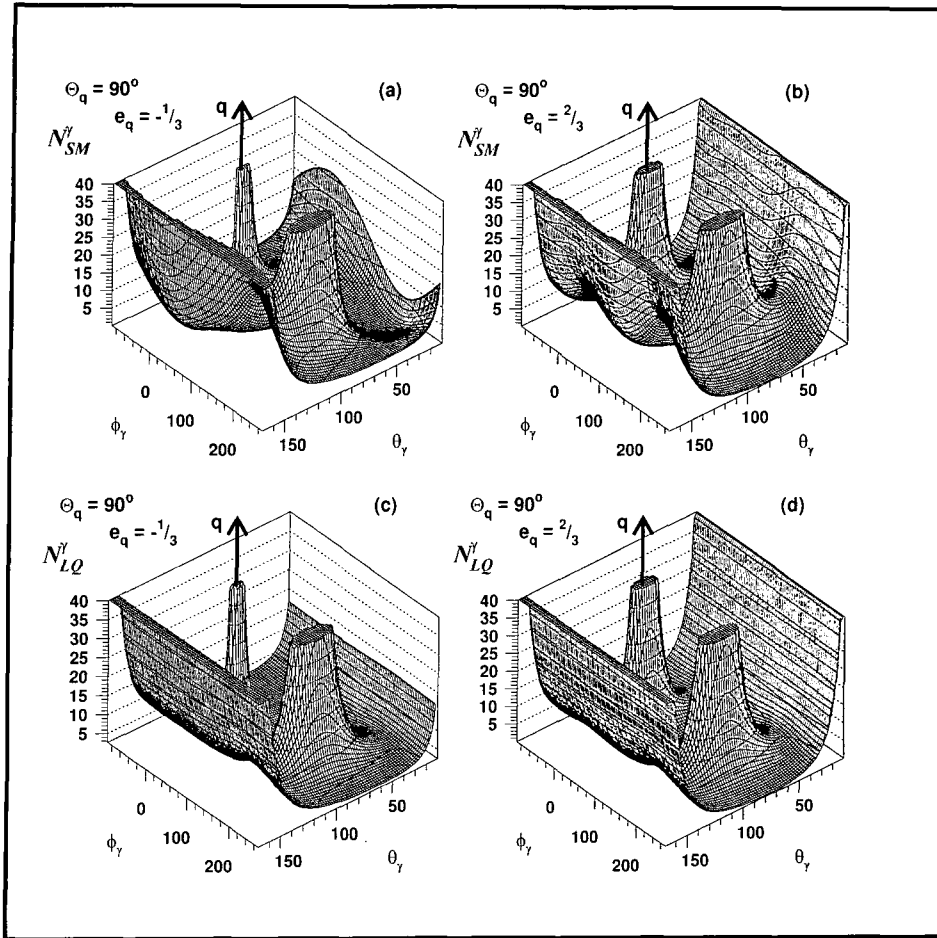
Figure 3.19: The pattern of soft γ radiation according to Eqs. (3.123,3.125) with $\mathcal{N}^\gamma_{\rm SM,LQ} = \omega_\gamma^2 \mathcal{F}^\gamma_{\rm SM,LQ}$, for e^+d scattering [(a),(c)] and e^+u scattering [(b),(d)]. The overall c.m.s. scattering angle is fixed at $\Theta_q = 90°$.

(ii) For $\Theta_q = 2\theta_0$ there is one solution,

$$\theta_\gamma = \theta_0 , \qquad \phi_\gamma = 0° , \tag{3.130}$$

corresponding to the bisector of the quark directions in the scattering plane.

(iii) For $\Theta_q = 0°$ there is a cone of solutions corresponding to $\theta_\gamma = \theta_0$.

Although the above results on the location of the radiation zeros have been derived for the leptoquark radiation pattern, they apply equally well for the SM distribution (3.123), or indeed for the generic distribution (3.124) for arbitrary $\chi_{\rm LQ}$. This follows from the fact that the zeros are the result of completely destructive interference between the classical electric fields associated with the different charged particles. They depend only on the relative orientation of the various particles, irrespective of whether intermediate resonances are formed.

As a numerical illustration of these results, we show in Fig. 3.19 the antenna patterns $\mathcal{N}^\gamma_{\rm SM}$, $\mathcal{N}^\gamma_{\rm LQ}(e_q = 2/3)$ and $\mathcal{N}^\gamma_{\rm LQ}(e_q = -1/3)$, with $\Theta_q = 90°$. To exhibit the radiation zeros
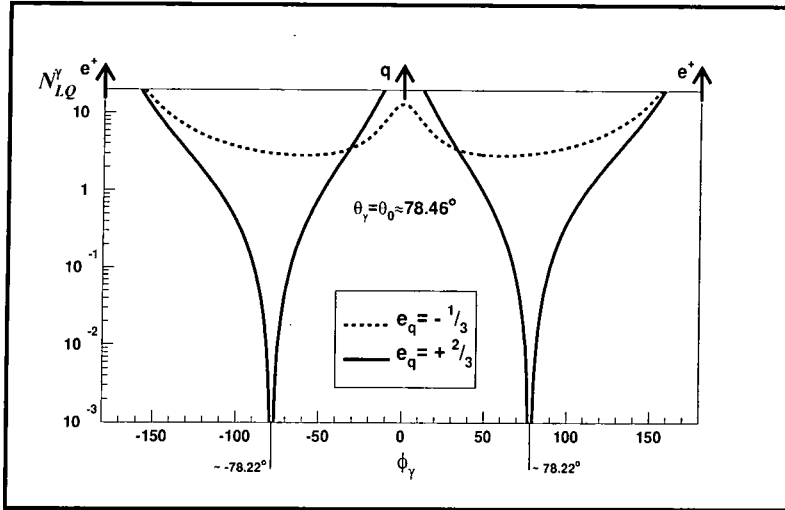
Figure 3.20: The soft photon antenna pattern $\mathcal{N}_{LQ}^{\gamma}$ for $\Theta_q = 90°$ at the critical angle $\theta_\gamma = \theta_0 \simeq 78.46°$ for e^+u (solid line) and e^+d (dashed line) scattering. Note the radiation zeros at $\phi_\gamma \simeq 78.22°$ (cf. Eq. (3.129)). The positions of the e^+ and q jets are indicated. Note also that $\mathcal{N}_{SM}^{\gamma}$ shows quantitatively the same behaviour for this choice of θ_γ.

more clearly, Fig. 3.20 shows the ϕ_γ dependence of the leptoquark $e_q = 2/3, -1/3$ distributions at the critical polar angle $\theta_\gamma = \theta_0$, i.e. the slices through the two–dimensional distributions of Fig. 3.19 at this value of θ_γ. The two zeros of the e^+u distribution at the ϕ_γ angles given by Eq. (3.129) are clearly visible. Note also that the behaviour of the distributions near the positron and the quark jet directions simply reflects the magnitude of the charge of the corresponding particles.

If the observation of an excess of high–Q^2 events at HERA persists (see discussion below), it will be important to devise new analysis techniques for identifying the origin of the excess. We have shown that the angular distribution of the accompanying hadronic radiation – the antenna pattern – is a potentially powerful tool for discriminating standard DIS events from those arising from the production of a long–lived coloured scalar 'leptoquark' resonance. The main qualitative difference is the absence for the latter of an enhancement of hadronic radiation between the incoming and outgoing quark jet directions (string effect), as shown in Fig. 3.16. It follows that soft hadrons are distributed more uniformly in azimuth around the final state quark jet direction in events where a leptoquark is produced, see Fig. 3.17. Our quantitative predictions are based on the phenomenologically successful principle of Local Parton Hadron Duality, and should therefore be a good guide to the behaviour of the distributions of soft hadrons and jets in the detectors. Ultimately, however, there will be no substitute for detailed Monte Carlo studies based on parton–shower/hadronisation models, provided that these include the correct underlying colour structure.

Finally we have extended our results to include soft photon radiation. Here the distributions have an additional sensitivity to the electric charge of the leptoquark, which is a crucial parameter in distinguishing models. For the case of charge 5/3 leptoquarks, produced for example in e^+u collisions, we discussed radiation zeros as a powerful tool

to pin down the leptoquark charge. We shall discuss these *classical* radiation zeros in the following chapter and focus on a *new type of radiation zeros* introduced into high–energy phenomenology recently by W.J. Stirling and the author of this thesis.

3.4.3 The status of high–Q^2 events at HERA

The two HERA experiments ZEUS [ZEUS97] and H1 [H1.97] reported an excess of events at very high values of momentum transfer Q^2 in e^+q scattering. The excess rates are shown in Table 3.1. There was a lot of speculation going on, what might trigger such

Experiment	events observed	events expected
H1 $Q^2 > 15000$ GeV^2	12	4.71 ± 0.76
ZEUS $Q^2 > 35000$ GeV^2	2	0.145 ± 0.013

Table 3.1: Analysis of the 1994–1996 data of high–Q^2 events from H1 and ZEUS. The number of events as they were observed are compared to the numbers of events expected from SM calculations.

an observation.

- **contact interaction:** (*cf.* [BW97]) This corresponds to the exchange of a very massive particle between the positron and quark, e.g. a heavy gauge boson Z' as we discussed in Chapter 2. This is called contact interaction, since the exchange of a heavy particle with mass M_X is restricted to a tiny range $\hbar/(M_X c)$ via the *uncertainty principle*. However both LEP and TEVATRON rule out the effect caused by contact interaction as it might have been observed in these experiments. For example a Z' of mass $M_{Z'} = 1$ TeV as we discussed earlier to explain the jet–excess data from the TEVATRON cannot simultaneously explain the HERA excess in Q^2.

- **compositeness:** The proliferation of quarks and leptons has inspired the speculation that they are composite structures, bound states of more fundamental constituents, often called *preons*. The basic assumption that underlines almost all composite model building is that the constituent preons interact by means of a new strong gauge interaction, sometimes called *metacolour* [EHLQ84]. Below a certain energy scale, the metacolour interaction becomes strong and binds the preons into metacolour–singlet states including the observed quarks and leptons.

  Compositeness of partons in terms of the HERA high–Q^2 events was first discussed by Adler [Adl97]. In his SU(4) model for preons, the positron interacts with a gluon and makes a transition to a $\mathcal{E}^+$ state, a kind of *leptogluon*, which decays into e^+ and a jet.

- **R–parity violating squark:** the kinematic distribution of the anomalous HERA events clearly favours the formation and the decay of a bound state in the e^+q system – i.e. a generic *leptoquark* (*cf.* [BRW87]). Leptons and quarks are unified in *grand unified theories* (GUT), which naturally predict leptoquark states. The

exchange of leptoquarks generally leads to violation of lepton and baryon number, and in particular to proton decay. Therefore the mass of the leptoquarks is assumed to be very heavy. From proton decay one has as lower limit $M_{\mathrm{LQ}} > 10^{15}$ GeV.

A more plausible scenario for such generic leptoquarks is the scalar superpartner of the quark (the *squark*) in the R–parity violating SUSY model [Alt97, DM97]. R–parity[12] is assumed to be preserved in the minimal supersymmetric SM. This implies that SUSY particles can only be produced in pairs and the lightest SUSY particle, the blessed *neutralino*, is stable and weakly interacting. R–parity violating squarks posess a *Yukawa coupling* λ' to lepton–quark pairs and can be singly produced as s–channel resonances. Using positron beams at HERA and neglecting interactions with sea quarks inside the proton, possible R–parity violating squarks are $\tilde{u}_L$, $\tilde{c}_L$ or $\tilde{t}_L$ via e^+d collison and thus electric charge $+\frac{2}{3}$.
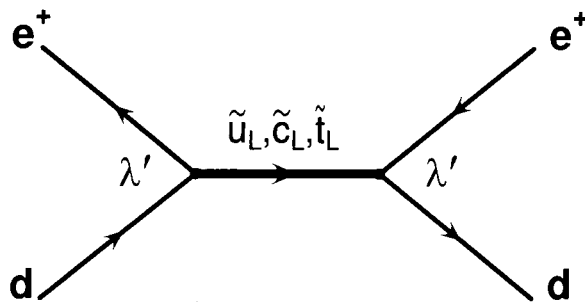
Limits on the Yukawa couplings can be found experimentally. For a recent review on the quest for (R–parity violating) squarks at HERA and limits on couplings and masses we refer to [Noy97].

These particles appear in a mass range of a few hundred GeV. And this fact favours the HERA data. Both collaborations observed the high–Q^2 events concentrated along a constant x value. And as $x = M^2/s$ at a constant value of M, M can be interpreted as the mass of the resonance produced in e^+q scattering. In Fig. 3.21 we show the result of the 1994–1996 analysis of the neutral current data by H1.

The figure shows selected neutral current DIS events in the $M - y$ plane. As the e^+ was tagged, all quantities are expressed in terms of the e^+ tagging method, i.e.

$$M_e = \sqrt{s x_e} = \sqrt{\frac{Q_e^2}{y_e}}, \quad Q_e^2 = \frac{E_{T,e}^2}{1 - y_e}.$$

Note the clustering of the high–Q^2 events at $M_e \simeq 200$ GeV. It is therefore *natural* to explain the anomalies in terms of an s–channel resonance, coupling and decaying into e^+q. This model was the focus in our studies of (hadronic) antenna patterns in Section 3.4.

As we discussed earlier these leptoquarks can have both lepton and baryon number violating Yukawa couplings and mediate proton decay. Usually these couplings are set to

---

[12] $R = (-1)^{3B+L+2S}$ with

B : baryon number,

L : lepton number,

S : spin.
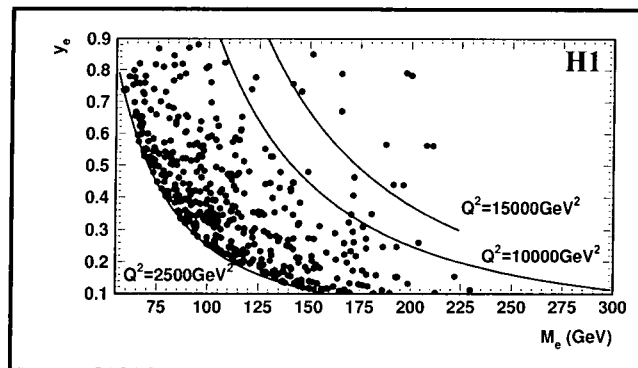
Figure 3.21: Selected neutral current DIS candidate events in the $M_e - y_e$ plane; three contours of fixed Q^2 are shown.

be zero by assuming R–parity conservation. These Yukawa couplings are not connected to any symmetry considerations and therefore one can assume a finite value for the lepton number violating coupling, which ensures squark coupling to the e^+q channel, while setting the baryon number violating coupling to zero, which prevents proton decay, thus

HERA "leptoquark": R–parity violating squark ?

A scalar leptoquark is more likely than a vector one, as a vector leptoquark has a coupling $\phi_\mu^\dagger G^{\mu\nu} \phi_\nu$ to gluons and would be produced by $q\bar{q} \to g \to \phi^\dagger \phi$ at the TEVATRON. But there was no such event observed within the postulated leptoquark mass range of about 200 GeV [CDF97]. The CDF collaboration reports a lower limit for the leptoquark mass of 300 GeV at a 95% confidence level.

latest results from HERA (1998)

Since the publications of the analysis of the 1994–1996 data, both HERA collaborations published results including 1997 data [Str97]. In the mass range $187.5 < M < 212.5$ GeV and $y > 0.4$ the ZEUS collaboration observes 3 events and expects from Monte Carlo studies 2.92 ± 0.24 events and is therefore in agreement with the SM in this mass range. The H1 collaboration observes in the same mass range 8 events and expects 1.53 ± 0.29 events, thus concludes that there is an apparent excess in this mass range.

In a higher mass bin ($M > 225$ GeV and $y > 0.25$) suddenly ZEUS observes 5 events compared to an expected 1.51 ± 0.13 events and verifies an excess rate. H1, however, is in perfect agreement with the SM in this mass bin. They observe 1 event and expect 0.752 ± 0.305 events. Thus both experiments seem to exclude each other concerning the mass bins of the observed excess rates.

In 1998 the e^-q data will be available [Els97] and in 2000 a luminosity upgrade is expected. One has to see, whether this high-Q^2 excess rates are physically genuine or whether everything is due to statistical fluctuations.

3.5   The main results revised

In this chapter we studied the emission of soft photons and gluons in high–energy processes. We realised that soft photon radiation is an ideal tool to probe colour and electric charges in a given process. We used photon antenna patterns to study the charge and radiation pattern of an s–channel resonance at HERA to gain further insight into the reported high-Q^2 events, assuming the formation of a "squark" or "leptoquark" as intermediate state. The study of photon radiation will also be the focus of Chapter 4, where we introduce radiation zeros as a probe of the SM in high–energy collider phenomenology. This discussion is directly based on the results we obtained so far.

To understand the dynamics of soft gluon radiation from a physical point of view we discussed colour coherence and the connected "drag" or "string" effect. This formed the basis of the important study of Higgs production at the LHC with additional gluon radiation. We showed how this additional gluon acts like a partonometer for the signal and QCD background processes and finally is a wonderful discriminator between the two processes. According to the different colour flows it was possible to locate a well–defined region in the gluon phase space where the signal/background ratio is maximal. We discussed also massive quarks and the phenomenon of the *"dead cone"*.

Colour coherence gained evidence by recent measurements at the TEVATRON and LEP1, as we discussed above. The verification of colour coherence allows further studies of the kind that were presented in this chapter. Of course, higher order corrections play an important role, especially the NLO and NNLO corrections for Higgs production at the LHC are quite large. As long as the emitted gluon is soft, then it was shown [Dok91] that a factorisation in a hard and soft part is in principle always possible. We say *in principle* because sometimes the colour structure is too complicated and factorisation is strictly only possible *graph–by–graph*.
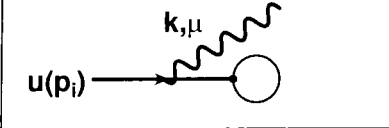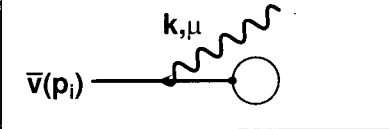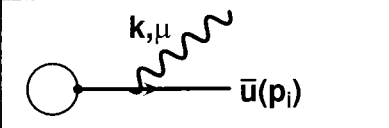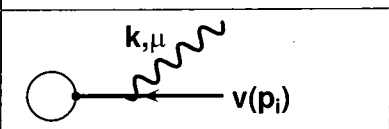
Understanding the soft gluon radiation pattern and assuming the Local Parton Hadron Duality to be valid allows for predicting the angular distribution of soft hadrons produced by the soft gluon jets. This is an *interjet* phenomena. Jet geometry like opening angle, 'hardness', etc. are topics of *intrajet* phenomena. We presented *angular ordering* as a typical intrajet feature in this work.

Appendix A

General formulation of soft radiation

A.1 Soft photon emission

We present the Feynman rules for the emission of a soft photon off external and internal charged spin-$\frac{1}{2}$ particles. The formalism can easily be extended to an arbitrarily charged particle of any spin. For our studies fermions with spin $\frac{1}{2}$ play the pivotal role. The rules for emission of *external* legs (particles and antiparticles) can be summarised as follows. We introduced the notation in Section 3.1.

	$\left(\mathcal{M}_{i,\mathrm{in}}^{\gamma}\right)^{\mu} = ee_i \left[-\dfrac{p_i^{\mu}}{p_i \cdot k} \right] u(p_i)$
	$\left(\mathcal{M}_{i,\mathrm{in}}^{\gamma}\right)^{\mu} = ee_i \left[\dfrac{p_i^{\mu}}{p_i \cdot k} \right] \bar{v}(p_i)$
	$\left(\mathcal{M}_{i,\mathrm{ex}}^{\gamma}\right)^{\mu} = ee_i \left[\dfrac{p_i^{\mu}}{p_i \cdot k} \right] \bar{u}(p_i)$
	$\left(\mathcal{M}_{i,\mathrm{ex}}^{\gamma}\right)^{\mu} = ee_i \left[-\dfrac{p_i^{\mu}}{p_i \cdot k} \right] v(p_i)$

We define the fermion propagator for a massive particle of four-momentum q^{μ} as

$$\Pi_f = i\frac{\slashed{q} + m}{q^2 - m^2 + i\epsilon},$$
(A.1)

and for the corresponding antifermion $(q^{\mu} \to -q^{\mu})$

$$\Pi_{\bar{f}} = i\frac{-\slashed{q} + m}{q^2 - m^2 + i\epsilon}.$$
(A.2)

134

If there is additional emission from an internal line, the formalism becomes slightly more difficult. As an example we show a process with 2 incoming particles (charged) and $n - 2$ outgoing particles (charged). Imagine there is an s-channel on-shell internal particle and $e_1 + e_2 \neq 0$.
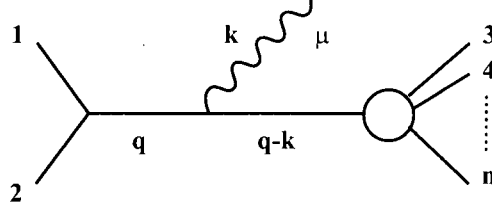
With the results of Section 3.1 we may write for the charge–weighted current of above process

$$\sum_{i=1}^{n+1} e_i J_i^{\mu} = \left\{ -e_1 \frac{p_1^{\mu}}{p_1 \cdot k} - e_2 \frac{p_2^{\mu}}{p_2 \cdot k} \right\} \mathcal{D}(q - k)$$

$$+ \left\{ e_3 \frac{p_3^{\mu}}{p_3 \cdot k} + e_4 \frac{p_4^{\mu}}{p_4 \cdot k} + \ldots + e_n \frac{p_n^{\mu}}{p_n \cdot k} \right\} \mathcal{D}(q)$$

$$+ (e_1 + e_2) \frac{q^{\mu}}{q \cdot k} \left\{ \mathcal{D}(q - k) - \mathcal{D}(q) \right\} , \qquad (A.3)$$

with $\mathcal{D}(q) = [q^2 - m^2 + i\epsilon]^{-1}$ (cf. Eq. (3.6)). It is straightforward to extend above formula to l incoming charged particles or more than one internal line. As long as there is radiation off *internal lines*, it proved convenient to absorb the propagator functions $\mathcal{D}(q)$ into the definition of the currents J_i^{μ}.

In order to calculate cross sections and thus the antenna pattern of a process with photon emission off internal lines, one has to calculate the product $J_{\mu} J^{\mu}$ according to the definition of the antenna pattern in Eq. (3.9). This means solve integrals over the virtuality q of the internal particles. It is straightforward to show that[1]

$$\int \mathrm{d}q^2 \, \mathcal{D}(q) \mathcal{D}^*(q) = \int \mathrm{d}q^2 \, \frac{1}{(q^2 - m^2)^2 + (m\Gamma)^2} = \frac{\pi}{m\Gamma} , \qquad (A.4)$$

$$\int \mathrm{d}q^2 \, \mathcal{D}(q - k) \mathcal{D}^*(q - k) = \int \mathrm{d}q^2 \, \frac{1}{((q - k)^2 - m^2)^2 + (m\Gamma)^2} = \frac{\pi}{m\Gamma} , \qquad (A.5)$$

$$\int \mathrm{d}q^2 \, \mathcal{D}(q) \mathcal{D}^*(q - k) = \int \mathrm{d}q^2 \, \frac{1}{q^2 - m^2 + i\epsilon} \frac{1}{(q - k)^2 - m^2 - i\epsilon}$$

$$= \frac{\pi}{\sqrt{(q \cdot k)^2 + m^2 \Gamma^2}} , \qquad (A.6)$$
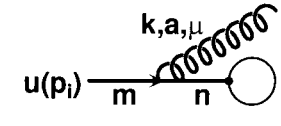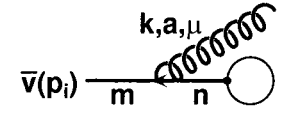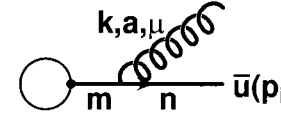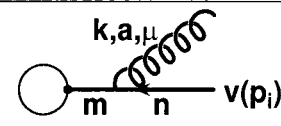
where we introduced the decay width Γ of the internal particle of mass m, i.e. $\epsilon = m\Gamma$.

---

[1]Use
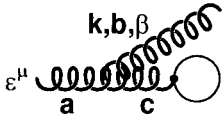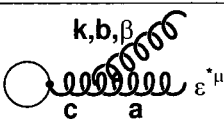
$$\int \frac{\mathrm{d}x}{x^2 + a^2} = \frac{1}{a} \arctan\left(\frac{x}{a}\right) .$$

A.2　Soft gluon emission

As before for soft photons we present the general rules for emission of soft gluons off external quark and antiquark legs.

	$$\left(\mathcal{M}^g_{i,\text{in}}\right)^\mu = g_s T^a_{mn}\left[-\frac{p^\mu_i}{p_i\cdot k}\right]u(p_i)$$
	$$\left(\mathcal{M}^g_{i,\text{in}}\right)^\mu = g_s T^a_{mn}\left[\frac{p^\mu_i}{p_i\cdot k}\right]\bar{v}(p_i)$$
	$$\left(\mathcal{M}^g_{i,\text{ex}}\right)^\mu = g_s T^a_{mn}\left[\frac{p^\mu_i}{p_i\cdot k}\right]\bar{u}(p_i)$$
	$$\left(\mathcal{M}^g_{i,\text{ex}}\right)^\mu = g_s T^a_{mn}\left[-\frac{p^\mu_i}{p_i\cdot k}\right]v(p_i)$$

Additionally we have emission off external gluons

	$$\left(\mathcal{M}^g_{i,\text{in}}\right)^\mu = g_s f^{abc}\left[-\frac{p^\beta_i}{p_i\cdot k}\right]\epsilon^{*\beta}(\lambda_1)\epsilon^\mu(\lambda_2)$$
	$$\left(\mathcal{M}^g_{i,\text{ex}}\right)^\mu = g_s f^{abc}\left[\frac{p^\beta_i}{p_i\cdot k}\right]\epsilon^{*\beta}(\lambda_1)\epsilon^{*\mu}(\lambda_2)$$

We want to study gluon emission off *internal* legs by addressing the example of Section 3.4, the production of a R–parity violating squark in the s–channel of e^+q collisions. The process $e^+q \to \tilde{q} \to e^+q + g$ is sketched below
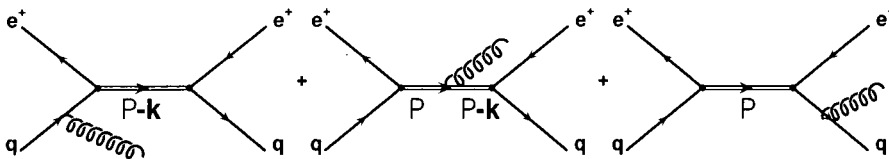
Adopting the notation from Appendix A.1 we may write for the colour charge current

$$\sum_{i=1}^{3} J^\mu_i = J^\mu_{q_{\text{in}}} + J^\mu_{\tilde{q}} + J^\mu_{q_{\text{out}}}$$

$$= -\frac{p_{q_{\text{in}}}^{\mu}}{p_{q_{\text{in}}} \cdot k} \mathcal{D}(\mathcal{P} - k) + \frac{\mathcal{P}^{\mu}}{\mathcal{P} \cdot k} \left\{ \mathcal{D}(\mathcal{P} - k) - \mathcal{D}(\mathcal{P}) \right\}$$
$$+ \frac{p_{q_{\text{out}}}^{\mu}}{p_{q_{\text{out}}} \cdot k} \mathcal{D}(\mathcal{P}) \,.$$

$\mathcal{P}^{\mu}$ is the four momentum of the squark $\tilde{q}$. With the right colour factor the antenna pattern reads

$$\frac{1}{2} \mathcal{F}_{\tilde{q}}^{g} = C_{\mathsf{F}} \left\{ [q_{\text{in}}\tilde{q}] + [q_{\text{out}}\tilde{q}] - [\tilde{q}\tilde{q}] + \chi_{\tilde{q}} \left[[\tilde{q}\tilde{q}] - [q_{\text{out}}\tilde{q}] - [q_{\text{in}}\tilde{q}] + [q_{\text{in}}q_{\text{out}}] \right] \right\} . \tag{A.7}$$

Again we absorb the propagators into the definition of the colour charge currents and define for radiation off internal lines a somewhat modified antenna pattern [Dok93, Jik91, KOS92]

$$\mathcal{F}^{g} = - \left(\frac{m\Gamma}{\pi} \right)^{2} \sum_{i,j} \mathcal{C}_{ij} \int \mathrm{d}q_{1}^{2} \mathrm{d}q_{2}^{2} J_{i}^{\mu}(q_{1}^{2}) J_{\mu,j}^{*}(q_{2}^{2}) \tag{A.8}$$

i.e. the antenna pattern of Eq. (3.23) normalised to the leading order contributions given in Eqs. (A.4,A.5). The integration variables q_1 and q_2 define again the four momentum of the internal particle which the radiation takes off from. From Eqs. (A.4,A.5,A.6) we immediately see that

$$\chi_{\tilde{q}}^{2} = \frac{M_{\tilde{q}}^{2}\Gamma_{\tilde{q}}^{2}}{(\mathcal{P} \cdot k)^{2} + M_{\tilde{q}}^{2}\Gamma_{\tilde{q}}^{2}} \tag{A.9}$$

for our example of s-channel squark production at HERA in Eq. (A.7) (cf. Eq. (3.117)).

Appendix B

Multi–photon (multi–gluon) amplitudes

We want to study the emission of more than one soft photon off a typical tree graph process. We start by investigating two–photon emission and shall expand this formalism to N photons in the aftermath. A typical process for the emission of two soft photons off an external leg is shown below.
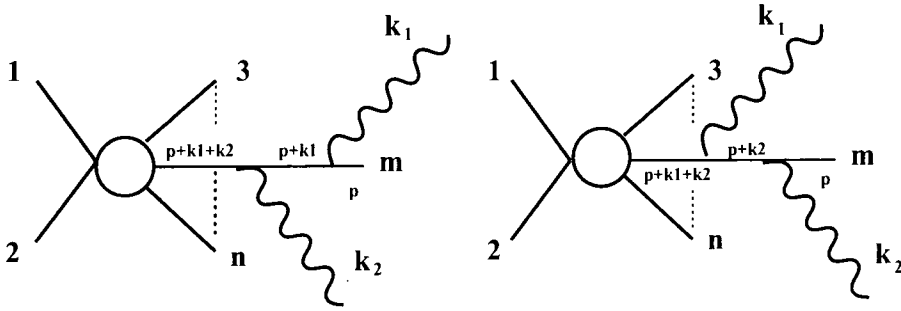
The matrix element in this case is the sum of the two matrix elements shown above. On the left–hand side we show the case that photon 2 is emitted prior to photon 1 and the matrix element of this topology reads

$$\mathcal{M}_{21} = e^2 \left\{ e_m J_{21}^{\mu_1} \epsilon_{\mu_1}(\lambda_1) \times e_m J_{21}^{\mu_2} \epsilon_{\mu_2}(\lambda_2) \right\} \mathcal{M}^0 \,, \tag{B.1}$$

with

$$J_{21}^{\mu_1} = \frac{p_m^{\mu_1}}{p_m \cdot k_1} \,, \quad J_{21}^{\mu_2} = \frac{p_m^{\mu_2}}{p_m \cdot (k_1 + k_2)} \,. \tag{B.2}$$

The currents for emission of photon 1 prior to photon 2 as shown on the right–hand side of above picture read

$$J_{12}^{\mu_1} = \frac{p_m^{\mu_1}}{p_m \cdot (k_1 + k_2)} \,, \quad J_{12}^{\mu_2} = \frac{p_m^{\mu_2}}{p_m \cdot k_2} \,. \tag{B.3}$$

So the total matrix element for the emission of two soft photons k_1 and k_2 off the external leg m reads

$$\mathcal{M}_m^{2\gamma} = e^2 e_m^2 \left\{ J_{21}^{\mu_1} J_{21}^{\mu_2} + J_{12}^{\mu_1} J_{12}^{\mu_2} \right\} \epsilon_{\mu_1}^*(\lambda_1) \epsilon_{\mu_2}^*(\lambda_2) \mathcal{M}^0 \,. \tag{B.4}$$

It is easy to show that

$$
\left\{ J_{21}^{\mu_1} J_{21}^{\mu_2} + J_{12}^{\mu_1} J_{12}^{\mu_2} \right\} = \frac{p_m^{\mu_1} p_m^{\mu_2}}{p_m \cdot k_1 \, p_m \cdot (k_1 + k_2)} + \frac{p_m^{\mu_1} p_m^{\mu_2}}{p_m \cdot k_2 \, p_m \cdot (k_1 + k_2)}
$$

$$
= p_m^{\mu_1} p_m^{\mu_2} \left\{ \frac{1}{(p_m \cdot k_1)^2 + p_m \cdot k_1 \, p_m \cdot k_2} + \frac{1}{(p_m \cdot k_2)^2 + p_m \cdot k_1 \, p_m \cdot k_2} \right\}
$$

$$
= \frac{p_m^{\mu_1}}{p_m \cdot k_1} \frac{p_m^{\mu_2}}{p_m \cdot k_2} \, .
$$

More generally, in emitting an *arbitrary* number N of soft photons from an external line m we can proceed via mathematical induction. We showed for two photons that

$$
\frac{1}{p_m \cdot k_1 \, p_m \cdot (k_1 + k_2)} + \frac{1}{p_m \cdot k_2 \, p_m \cdot (k_1 + k_2)} = \frac{1}{p_m \cdot k_1} \frac{1}{p_m \cdot k_2} \, . \tag{B.5}
$$

Imagine we proved for $N - 1$ photons that

$$
\prod_{i=1}^{N-1} \frac{1}{p_m \cdot \sum\limits_{j=1}^{i} k_j} + \text{permutations} = \prod_{i=1}^{N-1} \frac{1}{p_m \cdot k_i} \, , \tag{B.6}
$$

then we can write for N photons

$$
\prod_{i=1}^{N} \frac{1}{p_m \cdot \sum\limits_{j=1}^{i} k_j} + \text{permutations} = \frac{1}{p_m \cdot \sum\limits_{j=1}^{N} k_j} \prod_{i=1}^{N-1} \frac{1}{p_m \cdot k_i} + \text{permutations}
$$

$$
= \sum_{l=1}^{N} \frac{1}{p_m \cdot \sum\limits_{j=1}^{N} k_j} \prod_{j \neq l} \frac{1}{p_m \cdot k_j}
$$

$$
= \left\{ \sum_{l=1}^{N} \frac{1}{p_m \cdot \sum\limits_{j=1}^{N} k_j} \times (p_m \cdot k_l) \right\} \prod_{j=1}^{N} \frac{1}{p_m \cdot k_j} = \prod_{j=1}^{N} \frac{1}{p_m \cdot k_j} \, .
$$

Thus in extension to Eqs. (3.7, 3.15) we may write for the emission of N photons from one external leg m (incoming or outgoing)

$$
J_m^{\mu_1 \mu_2 \cdots \mu_N} = (\eta_m)^N \prod_{i=1}^{N} \frac{p_m^{\mu_i}}{p_m \cdot k_i} \, , \tag{B.7}
$$

with $\eta_m = -1$ for an incoming and $\eta_m = +1$ for an outgoing external leg. The matrix element of this process thus reads

$$
\mathcal{M}_m^{N\gamma} = (e e_m)^N J_m^{\mu_1 \mu_2 \cdots \mu_N} \epsilon_{\mu_1}^*(\lambda_1) \epsilon_{\mu_2}^*(\lambda_2) \ldots \epsilon_{\mu_N}^*(\lambda_N) \times \mathcal{M}^0 \, . \tag{B.8}
$$

What we derived so far also holds for the emission of an *arbitrary* number of soft photons from internal lines. But again care has to be taken and formula (B.7) cannot be applied straightforwardly. In principle a decomposition of the propagators $\mathcal{D}(q)$ in extension to (3.6) is possible, however the redefinition of the current is non–trivial.

As far as emission off external legs are concerned, the reader should be able to write down the antenna pattern for emission off an *arbitrary number of photons* off an *arbitrary number of external legs* of an arbitrary process. The extension to emission off boson lines should be regarded as an "exercise" and will not be presented here.

The same argumentation holds for multi gluon emission and will not be presented here in length. The main differences are additional colour factors as they were discussed in Section 3.1.2 and the self–coupling of the gluons, i.e. the gluon triple vertex V_{ggg}. As we showed in Section 3.1.2, the basic structure of the additional factors for emission off quarks or gluons are identical (modulo colour factors). The results are summarised in Appendix A.2. We also discussed gluon emission off internal legs, carrying a colour charge. With the formalism developed for multiphoton emission, the reader should be able to formulate soft multi gluon emission.

References for Chapter 3

— A —

[AGIS83]   B. Andersson, G. Gustafson, G. Ingelman and T. Sjöstrand, *Phys. Rep.* **97** (1983) 31.

[AGS80]   B. Andersson, G. Gustafson and T. Sjöstrand, *Phys. Lett.* **B94** (1980) 211.

[APS98]   J. Amundson, J. Pumplin and C. Schmidt, *Phys. Rev.* **D57** (1998) 527.

[ATLAS94]   ATLAS Technical Proposal, CERN/LHC/94-43 LHCC/P2 (December 1994).

[Adl97]   S.L. Adler, SU(4) Preonic Interpretation of the HERA Positron–Jet Events, hep-ph/9702378, (1997).

[Alt97]   G. Altarelli, J. Ellis, G.F. Giudice, S. Lola and M.L. Mangano, *Nucl. Phys.* **B506** (1997) 3.

[Azi85a]   Ya.I. Azimov, Yu.L. Dokshitzer, V.A. Khoze and S.I. Troyan, *Z. Phys.* **C27** (1985) 65.

[Azi85b]   Ya.I. Azimov, Yu.L. Dokshitzer, V.A. Khoze and S.I. Troyan, *Phys. Lett.* **B165** (1985) 147.

[Azi86a]   Ya.I. Azimov, Yu.L. Dokshitzer, V.A. Khoze and S.I. Troyan, *Z. Phys.* **C31** (1986) 213.

[Azi86b]   Ya.I. Azimov, Yu.L. Dokshitzer, V.A. Khoze and S.I. Troyan, *Sov. J. Nucl. Phys.* **43** (1985) 95.

— B —

[BN37]   F. Bloch and A. Nordsieck, *Phys. Rev.* **37** (1937) 54.

[BRW87]   W. Buchmüller, R. Rückl and D. Wyler, *Phys. Lett.* **B191** (1987) 442.

[BW97]   W. Buchmüller and D. Wyler, *Phys. Lett.* **B407** (1997) 147.

— C —

[CDF94]   CDF Collaboration: F. Abe *et al.*, *Phys. Rev.* **D50** (1994) 5562.

[CDF97]   CDF Collaboration: F. Abe *et al.*, *Phys. Rev. Lett.* **79** (1997) 4327.

[CMS94]   CMS Technical Proposal, CERN/LHC/94-43 LHCC/P1 (December 1994).

[Chu55]   A.E. Chudakov, *Ser. Fiz.* **19** (1955) 650.

— D —

[DØ.95]   DØ Collaboration: S. Abachi *et al.*, Proc. International Europhysics Conference on High Energy Physics (HEP 95), Brussels, Belgium, 1995.

[DØ.97]   DØ Collaboration: S. Abachi *et al.*, Contributed to 18th International Symposium on Lepton - Photon Interactions (LP 97), Hamburg, Germany, 1997.

[DEL96]   DELPHI Collaboration: P. Abreu *et al.*, *Z. Phys.* **C70** (1996) 179.

[DKS92]   Yu.L. Dokshitzer, V.A. Khoze and T. Sjöstrand, *Phys. Lett.* **B274** (1992) 116.

[DKT87]   Yu.L. Dokshitzer, V.A. Khoze and S.I. Troyan, *Sov. J. Nucl. Phys.* **46** (1987) 712.

[DKT91]   Yu.L. Dokshitzer, V.A. Khoze and S.I. Troyan, *J. Phys.* **G17** (1991) 1481; *J. Phys.* **G17** (1991) 1602.

[DM97]   H. Dreiner and P. Morawitz, *Nucl. Phys.* **B503** (1997) 55.

[Dok91]   Yu.L. Dokshitzer, V.A. Khoze, A.H. Mueller and S.I. Troyan, Basics of Perturbative QCD, ed. J. Tran Thanh Van, (Editions Frontiéres), Gif-sur-Yvette 1991.

[Dok93]   Yu.L. Dokshitzer, V.A. Khoze, L.H. Orr and W.J. Stirling, *Nucl. Phys.* **B403** (1993) 65.

— E —

[EHLQ84]   E. Eichten, I. Hinchliffe, K. Lane and C. Quigg, *Rev. Mod. Phys.* **56** (1984) 579.

[EKS97]   J. Ellis, V.A. Khoze and W.J. Stirling, *Z. Phys.* **C75** (1997) 287.

[Els97]   E. Elsen, talk presented at the International Europhysics Conference on High–Energy Physics (EPS97), Jerusalem, 1997.

— F —

[FSY61]   S.C. Frautschi, H. Suura and D.R. Yennie, *Ann. Phys. (NY)* **13** (1961) 379.

— H —

[H1.97]   H1 Collaboration: C. Adloff *et al.*, *Z. Phys.* **C74** (1997) 191.

[HR97]   J.L. Hewett and T.G. Rizzo, *Phys. Rev.* **D56** (1997) 5709.

— J —

[JADE88]   JADE Collaboration: F. Ould–Saada *et al.*, *Z. Phys.* **C39** (1988) 1.

[Jik91]   G. Jikia, *Phys. Lett.* **B257** (1991) 196.

— K —

[KKT96]   K. Kimura, M. Kitazawa and K. Tesima, *Z. Phys.* **C72** (1996) 271.

[KMS97]   Z. Kunszt, S. Moretti and W.J. Stirling, *Z. Phys.* **C74** (1997) 479.

[KO97]   V.A. Khoze and W. Ochs, *Int. J. Mod. Phys.* **A12** (1997) 2949.

[KOS92]   V.A. Khoze, L.H. Orr and W.J. Stirling, *Nucl. Phys.* **B378** (1992) 413.

[KOS94]   V.A. Khoze, J. Ohnemus and W.J. Stirling, *Phys. Rev.* **D49** (1994) 1237.

[KS97a]   Z. Kunszt and W.J. Stirling, *Z. Phys.* **C75** (1997) 453.

[KS97b]   V.A. Khoze and W.J. Stirling, *Z. Phys.* **C76** (1997) 59.

— L —

[L3.95]   L3 Collaboration: M. Acciarri *et al.*, *Phys. Lett.* **B345** (1995) 74.

[LHC90]   Proceedings of the Large Hadron Collider Workshop, Aachen, 1990, eds. G. Jarlskog and D. Rein.

— M —

[MW84]   G. Marchesini and B.R. Webber, *Nucl. Phys.* **B238** (1984) 1.

[MW90]   G. Marchesini and B.R. Webber, *Nucl. Phys.* **B330** (1990) 261.

— N —

[Noy97]   V.A. Noyes, talk presented at the Hadron Collider Physics conference, Stony Brook, 1997.

— O —

[OPAL95]   OPAL Collaboration: R. Akers *et al.*, *Z. Phys.* **C68** (1995) 531.

— P —

[PSZ97]   T. Plehn, H. Spiesberger, M. Spira and P.M. Zerwas, *Z. Phys.* **C74** (1997) 611.

— S —

[SMW94]   A. Stange, W. Marciano and S. Willenbrock, *Phys. Rev.* **D50** (1994) 4491.

[Str97]   B. Straub, talk presented at the Lepton–Photon conference (LP97), Hamburg, 1997.

— T —

[TPC86]   TPC/2γ Collaboration: H. Aihara *et al.*, *Phys. Rev. Lett.* **57** (1986) 945.

— W —

[Web84]   B.R. Webber, *Nucl. Phys.* **B238** (1984) 492.

— Z —

[ZEUS97]   ZEUS Collaboration: J. Breitweg *et al.*, *Z. Phys.* **C74** (1997) 207.

Chapter 4

Radiation zeros — more about nothing

> "It is so much easier to do
> a measurement than knowing
> what one is really measuring."
>
> (J.W.N. Sullivan)

In the previous chapter we discussed antenna patterns for processes with soft gluons or soft photons in the final state. We discussed that these antenna patterns act as *partonometer* for a given process, specific to final–state kinematics, masses, colour and electric charges. In this chapter we shall study another feature of antenna patterns (i.e. amplitudes with additional radiation of photons and gluons, not necessarily being soft): the occurence of *radiation zeros* in certain processes. Almost all Born (tree–level) amplitudes for the radiation of photons and gluons and *other massless gauge bosons* have such zeros. But it is not always possible to find a real (*physical*) solution. Basically we shall see that this is strictly speaking mostly the case for photon radiation. Radiation zeros can be observed under certain circumstances as will be discussed in Section 4.1 where we shall work out the general features and properties of them which may be shortly characterised as vanishing of radiation in a certain region of the photon phase–space due to complete destructive interference between initial and final–state radiation.

The discussion of radiation zeros in the literature goes back to the early 80's when general theorems for their existence have been formulated. Very recently, however, we discovered a *new type of radiation zeros* with some important different features compared to the "classical" ones.

We shall then study radiation zeros at HERA in Section 4.2 and at the LEP collider in Section 4.3 and show some important applications for high–energy phenomenology.

Finally we shall review the main results of this chapter, the main results obtained elsewhere and give some ideas for further studies of radiation zeros in Section 4.4.

4.1 Introducing radiation zeros

In certain high–energy scattering processes involving the emission of one or more photons, the scattering amplitude vanishes for particular configurations of the final–state particles. Such configurations are known as *radiation zeros*. They also appear for the emission of other massless gauge bosons in the physical region, i.e. not yielding complex solutions. We shall not discuss radiation zeros in gluon radiation, as from the structure of the colour factors there were no zeros found so far in SU(3). It is, however, shown, that for SU($\sqrt{2}$) there *are* radiation zeros in the physical region [Bro97] but this discussion can not be the focus of this thesis. Therefore, if we talk about radiation zeros, we shall basically only refer to γ radiation, even though we mean all massless gauge bosons in principle.

Radiation zeros have an interesting history. Although they are in principle present in QED amplitudes, they first attracted significant attention in processes involving weak bosons. For example, the pioneering papers of Mikaelian, Sahdev and Samuel [MSS79] and Brown, Sahdev and Mikaelian [BMS79] considered radiative charged weak boson production in $q'\bar{q}$ and νe collisions. The cross sections for these processes vanish when the photon is emitted in certain directions. As an example [MSS79, BMS79] one finds for the W production mechanism at hadron–hadron colliders via $d(p_1) + \bar{u}(p_2) \to W^-(p_3) + \gamma(k)$ a radiation zero at

$$\cos\theta_\gamma = \frac{1}{3}, \tag{4.1}$$

where θ_γ is the polar angle of the photon in the c.m.s. frame with $\theta_\gamma = 0°$ in the incoming d–quark direction. Recently, experimental evidence for zeros of this type has been found at the Fermilab TEVATRON $p\bar{p}$ collider [CDF97]. We shall come back to this important fact in Section 4.4.

In addition to the phenomenological analyses, a deeper theoretical understanding was developed in the pioneering papers by Brodsky and Brown [BB82] and Brodsky, Brown and Kowalski [BBK83]. More extensive studies followed by Passarino [Pas83] and Laursen, Samuel, Sen and Sylvester [LSS83, Lau84, Lau85].

4.1.1 Classical (type 1) radiation zeros

The vanishing of the (tree–level) scattering amplitude can be understood as arising from complete destructive interference of the classical radiation patterns of the incoming and outgoing charged particles. As we discussed in the previous chapter any process of the form

$$1, 2, \cdots, l \to (l+1, l+2, \cdots, n) + \gamma,$$

where we assume the emission of one soft photon, can be written as (*cf.* Eq. (3.7))

$$\mathcal{M}^\gamma \simeq e \left\{ \sum_i e_i J_i^\mu \epsilon_\mu^*(\lambda_i) \right\} \mathcal{M}^0. \tag{4.2}$$

We adopt the definition of the charge current (*cf.* Eq. (3.15))

$$\sum_i e_i J_i^\mu = \sum_{i=1}^n \eta_i e_i \frac{p_i^\mu}{p_i \cdot k}, \tag{4.3}$$

with $\eta_i = -1$ for emission from an *incoming* and $\eta_i = +1$ for emission off an *outgoing* particle and e_i being the charge of the ith particle. The classical [BB82, BBK83] radiation zeros are obtained by noting that the condition

$$\frac{e_1}{p_1 \cdot k} = \frac{e_2}{p_2 \cdot k} = \cdots = \frac{e_n}{p_n \cdot k},$$
(4.4)

immediately yields $\mathcal{M}^\gamma = 0$ (i.e. radiation zeros) if

(a) energy and momentum is conserved: $\sum_i \eta_i p_i^\mu = 0$,

(b) charge is conserved: $\sum_i \eta_i e_i = 0$,

(c) all particles are electrically charged,

(d) all particles have the same sign of electric or colour charge, i.e. $e_i e_j > 0 \ \forall i, j$.

To understand the *same sign rule* it is necessary to note that $p_i \cdot k \geq 0 \ \forall i$ and thus from Eq. (4.4) follows (d). This condition (4.4) was first formulated by Brodsky and Brown [BB82] and we shall call the radiation zeros obeying Eq. (4.4) *classical* radiation zeros or *radiation zeros of type 1*. In principle, and we mentioned this study earlier, there are also radiation zeros with physical solutions in the process $e^- \bar{\nu}_e \to W^- \gamma$, i.e. for one chargeless fermion. This process was studied in [BMS79, MSS79]. Defining the polar angle of the photon with respect to the direction of the incoming e^- we obtain by solving Eq. (4.4)

$$\frac{-1}{1 - \cos\theta_\gamma} = \frac{e_{\bar{\nu}_e}}{1 + \cos\theta_\gamma} = 0, \quad \Rightarrow \quad \cos\theta_\gamma = 1.$$
(4.5)

We find a solution but the radiation zero of above process lies *on* the beam line and gets swamped by the collinear singularity. Thus, even though there is a solution for chargeless fermions, it is of no phenomenological interest and thus assumption (c) makes a great deal of sense.

Let us study the paradigm process that we mentioned above in more detail: W^- production via $d\bar{u}$ fusion plus additional (soft) photon.
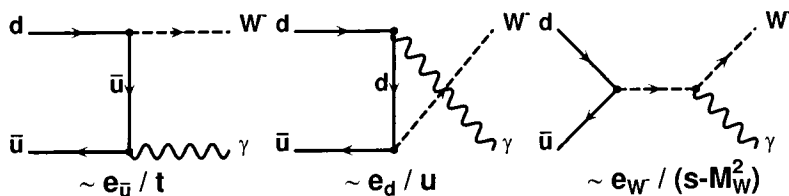
At the tree level there are three diagrams contributing to the matrix element. A t–channel diagram with an amplitude proportional to $e_{\bar{u}}/t$, a u–channel diagram proportional to e_d/u and a s–channel diagram proportional to $e_{W^-}/(s - M_W^2)$. We further note that if the polar angle of the photon is again defined with respect of the incoming d quark direction that $t = -\frac{1}{2}(s - M_W^2)(1 + \cos\theta_\gamma)$. With $s + t + u = M_W^2$ and $e_d + e_{\bar{u}} = e_{W^-}$ we finally can write the amplitude as

$$\mathcal{M}_{W^-}^\gamma = \left\{ \frac{e_{\bar{u}}}{t} - \frac{e_d}{u} \right\} \times F(\sigma_i, \lambda_i, p_i),$$
(4.6)

where $F(\sigma_i, \lambda_i, p_i)$ denotes a reduced matrix element as a function of the fermion helicity σ_i, the vector boson polarisation λ_i and the external momenta p_i. Solving $\mathcal{M}_{W^-}^\gamma = 0$ immediately yields

$$\cos\theta_\gamma = \frac{e_{\bar{u}} - e_d}{e_{\bar{u}} + e_d} = \frac{1}{3}, \tag{4.7}$$

which is exactly what one finds by solving Eq. (4.4), i.e.

$$\frac{e_{\bar{u}}}{p_{\bar{u}} \cdot k} = \frac{e_d}{p_d \cdot k} \quad \Leftrightarrow \quad \frac{e_{\bar{u}}}{1 + \cos\theta_\gamma} = \frac{e_d}{1 - \cos\theta_\gamma}. \tag{4.8}$$

What happens if a *massive* gauge boson is "radiated", i.e. how would the process $d\bar{u} \to W^- Z$ look like with focus on radiation zeros? The question was answered by Baur, Han and Ohnemus [BHO94]. The amplitude can be written as

$$\mathcal{M}_{W^-}^Z = \mathcal{X} F_{\mathcal{X}}(\sigma_i, \lambda_i, p_i) + \mathcal{Y} F_{\mathcal{Y}}(\sigma_i, \lambda_i, p_i), \tag{4.9}$$

where $\mathcal{X}$ and $\mathcal{Y}$ are combinations of left–handed gauge couplings

$$\mathcal{X} = \frac{s}{2}\left(\frac{g_{\bar{u}}^L}{t} - \frac{g_d^L}{u}\right), \quad \mathcal{Y} = g_d^L \frac{s M_Z^2}{2u(s - M_W^2)}. \tag{4.10}$$

We see from Eq. (4.9) that the helicity amplitudes would factorise for $M_Z = 0$ and we could locate the radiation zeros by solving $g_d^L t - g_{\bar{u}}^L u = 0$, which would yield exactly the same solution as for radiation of a massless γ in Eq. (4.7) but now with different gauge couplings (g_i^L rather than e_i), if and only if $\mathcal{Y} = 0$. As long as the radiated gauge boson is massive we always have $\mathcal{Y} \neq 0$. But, and this was the discussion in Ref. [BHO94], in the high–energy limit $s \gg M_Z$ we achieve $\mathcal{Y} \simeq 0$ and thus an approximate solution

$$\cos\theta_Z = \frac{g_{\bar{u}}^L - g_d^L}{g_{\bar{u}}^L + g_d^L} + \mathcal{O}\left(\frac{M_Z^2}{s}\right). \tag{4.11}$$

One easily sees the coincidence of this solution with Eq. (4.7) in the high–energy limit. Why do we mention this example? Radiation zeros are dependent on the gauge couplings $(e_i, g_i^L, \cdots)$. This dependence turns out to be very subtle. Thus, any anomaly from the gauge coupling quite strongly influences the position of the radiation zeros. One of the hopes is to use radiation zeros as diagnostic tool to pin down gauge couplings with extreme accuracy, only limited by the resolution (i.e. detectability of radiation zeros) of the detector. We shall discuss further details at the end of this chapter in Section 4.4.

This is a typical example of an *approximate radiation zero*.

Brodsky and Brown showed [BB82] that condition (4.4) holds for any tree level amplitude including contact (seagull) graphs, independent of the spin of the particles and the photon helicities. Radiation zeros also survive the transition from a soft to a hard photon. The constraint (4.4) is also valid for massive particles. Imagine as an easy example massive incoming charged particles, e.g. two massive quarks, and let their masses m and energies E be equal. Then we find for the polar angle[1] $\widehat{\theta}_\gamma$ where radiation zeros can be observed

$$\frac{e_1}{p_1 \cdot k} = \frac{e_2}{p_2 \cdot k} \quad \Rightarrow \quad \cos\widehat{\theta}_\gamma = \frac{e_2 - e_1}{e_1 + e_2} \frac{1}{\rho}, \tag{4.12}$$

---

[1] From now on we denote the position of the radiation zeros in the photon phase space with $\widehat{\theta}_\gamma$ and $\widehat{\phi}_\gamma$.

where θ_γ is defined with respect to the incoming particle 1 and $\rho = \sqrt{1 - (m/E)^2}$. From this simple example we may already derive some interesting features of radiation zeros:

- For $e_1 = e_2 = Q$ we find for the polar angle $\widehat{\theta_\gamma} = 90°$, i.e. the position of the radiation zero is *symmetric* with respect to the beam line. Complete destructive interference only takes place orthogonal to the direction of the equally charged incoming particles;

- In order to obtain *physical solutions*, we obviously require

$$-1 < \frac{e_2 - e_1}{e_1 + e_2} \frac{1}{\rho} < 1$$

and thus

$$\frac{m}{E} < 2 \frac{\sqrt{e_1 e_2}}{|e_1 + e_2|} .$$

Not only can one realise the important fact that only the *same sign rule* yields physical solutions, i.e. $e_1 e_2 > 0$ but also that there is a critical mass m_{crit} for which the radiation zeros move out of the physical phase space for $m > m_{\text{crit}}$. Again for $e_1 = e_2 = Q$ we find as condition for the occurence of radiation zeros $m < E$. At threshold $m = E$ the incoming particles are *at rest* and therefore do not radiate.

We may now summarise our results on type 1 radiation zeros

(1) The underlying condition for the vanishing of the matrix element $\mathcal{M}^\gamma$ is given in Eq. (4.4). Additionally we need energy–momentum and charge conservation.

(2) This condition holds for emission off scalar as well as vector particles of arbitrary spin.

(3) From the physical point of view radiation zeros are due to complete destructive interference of the classical radiation patterns of the incoming and outgoing particles.

(4) All particles must have the same sign of charge (colour charge, electric charge) and any chargeless particle in the external legs yields "collinear radiation zeros" (see discussion above).

(5) Radiation zeros are only observable in tree–amplitudes, including contact interactions. One loop corrections spoil the destructive interference as was shown by Laursen, Samuel and Sen [LSS83]. Considering the amplitude for the radiative decay of W^- into two scalars, i.e. $W^- \to \phi_1 \phi_2 \gamma$ including one–loop gluon corrections, the authors showed that *triangle* (and *box*) graphs spoil radiation zeros, whereas gluon self–energy graphs and contact interactions (seagull graphs) do not.
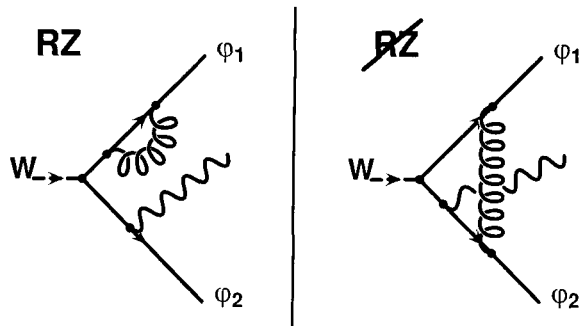
This is easy to see, as from the self–energy diagrams additional factors $e_i/(p_i \cdot \ell)$ are picked up yielding internal momenta ℓ that have to be integrated over. For emission from a triangle graph (picture on the right) it is impossible to tell what the underlying factor $e_i/(p_i \cdot \ell)$ is which finally should fulfill Eq. (4.4), or let us argue more physically motivated: if there is gluon emission and reabsorption from the same leg during a time Δt, then there will be certainly no emission of a photon from this leg during Δt. There might be a small probability but the uncertainty relation governs the limits. This is different for the triangle graph on the right hand side. Imagine we have gluon emission off leg 1 and absorption from leg 2. During this time the two legs gained a further transverse separation which in principle gives leg 2 enough time to radiate off photons, before absorbing the gluon from leg 1.

Brodsky, Brown and Kowalski found same results for radiative decay of W into fermions [BBK83].

(6) The positions of radiation zeros $(\hat{\theta}_\gamma, \hat{\phi}_\gamma)$ are dependent on the charge, the kinematical configuration and the masses of the underlying particles.

(7) Radiation zeros are independent of the helicity of the photon (massless gauge boson, gluon) and show up for soft and hard radiation. The emitted particle should have a spin $\jmath \leq 1$. Passarino showed [Pas84] how gravitons (spin 2 particles) spoil the radiation symmetry and that no radiation zeros can be found.

Besides the important contributions to the understanding of radiation zeros in relativistic field theory which we cited above we would like to mention the studies of Grose and Mikaelian [GM81]. The question which these authors address is how radiation zeros can be used as diagnostic tool to distinguish purely hadronic decays of the gauge bosons from radiative decays, i.e. distinguish $W \to q'\bar{q}g$ and $Z \to q\bar{q}g$ from $W \to q'\bar{q}\gamma$ and $Z \to q\bar{q}\gamma$.

A nice phenomenological application was presented by Hagiwara, Halzen and Herzog [HHH84]. They studied subprocesses like $q'q \to q'q\gamma$ at a $p\bar{p}$ collider to pin down the colour charge of the participating quarks by measuring the positions of the radiation zeros. The main reason for this study was the experimental verification of quarks with charges $-1/3$ and $+2/3$ instead of colour charges 0 or 1 as they were postulated in the *Han–Nambu quark model.*

Very recently studies of radiation zeros in multiple photon emission processes like $p\bar{p} \to W^{\pm}\gamma\gamma \to \ell^{\pm}\nu\gamma\gamma$ were presented [Bau97]. This process is of some importance for measuring possible anomalous couplings of the trilinear $WW\gamma$ vertex and also deals as discriminator for the W signal at the TEVATRON.

4.1.2 Classical interpretation of radiation zeros

Radiation zeros are not a special feature of relativistic high–energy processes but have their origin in non–relativistic dipole scattering (*cf.* [LL75]).

Imagine a system of particles with charges Q_i and masses m_i. Imagine further that the distances a_{ij} between these charges is small compared to the wavelength λ_i of the emitted radiation. All particles must be in accelerated motion in order to radiate but because of $a_{ij} \ll \lambda_i$ we have

$$v_i \ll c.$$

Defining the total dipole moment of a system of n charged particles as

$$\vec{\mathbf{d}} \equiv \sum_{i=1}^{n} e_i \vec{\mathbf{r}}_i \,,$$

the electric field is equal to

$$\vec{\mathcal{E}} = \frac{1}{c^2}(\ddot{\vec{\mathbf{d}}} \times \vec{\mathbf{n}}) \times \vec{\mathbf{n}} \,,$$

and for the magnetic field one finds

$$\vec{\mathcal{H}} = -\frac{1}{c^2}\ddot{\vec{\mathbf{d}}} \times \vec{\mathbf{n}} \,.$$

Note that we defined the time derivative $\dot{\vec{\mathbf{x}}} = \frac{d}{dt}\vec{\mathbf{x}}$.

The observation is now: suppose for all n particles the charge to mass ratios are the same, i.e.

$$\frac{e_i}{m_i} = \kappa \quad \forall i \in \{1, 2, \cdots, n\} \,.$$

Then

$$\vec{\mathbf{d}} = \sum_{i=1}^{n} e_i \vec{\mathbf{r}}_i = \kappa \sum_{i=1}^{n} m_i \vec{\mathbf{r}}_i = \kappa \vec{\mathcal{R}} \sum_{i=1}^{n} m_i \,,$$

where $\vec{\mathcal{R}}$ is the radius vector of the centre of inertia of the system (this definition is possible due to the fact that $v_i \ll c$). The electric $\vec{\mathcal{E}}$ and magnetic $\vec{\mathcal{H}}$ fields are proportional to $\ddot{\vec{\mathbf{d}}}$ and thus proportional to $\ddot{\vec{\mathcal{R}}}$. But as the centre of inertia moves with *constant* velocity we find $\ddot{\vec{\mathcal{R}}} = 0$ and thus *no radiation*.

Eq. (4.4) as it was derived by Brodsky and Brown [BB82] may be interpreted as the *relativistic* continuation of non–relativistic dipole radiation, giving a more general condition for the occurence of radiation zeros.

In the following we shall present a *new type of radiation zeros* <u>not</u> fulfilling condition (4.4). But besides a few other remarkable feature we shall discuss below, everything we said about type 1 radiation zeros ((1)–(7)) will still be valid.

4.1.3 New (type 2) radiation zeros

There is a new type of radiation zeros that only arises when the scattering is *planar*, i.e. the three–momenta of all the particles including the photon lie in the same plane. This was not the case for the classical type 1 radiation zeros which basically are not restricted to a certain region of the phase space as the kinematical configuration changes. Type 2

radiation zeros, however, only *exist inside the scattering plane.* In this case, if one chooses one of the photon polarisation vectors $\epsilon_\perp$ to be orthogonal to the scattering plane then $\epsilon_\perp \cdot p_i = 0$ for all i gives $\epsilon_\perp \cdot J = 0$ for *any* orientation of the particles and photon in the plane.
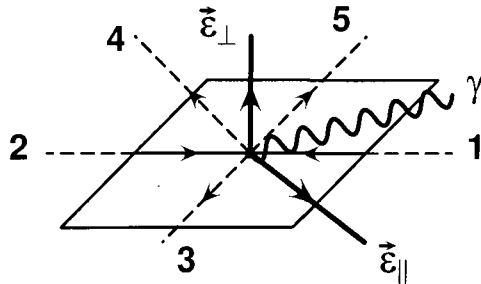
The requirement that the amplitude $\mathcal{M}^\gamma$ vanishes for *all* helicities and polarisations means that one must also have $\epsilon_\| \cdot J = 0$, where (the spatial part of) $\epsilon_\|^\mu$ is inside the scattering plane and orthogonal to the photon direction. The solution of $\epsilon_\| \cdot J = 0$ then gives the position in photon angular phase of the radiation zero. If we denote the direction of the three–momentum of particle i by $\vec{n}_i$ and the direction of the photon by $\vec{n}$, then the condition is (for massless particles)

$$\sum_i e_i \eta_i \frac{\vec{\epsilon}_\| \cdot \vec{n}_i}{1 - \vec{n} \cdot \vec{n}_i} = 0 \,, \tag{4.13}$$

with $\vec{\epsilon}_\| \cdot \vec{n} = 0$.
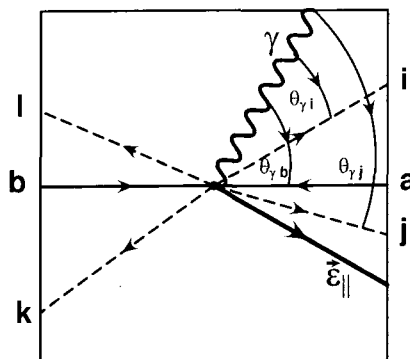
If we define $\theta_{\gamma i}$ as the angle between the photon and particle i directions, then we arrive at

$$\vec{\epsilon}_\| \cdot \vec{n}_i \;=\; \cos\left(\frac{\pi}{2} - \theta_{\gamma i}\right) = \sin\theta_{\gamma i} \,, \tag{4.14}$$

$$\vec{n} \cdot \vec{n}_i \;=\; \cos\theta_{\gamma i} \,, \tag{4.15}$$

and finally condition (4.13) can be cast into the simpler form

$$\sum_i e_i \eta_i \cot(\theta_{\gamma i}/2) = 0 \,. \tag{4.16}$$

Note that $\theta_{\gamma i}$ must be defined in the same sense (clockwise or anticlockwise from the γ direction) for each particle, so that the cot can have either sign. Eq. (4.16) allows us to derive an existence proof for the zeros.

First we note that $\cot(\theta_{\gamma i}/2) \to \infty$ as $\theta_{\gamma i} \to 0$ — these are the usual collinear singularities for massless gauge boson emission from massless fermions. Second, we note that not all the $e_i\eta_i$ can have the same sign (charge conservation). Therefore there exists at least one angular sector, between j and k say, where the collinear singularity has the opposite sign (i.e. $\to \pm\infty$) on the boundaries of the sector. Since the left–hand side of (4.16) defines a continuous function of the photon polar angle away from the collinear singularities, according to the *Intermediate Value Theorem* the function must vanish somewhere in the sector between j and k. The exact location of the zero depends not only on the strength of the collinear singularities at $\theta_{\gamma j}, \theta_{\gamma k} = 0$ but also on the other non–singular contributions ($i \neq j, k$) to the current in that region.

For $2 \to 2$ scattering the solutions to (4.13) or (4.16) can be found analytically, for more complicated scattering numerical methods can be used. The existence of zeros requires certain constraints on the charges, masses and scattering kinematics to be satisfied, as we shall see in the following sections. For example, there are no collinear singularities for massive fermions, and therefore the existence of a radiation zero in the angular sector depends on how strongly the distribution is peaked close to the massive particles, which in turn depends on the exact value of the mass.

Type 2 zeros do not require that all the charges have the same sign. For example, the process $e^-d \to e^-d\gamma$ has zeros of both types, whereas $e^-e^+ \to d\bar{d}\gamma$ only has type 2 zeros. Although for simplicity we have used soft–photon matrix elements and kinematics in the discussion above, radiation zeros of both types are also found when exact kinematics and matrix elements are used.

Let us summarise the main differences between type 1 and type 2 zeros.

(1) Type 2 zeros can only be found inside the scattering plane.

(2) To locate radiation zeros of type 2 for a given process including massless particles one has to create a suitable set of polarisation vectors $\epsilon^\mu(\lambda = \pm) = \left\{\epsilon_\perp^\mu, \epsilon_\parallel^\mu\right\}$ fulfilling the following conditions

   - $\epsilon^2 = -1$,
   - $\epsilon_\perp \cdot k = 0$ and $\epsilon_\parallel \cdot k = 0$,
   - $\epsilon_\perp \cdot p_i = 0$.

   and solve Eq. (4.16) or in simple cases Eq. (4.13).

(3) As it is obvious from Eq. (4.16) there is *no* need for a *same sign rule* as was needed for type 1 zeros. This means that only with type 2 zeros studies of radiation zeros at, e.g., LEP become possible.

The point (3) is quite remarkable. Constrained by the same sign rule there were never predictions for radiation zeros at e^+e^- colliders. Nearly every process in leading order contains radiation zeros and it is also easy to see from Eq. (4.16) that not necessarily *all* particles need to have electric or colour charge.

There is still a lot to be done about type 2 radiation zeros; a huge realm of applications for high–energy phenomenology opens. Radiation zeros are the fingerprints of a given process, depending on the underlying particles, kinematics, masses, etc. as will be shown below. The aim is to distinguish signal and background processes using radiation patterns as we discussed in Chapter 3 and additionally radiation zeros if they exist for a given process. In the ideal case one hopes that there will be radiation zeros exclusively in either the signal or background process. As we shall discuss in the following there should be a clear signal in the signal/background ratio where the radiation zero is expected. In reality the radiation zeros will be *"washed out"*, i.e. one observes *radiation* DIPS rather than exact *zeros*.

In the following we shall discuss radiation zeros at the HERA *ep* and the LEP e^+e^- collider demonstrating in detail what we tried to summarise in this introduction.

4.2 Radiation zeros in $eq \to eq\gamma$ scattering

Same–sign charge scattering occurs naturally in high–energy hadron collisions in subprocesses such as $u\bar{d} \to W^+\gamma$. However similar phenomena can be expected in lepton–hadron collisions, and in particular at HERA in processes such as $eq \to eq + \gamma$ for $eq = e^+u$ or e^-d. Studies of radiation zeros for these processes at HERA were first performed by Bilchak [Bil85], Couture [Cou89], Li, Reid, and Samuel [LRS90] and more recently by Doncheski and Halzen [DH91], in the framework of type 1 zeros.

With the introduction of the new type of radiation zeros in Section 4.1.3 we are no longer restricted to the same sign rule, but might explore the Standard Model $e^+q \to e^+q + \gamma$ process with no restrictions on q.

From an experimental point of view the detection of photons in the final state is highly non–trivial. The rates are small (suppressed by $\mathcal{O}(\alpha)$ compared to the total cross section) and the photons must be well–separated from the beam and from the other final–state particles, and contained within the detector. The basic question is whether the radiation zeros of the scattering amplitude correspond to 'detectable' photons at HERA. In this study we will present results for typical values of the DIS variables y and Q^2 which correspond to observable quark jets and scattered positrons. For these values we will investigate the location of the radiation zeros for photons with an energy greater than 5 GeV.

The strategy is as follows. We first consider soft–photon emission and derive analytic solutions for the location of the radiation zeros in the eq c.m.s. frame. We then show how the transition from soft– to hard–photon emission shifts the position of the zeros. Finally we move to the HERA lab frame to see where the zeros occur in the detector. We also compare our exact matrix–element results with an approximate calculation in which photon emission is included in the collinear approximation, which could correspond for example to a parton–shower implementation of such emission. This model has no radiation zeros and serves as a benchmark for the amplitude suppression in the exact result.

In the following we shall study the reactions

$$e^+(p_1)\, u(p_2) \quad \to \quad e^+(p_3)\, u(p_4) + \gamma(k)\,, \tag{4.17}$$

$$e^+(p_1)\, d(p_2) \quad \to \quad e^+(p_3)\, d(p_4) + \gamma(k)\,. \tag{4.18}$$

Other scattering combinations $(e^+\bar{u}, e^-u, \ldots)$ can be obtained from these basic processes by readjusting the charge factors. The expression for the matrix element squared (summed and averaged over spins) may for example be obtained by crossing the expression for $e^+e^- \to \mu^+\mu^- + \gamma$ given in Ref. [Ber81]. In terms of the four–momenta defined in Eqs. (4.17,4.18) the matrix element for massless quarks and leptons is

$$|\overline{\mathcal{M}}_3|^2(e^+q \to e^+q + \gamma) = e^6 e_q^2 \frac{(p_1 \cdot p_2)^2 + (p_3 \cdot p_4)^2 + (p_1 \cdot p_4)^2 + (p_2 \cdot p_3)^2}{(p_1 \cdot p_3)(p_2 \cdot p_4)} \mathcal{F}_{eq}^\gamma, \quad (4.19)$$

with the antenna pattern (*cf.* Section 3.1.1)

$$\frac{1}{2}\mathcal{F}_{eq}^\gamma = e_q^2[24] - e_q\{[12] + [34] - [14] - [23]\} + [13]. \quad (4.20)$$

The eikonal factors $[ij]$ are defined in Eq. (3.11).

The antenna pattern of Eq. (4.20) contains collinear $(\vec{k} \cdot \vec{p}_i \to 0)$ as well as infrared $(\omega_\gamma \equiv E_{\text{photon}} \to 0)$ singularities. It is this factor which vanishes for certain configurations of the momenta. Note that we only take the neutral current γ^*–exchange into account as the antenna pattern in Eq. (4.20) is independent of the exchanged particles as long as they do not themselves emit photons. This approximation will influence the cross section rate slightly at high Q^2, but will not affect the position of the radiation zeros.

Type 1 radiation zeros

To see under what conditions $\mathcal{F}_{eq}^\gamma$ vanishes, we first recall the 'single–photon theorem' from Section 4.1.1 which states that the amplitude vanishes when the charge–weighted scalar products $Q_i/(p_i \cdot k)$ are equal (*cf.* (4.4)). If we denote the common value by λ, then

$$[ij] = (Q_iQ_j)^{-1}\lambda^2 \, p_i \cdot p_j \quad (4.21)$$

and it is straightforward to show by substitution in Eq. (4.20) that this gives $\mathcal{F}_{eq}^\gamma = 0$. In the present context, the equality of the charge–weighted scalar products corresponds to

$$\frac{1}{p_1 \cdot k} = \frac{e_q}{p_2 \cdot k} = \frac{1}{p_3 \cdot k} = \frac{e_q}{p_4 \cdot k}. \quad (4.22)$$

We can obtain a simple analytic solution to these equations by taking the soft–photon limit in which $\omega_\gamma/E_i \to 0$. In this limit we have simple two–body kinematics for the quarks and leptons, $p_1 + p_2 = p_3 + p_4$. If we work in the e^+q c.m.s. frame, and define θ_2, θ_4 to be the angle between the photon and the incoming and outgoing quarks respectively, then the equations (4.22) become

$$\frac{1}{1 + z_2} = \frac{e_q}{1 - z_2} = \frac{1}{1 + z_4} = \frac{e_q}{1 - z_4}, \quad (4.23)$$

where $z_i = \cos\theta_i$. Equivalently,

$$z_2 = z_4 = \frac{1 - e_q}{1 + e_q}. \quad (4.24)$$

A necessary condition for such a solution to physically exist is $e_q \geq 0$ $(\Rightarrow |z_i| \leq 1)$, i.e. e^+u or $e^+\bar{d}$ scattering. This reproduces the well–known result for scattering of particles

with the same sign of electric charge, as discussed in Section 4.1.1. By itself, however, the condition $e_q \geq 0$ is not sufficient to guarantee a zero in the scattering amplitude. The equation $z_2 = z_4$ can only be satisfied for certain configurations of the final–state particles. To see this, we introduce an explicit representation of the c.m.s. four–momenta:

$$p_1^\mu = \frac{\sqrt{s}}{2}(1,0,0,-1), \tag{4.25}$$

$$p_2^\mu = \frac{\sqrt{s}}{2}(1,0,0,1), \tag{4.26}$$

$$p_4^\mu = \frac{\sqrt{s}}{2}(1,\sin\Theta_q,0,\cos\Theta_q), \tag{4.27}$$

$$p_3^\mu = \frac{\sqrt{s}}{2}(1,-\sin\Theta_q,0,-\cos\Theta_q), \tag{4.28}$$

$$k^\mu = \omega_\gamma(1,\sin\theta_\gamma\cos\phi_\gamma,\sin\theta_\gamma\sin\phi_\gamma,\cos\theta_\gamma). \tag{4.29}$$

These variables are illustrated in Fig. 4.1.
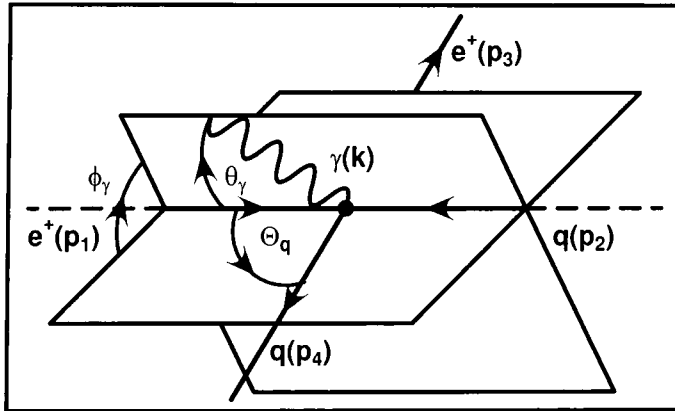
Figure 4.1: Parametrisation of the kinematics for $e^+(p_1)q(p_2) \to e^+(p_3)q(p_4) + \gamma(k)$ scattering in the e^+q c.m.s. frame. The orientation of the photon relative to the scattering plane is denoted by θ_γ and ϕ_γ.

It is straightforward to show that the conditions for $\mathcal{F}^\gamma_{eq} = 0$ defined in Eq. (4.24) correspond to

$$\cos\widehat{\theta}_\gamma = \frac{1-e_q}{1+e_q}, \tag{4.30}$$

and

$$\widehat{\phi}_\gamma = \pm \arccos\left(\frac{\tan(\Theta_q/2)}{\tan\widehat{\theta}_\gamma}\right). \tag{4.31}$$

Thus for $e_u = +2/3$ we find radiation zeros at $\widehat{\theta}_\gamma \simeq 78.46°$ and for $e_{\bar{d}} = +1/3$ at $\widehat{\theta}_\gamma = 60°$. We present the positions of the radiation zeros $(\widehat{\phi}_\gamma,\widehat{\theta}_\gamma)$ for process (4.17) (e^+u scattering) in Fig. 4.2(a).

Note that the requirement of a physical solution for $\widehat{\phi}_\gamma$ places restrictions on Θ_q. There are two radiation zeros in the $(\phi_\gamma,\theta_\gamma)$ plane for $\Theta_q < 2\widehat{\theta}_\gamma \simeq 156.94°$. The cones around the incoming and outgoing quarks defined by $z_2, z_4 = 1/5$ have two lines of
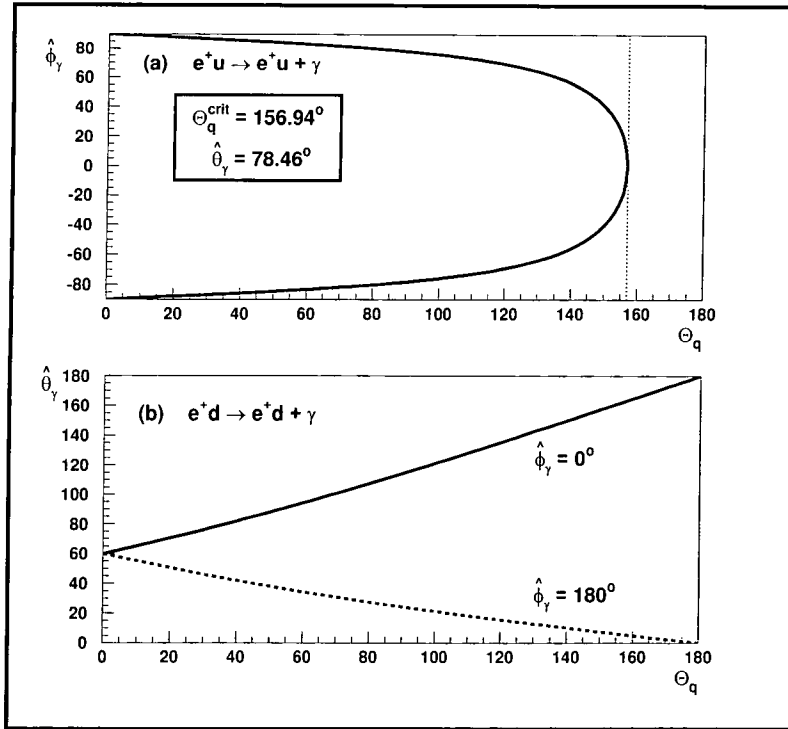
Figure 4.2: The position of the radiation zeros as a function of the quark scattering angle Θ_q for soft–photon emission in (a) $e^+u \to e^+u + \gamma$ and (b) $e^+d \to e^+d + \gamma$ in the $(\phi_\gamma, \theta_\gamma)$ c.m.s. phase space of the soft photon.

intersection along which there is completely destructive interference of the radiation. Note also that at $\Theta_q = 2\widehat{\theta}_\gamma = \Theta_q^{\mathrm{crit}}$ the radiation zeros degenerate to a single line (i.e. single point in $(\phi_\gamma, \theta_\gamma)$ space) located in the scattering plane ($\widehat{\phi}_\gamma = 0°$). There are no radiation zeros for $\Theta_q > 2\widehat{\theta}_\gamma \simeq 156.94°$. Finally, for $\Theta_q = 0°$ there is an *infinite number of radiation zeros* (*'null zone'*) located on a cone around the beam line with opening angle $\widehat{\theta}_\gamma$.

Type 2 radiation zeros

The processes (4.17,4.18) exhibit a second class of radiation zeros, which we discussed in Section 4.1.3, which do not satisfy the 'single–photon theorem'. These zeros are located in the scattering plane at $\widehat{\phi}_\gamma = 0°$ and $\widehat{\phi}_\gamma = 180°$. The corresponding θ_γ values may be calculated straightforwardly in the soft–photon approximation as a function of the quark charge e_q and the quark scattering angle Θ_q. The result is

$$\cos\widehat{\theta}_\gamma = \frac{1}{2}\frac{\left(1 - e_q^2\right)(1 + \cos\Theta_q) \pm \sqrt{\Delta_\gamma(e_q, \cos\Theta_q)}}{(1 - e_q)^2}, \qquad (4.32)$$

with

$$\Delta_\gamma(e_q, \cos\Theta_q) = \left[\left(e_q^2 - 1\right)(1 + \cos\Theta_q)\right]^2$$
$$- 4(1 - e_q)^2 \left(e_q^2 \cos\Theta_q + 2e_q + \cos\Theta_q\right). \qquad (4.33)$$

The condition $\Delta_\gamma\left(e_q, \cos\Theta_q\right) \geq 0$ constrains the range of e_q for which physical zeros exist. In terms of the polar angle Θ_q we have

$$-\infty < e_q \leq \frac{\cos\Theta_q + 3 - 2\sqrt{2(1 + \cos\Theta_q)}}{1 - \cos\Theta_q} \leq 1, \qquad (4.34)$$

or

$$1 \leq \frac{\cos\Theta_q + 3 + 2\sqrt{2(1 + \cos\Theta_q)}}{1 - \cos\Theta_q} \leq e_q < +\infty, \qquad (4.35)$$

the latter being actually redundant since Standard Model quarks have $|e_q| \leq +2/3$. From Eq. (4.34) we obtain constraints on the quark scattering angle Θ_q for particular flavours of quark. There are radiation zeros for all $e_q < 0$ and for positively charged quarks in a limited range of Θ_q. We summarise the results in Table 4.1.

e^+u	$e_q = +2/3$	$\cos\Theta_q \leq \pi - \arccos\left(\frac{23}{25}\right)$	$\Theta_q \gtrsim 157°$
$e^+\bar{d}$	$e_q = +1/3$	$\cos\Theta_q \leq -\frac{1}{2}$	$\Theta_q \geq 120°$
e^+d	$e_q = -1/3$	$\forall\ \cos\Theta_q$	$\forall\ \Theta_q$
$e^+\bar{u}$	$e_q = -2/3$	$\forall\ \cos\Theta_q$	$\forall\ \Theta_q$

Table 4.1: Ranges of the quark scattering angle Θ_q, for different quark charges, for which radiation zeros exist. Note that for $e_q < 0$ there are always two radiation zeros in the scattering plane for $\widehat{\phi}_\gamma = (0°, 180°)$ with the $\widehat{\theta}_\gamma$ value given by Eq. (4.32).

Note that e^+u scattering has both type 1 and 2 zeros. However, the latter are located very close to the beam direction, making their observation difficult in practice. They also require very high Q^2 (back–scattered quarks) and therefore have a small event rate. The positions of the type 2 zeros for e^+d scattering are shown in Fig. 4.2(b) as a function of Θ_q. Finally, Table 4.2 lists the numerical values of the radiation zero angles $(\widehat{\phi}_\gamma, \widehat{\theta}_\gamma)$ for several values of Θ_q.

Θ_q	e^+d scattering		e^+u scattering	
30°	$(0°, 76.12°)$	$(180°, 46.12°)$	$(-86.86°, 78.46°)$	$(86.86°, 78.46°)$
45°	$(0°, 84.98°)$	$(180°, 39.98°)$	$(-83.23°, 78.46°)$	$(83.23°, 78.46°)$
90°	$(0°, 114.29°)$	$(180°, 24.29°)$	$(-78.22°, 78.46°)$	$(78.22°, 78.46°)$

Table 4.2: Position of the radiation zeros $(\widehat{\phi}_\gamma, \widehat{\theta}_\gamma)$ for three different quark scattering angles Θ_q, in the soft–photon approximation.

4.2.1   Zeros for arbitrary photon energies

The analytic results obtained above use the soft–photon approximation. However radiation zeros of both types exist for *all* photon energies and can be located using numerical techniques.[2] We continue to work in the e^+q c.m.s. frame but now use exact $2 \to 3$ kinematics. Without any essential loss of generality, we can keep the direction (Θ_q) and the energy (E'_q) of the outgoing quark fixed and vary the direction and energy of the outgoing photon, constructing simultaneously the four–momentum of the outgoing positron to conserve energy and momentum. The new four–vectors of the outgoing quark, lepton and photon momenta are then

$$p_4^\mu = E'_q \left(1, \sin\Theta_q, 0, \cos\Theta_q\right) , \tag{4.36}$$

$$p_3^\mu = p_1^\mu + p_2^\mu - p_4^\mu - k^\mu , \tag{4.37}$$

$$k^\mu = \omega_\gamma \left(1, \sin\theta_\gamma \cos\phi_\gamma, \sin\theta_\gamma \sin\phi_\gamma, \cos\theta_\gamma\right) . \tag{4.38}$$

Once again we obtain a vanishing matrix element in Eq. (4.19) if the antenna pattern $\mathcal{F}^\gamma_{eq}$ of Eq. (4.20) is zero. For type 1 radiation zeros, the single–photon theorem again leads to the conditions in Eq. (4.22). The equality of $p_1 \cdot k$ and $p_2 \cdot k$ leads immediately to Eq. (4.30), i.e. the radiation zeros are at fixed $\widehat{\theta}_\gamma$ *independent of the photon energy*. However the azimuthal angle $\widehat{\phi}_\gamma$ does vary with ω_γ, since the supplementary condition $z_2 = z_4$ only applies in the $\omega_\gamma \to 0$ limit. For type 2 zeros, it can be shown that the condition $\widehat{\phi}_\gamma = 0°, 180°$ again applies for arbitrary ω_γ, i.e. the zeros are always located in the scattering plane.

In Fig. 4.3 we show the dimensionless quantity $\mathcal{N}^\gamma_{eq} = \omega^2_\gamma \mathcal{F}^\gamma_{eq}$ for different photon energies and fixed final–state quark kinematics.

The figures (a) and (b) correspond respectively to slices through the $(\phi_\gamma, \theta_\gamma)$ plane according to the positions of the soft–photon type 1 and 2 radiation zeros of the previous sections. As the photon energy increases, there is a systematic shift in the positions of the zeros. As radiation zeros are semi–classical effects due to destructive interference, it is easy to understand that fixing the position of the outgoing quark and simultaneously increasing ω_γ shifts the interference regions between the participating charged particles as the outgoing positron must balance energy and momentum and thus changes its relative orientation. Thus the asymmetric ω_γ dependence of the two radiation zeros in Fig. 4.3(a) is due simply to our choice of fixing the final–state quark direction rather than the direction of the scattered positron. The zero in the quadrant between the (fixed) incoming positron and outgoing quark directions is relatively insensitive to the changes in the positron direction induced by varying ω_γ. The other zero follows the direction of the outgoing positron as ω_γ increases. The same effect also explains the symmetric dependence of the two radiation zeros for the process $e^+u \to e^+u + \gamma$. The zeros are located symmetrically above and below the scattering plane and are influenced equally by changes in the scattered positron direction.

Figs. 4.4(a,b) show the positions[3] of the radiation zeros $\mathcal{Z}_d$ and $\mathcal{Z}_u$ for the two processes as a function of the photon energy at various fixed Θ_q. $\mathcal{Z}_d(\Theta_d, \omega_\gamma)$ is located in the quadrant between the outgoing positron and the incoming d quark and $\mathcal{Z}_u(\Theta_u, \omega_\gamma)$

---

[2]Note that we use massless quarks and leptons to calculate the matrix elements. However both types of radiation zero are also present for non–zero masses.

[3]The exact locations of the zeros are determined by a numerical procedure.
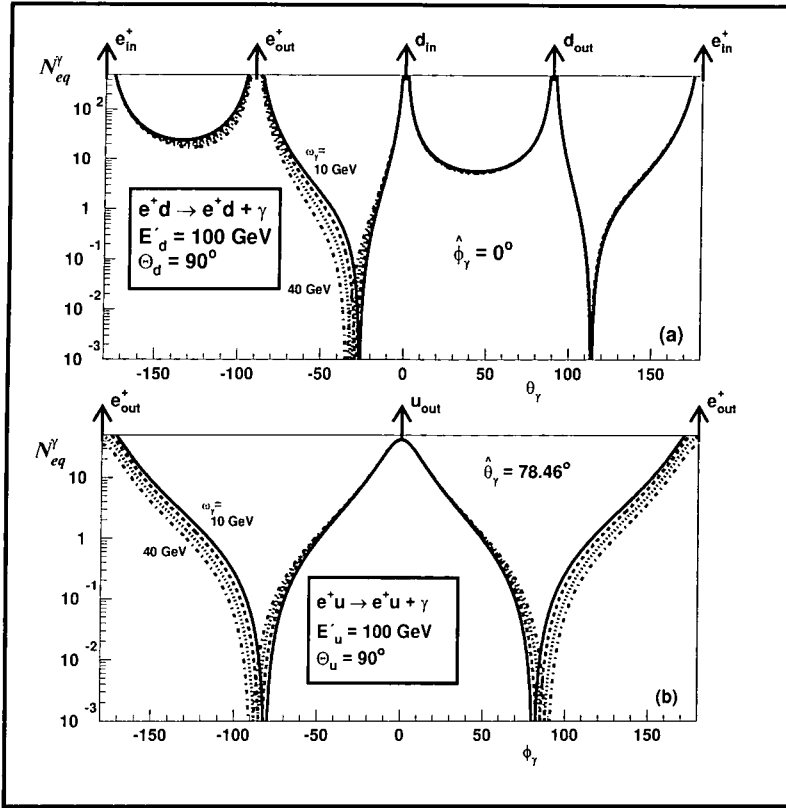
Figure 4.3: The dimensionless antenna pattern $\mathcal{N}_{eq}^{\gamma} = \omega_{\gamma}^2 \mathcal{F}_{eq}^{\gamma}$ for (a) $e^+ d \to e^+ d + \gamma$ (at fixed $\widehat{\phi}_{\gamma} = 0°$) and (b) $e^+ u \to e^+ u + \gamma$ (at fixed $\widehat{\theta}_{\gamma} \simeq 78.46°$) for different photon energies ($\omega_{\gamma} = 10, 20, 30, 40$ GeV). The outgoing quark direction is fixed at $\Theta_q = 90°$ with energy $E_q' = 100$ GeV. The directions of the incoming and outgoing quarks and leptons are indicated.

is located in the quadrant between the outgoing u quark and the outgoing positron (see Figs. 4.3(a,b)). The values on the axes at $\omega_{\gamma} = 0$ coincide with the analytic results obtained previously (see Table 4.2).

The dashed lines in Figs. 4.4(a,b) are simple polynomial fits. For $e^+ d$ scattering we fit $\widehat{\theta}_{\gamma}$ for fixed $\widehat{\phi}_{\gamma} = 180°$ using a quadratic polynomial,

$$\mathcal{Z}_d(\Theta_d, \omega_{\gamma}) = \mathcal{Z}_d^0(\Theta_d) + d_1 \omega_{\gamma} + d_2 \omega_{\gamma}^2, \qquad (4.39)$$

where $\mathcal{Z}_d^0(\Theta_d)$ corresponds to the soft–photon results listed in Table 4.2. The radiation zeros for $e^+ u$ scattering (i.e. a fit for $\widehat{\phi}_{\gamma}$ at fixed $\widehat{\theta}_{\gamma} = 78.46°$) can be approximated by a first–order polynomial

$$\mathcal{Z}_u(\Theta_u, \omega_{\gamma}) = \mathcal{Z}_u^0(\Theta_u) + u_1 \omega_{\gamma}. \qquad (4.40)$$

The results of the fit are presented in Table 4.3.

As a final exercise in our c.m.s. studies we calculate the differential cross section for the two subprocesses. The general form of the differential subprocess cross section in the
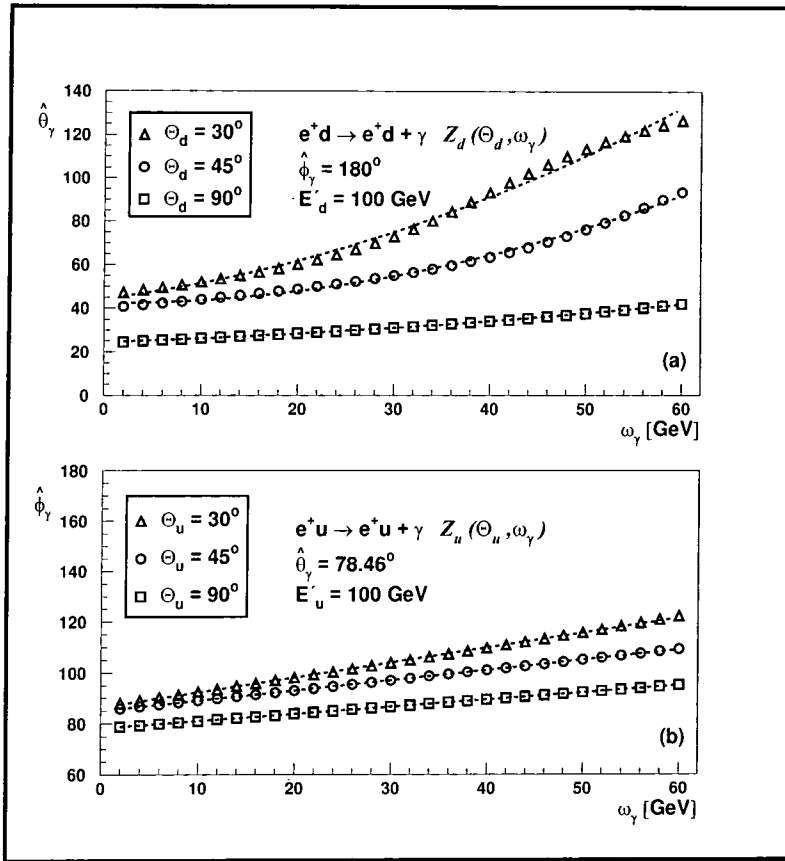
Figure 4.4: The positions of the radiation zeros $\mathcal{Z}_q$ as a function of the quark scattering angle Θ_q and the photon energy ω_γ for (a) e^+d scattering and (b) e^+u scattering. The analytic results for the soft–photon limit ($\omega_\gamma \to 0$) are summarised in Table 4.2. The dashed lines are a polynomial fit in the photon energy for given Θ_q. Note that in (a) we employ a second–order fit whereas in (b) a first–order fit is sufficient. The fit parameters are listed in the text.

e^+q c.m.s. frame may be written as

$$\frac{\mathrm{d}^2\hat{\sigma}}{\mathrm{d}\Omega_\gamma \mathrm{d}\Omega_q}(eq \to eq + \gamma) = \frac{2}{(4\pi)^5} \int\limits_{\omega_\gamma^{\mathrm{cut}}} \mathrm{d}\omega_\gamma \, \frac{E_q'^2 \omega_\gamma}{\hat{s}^{3/2}|\sqrt{\hat{s}}/2 - \omega_\gamma|} \, |\overline{\mathcal{M}}_3|^2 (eq \to eq + \gamma), \quad (4.41)$$

where

$$E_q' = \frac{\hat{s} - 2\omega_\gamma\sqrt{\hat{s}}}{2\sqrt{\hat{s}} - 2\omega_\gamma(1 - \cos\theta_{q\gamma})}. \quad (4.42)$$

The integration over ω_γ smears out the radiation zeros to form a sharp *dip* in the cross section. Since the cross section decreases rapidly with increasing ω_γ, the dip is close to the location of the zero corresponding to fixed $\omega_\gamma = \omega_\gamma^{\mathrm{cut}}$.

The distributions for the two subprocesses are shown in Figs. 4.5(a,b) for $\omega_\gamma^{\mathrm{cut}} = 5$ GeV. Note that we have also imposed an angular cut around the beam line of $5°$ in Fig. 4.5(a). The transition from radiation zeros to radiation dips can be seen by

	d–quarks			u–quarks	
Θ_q	d_1	d_2	χ^2	u_1	χ^2
30°	0.576	0.015	5.91	0.59	5.3×10^{-2}
45°	0.012	0.014	0.76	0.40	3.0×10^{-3}
60°	0.149	0.002	0.01	0.28	1.3×10^{-4}

Table 4.3:   Fits for the ω_γ dependence of the two selected radiation zeros shown in Figs. 4.4(a,b) according to the definitions given in Eqs. (4.39, 4.40).

comparing Figs. 4.4 and 4.5. Choosing larger values of $\omega_\gamma^{\text{cut}}$ shifts the radiation dips to higher values of $\hat\phi_\gamma$ and $\hat\theta_\gamma$ at the same time decreasing the overall value of the subprocess cross section.

4.2.2   Choosing HERA kinematics

In this section we shall discuss the possible observation of radiation zeros at HERA. To do this we modify the previous calculation by (a) moving to the HERA lab frame, (b) including the parton distribution functions, and (c) summing over all flavours of quarks in the initial state.

In neutral current DIS the cleanest way to reconstruct the kinematics of a given event is by measuring the energy E_e' and the laboratory angle Θ_e^{lab} of the outgoing positron. In terms of the Bjorken scaling variables x and y we may write (see for example Refs. [ZEUS95, H1.95])

$$y = 1 - \frac{E_e'}{2E_e}\left(1 - \cos\Theta_e^{\text{lab}}\right), \qquad (4.43)$$

$$x = \frac{1}{y}\frac{E_e'}{2E_p}\left(1 + \cos\Theta_e^{\text{lab}}\right), \qquad (4.44)$$

$$Q^2 = xys, \qquad (4.45)$$

where E_p is the energy of the incoming proton and $s = 4E_eE_p$ is the c.m.s. energy of the e^+p system. The polar angle of the positron Θ_e^{lab} is defined with respect to the incident proton beam direction. The precision of the y measurement typically degrades as $1/y$, and thus one naturally assumes $y \gtrsim 0.05$ [H1.95].

Since we are interested in DIS events with an additional hard photon emitted at different angles in phase space, the natural quantity to consider is the triple–differential cross section $d^3\sigma/\left(dydQ^2d\Omega_\gamma^{\text{lab}}\right)$. In the HERA lab frame this is given by

$$\frac{d^3\sigma}{dydQ^2d\Omega_\gamma^{\text{lab}}}(ep \to eq + \gamma + X) = \frac{1}{256\pi^4 s}$$

$$\times \sum_q \int_{\omega_\gamma^{\text{cut}}} d\omega_\gamma \ \frac{\omega_\gamma}{\xi_q(Q^2/x - 2p\cdot k)}\ |\overline{\mathcal{M}}_3|^2(eq \to eq + \gamma)\ f_{q/p}(\xi_q, Q^2), \qquad (4.46)$$
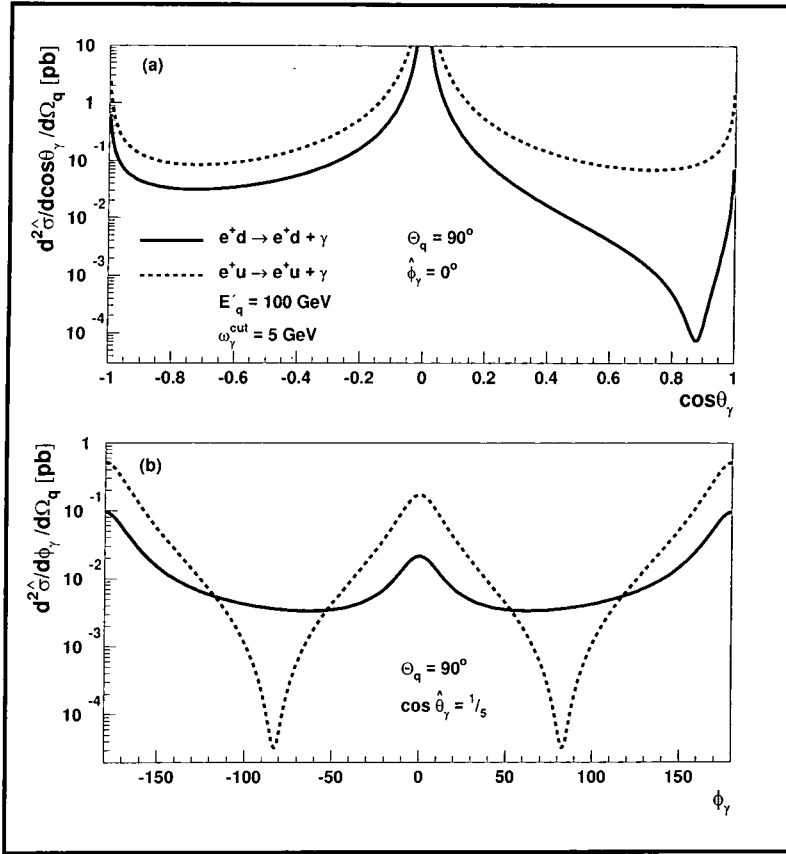
Figure 4.5: The subprocess differential cross section $d^2\hat{\sigma}/d\Omega_\gamma d\Omega_q$ of Eq. (4.41) for c.m.s. e^+d scattering (solid lines) and e^+u scattering (dashed lines). We again choose those slices through the photon parameter space $(\phi_\gamma, \theta_\gamma)$ that contain radiation zeros in the soft limit (i.e. a choice of $\hat{\phi}_\gamma = 0°$ in (a) and $\cos\hat{\theta}_\gamma = 1/5$ in (b)). Note that we integrate over the photon energy ω_γ and fix the position of the outgoing quark at $\Theta_q = 90°$ with energy $E'_q = 100$ GeV. In (a) we impose an additional angular cut of 5° around the beam line.

where

$$\xi_q = \frac{Q^2 - 2q \cdot k}{Q^2/x - 2p \cdot k} \geq x. \qquad (4.47)$$

In the calculations which follow we choose $E_e = 27.5$ GeV, $E_p = 820$ GeV and neglect all quark and lepton masses. We again take $\omega_\gamma^{cut} = 5$ GeV for the lower limit of the photon energy. For the quark distribution functions $f_{q/p}(\xi_q, Q^2)$ we use the MRS(A') set of partons introduced in Ref. [MRS95], with QCD scale parameter $\Lambda_{\overline{MS}}^{N_f=4} = 231$ MeV corresponding to $\alpha_s(M_Z^2) = 0.113$. In order to stay in the valence–quark scattering region (i.e. large ξ_q), where we expect the radiation zeros to be most visible, we choose $Q^2 = 10^4$ GeV^2 and $y \in [0.1, 1.0]$. Typical values for x and the positron variables Θ_e^{lab} and E'_e are listed in Table 4.4.

As we move from the e^+q c.m.s. frame to the HERA lab frame, all four–momenta are boosted along the beam direction. Although this has no effect on the azimuthal angles, the polar angles and hence the locations of all radiation zeros, in particular $\hat{\theta}_\gamma$,

y	x	Θ_e^{lab}	E_e'
0.20	0.55	52.4°	112.9 GeV
0.40	0.27	46.2°	107.4 GeV
0.60	0.18	38.4°	101.9 GeV
0.80	0.14	27.6°	96.4 GeV

Table 4.4: Typical values of the scattered positron energy and angle for our parameter choice $Q^2 = 10^4$ GeV^2 and different values of y.

are changed. The simplest consequence of this is that the e^+d radiation scattering zeros remain located in the scattering plane at $\widehat{\phi}_\gamma = 0°$ and $180°$. To find the locations of the radiation zeros for process (4.18) we therefore fix $\widehat{\phi}_\gamma = 0°$ and numerically determine their positions in θ_γ.

Radiation zeros for d quark scattering

In Fig. 4.6 we present the cross section of Eq. (4.46) for the process $e^+p \to e^+ +$ jet $+ \gamma + X$ via $e^+d \to e^+d + \gamma$ scattering (dashed line) as well as via the sum over all subprocesses $e^+q \to e^+q + \gamma$ with $q = u, d, s, \bar{u}, \bar{d}$ and $\bar{s}$. We have chosen to focus on the radiation zero located between the incoming quark and outgoing positron. We fix $Q^2 = 10^4$ GeV^2 and vary y from $y = 0.2$ in Fig. 4.6(a) to $y = 0.8$ in Fig. 4.6(d), which corresponds to x values in the region $0.1 < x < 0.6$ (cf. Table 4.4). Again we observe radiation dips instead of radiation zeros due to the integration over the photon energy. Increasing y pulls the radiation dips closer to the beam line and thus makes their observation more difficult. Already at $y = 0.2$ the e^+d radiation dip in Fig. 4.6(a) is only about $14°$ ($\cos\widehat{\theta}_\gamma \simeq 0.97$) from the beam line, and gets even closer with increasing y. Note that we impose a cut of $5°$ around the beam line. Increasing y means decreasing the polar angle of the outgoing positron Θ_e^{lab} (cf. Table 4.4). Thus the zone of destructive interference approaches the beam line as the e^+ approaches the beam line. The conclusion is that observation of the radiation dips in the sector between the incoming quark and outgoing e^+ in high–Q^2 events is only possible for small values of y.

The second radiation zero we found in our studies was located between the incoming positron and the outgoing quark. In Fig. 4.7 we display this region again for processes only involving d quarks (dashed lines) as well as for processes involving all light quark and antiquark flavours. The obvious singularities in Figs. 4.7(a,b,c,d) are caused by collinearity of the photon with the outgoing quark. Now the problem is that the zeros are close (always within $10°$) to the outgoing quark jet, even though the radiation dips here are well separated from the beam line ($\simeq 35°$ for $y = 0.6$).

A more serious problem evident in Figs. 4.6 and 4.7 is the enormous background from the other quark scattering subprocesses, which completely fills in the radiation dip. We observe a ratio (away from the singularities) of signal/background $\simeq 1/(200 - 300)$. The dominance of the u quark contribution is striking. For the given values of x and thus
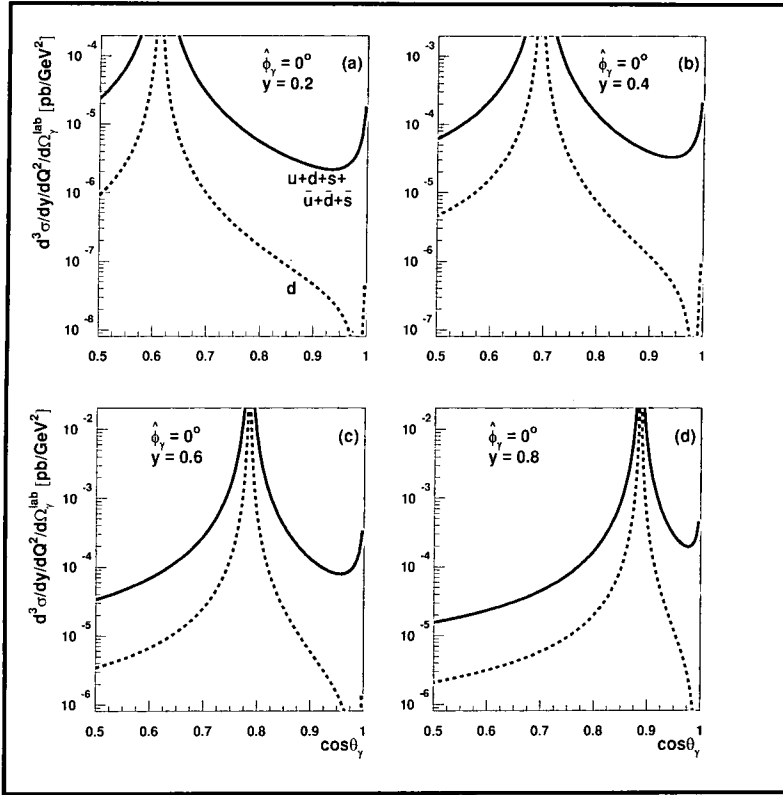
Figure 4.6: The positions of the radiation dips for the process $e^+ d \rightarrow e^+ d + \gamma$ (dashed lines) for different values of y for $\theta_\gamma \in [5°, 60°]$ (hemisphere of outgoing e^+). A cut of $5°$ around the beam line is imposed. The radiation zeros and thus the radiation dips for this process are again located within the plane $(\widehat{\phi}_\gamma = 0°)$. The Q^2 value is 10^4 GeV^2. The solid lines show the sum of the contributions from u, d, s quarks and antiquarks. The divergences in the plots show the positions of the outgoing e^+ at $\cos\theta_\gamma = \cos\Theta_e^{lab}$ with the values for Θ_e^{lab} given in Table 4.4.

ξ_q (cf. Eq. (4.47)) we find the following ratios for the MRS(A$'$) parton distributions at $Q^2 = 10^4$ GeV^2:

$$\xi_q = 0.1: \qquad \rightarrow \quad u(\xi_q) : d(\xi_q) : \bar{d}(\xi_q) : \bar{u}(\xi_q) \simeq 100 : 60 : 22 : 15, \qquad (4.48)$$

$$\xi_q = 0.6: \qquad \rightarrow \quad u(\xi_q) : d(\xi_q) : \bar{d}(\xi_q) : \bar{u}(\xi_q) \simeq 100 : 17 : 1 : 1. \qquad (4.49)$$

In addition to these parton distribution factors there are the usual quark charge squared (e_q^2) factors from the leading order $eq \rightarrow eq$ scattering, which further enhance the u-quark contribution. Note that the s-quark contribution plays a minor role; it is roughly 70% of the $\bar{u}$ contribution at $\xi_q = 0.1$ and comparable to the latter at higher values of ξ_q. Even though d, s and $\bar{u}$ quarks all yield radiation dips in the scattering plane (the d– and s–quark zeros coincide) none of these are likely to be observable. The only possibility might be to try to flavour–tag the d or s quark jets, for example by selecting only those jets with a leading negatively charged track.
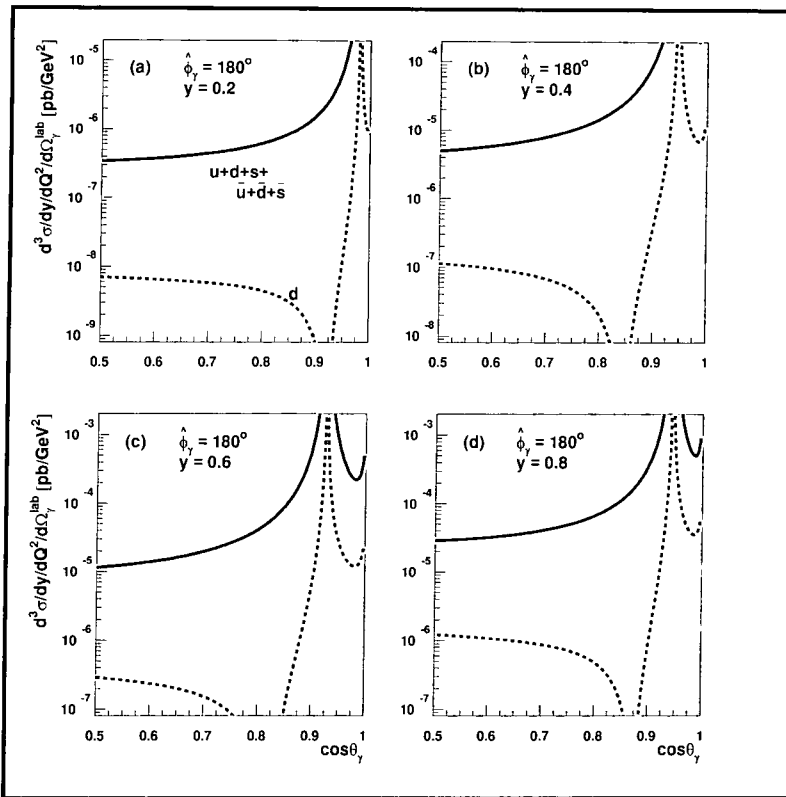
Figure 4.7: The positions of the radiation dips for the process $e^+d \to e^+d+\gamma$ (dashed lines) for different values of y for $\theta_\gamma \in [5°, 60°]$ (the hemisphere of the outgoing quark). A cut of $5°$ around the beam line is imposed. Note that $\widehat{\phi}_\gamma = 180°$.

Radiation zeros for u quark scattering

According to the parton distribution hierarchy presented in the previous section we might expect that the type 1 radiation zeros, which we identified with the *traditional* radiation zeros already discussed in the literature, are the most promising for detection. We recall that in the soft–photon limit and in the c.m.s. frame these zeros are located at fixed polar angle $\cos\widehat{\theta}_\gamma = 1/5$ (*cf.* Eq. (4.30)). Their position in ϕ_γ may then be directly computed using Eq. (4.31). We found that they are located well outside the scattering plane (except for $\Theta_q = 2\widehat{\theta}_\gamma = 2\arccos(1/5)$) as discussed earlier. Integrating over the photon energy ω_γ and using exact $2 \to 3$ kinematics slightly shifts the position of the corresponding radiation dips. The ω_γ dependence for different kinematical situations was shown in Fig. 4.4(b).

Moving to the HERA lab frame boosts the polar angles and changes the position of the radiation dips for $e^+u \to e^+u + \gamma$. In Figs. 4.8(a,b,c) we show the differential cross section of Eq. (4.46) for this process over the full $(\phi_\gamma, \theta_\gamma)$ space. As before we fix $Q^2 = 10^4$ GeV^2 and chose the three y values: 0.2, 0.4 and 0.6. We impose cuts of $5°$ around the beam line (by definition located at $\theta_\gamma = 0°$ and $180°$) and cut the differential cross section at $d\sigma < 10^{-4}$ pb/GeV^2 to avoid the collinear singularities along the directions of the outgoing e^+ (located at $\phi_\gamma = 0°$) and the outgoing u quark (at
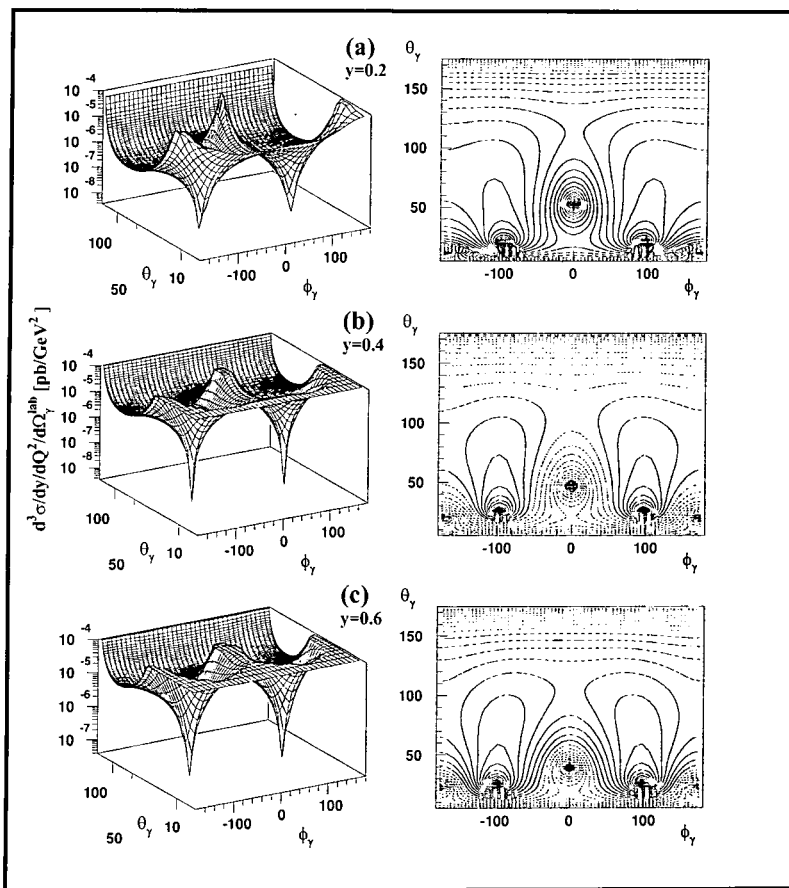
Figure 4.8: The differential cross section of Eq. (4.46) for the process $e^+u \to e^+u + \gamma$ in the $(\phi_\gamma, \theta_\gamma)$ phase space of the emitted photon. The corresponding contour plots are shown on the right–hand side. For fixed $Q^2 = 10^4$ GeV^2 we vary y (defined in Eq. (4.43)) from $y = 0.2$ in (a) and $y = 0.4$ in (b) to $y = 0.6$ in (c). The kinematic variables x, E'_e and Θ_e^{lab} for each y value can be read off from Table 4.4. Note that we introduce in the surface plots on the left–hand side a logarithmic scale in θ_γ. The radiation dips are symmetric in ϕ_γ. Again we impose a $5°$ cut around the beam line, and thus $\theta_\gamma \in [5°, 175°]$.

$\phi_\gamma = \pm 180°$). We see that the positions of the zeros are still symmetric in ϕ_γ, as expected. Note that since the collinear singularities and the radiation dips tend to concentrate around small values of θ_γ, we have introduced a logarithmic scale for θ_γ in the three–dimensional plots of Fig. 4.8.

We can numerically locate the positions of the radiation dips in the $(\phi_\gamma, \theta_\gamma)$ phase space for our different choices of y:

$$
\begin{aligned}
y = 0.2 &\to & \widehat{\phi}_\gamma &\simeq \pm 97.2°, & \widehat{\theta}_\gamma &\simeq 20.6°; \\
y = 0.4 &\to & \widehat{\phi}_\gamma &\simeq \pm 100.4°, & \widehat{\theta}_\gamma &\simeq 24.9°; \\
y = 0.6 &\to & \widehat{\phi}_\gamma &\simeq \pm 102.5°, & \widehat{\theta}_\gamma &\simeq 25.2°. & &(4.50)
\end{aligned}
$$

It is straightforward to verify that the radiation dips, if projected onto the scattering

plane, lie within the quadrants between the incoming (outgoing) e^+ and the outgoing (incoming) quark, the zone of destructive interference. As Fig. 4.8 shows, the radiation dips are clustered quite close to the (beam) direction of the incoming quark ($\theta_\gamma = 0°$) which is particularly true for high-Q^2 events (back–scattered positron). As we have already pointed out, they are also within $10°$ (in θ_γ) of the final–state quark jet. However, they *are* well–separated from the outgoing particles when the ϕ_γ angle is taken into account. It will be very important to perform realistic simulations of these photon radiation events, including jet fragmentation and detector effects, to see whether the dips are indeed observable in practice.
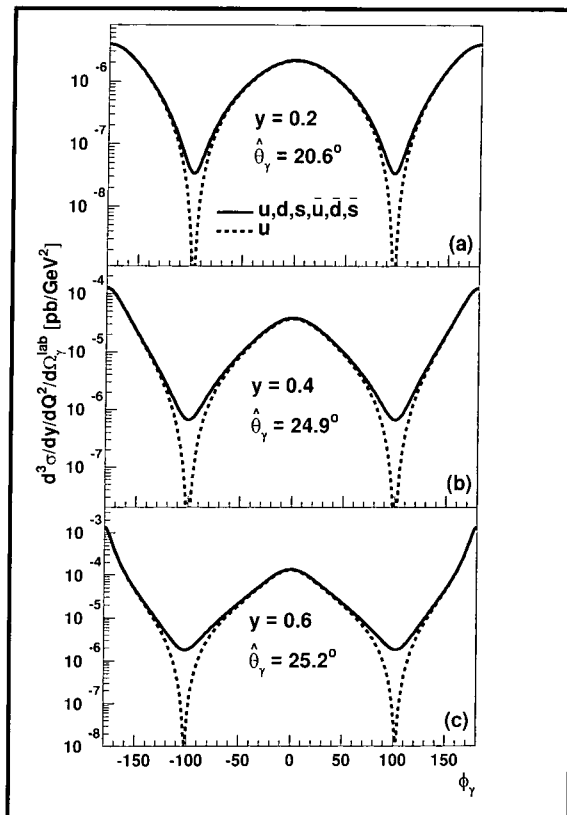

Figure 4.9: The differential cross section of Eq. (4.46) for three different y values at the position of the radiation dips $\widehat{\theta}_\gamma$ shown in Fig. 4.8 as a function of the azimuthal angle ϕ_γ. We show the process $e^+u \to e^+u + \gamma$ (dashed lines) as well as the contribution (solid lines) of all light quark flavours (u, d, s quarks and antiquarks).

Finally, in Fig. 4.9 we show the ϕ_γ dependence for slices through the $\widehat{\theta}_\gamma$ values given in Eq. (4.50) which define the numerical location of the radiation dips of Fig. 4.8. We show the contributions of u quarks only, as well as the contributions from all light flavours (i.e. u, d and s quarks and antiquarks). At the critical values of $\widehat{\phi}_\gamma$ (4.50) the obvious dips for pure u–quark scattering are somewhat filled in by the other 'background' (mainly d–quark) processes — the cross section at the bottom of the dip is increased by about two orders of magnitude — although they are still significant.

4.2.3 Radiation zeros and 'parton shower' models

To gauge the quantitative significance of the radiation zeros described in the previous sections, and in particular to factor out the effects of phase space constraints on the distributions, it is useful to make comparison with an approximate calculation in which radiation zeros are absent. Parton shower Monte Carlo programs, such as HERWIG [Mar92] or PYTHIA [Sjo94], are based on the principle of the leading–pole (collinear) approximation. In particular they do not usually include the interference effects which are crucial for producing radiation zeros in the scattering amplitudes. We can easily emulate such models by removing the interference terms from the antenna pattern in Eq. (4.20) (i.e. the terms linear in e_q):

$$\frac{1}{2} \mathcal{F}_{eq}^{\gamma \; \text{approx}} = e_q^2 [24] + [13] \,, \tag{4.51}$$

The approximate matrix element thus obtained still contains the correct leading collinear singularities when the photon is emitted parallel to the incoming and outgoing quarks and leptons. In Fig. 4.10 we present the ratio

$$R_\gamma^u = \frac{\mathrm{d}^3 \sigma^{\text{approx}}}{\mathrm{d}^3 \sigma} \left(e^+ u \to e^+ u + \gamma \right) \,, \tag{4.52}$$

where $\mathrm{d}^3 \sigma^{\text{approx}} / \mathrm{d}y \mathrm{d}Q^2 \mathrm{d}\Omega_\gamma^{\text{lab}}$ includes the antenna pattern without interference terms, as defined in Eq. (4.51). Again we slice through ϕ_γ at the values $\widehat{\theta}_\gamma$ of Eq. (4.50) where we numerically located the positions of the radiation dips for each y value. Note that away from the dips the ratio is $\mathcal{O}(1)$, as expected. However Fig. 4.10 also shows that close to the dips the approximate cross section is up to three orders of magnitude larger than the exact result, for all y values. In these particular regions of phase space, therefore, such 'parton–shower' models would dramatically overestimate the photon emission cross section.

4.2.4 Concluding remarks on radiation zeros in $eq \to eq\gamma$ scattering

The scattering amplitude for the process $eq \to eq + \gamma$ vanishes for certain configurations of the final–state momenta. In this section we have studied these radiation zeros and in particular their observability at HERA. In addition to the well–known class of (type 1) same–charge zeros, which have been discussed in the pioneering work of Refs. [Bil85, Cou89, LRS90, DH91], we have studied a second class of (type 2) zeros located in the eq scattering plane, which we introduced in Section 4.1.3.

Experimentally, one might hope to be able to measure the four–momenta of the final–state lepton, quark (jet) and photon sufficiently accurately that the kinematic configurations which lead to zeros could be reconstructed. However a more realistic approach, which we have adopted here, is to study DIS + photon events for fixed lepton variables y and Q^2 and for a range of photon energies above a given threshold. This leads to sharp radiation dips instead of zeros. We performed such a study using the HERA lab frame. Although the radiation dips, i.e. the photon directions for which the cross section has a minimum, of both types are quite well separated from the beam direction and from the final–state jet, the $e^+ d$ scattering dips are completely swamped by the contributions from the other quark scattering processes. The $e^+ u$ (type 1) dips offer a more promising hope of detection, since $e^+ u$ scattering is the dominant subprocess at high x.
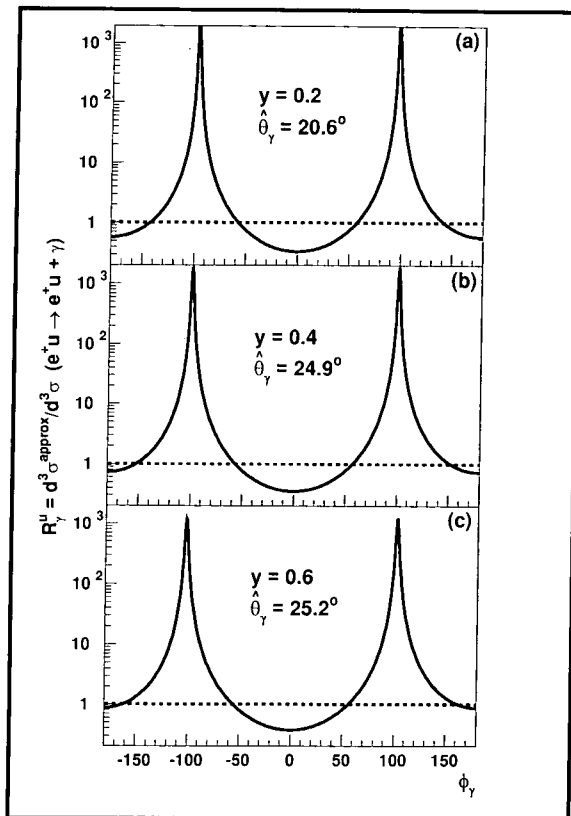
Figure 4.10: Same as Fig. 4.9, but now for the process $e^+u \to e^+u + \gamma$ only. R_γ^u is the ratio of the differential cross sections of Eq. (4.46) without and with interference terms, see Eq. (4.52).

Finally we address the question of whether the cross section dips can realistically be observed at HERA. For a given total luminosity, we can calculate the expected number of events with observable photons together with their distributions in solid angle, $dN/d\Omega_\gamma^{lab}$. Fig. 4.11 shows the event numbers in bins of the photon angles θ_γ and $|\phi_\gamma|$ for the following cuts:

(a) $0.1 \le y \le 0.3$,

(b) $0.3 \le y \le 0.5$,

(c) $0.5 \le y \le 0.7$,

with $x \in [0.1, 1]$, a lower cut on the photon energy of $\omega_\gamma^{cut} = 5$ GeV and an integrated luminosity $\int dt \mathcal{L} = 100$ pb^{-1}. Additionally we impose a $5°$ cut to separate the photon from the beam direction and the final-state positron and quark jet. For these cuts we find a total of (a) 2615.2, (b) 1723.2 and (c) 1237.4 $e^+ + \text{jet} + \gamma$ events in the three y bins respectively.[4] The two numbers in each bin in Fig. 4.11 correspond to the exact and approximate (i.e. with *no* radiation zeros as defined in Eq. (4.51)) matrix elements.

---

[4]Note that the *total* $e^+ + \text{jet}$ rate for these bins is approximately two orders of magnitude larger.

(a) $0.1 \le y \le 0.3$					
130.9	30.9	10.0	5.1	5.2	5.0
(96.5)	(31.7)	(18.9)	(14.0)	(15.8)	(16.4)
76.9	38.1	17.8	10.8	9.3	9.5
(45.9)	(31.9)	(25.4)	(24.0)	(24.7)	(25.6)
98.8	74.5	51.5	38.6	33.5	32.2
(57.4)	(55.2)	(54.4)	(35.7)	(58.0)	(59.9)

Θ_γ: 40, 30, 20, 10
$|\phi_\gamma|$: 0, 30, 60, 90, 120, 150, 180

(b) $0.3 \le y \le 0.5$					
166.9	12.2	3.3	1.5	1.2	1.5
(158.0)	(16.0)	(8.7)	(7.2)	(7.0)	(7.2)
49.5	15.9	5.9	3.1	2.6	2.7
(34.8)	(16.3)	(11.3)	(10.1)	(10.2)	(10.5)
43.7	28.5	17.3	11.8	9.8	9.4
(25.8)	(22.8)	(22.0)	(21.1)	(21.8)	(22.4)

Θ_γ: 40, 30, 20, 10
$|\phi_\gamma|$: 0, 30, 60, 90, 120, 150, 180

(c) $0.5 \le y \le 0.7$					
147.3	6.3	1.7	0.7	0.7	0.8
(139.8)	(9.4)	(6.4)	(5.3)	(5.1)	(5.2)
268.2	11.3	3.0	1.3	1.1	1.3
(218.1)	(15.7)	(8.5)	(7.2)	(7.1)	(7.3)
52.3	20.9	9.2	5.3	4.2	4.1
(34.4)	(19.4)	(14.8)	(13.8)	(14.0)	(14.3)

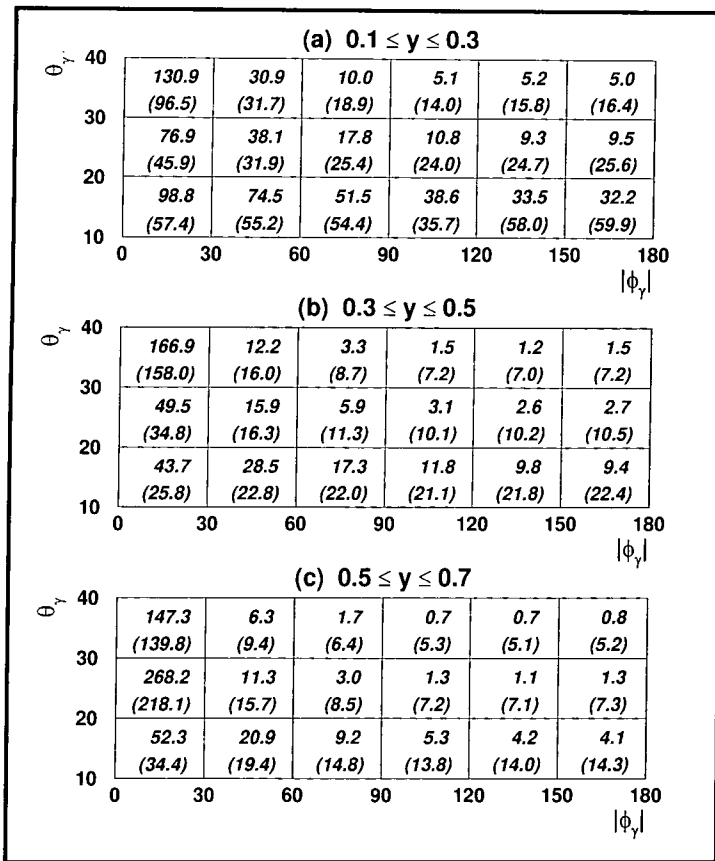Θ_γ: 40, 30, 20, 10
$|\phi_\gamma|$: 0, 30, 60, 90, 120, 150, 180

Figure 4.11: The event rates $dN/d\Omega_\gamma^{lab}$ for the production of $e^+ + \text{jet} + \gamma$ mediated by the subprocess $e^+ q \to e^+ q + \gamma$ $(q = u(\bar{u}), d(\bar{d}), s(\bar{s}))$ in three different y bins. We choose $x \in [0.1, 1]$ and this determines the range of Q^2 in a given y bin. We integrate the differential cross section of Eq. (4.46) over y, Q^2 and a given phase–space element $d\Omega_\gamma^{lab}$ of the photon and assume an integrated luminosity $\int dt \mathcal{L} = 100$ pb^{-1}. The upper line in each bin shows the result of the exact calculation, and the lower line shows the results in the approximate calculation (employing the antenna pattern of Eq. (4.51)). Note that we impose a 5° cut around the beam line and the outgoing positron and quark jet. The lower cut on the photon energy spectrum is again $\omega_\gamma^{cut} = 5$ GeV.

Because of the y and x integrations and the finite bin size, the effect of the radiation zeros is smeared out. Nevertheless one can clearly see the expected suppression of the event rate in the exact case due to the presence of the type 1 radiation zeros (in particular for $90° < |\phi_\gamma| < 180°$, as anticipated in Fig. 4.10). Furthermore the event rate (for this luminosity) does appear to be large enough for the effect to be observable.

We conclude, in agreement with Ref. [DH91], that the effect of radiation zeros should be visible at HERA.

4.3 Zeros in high–energy e^+e^- annihilation into hadrons

In this section we present a detailed theoretical and phenomenological study of (type 2) radiation zeros in the scattering process $e^-e^+ \to q\bar{q}\gamma$ at high energy. We shall show that zeros exist for both u– and d–type quarks for all helicities and polarisations. The zeros occur in photon directions which are reasonably well separated from the directions of the other particles in the scattering. Unfortunately it is very difficult to obtain analytic expressions for the positions of the zeros with exact matrix elements and phase space. Results for the general case, obtained numerically, will be presented in Section 4.3.4. However in the soft–photon approximation (which in fact is the dominant experimental configuration) it *is* possible to obtain reasonably compact expressions. We shall then use the soft–photon approximation to locate the zeros, first for massless and then for massive quarks. We include a brief discussion of radiation at the Z pole. In Section 4.3.5 we perform a Monte Carlo study, based on the exact matrix elements and phase space, to obtain 'realistic' distributions of the type which might be accessible experimentally. Finally, our conclusions are presented in Section 4.3.6.

4.3.1 Massless quarks in the soft limit

We consider the processes

$$e^-(1)\, e^+(2) \quad\longrightarrow\quad q(3)\, \bar{q}(4) + \gamma(k)\,, \tag{4.53}$$

$$e^-(1)\, e^+(2) \quad\longrightarrow\quad q(3)\, \bar{q}(4) + g(k)\,. \tag{4.54}$$

The gluon emission process (4.54) does *not* contain radiation zeros, but is useful for comparison. To begin with we shall consider s–channel γ^* exchange only, as this fully determines the positions of the radiation zeros. The exact matrix elements for these processes are (for massless quarks and leptons, see for example Ref. [Ber81])

$$|\overline{\mathcal{M}}_3|^2(e^-e^+ \to q\bar{q} + \gamma) \;=\; -3e^6 e_q^2\, \frac{t^2 + t'^2 + u^2 + u'^2}{ss'}\, (v_{12} + e_q v_{34})^2\,, \tag{4.55}$$

$$|\overline{\mathcal{M}}_3|^2(e^-e^+ \to q\bar{q} + g) \;=\; -4e^4 e_q^2 g_s^2\, \frac{t^2 + t'^2 + u^2 + u'^2}{ss'}\, (v_{34})^2\,, \tag{4.56}$$

with the standard definitions for the $2 \to 3$ Mandelstam variables

$$s = (p_1 + p_2)^2\,, \quad t = (p_1 - p_3)^2\,, \quad u = (p_1 - p_4)^2\,,$$
$$s' = (p_3 + p_4)^2\,, \quad t' = (p_2 - p_4)^2\,, \quad u' = (p_2 - p_3)^2\,, \tag{4.57}$$

and

$$v_{ij} = \frac{p_i^\mu}{p_i \cdot k} - \frac{p_j^\mu}{p_j \cdot k}\,. \tag{4.58}$$

In the soft limit, i.e. $\omega_{\gamma,g}/E_i \to 0$, we may use $2 \to 2$ kinematics for the $e^-e^+ \to q\bar{q}$ part of the process. The four–vectors in the c.m.s. frame can then be written as

$$p_1^\mu \;=\; \frac{\sqrt{s}}{2}\, (1,0,0,-1)\,, \tag{4.59}$$

$$p_2^\mu \;=\; \frac{\sqrt{s}}{2}\, (1,0,0,1)\,, \tag{4.60}$$

$$p_3^\mu = \frac{\sqrt{s}}{2}\left(1, -\sin\Theta_{\rm cm}, 0, -\cos\Theta_{\rm cm}\right), \tag{4.61}$$

$$p_4^\mu = \frac{\sqrt{s}}{2}\left(1, \sin\Theta_{\rm cm}, 0, \cos\Theta_{\rm cm}\right), \tag{4.62}$$

$$k^\mu = \omega_{\gamma,g}\left(1, \sin\theta_{\gamma,g}\cos\phi_{\gamma,g}, \sin\theta_{\gamma,g}\sin\phi_{\gamma,g}, \cos\theta_{\gamma,g}\right). \tag{4.63}$$
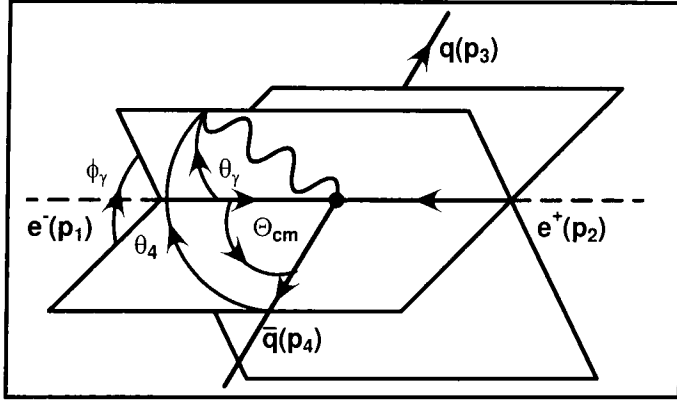
These kinematics are illustrated in Fig. 4.12.

Figure 4.12: Parametrisation of the kinematics for $e^-(p_1)e^+(p_2) \to q(p_3)\bar{q}(p_4) + \gamma(k)$ scattering in the e^-e^+ c.m.s. frame. The orientation of the photon relative to the scattering plane is denoted by the angles θ_γ and ϕ_γ. Note that $\theta_\gamma = \theta_2$.

Radiation zeros for process (4.53) arise from the vanishing of the $(v_{12} + e_q v_{34})^2$ term. This is the antenna pattern $\mathcal{F}^\gamma = -\sum_{i,j} e_i e_j J_i^\mu J_{\mu,j}$ of the soft emission process, as we discussed in Section 3.1.1 and defined in Eq. (3.9). A useful parametrisation is to introduce the variables $z_i = \cos\theta_i$ which specify the angular separation of the soft photon or gluon from particle i. The eikonal factors which make up the antenna pattern are then

$$[ij] \equiv \frac{p_i \cdot p_j}{(p_i \cdot k)(p_j \cdot k)} = \frac{1}{\omega^2}\frac{1 - \cos\theta_{ij}}{(1 - z_i)(1 - z_j)}, \tag{4.64}$$

and the antenna patterns themselves can be readily obtained from Eqs. (4.55,4.56)

$$\frac{1}{2}\mathcal{F}_{q\bar{q}}^\gamma = [12] + e_q^2[34] - e_q\left([13] + [24] - [14] - [23]\right), \tag{4.65}$$

$$\frac{1}{2}\mathcal{F}_{q\bar{q}}^g = [34]. \tag{4.66}$$

We see immediately that there are no radiation zeros of type 1, as this would require (for the vanishing of $\mathcal{F}_{q\bar{q}}^\gamma$)

$$\frac{-1}{1 + z_2} = \frac{1}{1 - z_2} = \frac{e_q}{1 + z_4} = \frac{-e_q}{1 - z_4}, \tag{4.67}$$

which has no solutions in the physical domain.

We shall study above process for the appearance of type 2 radiation zeros. For a complete set of kinematic variables in the soft–photon limit we may take the $q\bar{q}$ c.m.s. scattering angle $\Theta_{\rm cm}$ and two of the z_i variables introduced above: $\mathcal{F}^\gamma = \mathcal{F}^\gamma(\Theta_{\rm cm}, e_q, z_2, z_4)$,

since $z_1 = -z_2$ and $z_3 = -z_4$ in the c.m.s. frame. To locate the zeros we solve

$$\mathcal{F}_{q\bar{q}}^{\gamma}(\Theta_{\text{cm}}, e_q, z_2, z_4) = 0 \tag{4.68}$$

and find

$$\hat{z}_4 = -e_q z_2 \pm \sqrt{f(\Theta_{\text{cm}}, e_q)}, \tag{4.69}$$

with

$$f(\Theta_{\text{cm}}, e_q) = 1 + e_q^2 + 2e_q \cos\Theta_{\text{cm}}. \tag{4.70}$$

As we expect the (type 2) radiation zeros to be located in the scattering plane,[5] we set $\phi_\gamma = 0°$ and derive as an additional condition

$$\begin{aligned}
z_4 = \cos\theta_4 &= \cos(\theta_\gamma - \Theta_{\text{cm}}) = \sin\theta_\gamma \sin\Theta_{\text{cm}} + \cos\theta_\gamma \cos\Theta_{\text{cm}} \\
&= \sqrt{1 - z_2^2}\sin\Theta_{\text{cm}} + z_2 \cos\Theta_{\text{cm}}.
\end{aligned} \tag{4.71}$$

The solutions of Eqs. (4.69) are tangential hyperplanes to Eq. (4.71) in the Θ_{cm}, z_2 space for given charge e_q. Thus we find the positions of the radiation zeros for given e_q and c.m.s. scattering angle by solving

$$\frac{\text{d}}{\text{d}z_2}\hat{z}_4 = \frac{\text{d}}{\text{d}z_2}\left(\sqrt{1 - z_2^2}\sin\Theta_{\text{cm}} + z_2 \cos\Theta_{\text{cm}}\right), \tag{4.72}$$

which immediately yields

$$e_q = \frac{z_2}{\sqrt{1 - z_2^2}}\sin\Theta_{\text{cm}} - \cos\Theta_{\text{cm}}. \tag{4.73}$$

The solutions are

$$\hat{z}_2 = \cos\widehat{\theta}_\gamma = \pm \frac{e_q + \cos\Theta_{\text{cm}}}{\sqrt{f(\Theta_{\text{cm}}, e_q)}}, \tag{4.74}$$

with '+' if $\widehat{\phi}_\gamma = 0°$ and '−' if $\widehat{\phi}_\gamma = 180°$. Eq. (4.74) yields physical solutions for both $e_q = -1/3$ (d–type quarks) and $e_q = 2/3$ (u–type quarks) in the complete range of Θ_{cm}.
We mention several other interesting features.

(i) If we substitute the solution for $\hat{z}_2$ of Eq. (4.74) and $\hat{z}_4$ of Eq. (4.69) into the antenna pattern $\mathcal{F}_{q\bar{q}}^{\gamma}$ we find

$$[12] = e_q^2[34] = \frac{1}{2}e_q([13] + [24] - [14] - [23]), \tag{4.75}$$

i.e. the interference term exactly cancels the sum of the leading pole terms which are equal. Therefore solving $\mathcal{F}_{q\bar{q}}^{\gamma} = 0$ is equivalent to solving $[12] = e_q^2[34]$ in the massless case. We shall test this feature later for massive quarks.

(ii) From Eq. (4.74) we see that the radiation zeros are orthogonal to the beam direction for $\cos\Theta_{\text{cm}} = -e_q$ which means $\Theta_{\text{cm}} \sim 131.8°$ for u–type quarks and $\Theta_{\text{cm}} \sim 70.5°$ for d–type quarks.

---

[5]Note that it is straightforward to show that there are no additional zeros with $\phi_\gamma \neq 0°, 180°$.

(iii) The radiation zeros are located in different sectors: for u–type quarks they are located between the directions of the incoming e^+ and outgoing $\bar{q}$ and between the incoming e^- and outgoing q directions, respectively. For d–type quarks the radiation zeros can be found between the incoming e^- and outgoing $\bar{q}$ and between the incoming e^+ and outgoing q directions, respectively. This makes the discrimination between different charged quarks straightforward, at least in principle.

(iv) There is one kinematic configuration for which the separation between the radiation zero direction and the direction of the outgoing quark (antiquark) is maximal. By solving

$$\frac{d}{d\Theta_{\rm cm}}\left\{\arccos\left(\pm\frac{e_q+\cos\Theta_{\rm cm}}{\sqrt{f(\Theta_{\rm cm},e_q)}}\right)-\Theta_{\rm cm}\right\}=0\,,\qquad(4.76)$$

we can show that this is the case if the radiation zeros are located *orthogonal* to the beam direction (the corresponding values of $\Theta_{\rm cm}$ are given above). The separations are then

$$\Delta\theta_\gamma^{\rm max}\ =\ 41.8°\qquad\text{for }u\text{–type quarks}\,,\qquad(4.77)$$

$$\Delta\theta_\gamma^{\rm max}\ =\ 19.5°\qquad\text{for }d\text{–type quarks}\,.\qquad(4.78)$$

In Figs. 4.13,4.14 we show the antenna patterns $\mathcal{F}_{q\bar{q}}^\gamma$ of Eq. (4.65) for process (4.53) with three different c.m.s. frame scattering angles $\Theta_{\rm cm}=60°,90°$ and $120°$. Additionally we show a slice through the soft–photon phase space at $\hat{\phi}_\gamma=0°$ to illustrate the positions of the radiation zeros. For comparison we also show the antenna patterns for soft–gluon emission as defined in Eq. (4.66). This has no initial–, final–state interference and therefore no zeros.[6] Comparing the production of d–type quarks and u–type quarks, i.e. Figs. 4.13 and 4.14, shows that the most striking qualitative feature is the appearance of radiation zeros in different sectors, as discussed above.

In Fig. 4.15 we present the positions of the radiation zeros $(\hat{\phi}_\gamma=0°,\hat{\theta}_\gamma)$ given by Eq. (4.74), as a function of the c.m.s. frame scattering angle, for both d–type and u–type quarks. Note that radiation zeros exist in both cases for all values of $\Theta_{\rm cm}$, and also that the radiation zeros for u–type production are more clearly separated from the collinear singularities. For zero–angle scattering $(\Theta_{\rm cm}=0°,180°)$ the zeros become pinched along the beam direction. Note that the t–channel process $e^+q\to e^+q\gamma$ of Section 4.2 shows a qualitatively different behaviour in the zero–angle scattering limit: in that case the radiation zeros were located on a cone with fixed angle around the beam direction.

It should be obvious from the above that in order to locate a radiation zero one has to be able to distinguish a quark jet from an antiquark jet. Thus if one (3 ↔ 4) symmetrises the expression in Eq. (4.65) for $\mathcal{F}_{q\bar{q}}^\gamma$, the interference term vanishes and there is no zero. In practice distinguishing between the quark and antiquark jet is likely to be very difficult, but not impossible. For example, for light–quark jets one could try to tag on the charge of the fastest hadron in the jet. For heavy (charm, bottom) quark jets one could in principle use the charge of the lepton from the primary weak decay of the quark to distinguish the quark from the antiquark. Methods like these are likely to have poor efficiency, so in practice one would be looking for a slight dip in the photon

---

[6]Note that up to charge factors the final–state collinear singularities are the same in both cases however.
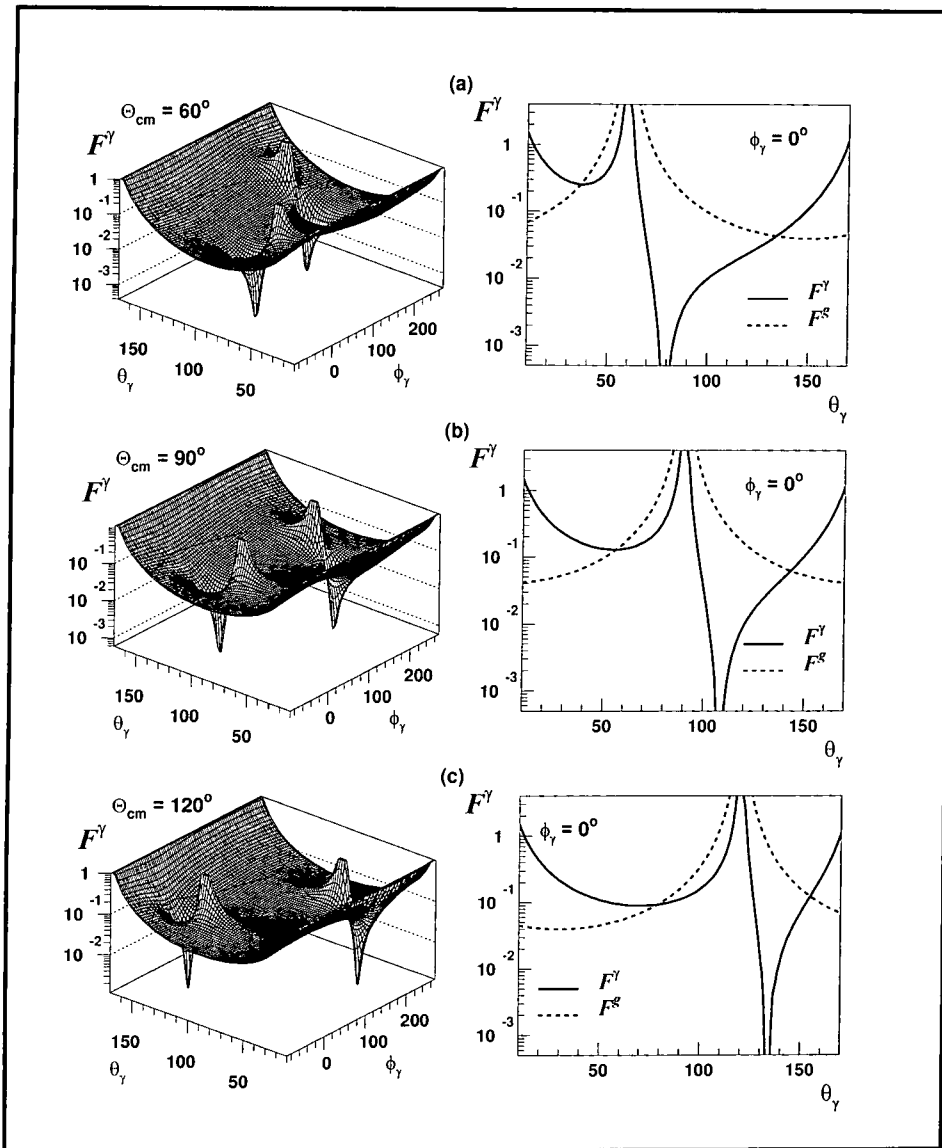
Figure 4.13: Surface plots of the antenna pattern $\mathcal{F}_{q\bar{q}}^{\gamma}$ in the angular phase space of the soft photon (left–hand side) and slices through the event plane (right–hand side) at $\widehat{\phi}_{\gamma} = 0°$ to illustrate the positions of the radiation zeros. We show the process $e^{-}e^{+} \to q_{d}\bar{q}_{d}\gamma$ for three different c.m.s. frame angles (a) $\Theta_{cm} = 60°$, (b) $\Theta_{cm} = 90°$ and (c) $\Theta_{cm} = 120°$. The dashed lines are the corresponding distributions for soft gluon emission.

distribution in the vicinity of a zero when a tagged sample is compared with an untagged sample with the same overall kinematics.

4.3.2 Radiation at the Z^{0} pole

The general discussion on radiation zeros presented in the Introduction assumed that the hard scattering is characterised by a single (large) energy scale, so that the incoming and outgoing particles emit photons on the same timescale. This corresponds to coherent
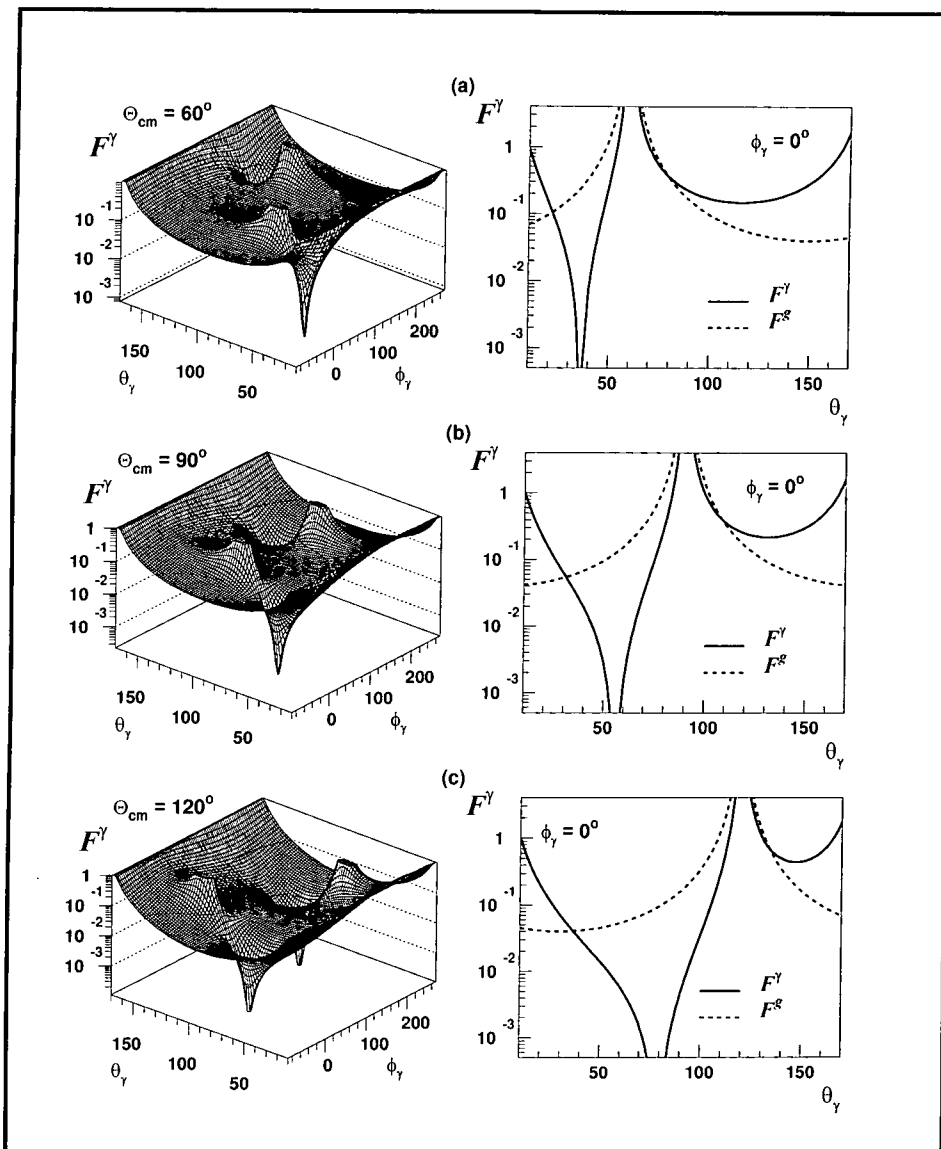
Figure 4.14: Same as Fig. 4.13, but for the process $e^-e^+ \to q_u\bar{q}_u\gamma$.

emission and allows the interference to be maximal. However, care must be taken when two timescales are involved, for example when there is an intermediate particle which is relatively long lived. In this case the emission off the initial– and final–state particles can occur at very different timescales and the interference between them can be suppressed. In fact this is exactly what happens for the process $e^+e^- \to f\bar{f}$ on the Z pole, i.e. when $\sqrt{s} \simeq M_Z$.

A formalism has been developed for taking these effects into account (see Refs. [Dok91, Dok93, Jik91] of Chapter 3 and in particular Ref. [KOS92] of Chapter 3). In simple terms, the interference between emission during the production and decay stages of a heavy unstable resonance of width Γ is suppressed by a factor $\chi = \Gamma^2/(\Gamma^2 + \omega^2)$, i.e. there can be no interference when the timescale for photon emission ($\sim 1/\omega$) is much
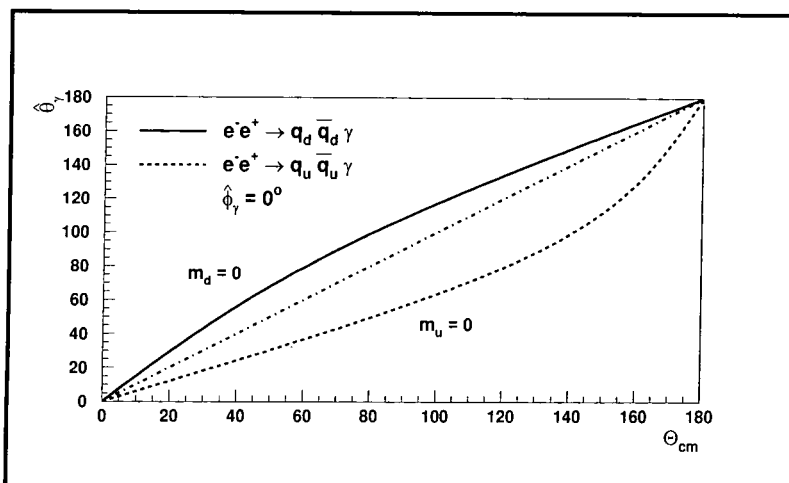
Figure 4.15: The positions $(\widehat{\phi}_\gamma, \widehat{\theta}_\gamma)$ of the radiation zeros for the processes $e^- e^+ \to q_d \bar{q}_d \gamma$ and $e^- e^+ \to q_u \bar{q}_u \gamma$ as a function of the c.m.s. frame scattering angle Θ_{cm} and fixed $\widehat{\phi}_\gamma = 0^\circ$. The dot–dashed line shows the position of the final–state collinear singularity (i.e. the direction of the outgoing antiquark). Massless quarks are assumed. Note that the distribution for $\widehat{\phi}_\gamma = 180^\circ$ shows a $\pi - \Theta_{cm}$ symmetry.

shorter than the lifetime of the resonance ($\sim 1/\Gamma$).

In the present context, the antenna pattern of Eq. (4.65) is only valid far away from the Z pole, $\sqrt{s} \ll M_Z$ or $\sqrt{s} \gg M_Z$. On the Z pole we have, in contrast,

$$\frac{1}{2}\mathcal{F}_Z^\gamma = [12] + e_q^2[34] - \chi_Z e_q\left([13] + [24] - [14] - [23]\right) , \qquad (4.79)$$

where

$$\chi_Z = \frac{M_Z^2 \Gamma_Z^2}{(P_Z \cdot k)^2 + M_Z^2 \Gamma_Z^2} = \frac{\Gamma_Z^2}{\omega^2 + \Gamma_Z^2} . \qquad (4.80)$$

The second expression in (4.80) corresponds to the c.m.s. frame. For $\omega \gg \Gamma_Z$ there is no interference (and therefore no radiation zero), and the radiation pattern corresponds to incoherent emission off the initial– and final–state particles. On the other hand the radiation zero reappears in the limit $\omega/\Gamma_Z \to 0$. It is straightforward to show that in this limit the minimum value of the distribution is $\mathcal{O}(\omega^2/\Gamma_Z^2)$.

The effect of the finite Z width on the interference between initial– and final–state radiation was studied in detail in Ref. [JW89]. The DELPHI collaboration [DEL96] subsequently confirmed the theoretical expectations and used the size of the measured interference to determine Γ_Z.

Since in the present study we are interested in radiation *zeros*, we must require that the collision energy (and the photon energy[7]) are such that the internal Z propagator is always far off mass–shell. This effectively guarantees that $\chi = 1$ and hence that the radiation pattern is again given by Eq. (4.65). Unfortunately this means that we are

---

[7]For $\sqrt{s} > M_Z$ we can avoid 'radiative return' to the Z pole by placing an upper bound on the photon energy.

unable to use the greatly enhanced statistics of LEP1 and SLC in searching for radiation zeros.

4.3.3   Massive quarks in the soft photon limit

"The mere neglect
of a mass effect
is quite suspect
and often not correct."

In this section we repeat the analysis of Section 4.3.1 but now including a non–zero mass for the final–state quarks. The eikonal factors for massive particles read

$$[ij]_m = \frac{1}{\omega^2} \frac{1 - \rho_i \rho_j \cos \theta_{ij}}{(1 - z_i \rho_i)(1 - z_j \rho_j)} . \tag{4.81}$$

We continue to use massless initial–state electrons, so that $\rho_1 = \rho_2 = 1$ and $\rho_3 = \rho_4 = \rho = \sqrt{1 - 4m_Q^2/s}$. The antenna pattern of Eq. (4.65) now has additional contributions:

$$\begin{aligned}
\frac{1}{2}\mathcal{F}^\gamma_{m_Q} &= [12]_{m_Q} + e_Q^2 \left([34]_{m_Q} - \frac{1}{2} \frac{m_Q^2}{(p_3 \cdot k)^2} - \frac{1}{2} \frac{m_Q^2}{(p_4 \cdot k)^2} \right) \\
&- e_Q \left([13]_{m_Q} + [24]_{m_Q} - [14]_{m_Q} - [23]_{m_Q} \right) .
\end{aligned} \tag{4.82}$$

We first consider the limits of $\rho \in [0, 1]$:

$$\rho = 0 : \quad \mathcal{F}^\gamma_{m_Q} = 2[12]_{m_Q} = \frac{4}{\omega_\gamma^2} \frac{1}{1 - \cos^2 \theta_\gamma} , \tag{4.83}$$

$$\rho = 1 : \quad \mathcal{F}^\gamma_{m_Q} = \mathcal{F}^\gamma . \tag{4.84}$$

The first of these limits is just the well–known result that heavy charged particles at rest do not radiate, and there are clearly no radiation zeros. As $\mathcal{F}^\gamma$ does contain radiation zeros, we might anticipate a non–trivial ρ dependence of their position as we increase the mass from zero, with the zeros eventually vanishing for some critical mass.

A numerical study confirms this result. We again find zeros in the scattering plane ($\phi_\gamma = 0°$). Solving $\mathcal{F}^\gamma_{m_Q} = 0$ now gives

$$\hat{z}_2^{m_Q} = \frac{2}{e_Q} \frac{e_Q \rho \cos \Theta_{\text{cm}} + 1 + \frac{g_\rho(\Theta_{\text{cm}}, e_Q)}{2f_\rho(\Theta_{\text{cm}}, e_Q)}}{\sqrt{-2f_\rho(\Theta_{\text{cm}}, e_Q)g_\rho(\Theta_{\text{cm}}, e_Q)}} , \tag{4.85}$$

with

$$f_\rho(\Theta_{\text{cm}}, e_Q) = \rho^2 + e_Q^2 + 2e_Q\rho \cos \Theta_{\text{cm}} , \tag{4.86}$$

$$h_\rho(\Theta_{\text{cm}}, e_Q) = -2e_Q \cos \Theta_{\text{cm}} \left(1 + \rho^2 \right) - \rho e_Q^2 \left(1 + \cos^2 \Theta_{\text{cm}} \right) - 2\rho , \tag{4.87}$$

$$\begin{aligned}
g_\rho(\Theta_{\text{cm}}, e_Q) &= \rho h_\rho(\Theta_{\text{cm}}, e_Q) \\
&+ \rho\sqrt{h_\rho(\Theta_{\text{cm}}, e_Q)^2 - 4f_\rho(\Theta_{\text{cm}}, e_Q) \left(e_Q\rho \cos \Theta_{\text{cm}} + 1 \right)^2} . \tag{4.88}
\end{aligned}$$

It is straightforward to show that in the massless limit ($\rho = 1$) Eq. (4.85) reduces to Eq. (4.74). Note that at the positions of the zeros we have, as in the massless case,

$$[12]_{m_Q} = e_Q^2 \left([34]_{m_Q} - \frac{1}{2} \left\{ [33]_{m_Q} + [44]_{m_Q} \right\} \right), \tag{4.89}$$

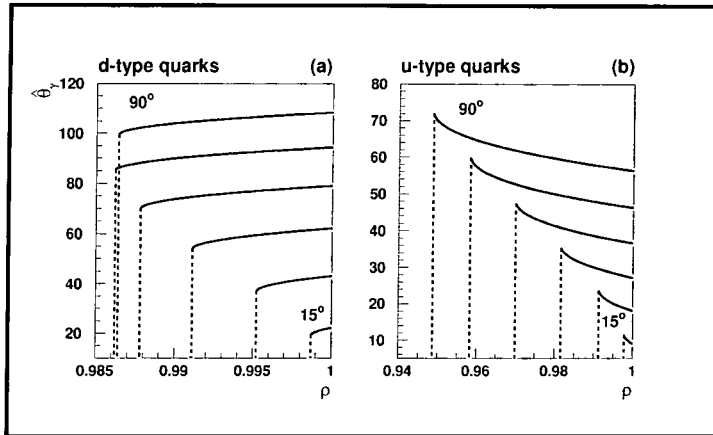with the interference again canceling the sum of these two terms.

Figure 4.16: The positions of the radiation zeros ($\hat{\phi}_\gamma = 0°, \hat{\theta}_\gamma$) for massive quarks $\rho = \sqrt{1 - 4m_Q^2/s}$ (beam energy $E_{e^-} = 100$ GeV) and different c.m.s. scattering angles ($\Theta_{cm} = 15° - 90°, \Delta\Theta_{cm} = 15°$). The dashed lines show the values of ρ_{crit}.

Taken together, the equations (4.85–4.88) only have physical solutions for a certain range of $\rho \in [\rho_{crit}, 1]$. In particular, if the ratio m_Q/E_{e^-} (quark mass over beam energy) becomes too large the radiation zeros disappear. Fig. 4.16 shows the positions $\hat{\theta}_\gamma$ of the radiation zeros inside the event plane ($\hat{\phi}_\gamma = 0°$) as a function of ρ for a fixed beam energy $E_{e^-} = 100$ GeV, for both d–type and u–type quarks, and for different values of the c.m.s. scattering angle Θ_{cm}. The dashed lines indicate the values of ρ_{crit}. There is one kinematic configuration $\widetilde{\Theta}_{cm}$ for which m_Q^{crit} becomes maximal, i.e. an upper limit on the quark mass for which radiation zeros can still be observed. We find

$$\widetilde{\rho}_{crit} = \frac{1}{2}\sqrt{4 - e_Q^2} \quad \Longleftrightarrow \quad \widetilde{m}_Q^{crit} = \frac{\sqrt{s}}{2}\frac{|e_Q|}{2} \quad \Longleftrightarrow \quad \cos\widetilde{\Theta}_{cm} = \frac{-e_Q}{\sqrt{4 - e_Q^2}}. \tag{4.90}$$

For the production of d–type quarks we obtain $\widetilde{m}_d^{crit} = 16.7$ GeV at $\widetilde{\Theta}_{cm} = 80.3°$, and for u–type quarks we find $\widetilde{m}_u^{crit} = 33.3$ GeV at $\widetilde{\Theta}_{cm} = 110.7°$. According to Eq. (4.90) we require a beam energy of at least $E_{e^-} = 525$ GeV to observe radiation zeros in the process $e^- e^+ \to t\bar{t}\gamma$ assuming a top quark mass of $m_t = 175$ GeV and an even higher energy to achieve a reasonable separation from the outgoing partons (see Fig. 4.17).[8]

For $\Theta_{cm} = 90°$ we can write the solutions in a very compact form. We find as a condition for which radiation zeros exist:

$$\rho \geq \rho_{crit} = \frac{2}{\sqrt{4 + e_Q^2}} \quad \Longleftrightarrow \quad m_Q \leq \frac{\sqrt{s}}{2}\frac{|e_Q|}{\sqrt{4 + e_Q^2}}. \tag{4.91}$$

---

[8] We do not consider here the contributions to the radiation pattern from photon emission off the decay products of heavy unstable quarks.
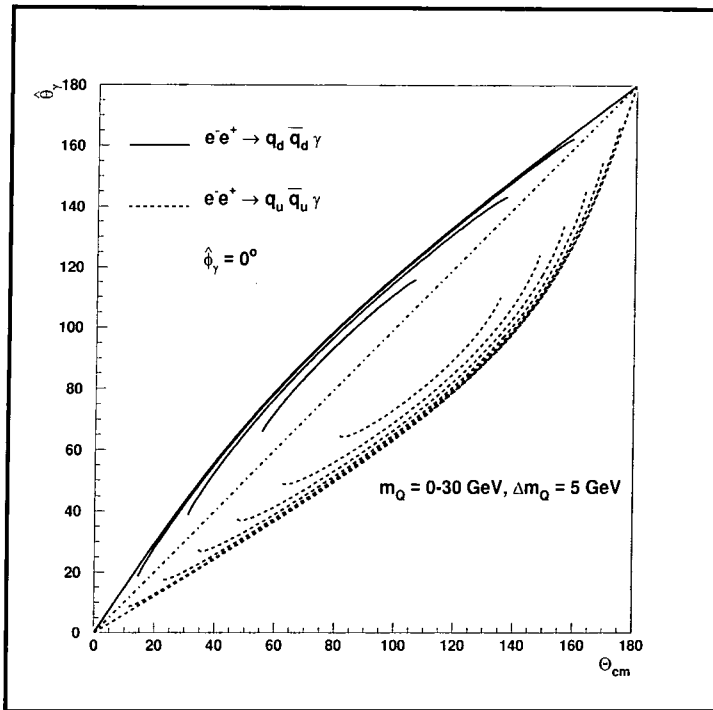
Figure 4.17: Same as Fig. 4.15 but now for massive quarks. The mass of the quarks is increased from $m_Q = 0$ GeV to $m_Q = 30$ GeV in steps of $\Delta m_Q = 5$ GeV. The higher the mass the closer the positions of the zeros move towards the collinear singularity (dash–dotted line). The beam energy is $E_{e^-} = \sqrt{s}/2 = 100$ GeV. Note that the appearance of radiation zeros is dependent on the quark mass and the c.m.s. scattering angle $\Theta_{\rm cm}$.

For example, in order to observe radiation zeros in $90°$ back–to–back scattering with $E_{e^-} = 100$ GeV we need $m_{d-\rm type} < 16.4$ GeV or $m_{u-\rm type} < 31.6$ GeV, conditions satisfied by all five light–quark flavours.

In Table 4.5 we present numerical values for $\rho_{\rm crit}$ and for $m_Q^{\rm crit}$, assuming a beam energy for the latter of $E_{e^-} = 100$ GeV. The values for $\rho_{\rm crit}$ are illustrated in Fig. 4.16.

An interesting conclusion from Table 4.5 concerns $e^- e^+ \to b\bar{b} + \gamma$. Assuming a mass for the b quark of $m_b \simeq 4.5$ GeV, the actual kinematics for the observation of radiation zeros become critical, especially at small c.m.s. scattering angles. For example, the outgoing b and $\bar{b}$ jets should be located at around $90° \pm 30°$ from the beam direction (*cf.* Fig. 4.17). Then the radiation zeros not only exist, but are also reasonably well separated from the collinear singularities (again *cf.* Fig. 4.17).

4.3.4 Arbitrary photon energies

We have so far identified radiation zeros using analytic techniques in the soft–photon approximation to the scattering matrix elements and phase space. However, as for the $eq \to eq\gamma$ scattering process studied in Section 4.2, zeros are also found in the *exact* cross section for fixed photon energies up to a critical maximum value.

To quantify this, we study planar $e^- e^+ \to q\bar{q}\gamma$ events in which (i) the polar angle of

	d–type quarks		u–type quarks	
Θ_{cm}	$\rho \geq$	$m_Q \leq$	$\rho \geq$	$m_Q \leq$
15°	0.9986	5.23 GeV	0.9977	6.72 GeV
30°	0.9951	9.82 GeV	0.9913	13.18 GeV
45°	0.9911	13.34 GeV	0.9815	19.13 GeV
60°	0.9878	15.60 GeV	0.9699	24.34 GeV
75°	0.9861	16.59 GeV	0.9583	28.58 GeV
90°	0.9864	16.44 GeV	0.9487	31.62 GeV

Table 4.5: Conditions for the appearance of radiation zeros for different c.m.s. frame scattering angles Θ_{cm}. The numbers in each row are ρ_{crit} and m_Q^{crit}, assuming a beam energy of $E_{e^-} = 100$ GeV for the latter. Critical mass values for other beam energies can be obtained by simple rescaling.

the quark (Θ_{cm}) is fixed, (ii) the energy of the photon (ω_γ) is fixed, and (iii) the polar angle of the photon (θ_γ) is varied. Note that the energy of the quark and the four–momentum of the antiquark are then fixed by energy–momentum conservation. In the limit $\omega_\gamma \to 0$ the kinematics of the soft–photon approximation studied in previous sections are reproduced. We find, as in Section 4.2.1, that the matrix element has radiation zeros for non–zero ω_γ, and that the position of the zero varies smoothly as ω_γ increases from zero. Note that we assumed *massless* quarks.

This is illustrated in Fig. 4.18, which shows the position $\widehat{\theta}_\gamma$ of the zero as a function of ω_γ, for d–type and u–type quarks and $\Theta_{\mathrm{cm}} = 90°$. The values at $\omega_\gamma = 0$ coincide with those obtained analytically in the soft–photon approximation, see for example Fig. 4.15. A variation of the position of the zero with the photon energy is to be expected, since with the above kinematics the direction of the antiquark changes as the photon energy is varied.

If the photon is too energetic then the zeros can disappear. This was also a feature of the $eq \to eq\gamma$ process studied in Section 4.2.1. For example, for $e_q = +2/3$ and $\Theta_{\mathrm{cm}} = 90°$ we only have radiation zeros for $\omega_\gamma/E_{\mathrm{beam}} < 0.47$. However because of the soft–photon energy spectrum, such upper limits are not particularly relevant in practice. Since the position of the zero varies with the photon energy, any binning in this quantity (above say some small threshold value $\omega_\gamma^{\mathrm{min}}$) will remove the zero and replace it with a sharp minimum located near the corresponding soft–photon approximation position. We will illustrate this in the following section.

4.3.5   A Monte Carlo study for $b\bar{b}\gamma$ production

Our study so far has been based on the ideal but unrealistic situation of well–defined four–momenta for the jets and the photon, fixed at particular directions in phase space.
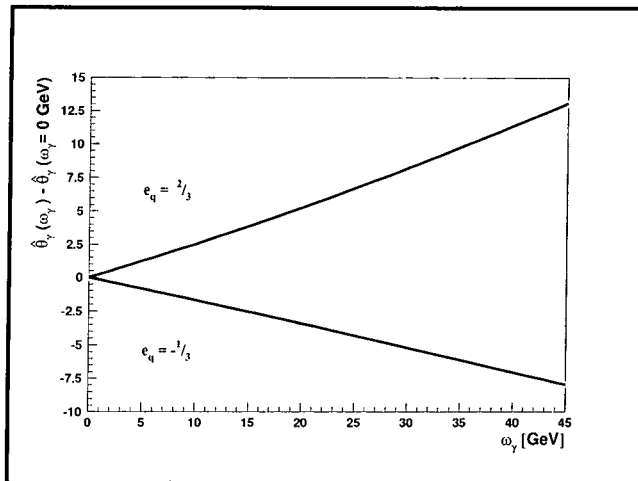
Figure 4.18: The positions $\widehat{\theta}_\gamma$ of the radiation zeros for the processes $e^-e^+ \to q_d\bar{q}_d\gamma$ and $e^-e^+ \to q_u\bar{q}_u\gamma$ as a function of the photon energy ω_γ, for $E_{e^-} = \sqrt{s}/2 = 100$ GeV and fixed c.m.s. frame (quark) scattering angle $\Theta_{\rm cm} = 90°$.

In practice, experiments deal with binned quantities and jets of finite mass and width. A more realistic study should therefore take these into account. Rather than try to model a particular detector capability, we can define a simple set of cuts which should take the main effects of smearing and binning into account. The aim is to see whether the radiation zeros remain visible after a more realistic analysis. We will, however, make the assumption that in our sample of $b\bar{b}\gamma$ events the b–jet can be distinguished from the $\bar{b}$–jet. This guarantees a radiation zero in the ideal case, as discussed in the previous sections.

We first generate a sample of $b\bar{b}\gamma$ events using a Monte Carlo which includes the exact phase space and matrix element. We choose a centre–of–mass energy of $\sqrt{s} = 200$ GeV. For this energy we can safely use the $m_b = 0$ massless quark approximation. As a further simplification we include only s–channel γ^* exchange.[9] The following sequence of cuts is applied:

$$10 \text{ GeV} < \omega_\gamma < 40 \text{ GeV} < E_{\bar{b}} < E_b , \qquad (4.92)$$

to ensure that the photon is the softest particle in the final state, and that the b–quark direction coincides with the thrust axis of the event. The photon is also required to be separated in angle from the beam and jet directions:

$$\theta_{\gamma,\text{beam}} > 20° , \qquad \theta_{\gamma,b}\theta_{\gamma,\bar{b}} > 10° . \qquad (4.93)$$

These cuts serve to define a 'measurable' sample of $b\bar{b}\gamma$ events.

To investigate the radiation zero we must introduce a planarity cut on the $b\bar{b}\gamma$ final state. We do this by requiring that the normals to the two planes defined by (i) the beam and outgoing b–quark directions and (ii) the $\bar{b}$–quark and photon directions are approximately parallel:

$$|\vec{n}_{13} \cdot \vec{n}_{4k}| > \cos 20° , \qquad (4.94)$$

---

[9]Including also Z exchange only affects the overall normalisation and not the shape of the photon distributions.

using the notation for momenta defined in Eq. (4.53). We can then study the polar angle
(θ_γ) distribution of the photon for various values of the polar angle (Θ_{cm}) of the thrust
axis (b–quark direction) with respect to the beam direction. In practice, we consider a
bin centred on $\theta_b = \Theta_{cm}$ of width $10°$, i.e. we integrate over

$$\Theta_{cm} - 5° < \theta_b < \Theta_{cm} + 5° \, . \tag{4.95}$$

Note that our cuts are deliberately chosen to mimic the soft–photon kinematics. However
because we integrate over the photon energy and smear the polar angle and planarity
criteria we expect to see DIPS in the photon distribution rather than strict zeros.
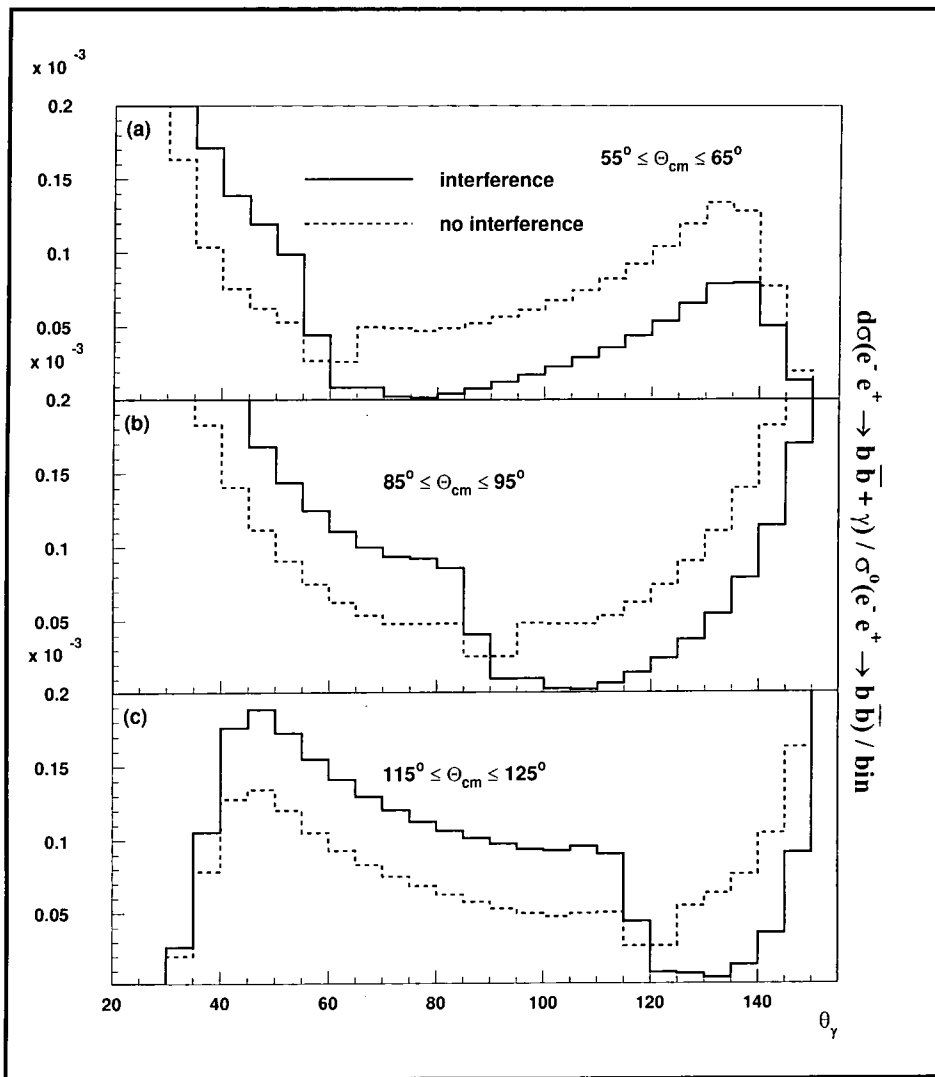
Figure 4.19: The θ_γ distribution (solid histograms) obtained in the Monte Carlo calculation of
$e^- e^+ \to b\bar{b}\gamma$ in the planar configuration. The various cuts are defined in the text. The Θ_{cm}
angles are (a) $60°$, (b) $90°$ and (c) $120°$. The dashed lines are the results of the corresponding
calculation with the interference terms removed.

Fig. 4.19 shows the θ_γ distribution for three different values of Θ_{cm}. Comparing with

Fig. 4.13, we once again see sharp dips at approximately the same position as in the 'ideal' soft–photon case. Note that the collinear singularities evident in Fig. 4.13 are now removed by the cuts. The suppression of the cross section at the position of the zeros can further be appreciated by comparing with the results obtained when the interference term in the matrix element squared is set to zero, corresponding to incoherent photon emission off the initial and final states. The results of this approximate calculation, shown as dashed lines in Fig. 4.19, do not exhibit any dip structure in the region of the zeros and are clearly distinguishable from the exact results.

4.3.6 Concluding remarks

Radiation zeros are an important consequence of the gauge structure of the electromagnetic interaction. They arise in different types of high–energy scattering processes. In this study we have investigated a particular type of radiation zero ('type 2' or 'planar') which is a feature of the process $e^+e^- \to q\bar{q}\gamma$. We derived expressions for the locations of the zeros in the soft–photon limit, and showed that the zeros persist for hard photons and massive quarks. However the experimental verification of such zeros is not straightforward. The zeros disappear on the Z^0 pole because the interference between initial– and final–state radiation is suppressed by the finite Z lifetime. The collision energy must therefore be greater or less than M_Z. Unfortunately the number of events beyond the Z^0 pole at present colliders is quite low. Apart from the resulting issue of the overall event rate, it is necessary to be able to distinguish quark from antiquark jets in order to compare with our predictions. This can perhaps we done with some efficiency for b–quark jets. We performed a Monte Carlo study which showed that 'realistic' distributions do indeed exhibit sharp dips in particular regions of phase space. Further studies using a more complete simulation of the final–state hadronisation process would be worthwhile.

4.4 The future of radiation zeros

> *"... thus measurements of radiation zeros are destined to be contaminated, compromised and ultimately corrupted."*
> *(R. W. Brown [Bro97])*

We already mentioned many problems that occur trying to experimentally measure the positions of radiation zeros, let us summarise the main obstructions

- Radiation zeros are dependent on the gauge couplings like charges, neutral current couplings g_i^L, etc. If a process is for example convoluted with the parton densities, then different subprocesses with different gauge couplings contribute to a reaction. So the radiation zeros are "smeared out" and it depends on the relative size of the radiation *dip* whether an identifiction is possible.

- Convolution with parton densities also includes particles with different masses. Again all these contributions together lead to a radiation dip. In Section 4.1 we

also mentioned *approximate* radiation zeros that occur if a massive gauge boson (Z) is radiated off.

- The particle jet is an object with finite size. Therefore the kinematics are not well defined and experimental cuts have to be introduced as we saw in the reaction $e^+e^-{\to}b\bar{b}\gamma$ in Section 4.3.5.

- Additional jets from higher QCD corrections will spoil the subtle gauge cancellation and thus 'fill up' the radiation zero. One has to reject the additional jets to recover the tree level kinematics. In practice one encounters a misidentification of a photon from a jet. A good γ–jet discrimination factor is needed to successfully identify the signal.

In this chapter we studied radiation zeros in $eq \to eq\gamma$ in Section 4.2 and $e^+e^- \to q\bar{q}\gamma$ in Section 4.3. We examined radiation zeros at a level with realistic experimental acceptance. Because the contribution of all partons destroys the sharp radiation zero it would be even worth looking at low–energy data at HERA or the TEVATRON, where mostly valence quarks contribute, to minimise this effect.

First results on successful measurements of radiation zeros are available. The CDF collaboration reports on such a measurement in the reactions $u\bar{d} \to W^+\gamma$ and $d\bar{u} \to W^-\gamma$ at the Fermilab TEVATRON collider [CDF97]. As the nature of radiation zeros is very sensitive to the gauge couplings of vector bosons and fermions, these studies provide probes to physics beyond the SM. The CDF collaboration concludes that anomalous couplings in above process can be ruled out.

As we discussed, radiation zeros are a general feature in gauge theories. There are in fact many more processes beyond the SM in which radiation zeros occur. Studies for the *classical* radiation zeros so far include

- A generalisation of the classical radiation zeros theorem (Eq. (4.4)) to supersymmetric theories with massless gaugino emission has been provided by Brown and Kowalski [BK84]. In theoretical studies radiation zeros have been found in the supersymmetric limit for processes such as $d\bar{u} \to \widetilde{W}\widetilde{\gamma}, \gamma e \to \widetilde{W}\widetilde{\nu}_e, \ldots$ [Rob85, Rob84]. In the supersymmetric limit these zeros are located at the same places as those for SM partners.

- Radiation zeros were also found in charged Higgs boson production $p\bar{p} \to H^{\pm}\gamma$ [HL88]. The small Yukawa couplings of $H^{\pm}$ to light fermions makes this process nearly unobservable. If kinematically accessible a process like $H^{\pm} \to t\bar{b}\gamma$ is more promising.

And these were studies for type 1 radiation zeros only.

What is left?

At the time of this thesis we still were not able to formulate a general theorem for the existence of the new type (type 2) (*cf.* Section 4.1.3) of radiation zeros in terms of gauge couplings. An existence proof, however, was possible, but more work on type 2 zeros has to follow. Our studies only marked a start. In principle all studies that have been done for type 1 zeros can be reconsidered for type 2 zeros. From the phenomenological point

of view type 2 zeros show the same features as their classical counterparts. But with the introduction of this new type of zeros many more processes, not obeying the 'same–sign rule' of Section 4.1.1, become accessible. In this framework we showed for the first time e^+e^- phenomenology as an example.

The process amplitudes are, as we have shown, very sensitive near the radiation zeros. They form a powerful diagnostic tool for gauge couplings and the hope is to find new physics in the vector boson sector of the SM.

This brings us back to the main focus of this thesis

> Probing the Standard Model and beyond at high–energy colliders !

References for Chapter 4

— B —

[BB82]   S.J. Brodsky and R.W. Brown, *Phys. Rev. Lett.* **49** (1982) 966.

[BBK83]   S.J. Brodsky, R.W. Brown and K.L. Kowalski, *Phys. Rev.* **D28** (1983) 624.

[BHO94]   U. Baur, T. Han and J. Ohnemus, *Phys. Rev. Lett.* **72** (1994) 3941.

[BK84]   R.W. Brown and K.L. Kowalski, *Phys. Lett.* **B144** (1984) 235.

[BMS79]   R.W. Brown, K.O. Mikaelian and D. Sahdev, *Phys. Rev.* **20** (1979) 1164.

[Bau97]   U. Baur, T. Han, N. Kauer, R. Sobey and D. Zeppenfeld, *Phys. Rev.* **D56** (1997) 140.

[Ber81]   F.A. Berends, R. Kleiss, P. De Causmaecker, R. Gastmans and T.T. Wu, *Phys. Lett.* **B103** (1981) 124.

[Bil85]   C.L. Bilchak, *J. Phys.* **G11** (1985) 1117.

[Bro97]   R.W. Brown, private communication.

— C —

[CDF97]   CDF Collaboration: Proceedings of the 10th Topical Workshop on Proton-Antiproton Collider Physics, Fermi National Accelerator Laboratory, Batavia, IL, May 9–13, 1995.

[Cou89]   G. Couture, *Phys. Rev.* **D39** (1989) 2527.

— D —

[DEL96]   DELPHI Collaboration: P. Abreu *et al.*, *Z. Phys.* **C72** (1996) 31.

[DH91]   M.A. Doncheski and F. Halzen, *Z. Phys.* **C52** (1991) 673.

— G —

[GM81]   T.R. Grose and K.O Mikaelian, *Phys. Rev.* **D23** (1981) 123.

— H —

[H1.95]   H1 Collaboration: T. Ahmed *et al.*, *Nucl. Phys.* **B439** (1995) 471.

[HHH84]   K. Hagiwara, F. Halzen and F. Herzog, *Phys. Lett.* **B135** (1984) 324.

[HL88]   X.G. He and H. Lew, *Mod. Phys. Lett.* **3** (1988) 1199.

— J —

[JW89]   S. Jadach and Z. Wąs, *Phys. Lett.* **B219** (1989) 103.

— L —

[LL75]   L.D. Landau and E.M. Lifshitz, The classical Theory of Fields, Pergamon Press, Oxford, 1975.

[LRS90]   G. Li, J. Reid and M.A. Samuel, *Phys. Rev.* **D41** (1990) 1675.

[LSS83]   M.L. Laursen, M.A. Samuel and A. Sen, *Phys. Rev.* **D28** (1983) 650.

[Lau84]   M.L. Laursen, M.A. Samuel, A. Sen and G.S. Sylvester, *Phys. Rev.* **D29** (1984) 994.

[Lau85]   M.L. Laursen, M.A. Samuel, A. Sen and G.S. Sylvester, *Phys. Rev.* **D31** (1985) 1657.

— M —

[MRS95]   A.D. Martin, R.G. Roberts and W.J. Stirling, *Phys. Lett.* **B354** (1995) 155.

[MSS79]   K.O. Mikaelian, D. Sahdev and M.A. Samuel, *Phys. Rev. Lett.* **43** (1979) 746.

[Mar92]   G. Marchesini, B.R. Webber, G. Abbiendi, I.G. Knowles, M.H. Seymour and L. Stanco, *Comp. Phys. Comm.* **67** (1992) 465.

— P —

[Pas83]   G. Passarino, *Nucl. Phys.* **B224** (1983) 265.

[Pas84]   G. Passarino, *Nucl. Phys.* **B241** (1984) 48.

— R —

[Rob84]   R. Robinett, *Phys. Rev.* **D30** (1984) 688.

[Rob85]   R. Robinett, *Phys. Rev.* **D31** (1985) 1657.

— S —

[Sjo94]   T. Sjöstrand, *Comp. Phys. Comm.* **82** (1994) 74.

— Z —

[ZEUS95]   ZEUS Collaboration: M. Derrick *et al.*, *Z. Phys.* **C65** (1995) 379.

Epilogue

"The pictures I contemplate painting would constitute a halfway state and an attempt to point out the direction of the future – without arriving there completely."

(J. Pollock)

In this thesis we studied different phenomenological aspects of modern topics in high–energy physics dealing either with tests of the SM or probes beyond it.

We showed how a non–perturbative soft Pomeron governs diffractive heavy flavour and Higgs cross sections at high–energy colliders and conclude that these predictions might be of great value for a further insight into the nature of soft and hard interactions. We also expect diffractive measurements of Higgs a great challenge for the experimentalists. Experimental results on diffractive W^+ production indicate that the soft–Pomeron model is not valid at high–energies. A possible explanation could be that the Pomeron has a two–component structure (soft and hard) and it is of theoretical interest to determine the scale dependent couplings of these components.

Beyond the SM we presented the Z' model and an additional heavy–vector quark triplet. Even though there is no evidence for a $R_{b,c}$ crisis anymore, i.e. the SM was proved once more successful, the jet–excess at the TEVATRON is still an open question. We performed a detailed analysis of the effects of a *leptophobic* Z' at the LHC and for further measurements at the TEVATRON and conclude that (especially at the LHC) the Z' should be *'visible'*.

Exploiting features of the SM we then discussed antenna patterns of soft photon and gluon radiation. We showed how these diagnostic tools may be used to search for new physics, like the Higgs boson at the future LHC. We also discussed *colour coherence* for which there is evidence from many high–energy experiments.

Finally we discussed another feature embedded in the SM which has not been detected before: a new type of radiation zero. Radiation zeros have been studied phenomenologically for some time and they have been *'seen'* experimentally at the TEVATRON. We propose measurements of the new type of radiation zeros at HERA and LEP by introducing physical cuts. These zeros, after their verification, can then be used to test, e.g., gauge couplings, especially the study of possible anomalous couplings.

Probing the SM sometimes leads to interesting and new physics. Many people are convinced that the SM is not the end of a long journey. A check of the new preprints appearing each day shows this quite dramatically. Understandable is the excitement among many if '*anomalies*' are reported from various experiments. We can assume that there is no evidence yet for a failure of the SM. And accepting this, one can concentrate on the many open problems within the SM. This thesis should be regarded as a contribution for this task.

Name Register